An Evaluation of Krypton Propellant in Hall Thrusters

by

Jesse Allen Linnell

A dissertation submitted in partial fulfillment
of the requirements for the degree of
Doctor of Philosophy
(Aerospace Engineering)
in The University of Michigan
2007

Doctoral Committee:

Professor Alec D. Gallimore, Chair
Professor Yue Ying Lau
Associate Professor John Edison Foster
Research Scientist Michael Keidar

"I would not give a fig for the simplicity this side of complexity, but I would give my life for the simplicity on the other side of complexity."

-Oliver Wendell Holmes, Jr.

Where is the Life we have lost in living?
Where is the wisdom we have lost in knowledge?
Where is the knowledge we have lost in information?

-T. S. Eliot

Acknowledgments

As it works out, it took me 143 days from the day that I started the "thesis.doc" file until the day that I turned the thesis in to my committee. Assuming I worked 8 hours a day, 7 days a week my typing speed works out to be about 1 word per minute. Ignoring the fact that there was a lot of copy-and-pasting from old articles, I guess that makes me the slowest typist of all time. Even still, the day I received my Ph.D. from the University of Michigan was a proud day and I couldn't have done it alone.

How is graduate school like a war in Iraq? If you don't have an exit strategy, then you'll probably get yourself into big trouble. With this said I'd like to thank my advisor, Alec Gallimore first and foremost. I always felt like there was a clear plan for my graduate work and when I started school, I knew I wouldn't spend the next 7-8 years of my life banging my head against the wall. Alec, you never did bed checks but you were always there for support if I needed you. While I was at PEPL, I had an interesting and well formed thesis topic, and I had access to one of the best facilities in the world. I really feel that I couldn't have gotten the breadth and quality of my education anywhere else.

Special thanks to my wife Lindsey. Thanks for putting up with my goofy hours and thanks for being understanding for these years. Thanks for the hour long commute to and from work so I could live close to the lab. Also, sorry for not taking out the trash because, "I'm too busy with work." I guess that excuse has finally run out.

I couldn't have completed my thesis if it weren't for a bunch of smart people that came before me. Thanks to Rich Hofer and James Haas. I've actually studied your entire dissertations and I probably know them as well as anyone. I wouldn't have gotten as far with my work if I didn't have your work to reference and build from. Thanks to Josh Rovey, Dan Herman, and Mitchell Walker. I really appreciated the help and insight that you gave me. Five minutes picking your brains are worth about 2 weeks trying to learn it myself. It really taught me the importance of asking for help. Josh an extra thanks to you for the late nights at the lab and having my back. Even if I asked you to swing by the lab between midnight and 4 a.m., I knew I could count on you. Oh yeah, thanks Erin Rovey for letting Josh spend his nights with me at work.

There are tons of other lab mates that bailed me out when I was stuck or just made my research life a lot easier. Thanks to Pete Peterson, Allen Victor, Tim Smith, Brian Beal, Dan Brown, David Kirtley, Kristina Lemmer, Thomas Liu, Robert Lobbia, Bailo Bah Ngom, Sonca Nguyen, and Bryan Reid. If I weren't already rambling I'd write you all a paragraph each. Also thanks go to Michael Keidar and Yevgeny Raitses for their fruitful discussion. There experience and expert point of view really helped my work and my understanding of the field.

I'd like to thank the François Xavier Bagnoud Foundation for funding during my time at University of Michigan. Thanks especially go to Madame Albina du Boisrouvray. I hope that I can follow your example and represent the Foundation with the class and dignity that that it deserves. Thanks to NASA Glenn Research Center for financial funding through research grant NCC04GA38G (grant monitor Mr. David Jacobson) and for use of government furnished equipment during my research. Also, thanks to my entire committee for taking the time to carefully review my thesis. With their help, this thesis is something that I am proud to put my name on.

Finally, I'd like to thank God for blessing me with the drive, diligence, and the focus necessary to complete my Ph.D.

Jesse Allen Linnell
January 29, 2007

Table of Contents

Acknowledgments .... **ii**

List of Figures .... **ix**

List of Tables .... **xviii**

List of Appendices .... **xx**

Nomenclature .... **xxi**

Abstract .... **xxx**

Chapter 1. Introduction **1**

1.1 Rocket Fundamentals 1
1.2 Electric Propulsion Overview 2
1.2.1 Types of Electric Propulsion 4
1.3 Hall Thruster Caricature 5
1.4 Characteristics of Krypton Propellant 10
1.4.1 Performance 10
1.4.2 Hall Thruster Operation with Krypton 12
1.4.3 Storage and Containment 13
1.4.4 Cost 14
1.4.5 Lifetime and Erosion Rates 14
1.5 Flight Performance of Xenon and Krypton 15
1.5.1 Constant Power Performance 18
1.5.2 Fixed Trip Time Performance 19
1.5.3 Variable Trip Time Performance 22
1.5.4 Trip Time Optimized for Cost 23
1.5.5 Summary of Krypton Mission Analysis 26
1.6 Motivation 27
1.7 Contribution to Research 27

Chapter 2. Facilities, Apparatus, and Techniques **30**

2.1 Facility 30
2.1.1 Large Vacuum Test Facility 30
2.1.2 Propellant Delivery 32
2.2 Thrusters 33

2.2.1 NASA-173Mv1 33
2.2.2 UM/AFRL P5 35
2.3 External Diagnostics 37
2.3.1 Thrust Stand 37
2.3.2 E×B Probe 39
2.3.3 Magnetically Filtered Faraday Probe 43
2.3.4 Retarding Potential Analyzer 46
2.4 Internal Diagnostics 50
2.4.1 High-Speed Axial Reciprocation Probe System 51
2.4.2 Floating Emissive Probe 52
2.4.2.1 Theory of Operation 53
2.4.2.2 Space-Charge Limited Sheath 54
2.4.2.3 Space-Charge Limited Sheath Correction 56
2.4.2.4 Emissive Probe Design 59
2.4.2.5 Floating Emissive Operation 62
2.4.3 Single Langmuir Probe 65
2.4.3.1 Theory of Operation 66
2.4.3.2 Langmuir Probe Design 67
2.4.3.3 Langmuir Probe Operation 68
2.4.3.4 Data Analysis 73

Chapter 3. Performance Study and Analysis 80

3.1 Efficiency Optimization Scaling 80
3.1.1 Discussion of Optimization Design Consideration 85
3.1.1.1 Discharge Channel Dimensions 85
3.1.1.2 Neutral Temperature 86
3.1.1.3 Cold Anode Experiment 87
3.2 Performance Results 89
3.2.1 Specific Impulse Trends 89
3.2.2 High-Voltage Krypton Operation 90
3.2.3 Voltage Trends 91
3.2.4 Flow Rate Trends 93
3.3 Faraday Probe Measurement of Propellant Utilization 94
3.4 Detailed Efficiency Analysis 96
3.4.1 Phenomenological Performance Model 97
3.4.2 Acceleration and Beam Divergence Efficiency 99
3.4.3 Efficiency Analysis Results 105
3.4.3.1 Operation Points of Interest 105
3.4.3.2 Retarding Potential Analyzer Results 106
3.4.3.3 E×B Probe Results 109
3.4.3.4 Magnetically Filtered Faraday Probe Results 110
3.4.3.5 Efficiency Analysis: Current, Propellant, and Beam Divergence Efficiency 111

Chapter 4. Internal Experimental Results.. 117

4.1 Perturbation Analysis..117
4.2 Internal Emissive Probe Results 122
4.2.1 Internal Emissive Operation Points 122
4.2.2 Magnetic Field Topology Trends..123
4.2.2.1 300-V Operation 125
4.2.2.2 500-V Operation 131
4.2.3 Krypton-Xenon Comparison...138
4.2.3.1 500-V Comparison...138
4.2.3.2 600-V Comparison...144
4.3 Internal Langmuir Probe Results 150
4.3.1 Internal Langmuir Operation Points 151
4.3.2 300-V Xenon Operation..152
4.3.3 Magnetic Field Topology Trends..154
4.3.4 Krypton-Xenon Comparison...158
4.3.4.1 500-V Krypton Case with Matched B-Field..163
4.4 Comparison of Electron Temperature Measurements 166

Chapter 5. Internal Analysis.. 169

5.1 Internal Electron Temperature Gradients...169
5.2 Thermalized Potential 172
5.3 Ion Particle Trajectories..174
5.4 Numerical Fluid Model..175
5.4.1 Description of Model 175
5.4.2 Axisymmetric Finite Volume Formulation...176
5.4.3 Numerical Method 183
5.4.4 Boundary Conditions 185
5.4.5 Initializations...185
5.4.6 Assumptions...186
5.4.6.1 Ionization Rate Source Term 186
5.4.6.2 Ion Number Density Modification...187
5.4.6.3 Radial Electric Field 187
5.4.6.4 Momentum Transfer Due to Ionization/Recombination.........................188
5.4.7 Discussion of Results..189
5.4.7.1 Ionization Rate 189
5.4.7.2 Neutral Number Density..192
5.4.8 Evaluation of the Model...194
5.5 Electron Motion 195
5.5.1 Fluid Equations of Motion 195
5.5.2 Hall Parameter and Electron Mobility 200
5.5.2.1 Classical Analysis 202
5.5.2.2 Experimental Analysis..204
5.5.2.3 Collision Rate Results...205
5.5.2.4 Hall Parameter Results...208
5.5.2.5 Electron Mobility Results 213

5.5.3 Azimuthal Current 217
5.5.3.1 Electron Fluid Drifts 217
5.5.3.2 Total Hall Current 218
5.5.3.3 Electron Drift Energy 220
5.5.3.4 Global Current Trends 222
5.5.4 Particle Drifts 222
5.5.4.1 Nonuniform Electric Field Drift 223
5.5.4.2 Curvature Drift 224
5.5.4.3 Grad-B Drift 225
5.6 Hall Thruster Zones 226
5.6.1 Acceleration Zone 227
5.6.2 Ionization Zone 234
5.6.2.1 Ion Number Density Trends 234
5.6.2.2 Numerical Fluid Method 236
5.6.2.3 Electron Impact Ionization Calculation 238
5.6.2.4 Comparison of Methods 240
5.6.3 Summary of Hall Thruster Zones 240

Chapter 6. Magnetic Field Topology Analysis 244

6.1 Modern Magnetic Field Design in Brief 245
6.2 Magnetic Field Gradient 246
6.3 Plasma Lens 249
6.4 Magnetic Mirror 252
6.5 Acceleration Zone Analysis 259

Chapter 7. Conclusions 266

7.1 Flight Performance Analysis 267
7.2 Krypton Performance 268
7.3 Krypton Internal Characterization 269
7.4 Design Suggestions for Krypton Thrusters 272
7.5 General Hall Thruster Findings 275
7.6 Suggestions for Future Work 278

Appendix A. NASA-173Mv1 Performance Data 280

Appendix B. UM/AFRL P5 Performance Data 287

Appendix C. Internal Emissive Probe Results 289

Appendix D. Internal Langmuir Probe Results 300

References 303

List of Figures

Figure 1-1. Generalized Hall Thruster Schematic 6

Figure 1-2. Hall Thruster Zones.. 7

Figure 1-3. Isometric View of a Hall Thruster 9

Figure 1-4. Performance Fits for Xenon and Krypton Propellant 11

Figure 1-5. Constant Power Performance Comparison for Xenon and Krypton Propellant 19

Figure 1-6. Payload Mass Fraction Optimization for a) 180, b) 270, and c) 360 Day Trip Times.. 21

Figure 1-7. Payload Mass Fraction with Variable Trip Time... 22

Figure 1-8. Propellant Related Costs Dependence on Trip Time 23

Figure 1-9. Minimized Costs for Given Delta-V Requirements. Case a) corresponds to modern technology with medium specific impulse, case b) corresponds to state-of-the-art technology with medium specific impulse, and case c) corresponds to modern technology with low specific impulse. 25

Figure 2-1. Photograph of the Large Vacuum Test Facility at The University of Michigan's Plasmadynamics and Electric Propulsion Laboratory 30

Figure 2-2. Schematic of the Large Vacuum Test Facility (Not to Scale) 32

Figure 2-3. NASA-173Mv1 Hall Thruster... 34

Figure 2-4. Schematic of the Hall Thruster Circuit 35

Figure 2-5. UM/AFRL P5 Hall Thruster 36

Figure 2-6. PEPL's Null Type Inverted Pendulum Thrust Stand 37

Figure 2-7. Real-Time Performance Optimization Example.. 38

Figure 2-8. E×B Ion Current Integration Method.. 43

Figure 2-9. Faraday Probe and Retarding Potential Analyzer Data Collection at Station 1 44

Figure 2-10. Retarding Potential Analyzer Schematic 47

Figure 2-11. Retarding Potential Analyzed Potential Diagram 47

Figure 2-12. Retarding Potential Analyzer Data Processing Example 50

Figure 2-13. Internal Probe Experimental Setup 51

Figure 2-14. Discharge Channel Probe Insertion 51

Figure 2-15. High-Speed Axial Reciprocating Probe System 52

Figure 2-16. Ideal Characteristic Emissive Probe Curve 53

Figure 2-17. Emissive Probe Sheath. The different operation regimes are shown by dashed lines and are labeled accordingly. (Not to scale) 55

Figure 2-18. Emissive Probe Schematic 60

Figure 2-19. Emissive Capabilities of Pure and 1% Thoriated Tungsten 61

Figure 2-20. Photograph of the Low SEE Ringlets 62

Figure 2-21. Floating Emissive Probe Circuit 63

Figure 2-22. Emissive Probe Sweep Example 64

Figure 2-23. Region Mapped by the Floating Emissive Probe 65

Figure 2-24. Single Langmuir Probe Design 68

Figure 2-25. Probe Bias for Data Collection 69

Figure 2-26. The Langmuir Probe Mapped Region 70

Figure 2-27. Stray Capacitance Causes by Voltage Oscillation 71

Figure 2-28. Langmuir Probe Circuit 72

Figure 2-29. The Effect of the Breathing Mode on the I-V Characteristic 76

Figure 2-30. Probe Radius to Debye Length Ratio Along the Thruster Centerline 79

Figure 3-1. Ratio of Krypton to Xenon Total Electron-Atom Impact Ionization Collision Cross Section versus Electron Energy 83

Figure 3-2. The Water Cooled Anode for Active Thermal Management........................ 87

Figure 3-3. Water Cooled Anode Schematic (Not to scale) 88

Figure 3-4. Cold Anode Experimental Setup.. 88

Figure 3-5. Krypton and Xenon Anode Specific Impulse versus Thrust......................... 90

Figure 3-6. NASA-173Mv1 Performance at a Discharge Voltage of 1200 V with Krypton Propellant.. 91

Figure 3-7. Anode Efficiency versus Discharge Voltage for the NASA-173Mv1 92

Figure 3-8. Anode Efficiency versus Discharge Voltage for the UM/AFRL P5 with 102.4 sccm Anode Flow Rate 93

Figure 3-9. Krypton Anode Efficiency versus Anode Flow Rate................................... 94

Figure 3-10. Anode Efficiency and Propellant Utilization Efficiency Comparison........ 96

Figure 3-11. Normalized Voltage Distribution Function for Operation Point 12.......... 107

Figure 3-12. Voltage Energy Distribution Comparison for Xenon and Krypton at 8 kW without the Trim Coil.. 109

Figure 3-13. Ion Current Density Comparison of the 8 kW Case without the Trim Coil 111

Figure 3-14. Anode Efficiency versus Anode Flow Rate... 113

Figure 3-15. Propellant Utilization Efficiency versus Anode Flow Rate...................... 114

Figure 3-16. Current Utilization Efficiency versus Anode Flow Rate 115

Figure 3-17. Beam Divergence Efficiency versus Anode Flow Rate........................... 116

Figure 4-1. Probe Induced Perturbations for the 500 V, Xenon Case 119

Figure 4-2. Plasma Potential Map for the UM/AFRL P5 Hall Thruster operation at 10 A and 300 V (Ref. 59) 124

Figure 4-3. Plasma Potential Map for the 300-V Cases (a) without and (b) with the Trim Coil... 126

Figure 4-4. Electron Temperature Map for the 300-V Cases (a) without and (b) with the Trim Coil.. 127

Figure 4-5. Axial Electric Field for the 300-V Cases (a) without and (b) with the Trim Coil... 128

Figure 4-6. Radial Electric Field Map for the 300-V Cases (a) without and (b) with the Trim Coil 129

Figure 4-7. Centerline Plasma Properties for the 300-V Non-Trim Coil and Trim Coil Conditions 130

Figure 4-8. Plasma Potential Map for the 500-V Cases (a) without and (b) with the Trim Coil 132

Figure 4-9. Electron Temperature Map for the 500-V Cases (a) without and (b) with the Trim Coil 133

Figure 4-10. Axial Electric Field Map for the 500-V Cases (a) without and (b) with the Trim Coil 134

Figure 4-11. Radial Electric Field Map for the 500-V Cases (a) without and (b) with the Trim Coil 135

Figure 4-12. Centerline Plasma Properties for the 500-V Non-Trim Coil and Trim Coil Conditions 137

Figure 4-13. Plasma Potential Map for (a) Xenon and (b) Krypton at a Discharge Voltage of 500 V 140

Figure 4-14. Electron Temperature Map for (a) Xenon and (b) Krypton at a Discharge Voltage of 500 V 141

Figure 4-15. Axial Electric Field Map for (a) Xenon and (b) Krypton at a Discharge Voltage of 500 V 142

Figure 4-16. Radial Electric Field Map for (a) Xenon and (b) Krypton at a Discharge Voltage of 500 V 143

Figure 4-17. Centerline Emissive Probe Results for Xenon and Krypton at a Discharge Voltage of 500 V 144

Figure 4-18. Plasma Potential Map for (a) Xenon and (b) Krypton at a Discharge Voltage of 600 V 145

Figure 4-19. Electron Temperature Map for (a) Xenon and (b) Krypton at a Discharge Voltage of 600 V 146

Figure 4-20. Axial Electric Field Map for (a) Xenon and (b) Krypton at a Discharge Voltage of 600 V 147

Figure 4-21. Radial Electric Field Map for (a) Xenon and (b) Krypton at a Discharge Voltage of 600 V 149

Figure 4-22. Centerline Emissive Probe Results for Xenon and Krypton at a Discharge Voltage of 600 V 150

Figure 4-23. Internal Langmuir Probe Results for 300-V Xenon Operation with the Trim Coil (Point 2) 152

Figure 4-24. Centerline Langmuir Probe Results for Xenon Operation at a Discharge Voltage of 300 V, with the Trim Coil (Point 2) 153

Figure 4-25. Ion Number Density Map for 500-V Xenon Operation without (a) and with the Trim Coil (b) 155

Figure 4-26. Electron Temperature Map for 500-V Xenon Operation without (Point 3) and with the Trim Coil (Point 4) 157

Figure 4-27. Centerline Langmuir Probe Results for 500-V Non-Trim Coil (Point 3) and Trim Coil (Point 4) Conditions 158

Figure 4-28. Ion Number Density Map for Xenon (Point 4) and Krypton (Point 6) at a Discharge Voltage of 500 V 159

Figure 4-29. Electron Temperature Map for Xenon (Point 4) and Krypton (Point 6) at a Discharge Voltage of 500 V 161

Figure 4-30. Centerline Langmuir Probe Results for Xenon (Point 4) and Krypton (Point 6) at a Discharge Voltage of 500 V 163

Figure 4-31. Internal Langmuir Probe Results for 500-V Krypton Operation with Matched B-field (Point 8) 164

Figure 4-32. Probe Induced Perturbations for the 500-V Krypton Case with Matched B-field (Point 8) 165

Figure 4-33. Comparison between Xenon and Krypton Discharge Current Oscillations 166

Figure 4-34. Comparison of Emissive Probe and Langmuir Probe Electron Temperature Measurements 168

Figure 5-1. Electron Temperature versus Plasma Potential for a) 500-V Xenon Operation and 500-V Krypton Operation 171

Figure 5-2. Thermalized Potential Maps for the a) 300-V and b) 500-V Xenon Cases, and c) 500-V Krypton case (all with the Trim Coil) 173

Figure 5-3. Ion Particle Trajectories for the 500-V Xenon and Krypton Cases with the Trim Coil 175

Figure 5-4. The Axisymmetric Control Volume 181

Figure 5-5. Ionization Rate from the Numerical Model 190

Figure 5-6. Ionization Rate from the Numerical Model with 5 mm Shifted Ion Number Density 191

Figure 5-7. Neutral Number Density Calculated from the Numerical Model 192

Figure 5-8. Neutral Number Density Calculated from the 1-Dimensional Analysis..... 193

Figure 5-9. Coordinate Transfer Relative to the Magnetic Field................................. 197

Figure 5-10. Electron-Neutral Momentum Exchange Collision Cross-Sections for Xenon 203

Figure 5-11. Electron-Neutral Momentum Exchange Collision Cross-Sections for Krypton 204

Figure 5-12. Centerline Collision Rates for the 500-V Xe and Kr Cases. a) 500-V xenon without the trim coil, b) 500-V xenon with the trim coil, and c) 500-V krypton with the trim coil. 206

Figure 5-13. Classical Hall Parameter for the 500-V Xenon and Krypton Cases 209

Figure 5-14. Experimental Hall Parameter for the 500-V Xenon and Krypton Cases .. 210

Figure 5-15. Centerline Hall Parameters for the 500-V Xenon and Krypton Cases. (a) 500-V xenon without the trim coil, b) 500-V xenon with the trim coil, and c) 500-V krypton with the trim coil) 212

Figure 5-16. Axial Electron mobility for the 500-V Xenon and Krypton Cases........... 214

Figure 5-17. Radial Electron mobility for the 500-V Xenon and Krypton Cases 215

Figure 5-18. R-Z Electron mobility for the 500-V Xenon and Krypton Cases 216

Figure 5-19. Azimuthal Electron Currents for the 300-V Xenon Case with the Trim Coil 218

Figure 5-20. Total Hall Current for the 500-V Xenon and Krypton Cases 219

Figure 5-21. Electron Drift Energy for the 500-V Xenon and Krypton Points 221

Figure 5-22. Nonuniform Electric Field Drift Current for the 300-V Xenon Case with the Trim Coil.. 224

Figure 5-23. Curvature Drift Current for the 300-V Xenon Case with the Trim Coil... 225

Figure 5-24. Grad-B Drift Current for the 300-V Xenon Case with the Trim Coil....... 226

Figure 5-25. Acceleration Zone and Peak Electric Field Description 228

Figure 5-26. Acceleration Zones for the 300-V Xenon Case with and without the Trim Coil... 230

Figure 5-27. Acceleration Zones for the 500-V Xenon and Krypton Cases................. 232

Figure 5-28. Acceleration Zones for the 600-V Xenon and Krypton Cases................. 233

Figure 5-29. Ion Production Rate Based on Number Density 235

Figure 5-30. Ionization Rate Calculation Based on the Numerical Model................... 237

Figure 5-31. Total Electron Impact Ionization Collision Cross Sections for Xenon and Krypton 238

Figure 5-32. Total Electron Impact Ionization Collision Rates for the 500-V Xenon and Krypton Cases.. 239

Figure 5-33. Comparison of All Ionization zone Calculation Methods for the 500-V Xenon Case with the Trim Coil 240

Figure 5-34. Hall Thruster Zones for the 300-V Xenon Cases.................................... 241

Figure 5-35. Hall Thruster Zones for the 500-V Xenon and Krypton Cases................ 243

Figure 6-1. Normalized F-function Comparison With and Without the Trim Coil....... 247

Figure 6-2. Normalized F-function for Xenon and Krypton Operation (Both with the trim coil) 249

Figure 6-3. Normalized Magnetic Field Curvature... 251

Figure 6-4. Normalized Ω-Function 256

Figure 6-5. Normalized Mirror Pressure Term 258

Figure 6-6. Electron Leakage Across the Field Lines.. 260

Figure 6-7. Mapping the Normalized Electron Impedance in the Acceleration Zone... 262

Figure 6-8. The Acceleration Zone's Start (a) and End (b) for Different Peak Magnetic Field Strengths 263

Figure 6-9. Beam divergence Efficiency as a Function of Peak Magnetic Field Strength 264

Figure C-1. Internal Emissive Probe Results for 600-V Xenon Operation without the Trim Coil (Point C-1)...290

Figure C-2. Internal Emissive Probe Results for 500-V Krypton Operation without the Trim Coil and Matched Flow (Point C-2)..291

Figure C-3. Internal Emissive Probe Results for 500-V Krypton Operation with the Trim Coil and Matched Flow (Point C-3)..292

Figure C-4. Internal Emissive Probe Results for 500-V Krypton Operation without the Trim Coil and Matched Power (Point C-4)..293

Figure C-5. Internal Emissive Probe Results for 600-V Krypton Operation without the Trim Coil and Matched Flow (Point C-5)..294

Figure C-6. Internal Emissive Probe Results for 600-V Krypton Operation with the Trim Coil and Matched Flow (Point C-6)..295

Figure C-7. Internal Emissive Probe Results for 600-V Krypton Operation without the Trim Coil and Matched Power (Point C-7)..296

Figure C-8. Internal Langmuir Probe Centerline Properties for 500-V Krypton Operation with the Trim Coil and Matched Flow (Point C-1)..297

Figure C-9. Internal Langmuir Probe Centerline Properties for 500-V Krypton Operation with the Trim Coil and Matched Flow (Point C-2)..297

Figure C-10. Internal Langmuir Probe Centerline Properties for 500-V Krypton Operation with the Trim Coil and Matched Flow (Point C-3)..297

Figure C-11. Internal Langmuir Probe Centerline Properties for 500-V Krypton Operation with the Trim Coil and Matched Flow (Point C-4)..298

Figure C-12. Internal Langmuir Probe Centerline Properties for 500-V Krypton Operation with the Trim Coil and Matched Flow (Point C-5)..298

Figure C-13. Internal Langmuir Probe Centerline Properties for 500-V Krypton Operation with the Trim Coil and Matched Flow (Point C-6)..298

Figure C-14. Internal Langmuir Probe Centerline Properties for 500-V Krypton Operation with the Trim Coil and Matched Flow (Point C-7)..299

Figure D-1. Internal Langmuir Probe Results for 300-V Xenon Operation without the Trim Coil (Point D-1) 300

Figure D-2. Internal Langmuir Probe Centerline Properties for 300-V Xenon Operation without the Trim Coil (Point D-1) 301

Figure D-3. Internal Langmuir Probe Results for 500-V Krypton Operation with the Trim Coil and Matched Flow (Point D-2) 301

Figure D-4. Internal Langmuir Probe Centerline Properties for 500-V Krypton Operation with the Trim Coil and Matched Flow (Point D-2) 302

Figure D-5. Internal Langmuir Probe Results for 500-V Krypton Operation with the Matched B-Field and Matched Flow (Point D-3) 302

List of Tables

Table 1-1. Typical Performance Parameters for Various Space Propulsion Systems 4

Table 1-2. Ionization Potentials for Xenon and Krypton 11

Table 3-1. Operation Points of Interest for the Faraday Probe Analysis 95

Table 3-2. Operating Conditions for the 700 V, 6 and 8 kW Cases 106

Table 3-3. RPA Results for the 700 V, 6 and 8 kW Operation Points........................... 107

Table 3-4. E×B Results for the 700 V, 6 and 8 kW Operation Points 109

Table 3-5. Magnetically Filtered Faraday Probe Results for the 6 and 8 kW Operation Points... 110

Table 3-6. The Complete Efficiency Analysis for Krypton and Xenon Operation Points 111

Table 4-1. Operation Points for Internal Plasma Potential Mapping............................ 123

Table 4-2. Thruster Operating Conditions for the Internal Langmuir Probe Mapping . 151

Table 5-1. Global Current Trends for the 500-V Xenon and Krypton Points 222

Table 5-2. Acceleration Zone Boundaries and Lengths.. 228

Table A-1. NASA-173Mv1 Performance Data Using Xenon Propellant, A 281

Table A-2. NASA-173Mv1 Performance Data Using Xenon Propellant, B 282

Table A-3. NASA-173Mv1 Performance Data Using Krypton Propellant, A 283

Table A-4. NASA-173Mv1 Performance Data Using Krypton Propellant, B 284

Table A-5. NASA-173Mv1 Performance Data Using Krypton Propellant, C 285

Table A-6. NASA-173Mv1 Performance Data Using Krypton Propellant, D 286

Table B-1. UM/AFRL P5 Performance Data Using Xenon Propellant..........................287

Table B-2. UM/AFRL P5 Performance Data Using Krypton Propellant 288

Table C-1. Additional Operation Points for Internal Emissive Probe Mapping.............289

Table D-1. Additional Operation Points for Internal Langmuir Probe Mapping 300

List of Appendices

Appendix A. NASA-173Mv1 Performance Data 280

Appendix B. UM/AFRL P5 Performance Data 287

Appendix C. Internal Emissive Probe Results 289

Appendix D. Internal Langmuir Probe Results..300

Nomenclature

Constants

e	Elementary charge	[1.6×10^{-19} C]
g	Gravitational constant	[9.81 m s^{-2}]
k_B	Boltzmann Constant	[1.38×10^{-23} m^2 kg s^{-2} K^{-1}]
m_e	Electron mass	[9.1×10^{-31} kg]
M_i	Ion mass	[2.2×10^{-25} for Xe and 1.4×10^{-25} kg for Kr]
n_o	Reference number density	[10^{12} cm^{-3}]

Variables

A_c	Collector area	[m^2]
A_{ch}	Discharge channel cross sectional area	[m^2]
A_{em}	Richardson's constant	[A cm^{-2} K^{-2}]
A_p	Probe Surface area	[m^2]
A_s	Probe collection area	[m^2]
B	Magnetic flux density	[G]
b	Discharge channel width	[m]
C_f	Pressure correction factor	[-]
D	Electron diffusivity	[m^2 s^{-1}]
d	Parallel plate gap distance	[m]
$D_\perp$	Electron cross-field diffusivity	[m^2 s^{-1}]

E	Electric field	[V m^{-1}]
$\hat{e}$	Unit vector normal to control volume surface	[-]
F	Flux term	[-]
$f(V)$	Ion voltage distribution function	[s m^{-1}]
f_B	Breathing mode frequency	[Hz]
$f_{b\text{-}t}$	Burn time to trip time ratio	[-]
F_M	Magnetic mirror force	[N]
F_∇	Function quantifying the magnetic field gradient	[-]
G	Source term	[-]
G_M	Mirror strength number	[-]
$g(\theta)$	Normalized ion current density function at angle θ	[A m^{-2}]
I_b	Beam current	[A]
I_D	Discharge current	[A]
I_i	Ion current	[A]
$I_{i,i}$	Current from the ith ion species	[A]
I_m	Streamline electron impedance	[Ω]
I_p	Probe current	[A]
I_{sp}	Specific impulse	[s]
$j(\theta)$	Ion current density at angle θ	[A m^{-2}]
j_{em}	Emitted electron current density	[A cm^{-2}]
j_{es}	Collected electron current density	[A cm^{-2}]
J_{ez}	Electron current density to the anode	[A cm^{-2}]
$J_{E\times B}$	E×B drift current	[A m^{-2}]

$j_{FP}(\theta)$	Ion current density measured by Faraday probe at angle θ	[A m^{-2}]
K	Undefined constant	[-]
K'	Undefined constant	[-]
K_{ft}	Fuel tank mass ratio	[-]
K_n	Knudsen number	[-]
L_{ch}	Discharge channel length	[m]
L_i	Ionization zone length	[m]
l_p	Probe length	[m]
$\dot{m}_a$	Anode mass flow rate	[kg s^{-1} or sccm]
$\dot{m}_b$	Total ion mass flow rate	[kg s^{-1}]
M_f	Final rocket mass	[kg]
M_{ft}	Fuel tank mass	[kg]
$\dot{m}_i(\theta)$	Ion mass flow rate at angle θ	[kg s^{-1}]
M_i	Mass of propellant atom	[kg]
M_o	Initial rocket mass	[kg]
M_{pow}	Power system mass	[kg]
$\dot{m}_{prop}$	Propellant mass flow rate	[kg s^{-1}]
M_{prop}	Propellant mass	[kg]
n_b	Total ion number density	[m^{-3}]
n_e	Electron number density	[m^{-3}]
n_i	Ion number density	[m^{-3}]
$n_{i,i}$	Number density of the i^{th} ion species	[m^{-3}]
n_n	Neutral number density	[m^{-3}]

P_b	Chamber base pressure	[Torr]
P_C	Corrected chamber pressure	[Torr]
P_D	Discharge power	[W]
P_i	Indicated chamber pressure or Ion pressure	[Torr or Pa]
P_m	Mirror pressure function	[-]
P_n	Neutral pressure	[Torr and Pa]
p_o	Containment vessel pressure	[Pa]
P_{sys}	Total system power	[W]
Q_{ei}	Electron-ion collision cross section	[m^2]
Q_{en}	Electron-neutral collision cross section	[m^2]
$Q_{i,n}$	Ionization collision cross section	[m^2]
r	Radial location	[m]
R_{Ioniz}	Total ionization rate	[$s^{-1}cm^{-3}$]
R_c	Radius of curvature	[m]
$r_{c,e}$	Electron cyclotron radius	[m]
$r_{c,i}$	Ion cyclotron radius	[m]
R_m	Magnetic mirror ratio	[-]
r_p	Probe radius	[m]
S	Area of control volume surface	[m^2]
$\overline{\overline{T}}$	Transformation tensor	[-]
T_e	Electron temperature	[K or eV]
t_b	Thruster burn time	[s]
t_i	Characteristic ionization time	[s]

t_{res}	Neutral residence time	[s]
T_n	Neutral temperature	[K]
t_t	Mission trip time	[s]
T_w	Emissive probe temperature	[K]
U	Conserved quantity	[-]
U_e	Propellant exit velocity	[m s^{-1}]
V	Voltage or Volume	[V or m^3]
V_a	Acceleration voltage	[V]
v_a	Ion velocity	[m s^{-1}]
$\dot{v}_a$	Anode volumetric flow rate	[sccm]
$V_{a,eff}$	Effective acceleration voltage	[V]
$V_{a,i}$	Acceleration voltage of the ith ion species	[V]
$v_{a,i}$	Velocity of the ith ion species	[m s^{-1}]
v_{coll}	Collected ion velocity	[m s^{-1}]
V_D	Discharge voltage	[V]
V_e	Electron velocity	[m s^{-1}]
V_E	Nonuniform electric field drift	[m/s]
$V_{E\times B}$	E×B drift	[m/s]
V_i	Ion velocity	[m s^{-1}]
V_k	Cathode potential	[V]
V_l	Loss voltage	[V]
V_{mp}	Most probable voltage	[V]
V_{MT}	Momentum transfer velocity	[m s^{-1}]

V_n	Neutral velocity	[m s^{-1}]
V_p	Plasma potential	[V]
V_p^*	Thermalized potential	[V]
V_{probe}	Probe voltage	[V]
V_R	Curvature drift	[m/s]
V_{th}	Thermal velocity	[m s^{-1}]
V_z	Axial acceleration voltage	[V]
$V_{z,i}$	Axial acceleration voltage of the ith ion species	[V]
$v_{z,i}$	Axial velocity of the ith ion species	[V]
$V_{\nabla B}$	Grad-B drift	[m/s]
W_{power}	Power system cost per Watt	[\$ W^{-1}]
x	Spatial variable	[m]
Y_{launch}	Launch cost per kg	[\$ kg^{-1}]
Y_{prop}	Propellant cost per kg	[\$ kg^{-1}]
z	Axial location or Distance from thruster face	[m]
Z_i	Charge-state of the ith ion species	[-]
Z_{oper}	Mission operation cost per time	[\$ yr^{-1}]
α_V	Scaling constant for efficient ionization	[m^2 s^{-1}]
α	Scaling constant using anode mass flow rate	[mg s^{-1} mm^{-1}]
α_B	Bohm coefficient	[-]
ΔV	Change in rocket velocity	[km s^{-1}]
δ	Emitted electron current to collected electron current ratio	[-]
δ_c	Critical electron emission ratio	[-]

δ_s	Sheath thickness	[m]
γ_{sys}	Power system specific power	[W kg^{-1}]
Γ_i	Ion mass flux	[kg s^{-1} m^{-2}]
γ_i	Secondary electron yield for the ith ion species	[-]
ζ_i	Species fraction of the ith ion species	[-]
η_a	Anode efficiency	[-]
η_{acc}	Acceleration efficiency	[-]
η_b	Current utilization efficiency	[-]
η_c	Cathode efficiency	[-]
η_d	Dispersion efficiency	[-]
η_{div}	Beam divergence efficiency	[-]
η_p	Propellant utilization efficiency	[-]
η_{ppu}	Power processing unit efficiency	[-]
η_{Mag}	Electromagnetic coil efficiency	[-]
η_q	Charge utilization efficiency	[-]
η_T	Total Hall thruster efficiency	[-]
η_v	Voltage utilization efficiency	[-]
θ	Angular position off centerline or Azimuthal location	[Radians]
κ	Curvature	[m^{-1}]
Λ	Plasma parameter	[-]
λ_D	Debye length	[m]
λ_{MFP}	Ion mean free path	[m]
μ	Electron mobility	[C s kg^{-1}]

$\mu_{\perp}$	Electron cross-field mobility	[C s kg^{-1}]
ν_{Bohm}	Bohm electron collision frequency	[Hz]
$\nu_{classical}$	Classical electron collision frequency	[Hz]
ν_c	Collision frequency	[Hz]
$\nu_{e,tot}$	Total electron momentum exchange collision frequency	[Hz]
ν_{ei}	Electron-ion collision frequency	[Hz]
ν_{en}	Electron-neutral collision frequency	[Hz]
ν_{Wall}	Wall electron collision frequency	[Hz]
σ_{CEX}	Charge exchange collision cross section	[m^2]
τ	Thrust	[mN]
τ_l	End effect parameter	[-]
Φ_w	Work function	[eV]
ϕ	Angle of rotation	[Radians]
χ_{pl}	Total propellant related costs per payload	[$ kg^{-1}]
Ω	Function quantifying the magnetic mirror strength	[-]
Ω_e	Electron Hall parameter	[-]
Ω_i	Current fraction of the i^{th} ion species	[-]
ω_c	Electron cyclotron frequency	[Hz]
ω_e	Electron plasma frequency	[Hz]

Acronyms

AFRL	Air Force Research Laboratory
BNC	Bayonet Neill-Concelman

CEX	Charge exchange collision
CLF	Courant, Friedrichs, and Lewy condition
EEDF	Electron energy distribution function
FEEP	Field emission electric propulsion
FFT	Fast Fourier transform
FWHM	Full width half maximum
HARP	High-Speed Axial Reciprocating Probe
ITAR	International Traffic in Arms Regulations
I-V	Current-voltage characteristic
LEO	Low earth orbit
LVTF	Large Vacuum Test Facility
MFFP	Magnetically filtered Faraday probe
MPD	Magnetoplasmadynamic thruster
NASA	National Aeronautics and Space Administration
OML	Orbital motion limited
PEPL	Plasmadynamics and Electric Propulsion Laboratory
PPT	Pulsed plasma thruster
PPU	Power processing unit
RPA	Retarding potential analyzer
SEE	Secondary electron emission
SPT	Stationary plasma thruster
TAL	Anode layer thruster
UM	The University of Michigan

Abstract

Due to its high specific impulse and low price, krypton has long sparked interest as an alternate Hall thruster propellant. Unfortunately at the moment, krypton's relatively poor performance precludes it as a legitimate option. This thesis presents a detailed investigation into krypton operation in Hall thrusters. These findings suggest that the performance gap can be decreased to 4% and krypton can finally become a realistic propellant option.

Although krypton has demonstrated superior specific impulse, the xenon-krypton absolute efficiency gap ranges between 2 and 15%. A phenomenological performance model indicates that the main contributors to the efficiency gap are propellant utilization and beam divergence. Propellant utilization and beam divergence have relative efficiency deficits of 5 and 8%, respectively.

A detailed characterization of internal phenomena is conducted to better understand the xenon-krypton efficiency gap. Krypton's large beam divergence is found to be related to a defocusing equipotential structure and a weaker magnetic field topology. Ionization processes are shown to be linked to the Hall current, the magnetic mirror topology, and the perpendicular gradient of the magnetic field.

Several thruster design and operational suggestions are made to optimize krypton efficiency. Krypton performance is optimized for discharge voltages above 500 V and flow rates corresponding to an α greater than 0.015 mg/(mm-s), where α is a function of

flow rate and discharge channel dimensions $\left(\alpha = \dot{m}_a b / A_{ch}\right)$. Performance can be further improved by increasing channel length or decreasing channel width for a given flow rate. Also, several magnetic field design suggestions are made to enhance ionization and beam focusing.

Several findings are presented that improve the understanding of general Hall thruster physics. Excellent agreement is shown between equipotential lines and magnetic field lines. The trim coil is shown to enhance beam focusing, ionization processes, and electron dynamics. Electron mobility and the Hall parameter are studied and compared to different mobility models. Azimuthal electron current is studied using a fluid and particle drift approach. Analyses of several magnetic field features are conducted and simple tools are suggested for the development of future Hall thrusters. These findings have strong implications for future Hall thruster design, lifetimes, and modeling.

Chapter 1.

Introduction

1.1 Rocket Fundamentals

A rocket is a vehicle that imparts energy and momentum to a propellant as it is expelled from the engine. As a consequence of the exhausted material, a reaction force is imparted on the vehicle and thrust is created. The earliest forms of rockets may have appeared as early as when the Han Dynasty (206 BC-220 AD) in China first began experimenting with gun powder.[1] Today, thanks to work done by giants of science such as Robert Goddard, Herman Oberth, Werner von Braun, and Konstantin Tsiolkovsky, rockets are used in wide variety of propulsion applications.[2]

The principal equation used to describe the behavior of a rocket is appropriately named the Tsiolkovsky rocket equation and can be seen in Equ. 1-1. Equation 1-1 is derived by using the conservation of momentum, setting the thrust equal to the ejected mass flow rate times the exhaust velocity, and integrating in time. This equation is named after Konstantin Tsiolkovsky who derived it toward the end of the 19th century.[3] However, it now appears that the earliest know derivation of this equation first appeared in a pamphlet entitled "A Treatise on the Motion of Rockets" by William Moore in 1813 and was used for weapons research.[4]

$$\frac{M_f}{M_o} = e^{-\Delta V / U_e} \quad \textbf{(1-1)}$$

$$M_o = M_{prop} + M_f \tag{1-2}$$

On the left hand side of Equ. 1-1, there is the ratio of the final dry mass (M_f) to the initial rocket mass (M_o). The initial mass includes both the dry rocket mass and the propellant mass (Equ. 1-2). In the exponential in Equ. 1-1, there is a ratio of delta-V (change in rocket velocity) and exit velocity of the propellant. This formulation implies that in order to accelerate a large mass fraction, the propellant exhaust velocity should be on the same order as the delta-V. This result illustrates the importance of high exhaust velocity for high delta-V missions.

Specific impulse is another important quantity in rocket performance. The specific impulse (Equ. 1-3) is a measure of the thrust per propellant flow rate and is effectively a measure of propellant efficiency. Stated yet another way, specific impulse is a measure of the effective exhaust velocity. In Equ. 1-3, τ is thrust, g is the gravitational constant, and $\dot{m}_{prop}$ is the propellant mass flow rate.

$$I_{sp} = \frac{\tau}{\dot{m}_{prop} g} = \frac{U_e}{g} \tag{1-3}$$

1.2 Electric Propulsion Overview

The most traditional form of rocket propulsion is the chemical rocket. In a chemical rocket, propellant (typically a fuel and an oxidizer) is reacted in a combustion chamber. The energy released from the chemical bonds heats the propellant and the propellant is then exhausted though a converging and diverging nozzle. This form of rocket propulsion, though complex, is relatively well understood. However, chemical propulsion is inherently limited to the energy stored in the propellant chemical bounds.

Electric propulsion has the advantage of not being limited in the amount of energy that can be added to the propellant by chemistry. Electric propulsion is defined as the acceleration of gases for the purpose of producing thrust by electric heating, electric body forces, and/or electric and magnetic body forces.[5] In electric propulsion, an external power supply is used to add energy to and accelerate a working fluid to high velocities.

The resultant high specific impulse is ideal for space applications with high delta-V requirements. Since many space missions are not possible or practical using standard chemical propulsion, electric propulsion is often referred to as "mission enabling."[6] The most commonly used applications for electric propulsion is north-south and east-west station keeping although electric propulsion has been studied for all forms of missions including interstellar volages.[7,8]

Equation 1-4 gives a relation for system power and electric propulsion performance parameters. In this equation, P is the electric propulsion system power and η_T is the efficiency of the electric propulsion thruster. This equation illustrates that thruster performance is bound to the limits of the input power. By increasing specific impulse in a constant power system, thrust decreases. An important characteristic of electric propulsion devices is low thrust.

$$P = \frac{g I_{sp} \tau}{2\eta_T} \tag{1-4}$$

1.2.1 Types of Electric Propulsion

According to Jahn[5] and Stuhlinger[3] electric propulsion can be organized into three basic types of engines.

1. Electrothermal: In an electrothermal propulsion system, the working fluid is electrically heated and then expanded through a converging/diverging nozzle. Examples include resistojets, arcjets, and microwave electrothermal thrusters.
2. Electrostatic: Electrostatic propulsion uses a static electric field to accelerate an ionized propellant. Examples include gridded ion thrusters, Hall effect thrusters, colloid thrusters, and field emission electric propulsion (FEEP).
3. Electromagnetic: Electromagnetic propulsion use both electric and magnetic fields to accelerate an ionized propellant. These thrusters are sometimes operated in pulsed or quasisteady modes. Examples include pulsed plasma thrusters (PPT), magnetoplasmadynamic thrusters (MPD), and pulse inductive thrusters.

Typical performance parameters for various space propulsion systems can be seen in Table 1-1. These electric propulsion devices span a large range of power and specific impulses, thus making electric propulsion suitable for a variety of mission applications.

Table 1-1. Typical Performance Parameters for Various Space Propulsion Systems

Thruster	Power Range, kW	I_{sp} Range, s	Efficiency Range, %	Refs.
Chemical (Bipropellant)	NA	300-450	NA	9
Resistojet	0.5-1.5	200-300	65-90	9,10
Arcjet	0.3-30	500-1,500	25-45	9-11
Xe Hall	0.1-20	1,000-3,000	45-65	10
Xe Ion	0.2-10	2,000-10,000	55-80	6,10
PPT	0.001-0.2	1,000-1,500	7-13	10,12
FEEP	10^{-5}-1	6,000-10,000	80	10
MPD	1-4,000	2,000-5,000	30-50	10

1.3 Hall Thruster Caricature

The electric propulsion device used in this research is a Hall thrusters[13,14] and for that reason a much deeper description of the Hall thruster anatomy and physics will be discussed. This section will lay the groundwork for future discussions and will effectively be a caricature of Hall thruster physics. Through the course of the thesis, greater detail will be given to specific areas of Hall thruster physics.

A Hall thruster uses a static electric field to accelerate ionized particles to high exhaust velocity. The Hall thruster is a griddless device, which means it is not subject to the space-charge current density limit associated with gridded ion engines. Typical performance parameters are between 1000-3000 s specific impulse and 45-65% anode efficiency with xenon propellant.

There are two basic types of Hall thruster: the stationary plasma thruster (SPT) and the anode layer thruster (TAL). Both designs share similar physics and performance characteristics. The main difference between the two designs is the discharge channel. The SPT has a relatively long, ceramic discharge channel where the TAL has a short metal discharge channel. The SPT, due to secondary electron emission (SEE) from the ceramic walls, has lower electron temperatures. The TAL's metallic walls have a lower SEE and hence higher electron temperatures. Also, due to the short discharge channel length of the TAL, it has a shorter acceleration zone and higher peak electric field. Although much of the discussion in this section applies to both thruster designs, this section will focus on the SPT.

A generalized schematic of a typical Hall thruster electrical circuit appears in Figure 1-1. A power supply is connected between the anode and cathode and a plasma discharge is established to complete the electrical circuit. A hollow cathode is typically used to emit electrons. The cathode electrons serve a dual purpose of neutralizing the ion beam and establishing the discharge plasma. About 80-90% of the electrons from the hollow cathode neutralize the ion beam and the remaining electrons travel into the discharge channel and are collected by the anode. The electron motion toward the anode is impeded due to the applied magnetic field. This region of low electron mobility results in the formation of a self-consistent electric field. These trapped electrons are responsible for the neutral ionization inside the discharge channel.

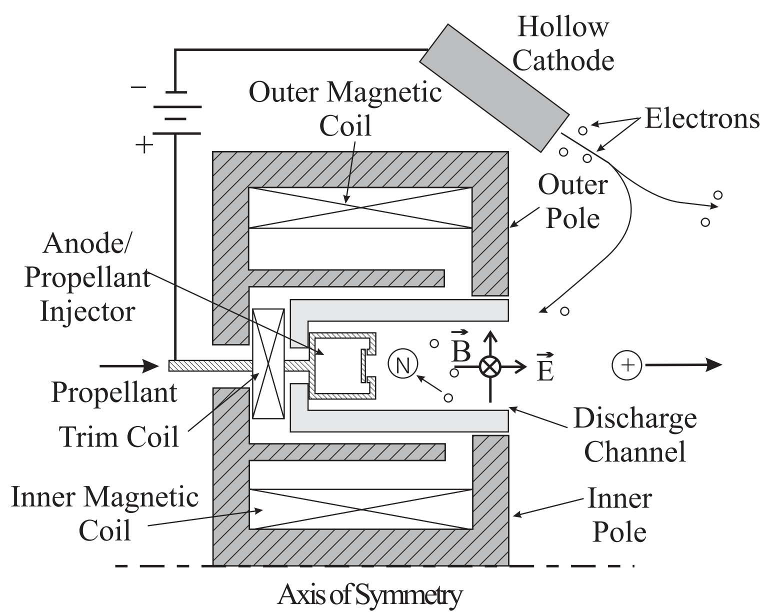

Figure 1-1. Generalized Hall Thruster Schematic

The anode typically also acts as a propellant injector for the neutral atoms. In general, noble gases are used for propellant, with xenon being the predominant choice. As the neutrals enter the discharge channel, they are ionized by the energetic electrons via electron impact ionization. For xenon propellant, approximately 90% of the neutral atoms are ionized. This region of significant ionization is often referred to as the ionization zone.

As the ions travel downstream, they enter the region of the electric field and the ions are accelerated to roughly 80-90% of the discharge voltage (the potential between the anode and cathode). Thrust is produced by these axially directed ions. This region where the potential energy is converted to kinetic energy is offer referred to as the acceleration zone. A cartoon showing the ionization and acceleration zones can be seen in Figure 1-2. Notice that the acceleration and ionization zones overlap. Unlike gridded ion engines, where there is a clear distinction between the ionization and acceleration regions, in Hall thrusters these zones are much more difficult to distinguish from each other.

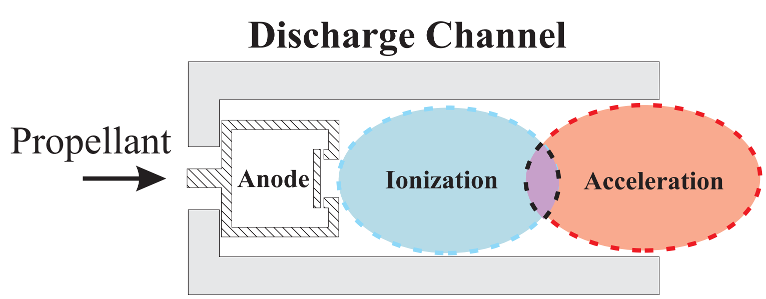

Figure 1-2. Hall Thruster Zones

The magnetic field inside the discharge channel is such that the electrons are magnetized but the ions are unmagnetized. The electron cyclotron radius is much smaller than the characteristic discharge channel width (b) while the ion cyclotron radius is much larger (Equ. 1-5). This magnetization criterion is one of the basic design parameters of Hall thrusters.

$$r_{c,e} = \frac{m_e V_{th,e}}{eB} < b < r_{c,i} = \frac{M_i V_{th,i}}{eB} \quad (1\text{-}5)$$

Arguably the most important design feature in Hall thrusters is the magnetic field circuit. As shown in Figure 1-1, typical Hall thrusters have inner and outer electromagnets to shape the magnetic field topology. The magnetic field is on the order of a few hundred gauss and increases and peaks near the exit of the discharge channel. The Hall thruster in this investigation uses an additional trim coil near the anode. Although, most thrusters operate with two electromagnets, it is not uncommon for thrusters to use four electromagnets or a combination of permanent magnets. The magnetic field topology is a very complicated design feature for modern Hall thrusters, but for the sake of the caricature, the magnetic field will be assumed to be purely radial. The magnetic field topology will be handled in the detail in later chapters.

Due to the orthogonal electric and magnetic fields, the electrons inside the discharge channel have an azimuthally directed current. This is referred to as the Hall current (Figure 1-3). This swirling electron current aids in the ionization of the neutrals.

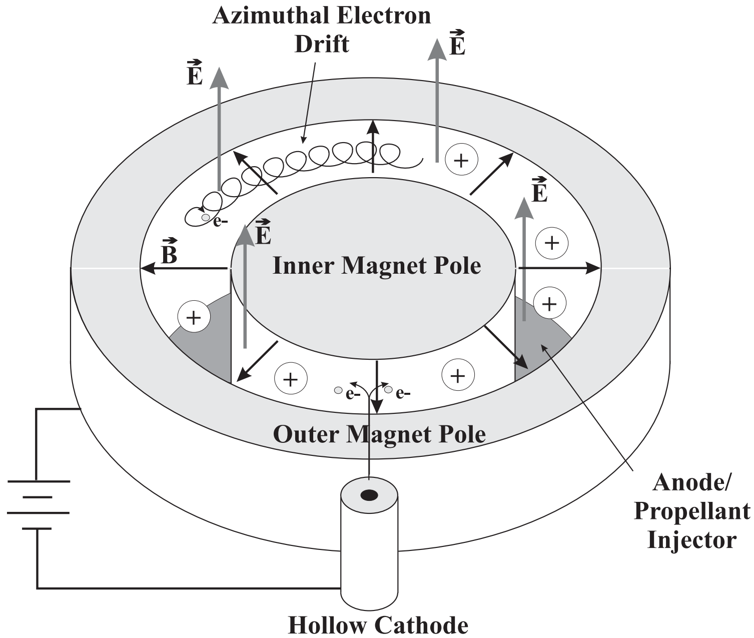

Figure 1-3. Isometric View of a Hall Thruster

In the absence of collisions, the electrons will swirl forever and never reach the anode. In reality, electrons undergo momentum exchange collisions with heavy particles and travel toward the anode. Additionally, plasma turbulence enhances this cross-field mobility as do particle-wall interactions (wall current). Electrons eventually migrate to the anode, are collected, and are lost to the system. The total discharge current is equal to the sum of the current due to the plume ions and the cathode electrons that are collected by the anode. As mentioned earlier, these cathode electrons that are collected by the anode account for 10-20% of the total discharge current and result in a loss in efficiency. The ratio of the swirling azimuthal current to the collected cathode electron current is a very important parameter for thruster operation and is referred to as the Hall parameter. The higher the Hall parameter, the more azimuthal orbits the electron goes through before being collected by the anode.

1.4 Characteristics of Krypton Propellant

Historically, a broad range of propellants have been used in electric propulsion thrusters. Hall thruster propellants in particular have ranged from cesium, mercury, bismuth, air, and the noble gases, just to name a few.[15-21] Due to metallic deposition on spacecraft surfaces and environmental concerns in ground testing, modern day Hall thrusters generally use noble gases of high atomic weight. The most common choice is xenon.

Although less common, krypton propellant has several interesting characteristics when operated in Hall thrusters. These traits have both sparked interest and caused reservations for mission designers. This section will discuss these characteristics and address the concerns associated with krypton propellant. In the next section xenon and krypton mission flight performance will be compared.

1.4.1 Performance

Several researchers have studied krypton propellant in Hall thruster with generally very poor performance.[21-29] However, more recent results using the NASA-457M and NASA-400M have demonstrated that it is possible to operate krypton at efficiencies comparable to those achieved with xenon.[30,31]

Due to the smaller mass of krypton, krypton operates at a higher specific impulse than xenon (theoretically 25% higher). Unfortunately, this smaller atomic mass also results in higher ionization potential than xenon. The ionization potentials for xenon and krypton appear in Table 1-2. Correspondingly, krypton propellant is bound by Mother Nature to perform with a lower efficiency than xenon.

Table 1-2. Ionization Potentials for Xenon and Krypton

Ionization Potential, eV	Xenon	Krypton
1st	12.13	14.00
2nd	21.21	24.36
3rd	32.10	36.95

The curve fit shown in Equ. 1-6 is used to model the Hall thruster performance on xenon and krypton propellant.[32,33] The xenon thruster efficiency is based on NASA-173Mv1 performance data presented in this thesis and other sources.[34] The krypton efficiency is based on the performance results presented in this thesis and projections for an optimally designed krypton Hall thruster. The curve fits for xenon and krypton performance are shown in Figure 1-4.

$$\eta_T = \frac{a\, I_{sp}^{\;2}}{I_{sp}^{\;2} + b} \tag{1-6}$$

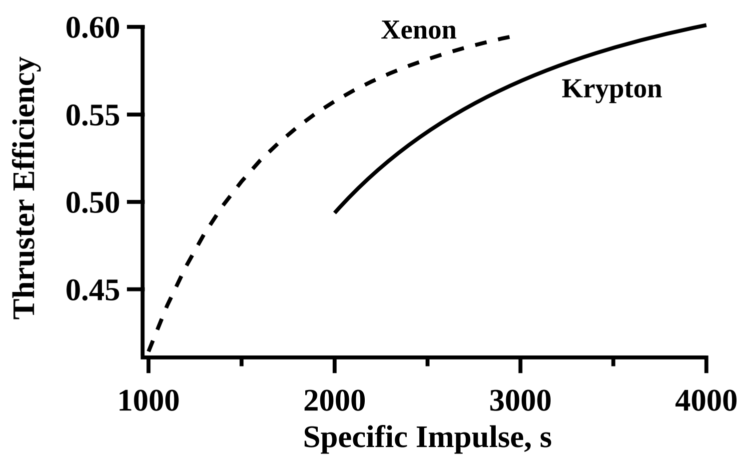

Figure 1-4. Performance Fits for Xenon and Krypton Propellant

Xenon performance is mapped between specific impulses of 1000 to 3000 s. Krypton is plotted between 2000 and 4000 s because krypton operates at approximately 25% higher specific impulse and at low specific impulses, krypton efficiency drops dramatically. This is related to the higher ion production costs of krypton and is clearly shown by Kieckhafer and King[35] (Also see Section 3.1, Figure 3-1).

1.4.2 Hall Thruster Operation with Krypton

There has been much discussion about the most appropriate way to operate Hall thrusters with krypton propellant. Opinions range from matching volumetric flow rate, to matching mass flow rate.

Marrese et al.,[27] suggest that the ionization zone length for krypton propellant will match the xenon case for krypton mass flow rates between 1 and 1.6 times that of xenon.[36,37] Marrese conclude that krypton performance is optimized for 18% greater mass flow rate as compared to the xenon case. However, in all of the results presented by Marrese et al., the efficiency gap remained greater than 20% (absolute).

By matching mass flow rate, the total number of propellant atoms flowing though the anode is 60% larger for krypton, resulting in a larger thrust for the krypton case and a much higher power level. (1 mg/s is equivalent to 10.24 sccm of xenon and 16.05 sccm of krypton.)

Other researchers[30,31] have concluded that it is more appropriate to match volumetric flow rate for the two propellants. This results in the same number of neutral particles passing through the anode and a lower thruster power due to the lower propellant utilization of krypton.

The goal of the present study is the optimization of krypton propellant. It is shown in the Performance Analysis section that there is a minimum flow rate below which krypton performance drops quickly and above which krypton performance plateaus. These results show that krypton does not need to be operated at excessively high power levels and flow rates to reach optimized performance. The flow rate found in the present investigation corresponds to a current density of about 80 mA/cm^2 and a flow density of around 1 sccm/cm^2. These numbers correspond to a discharge voltage above 500 V. At lower discharge voltages, the minimum flow rate is higher.

In this thesis, matched power is the most commonly used parameter in directly comparing experimental results. From a mission perspective, there are clear advantages to comparing propellants at the same power lever. In general, discharge current is matched when krypton operates with about 25% higher volumetric flow rate. Interestingly, since krypton atoms move 25% faster, using a simple particle flux argument, krypton neutral number density is closest matched to xenon neutral number density when krypton is operated at a 25% higher volumetric flow rate. So from a physical and mission perspective the most appropriate option is to match power levels for xenon and krypton propellant.

1.4.3 Storage and Containment

One major concern for mission planners is the storage and containment of krypton. Since krypton has a lower density and a lower boiling temperature than xenon, storage is a weakness of krypton.

Little or no work has been done to address the containment concerns of krypton. Arkhipov et al.,[38] addressed storage concerns assuming a krypton-xenon mixture (86.9% Kr). The study showed that for conditions in conventional xenon propellant tanks (25 ºC, and 2000-3500 psi) xenon has between 2-2.5 times the density of the krypton-xenon mixture. However, if cryogenic storage is used, this ratio drops to 1.5. Pure krypton will have a slightly lower density than the krypton-xenon mixture noted above; however these values represent a good starting point for krypton storage analysis.

The storage concerns are included in the Flight Performance section later in this chapter. Interestingly, storage proves to be a very manageable problem.

1.4.4 Cost

One of the most attractive features of krypton is its significantly lower price than xenon. The prices of xenon and krypton are $1138/kg and $295/kg, respectively.[35]

Aside from the propellant cost alone, krypton's higher specific impulse results in lower total propellant mass, which leads to huge financial savings in launch costs. A detailed analysis of propellant related costs is addressed in the Flight Performance section.

1.4.5 Lifetime and Erosion Rates

It is suggested by Kim[26] that since krypton has to run at higher anode flow rates and correspondingly higher power levels, the Hall thruster will run at higher temperatures and Hall thruster lifetime will suffer. As discussed previously, it is a misconception and krypton does not need to operate at exorbitantly higher power levels. However, higher specific impulses and lower thrust at the same power levels will result in longer trip times, which will make lifetime an important design criterion for krypton propellant Hall thruster. Additionally, krypton performance is optimized for higher discharge voltages than xenon. Higher voltage operation will result in higher erosion rates.

Kim[39] investigated the sputtering of boron nitride ceramic by xenon and krypton ions. Kim found 30-50% lower sputtering yield for krypton at a given ion energy. This result suggests that krypton thrusters will have longer lifetimes than xenon thrusters. This is an intuitive result since ion momentum is proportional to the square root of particle mass.

1.5 Flight Performance of Xenon and Krypton

A flight performance analysis is used to compare and contrast xenon and krypton propellant in Hall thrusters. This analysis is similar to Gulczinski and Spores[32] and Messerole.[40] The basic assumptions made in this analysis are outlined in the following list:

1. The orbit transfer performance is perfect so there are no losses associated with thrust vector misalignment.
2. There are no gravitational losses due to long thrust times. As opposed to chemical propulsion, which uses impulsive delta-Vs, electric propulsion has gravitational losses related to the long burn times.[41]
3. The trip time is assumed to be equal to the burn time.
4. The specific power is the same for both propellants and it incorporates the thruster, power processing unit (PPU), solar array, and radiator specific powers.
5. The system specific power is varied between 40 and 200 W/kg and is the same for both propellants.[42,43]
6. Power system degradation with trip time is ignored.

7. The payload mass is assumed to include the structural mass of the spacecraft and is the same for both propellants. (Propellant tank, power system, and propellant mass are not included in the payload.)
8. The propellant tank mass ratio is 5%[44,45] for xenon and varies between 7.5 to 12.5% for krypton (1.5-2.5 times that of xenon) to show best and worst case senarions.[38]
9. The efficiency of the PPU is assumed to be constant at 93% and the same for both propellants.[32,44,46]
10. The price of xenon and krypton are assumed to be \$1138/kg and \$295/kg, respectively.[35]
11. The launch cost to LEO (low earth orbit) is assumed to be \$10,000/kg.[9]
12. The solar array value is varied between 500 and \$1000/W to represent near and long term cost requirements.[10,42]
13. The total ground support operation costs are assumed to be \$5M/yr.[9,47]

The total mass breakdown of the spacecraft is shown in Equ. 1-7. In this equation, M_{pl} is the payload mass, M_{pow} is the mass of the power system, M_{ft} is the mass of the propellant tank, M_{prop} is the propellant mass, and the rest of the values have their normal meaning. The power systems mass includes the PPU, thruster mass, solar panels, gimbal, thruster support, and radiation protection.

$$M_o = M_{pl} + M_{pow} + M_{ft} + M_{prop} = M_f + M_{prop} \tag{1-7}$$

The propellant tank mass is related to the propellant mass by the tank mass ratio (K_{ft}) and this relation can be seen in Equ. 1-8. The power system mass can be related to the total system power by the specific power constant (γ_{sys}). Equation 1-9 shows a relation for the power source mass in the spacecraft. Specific power is varied between 40 and 200 W/kg. The worst case scenario is represented by the 40 W/kg and 200 W/kg is used to represent the state-of-the-art power system technology.[42,43]

$$M_{ft} = K_{ft} M_{prop} \tag{1-8}$$

$$M_{pow} = \frac{P_{sys}}{\gamma_{sys}} = \frac{M_{prop}\left(gI_{sp}\right)^2}{2t_b \eta_T \eta_{ppu} \gamma_{sys}} \tag{1-9}$$

By solving Equs. 1-1 and 1-7 through 1-9, one can find a relation for the payload mass fraction shown in Equ. 1-10. This equation shows that for a given trip time, there is an optimum specific impulse that maximizes the payload mass fraction. As specific impulse increase past this optimum value, the power system mass becomes too large and the payload mass fraction suffers.

$$\frac{M_{pl}}{M_o} = e^{-\Delta V / gI_{sp}} - \left(\frac{\left(gI_{sp}\right)^2}{2t_b \eta_T \eta_{ppu} \gamma_{sys}} + K_{ft} \right)\left(1 - e^{-\Delta V / gI_{sp}}\right) \tag{1-10}$$

As power systems technology improves and specific power increases, the optimum specific impulse for a given mission also increases. This is the reason for the drive toward higher specific impulse Hall thruster. Several researchers have shown that if the specific impulse of Hall thrusters can be increased it can result in significant improvements in payload mass fraction.[32,48-50] Additional improvements can be made for Hall thrusters with variable specific impulse.[46,51] Krypton propellant is an option to further increase thruster specific impulse.

To study the propellant related costs of the mission, Equ. 1-11 is used. The entire equation has been normalized by payload mass in order to compare different missions on the same scale. This equation shows that the total propellant related costs are a combination of propellant cost, launch costs (including propellant mass, power system mass, and propellant tank mass), costs related to ground operations, and the cost of the power system. In this equation, χ_{pl} is the total propellant related costs per payload mass, Y_{prop} is the propellant cost per kg, Y_{launch} is the launch cost per kg, Z_{oper} is the ground support operations costs per year, W_{pow} is the power system costs per Watt, and $f_{b\text{-}t}$ is the burn to trip time ratio and is assumed to be equal to one in this analysis.

$$\chi_{pl}\left[\frac{\$K}{kg}\right]=\frac{M_{prop}}{M_{pl}}Y_{prop}+\frac{M_{prop}\left(1+K_{ft}\right)+M_{pow}}{M_{pl}}Y_{launch}+\frac{t_b}{f_{b-t}M_{pl}}Z_{oper}+\frac{\gamma_{sys}M_{pow}}{M_{pl}}W_{pow} \tag{1-11}$$

Currently standard silicon cells cost between \$1000-1500/W[10] and the cost increases for more advanced technology. In one mission analysis, Frisbee used a value between \$500-1000/W to represent the power system costs.[42] With new technological developments, solar array costs are decreasing. For this analysis the solar array costs are assumed to range between \$500/W and \$1000/W to represent the near term and long term prices. Other costs are covered in the assumptions above.

1.5.1 Constant Power Performance

The first case considered is a performance comparison between xenon and krypton with constant power. The power is assumed to be a constant 10 kW, the specific power is 100 W/kg, and the payload is set to 1000 kg. Specific impulse is held constant for both propellants and is equal to 2000 and 2500 s for xenon and krypton, respectively.

The worst case scenario of 12.5% is used for the krypton propellant tank. The results are shown in Figure 1-5. It can be seen that due to krypton's higher specific impulse, a large payload fraction is possible although at a penalty of longer trip times. These are basic krypton-xenon trends that will be consistent for all mission studies.

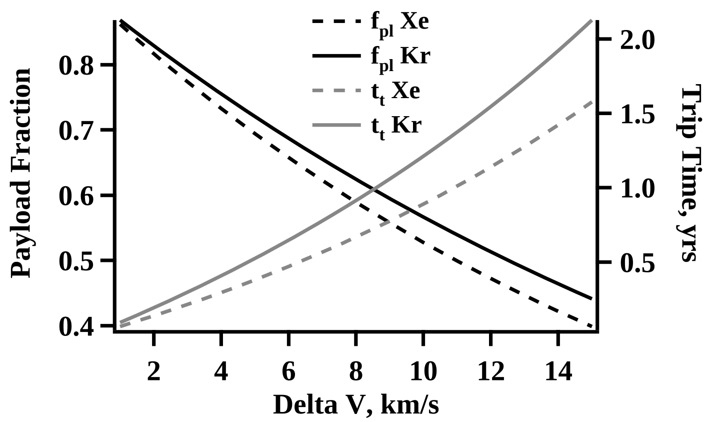

Figure 1-5. Constant Power Performance Comparison for Xenon and Krypton Propellant

1.5.2 Fixed Trip Time Performance

In this section a 6 km/s delta-V is studied assuming constant trip times of 180, 270, and 360 days. The 6 km/s delta-V is selected because it is representative of a 6-month (i.e. low thrust) transfer from LEO to geostationary orbit. Specific impulse is varied to find the optimum value for the given trip time. The best and worst case propellant tank scenarios are used for krypton so the krypton results are given by a set of lines. The results of this analysis can be seen in Figure 1-6.

For modern (γ_{sys}=100) and state of the art (γ_{sys}=200) power system technology, xenon only marginally outperforms krypton at a given specific impulse. This is due to krypton's lower efficiency and the higher power requirements in order to meet the trip time requirements. However, it is more appropriate to compare xenon and krypton realizing that for a given thruster voltage, krypton will operate with as much as 25% higher specific impulse. When operated at the same discharge voltage, krypton can deliver as much as a 5% larger payload fraction. With modern power systems, krypton performs at least as well as xenon and as trip time increases, the benefit of krypton also increases.

Another interesting trend is that except of short trip times with the conservative power system estimates, the payload fraction never plateau. This shows the benefit of higher specific impulse thrusters as power technology continues to improve. Also, these figures show that the propellant tank has only a marginal effect on the performance of the spacecraft. Therefore, krypton storage does not appear to be a significant issue.

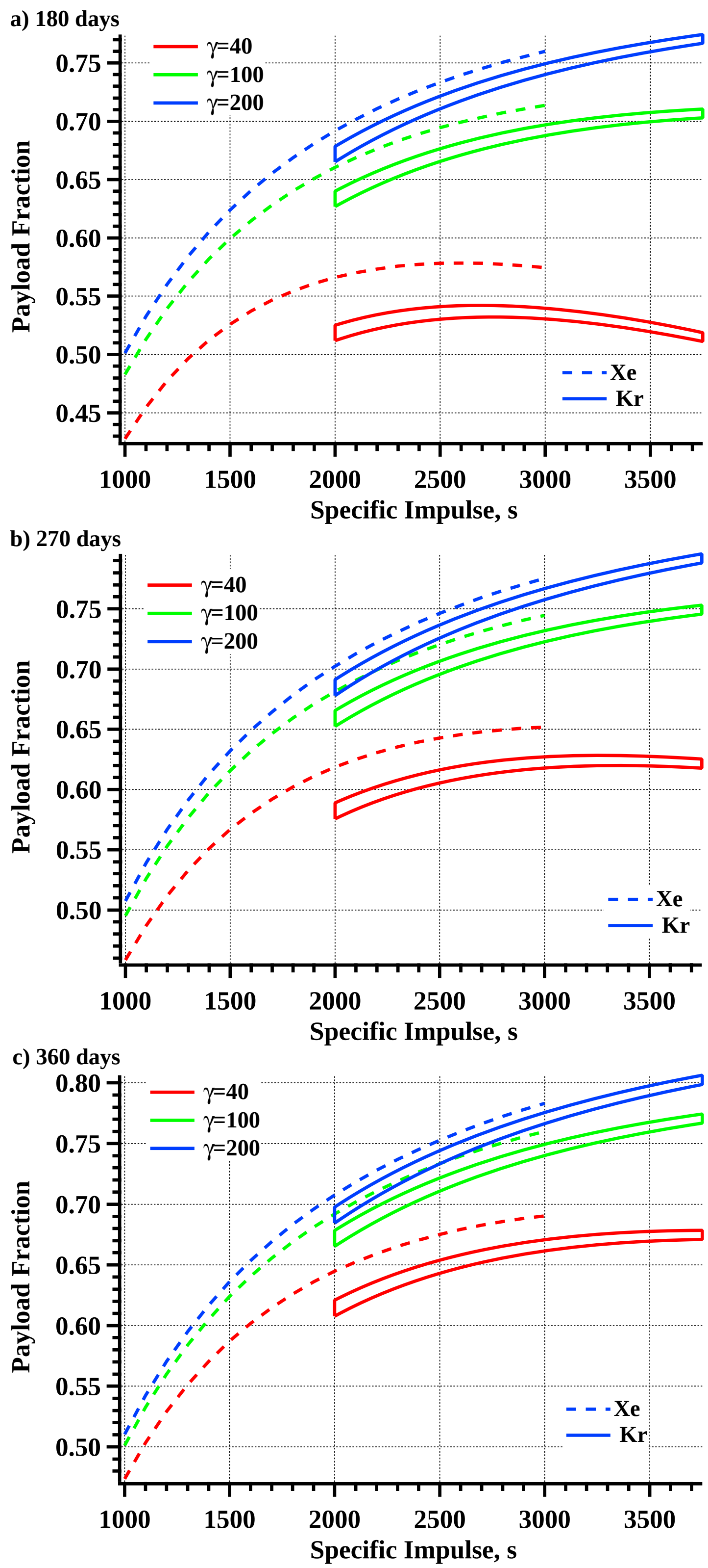

Figure 1-6. Payload Mass Fraction Optimization for a) 180, b) 270, and c) 360 Day Trip Times

1.5.3 Variable Trip Time Performance

Due to krypton's higher specific impulse and lower thrust as compared to xenon, krypton propellant requires longer mission trip time. If trip time is flexible, krypton has clear advantages over xenon. In this section, trip time is allowed to vary, the total delta-V is set equal to 6 km/s, and specific impulse is held constant at 2000 and 2500 s for xenon and krypton, respectively.

As specific power increases, the advantages of krypton propellant continue to increase. For the state-of-the-art power system, the advantage for krypton is clear. Krypton payload fraction peaks at a few percentage points higher than xenon (Figure 1-7). The improvement in payload fraction is due to the smaller power requirement associated with longer trip times.

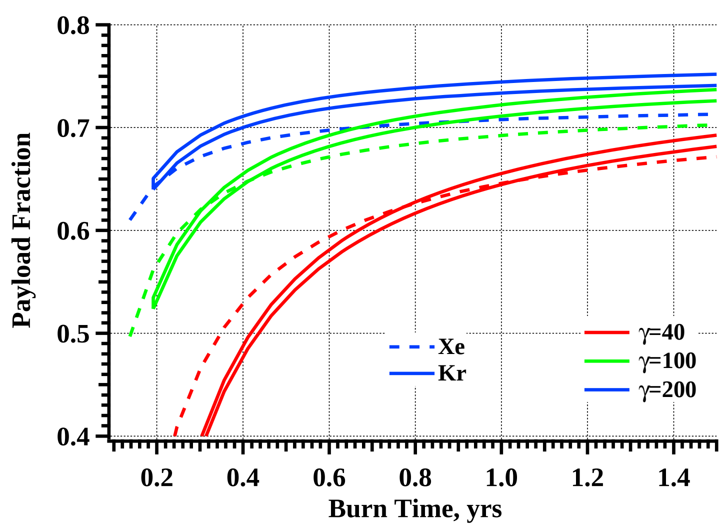

Figure 1-7. Payload Mass Fraction with Variable Trip Time

1.5.4 Trip Time Optimized for Cost

One of the major benefits that krypton is suggested to offer to mission planners is cost savings. By closely studying Equ. 1-11, it can be seen that propellant related costs are a function of trip time and can be minimized for a given delta-V and thruster operating conditions (Figure 1-8). As time increases, power requirements and launch costs decrease while ground operations costs increases. There features combine to establish a minimum in total costs.

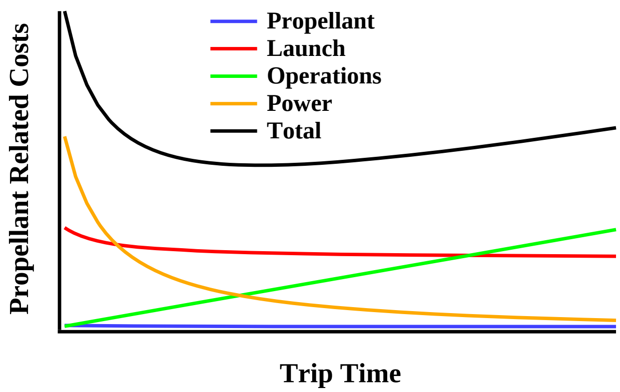

Figure 1-8. Propellant Related Costs Dependence on Trip Time

For a desired delta-V, payload mass, and specific impulse, the trip time is selected to minimize total costs. The minimized cost is then plotted as a function of delta-V. The trends for this analysis can be seen in Figure 1-9. The krypton tank mass fraction is set equal to 12.5% and system power is not restricted. The payload mass is set to 500, 2000, and 5000 kg. In this analysis, specific power and power system cost are varied. For the "modern technology" case (Cases a and c), the specific power is set equal to 100 W/kg and the cost of the power system per W is equal to \$1000/W. In the "state-of-the-art" case (Case b), the specific power is set equal to 200 W/kg and the cost of the power system per W is equal to \$500/W. The state of the art case is a projection of future specific power and costs and is meant to capture future mission trends. The specific impulse is also varied between 2000/2500 s and 1600/2000 s for xenon/krypton, respectively. These two case are referred to as the medium (Cases a and b) and low (Case b) specific impulse cases.

For the modern case, krypton savings can be significant for larger payload masses and increases in delta-V. For specific cases, krypton propellant can save a few thousand dollars per kilogram of payload. The savings are largely related to the launch costs of the additional xenon propellant needed for a given delta-V. Propellant costs are relatively insignificant compared to launch costs ($1138/kg-xenon and $10K/kg-launched). For small payload masses, xenon propellant offers greater savings. Smaller payload masses require less propellant to perform a given delta-V, reducing the cost saving benefits of krypton. Projected specific power and power system cost further increase krypton savings benefits. Krypton savings are highest for low specific impulse operation (i.e. high thrust) due to decreased trip times. The main variable limiting krypton savings is the increased trip time. In this analysis, krypton operation results in 10-20% longer trip times for a given delta-V.

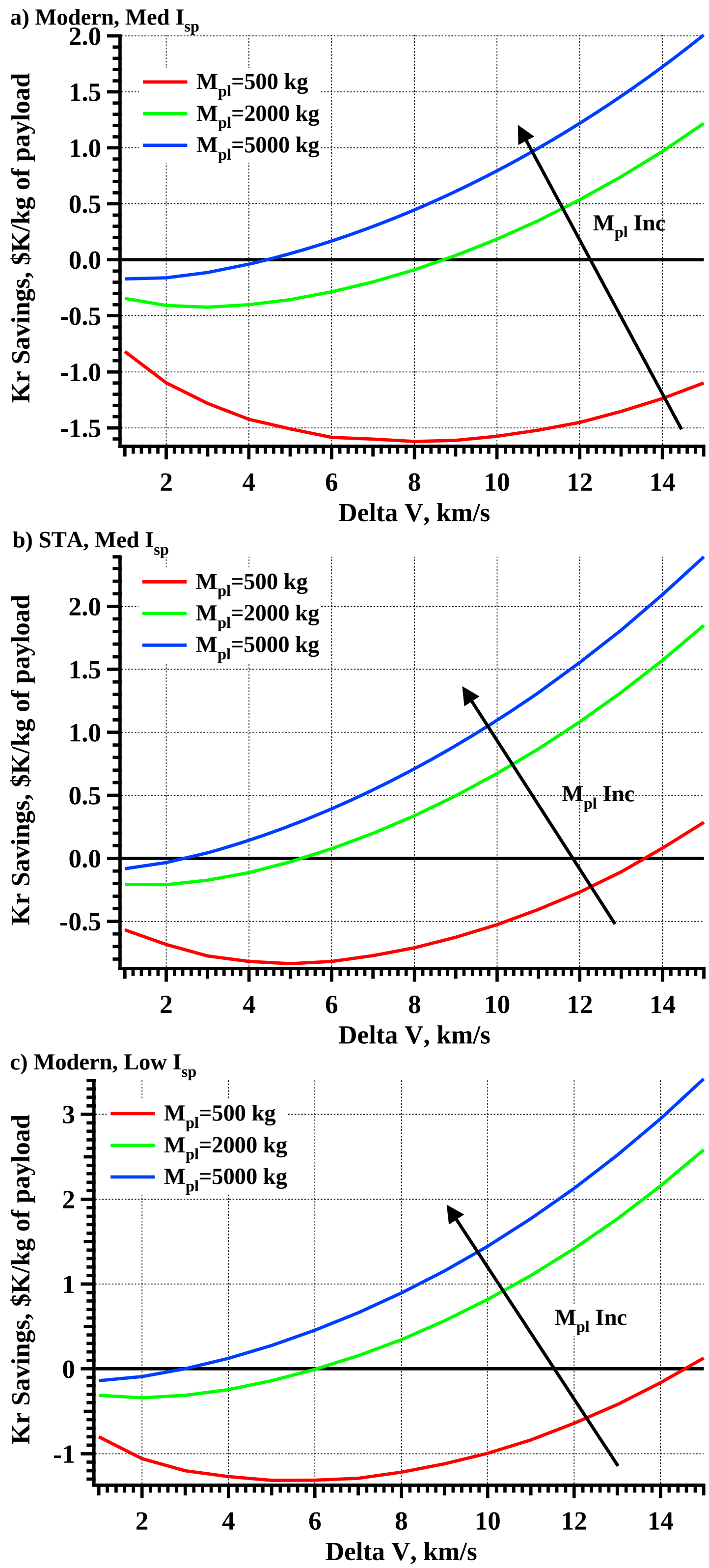

Figure 1-9. Minimized Costs for Given Delta-V Requirements. Case a) corresponds to modern technology with medium specific impulse, case b) corresponds to state-of-the-art technology with medium specific impulse, and case c) corresponds to modern technology with low specific impulse.

1.5.5 Summary of Krypton Mission Analysis

For certain missions, krypton Hall thrusters have significant saving and performance advantages over xenon Hall thruster. Krypton can result in saving of thousands of dollars per kilogram of payload. Also payload mass fraction is increased by a few percent when krypton is used as a propellant. In the near term, krypton will be a legitimate option for missions that will help bridge the gap between xenon Hall thrusters and xenon ion engines, and broaden the mission range of Hall thrusters. As power system and propellant tank technology continue to improve, krypton performance will outperform xenon by a greater degree.

Due to higher specific impulse, krypton operation increases payload mass fraction at the cost of longer trip times. Krypton storage does not appear to be a significant factor and can be readily addressed using modern propellant storage tanks.

For krypton to become a legitimate option for mission designers, a few conditions should be met:

1. Continued development and advancement of power system technology
2. Continued decrease in power system costs
3. Decrease in the krypton-xenon Hall thruster efficiency gap

The trend for improve power system technology at ever decreasing prices will likely be achieved in the near future. The only remaining piece of the krypton puzzle is to decrease the krypton performance gap.

1.6 Motivation

Krypton offers several enticing benefits for space missions. The two major benefits are higher specific impulse as compared to xenon and reduced mission and development costs. Furthermore, with the trend toward higher power system specific power, there is a trend toward higher optimum specific impulse and the need for higher specific impulse Hall thrusters.

The focus of this research is to decrease the performance gap between xenon and krypton in Hall thrusters. This is addressed by characterizing the krypton and xenon performance gap, conducting a detailed investigation of internal Hall thruster phenomena, finding basic operation parameters for krypton optimization, and identifying design improvements that can be applied to future krypton Hall thrusters.

1.7 Contribution to Research

The work and results presented in this thesis offers several contributions to the field of Hall thruster research and development. The bulk of the work focused on a rigorous study of krypton and xenon Hall thruster performance, internal Hall thruster plasma characterization, a thorough analysis of the internal Hall thruster processes, and a study of the influence of magnetic field topology on thruster operation. A summary of the specific contributions are listed below.

1. **Study of Krypton Performance Optimization:** Krypton performance is studied in great detail and major design improvements and operation conditions for performance optimization are discovered. The efficiency components are isolated and the specific causes for the krypton efficiency gap are pinpointed.

2. **Improvement of a Phenomenological Performance Model:** Improvements are made to an existing performance model[34] to account for performance effects of beam divergence better. With this improvement, the performance model is more complete.
3. **Internal Characterization of Discharge Phenomena and Plasma Properties:** Several plasma properties were successfully measured in this investigation. These properties include electron temperature, ion number density, and plasma potential. Additionally, several internal phenomena are characterized including the Hall parameter, electron mobility, azimuthal electron currents, electron drift energies, the electric fields, thermalized potentials, the acceleration zone, and the ionization zone.
4. **Development of Internal Diagnostics, Measurement Techniques, and Data Analysis:** New internal probes and techniques were required in order to complete some of the measurements. Analysis of the discharge current perturbations also yielded new information about the internal plasma and plasma-probe interactions.
5. **Identification of Magnetic Field Topology Effects on Hall thruster Performance:** A performance analysis is conducted to find the effects that the trim coil has on thruster performance. The trim coil is shown to offer several performance benefits.
6. **Identification of Magnetic Field Topology Effects on Internal Hall Thruster Phenomena:** The internal characterization of plasma properties revealed several plasma behavior effects related to the magnetic field topology. For example, the

focusing equipotential lines and the focused Hall current associated with the magnetic mirror and plasma lens magnetic field topography.

7. **Development of Tools for Magnetic Field Topology Study:** The magnetic field topology is studied using a number of analyses, and the results are compared to the experimental findings. These analyses addressed reasons for the xenon-krypton performance gap. It is the hope that these analyses will facilitate optimum magnetic field topological design in future Hall thrusters.

Chapter 2.

Facility, Apparatus, and Techniques

2.1 Facility

2.1.1 Large Vacuum Test Facility

The experimental investigations discussed in this thesis are conducted in Plasmadynamics and Electric Propulsion Laboratory's (PEPL) Large Vacuum Test Facility (LVTF). The LVTF is a cylindrical stainless-steel tank that is 9-m long and 6-m in diameter. Originally built in the early 1960's by the Bendix Corporation, the LVTF and was donated to The University of Michigan in 1982. The LVTF can be seen in Figure 2-1.

Figure 2-1. Photograph of the Large Vacuum Test Facility at The University of Michigan's Plasmadynamics and Electric Propulsion Laboratory

A pair of 900 l/s blowers and four, 200 l/s mechanical pumps are used to evacuate the LVTF to rough vacuum (80–100 mtorr). Once the chamber has reached rough vacuum, the blowers and mechanical pumps are shut off and isolated via gate valves, and the cryopumps are activated. The LVTF is equipped with 7 CVI model TM-1200 “nude” cryopumps. These seven cryopumps, surrounded by liquid nitrogen cooled baffles, give the LVTF a maximum pumping speed of 500,000 l/s on air, 240,000 l/s on xenon, and 252,000 l/s on krypton.

For the all of the experimental results presented, the LVTF is operated with seven cryopumps. The only exception to this is the UM/AFRL P5 performance measurements (Appendix B), which were conducted with four cryopumps.

The chamber pressure is monitored by using two hot-cathode ionization gauges. The primary pressure monitor is a Varian model UHV-24 nude gauge with a Varian UHV senTorr vacuum gauge controller. An auxiliary Varian model 571 gauge with an HPS model 919 hot cathode controller is used for verification and as a backup. The vacuum chamber operates at a base pressure of 1.5×10^{-7} torr and approximately 3.2×10^{-6} torr during both krypton and xenon thruster operation. Pressure measurements from the gauges are corrected using the known base pressure on air and a correction factor (C_f) of 2.87 for xenon and 1.96 for krypton according to Equ. 2-1.[52]

$$P_C = \frac{P_i - P_b}{C_f} + P_b \qquad \textbf{(2-1)}$$

A schematic of the LVTF indicating the two thruster stations and location of the various components is shown in Figure 2-2. The majority of the external measurements and all of the internal measurements are taken at station two. However, due to the location of the thrust stand and rotary probe (theta) table, the Faraday probe, retarding potential analyzer (RPA), and performance measurements are taken at station 1. For the internal measurements, the thruster was mounted on a computer controlled two-axis crossed-stage positioning table at station 2. A 2-m by 2.5-m louvered graphite panel beam dump is positioned approximately 4 m downstream of station 2 to reduce back sputtering.

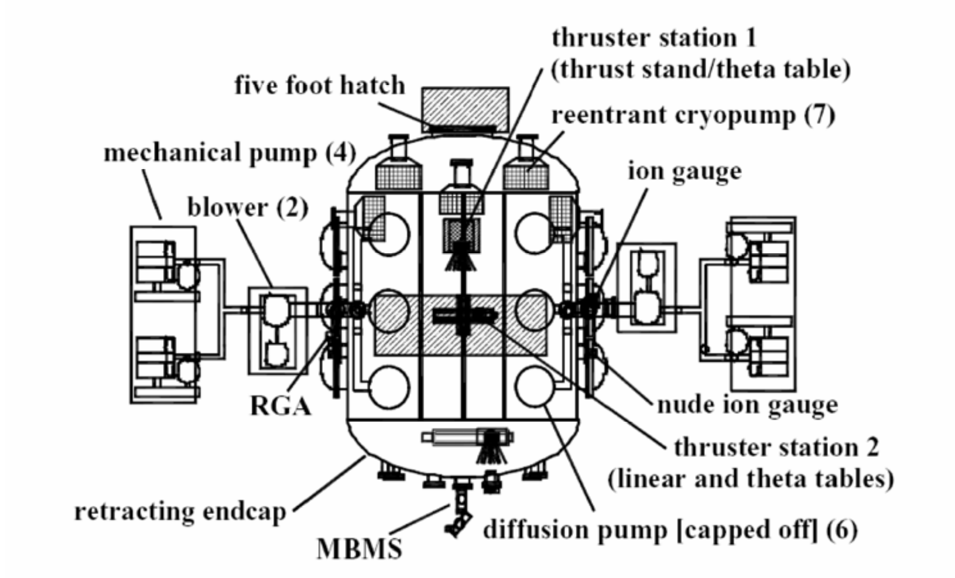

Figure 2-2. Schematic of the Large Vacuum Test Facility (Not to Scale)

2.1.2 Propellant Delivery

High-purity research grade xenon and krypton are used as propellants for all experiments. The purity level of xenon and krypton are at least 99.999%. The propellants are supplied through stainless-steel propellant feed lines using 20 and 200 sccm MKS 1159B sccm mass flow controllers for the cathode and anode, respectively. The mass flow controllers are calibrated using a constant volume method. The compressibility correction factor for xenon and krypton are calculated using the van der

Waals Equation,[53] the Virial Equation,[54] and the Redlich-Kwong equation of state. The pressure and temperature in the calibration volume are monitored every few seconds to calculate the flow rate into the volume. The mass flow calibration converges when the 5-sigma confidence interval around the average calculated flow rate decreases to below the manufacturer's error specification (±1% of full scale).

2.2 Thrusters

2.2.1 NASA-173Mv1

The NASA-173Mv1 Hall thruster is used for the majority of the measurements presented in this thesis and is shown in Figure 2-3. The NASA-173Mv1 has an outer diameter of 173 mm, discharge channel width of 25.4 mm, and a channel depth of 38 mm. In addition to the standard inner and outer magnetic coils, the NASA-173Mv1 uses a trim coil to shape the magnetic field topology. A generalized schematic of the NASA-173Mv1 magnetic circuit appears in Figure 1-1. Because of its location behind the anode, the trim coil modifies the radial magnetic field in the rear of the discharge channel. The internal trim coil primarily alters the axial gradient of the radial magnetic field, which changes the radius of curvature of the field lines. By using a negative coil current, the trim coil produces a negative magnetic field that increases the curvature of the electrostatic plasma lens and thus the axial gradient of the radial magnetic field. Additionally, the trim coil creates a magnetic mirroring effect, which results in the focusing of electrons and ions toward the center of the discharge channel. A more detailed description of the NASA-173Mv1 is coved by Hofer.[34,55,56] The thruster is operated for one hour for the initial conditioning and is warmed up for at least 30 minutes at a given operation point before data are taken. For every operation point used in the detailed efficiency analysis (Section 3.4), the thruster is allowed to warm up for 2 hours before data are taken.

A Busek BHC-50-3UM hollow cathode is used for all measurements. For all thruster operation points, the cathode flow rate is equal to 10% of the anode flow rate with a minimum flow rate of 0.93 sccm. The cathode axial centerline is mounted 30 degrees off the thruster axial direction and the center of the cathode orifice is placed 30 mm downstream and 30 mm above the thruster face.

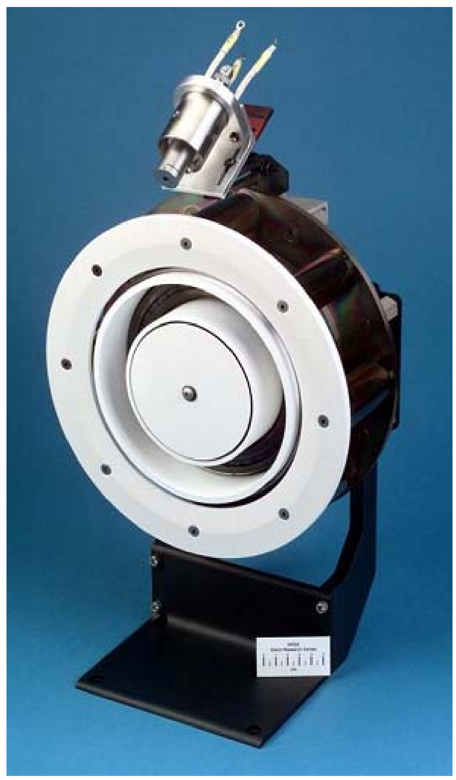

Figure 2-3. NASA-173Mv1 Hall Thruster

The electric schematic for the Hall thruster is shown in Figure 2-4. The thruster uses two power supplies connected in series in order to operate at the desired discharge voltage. The discharge supplies are connected to a filter consisting of a 1.3 Ω resistor in series and 95 μF capacitor in parallel. The filter damps out thruster discharge oscillations with a resulting cutoff frequency of 1.3 kHz. The same electrical circuit is used to power the UM/AFRL P5 thruster.

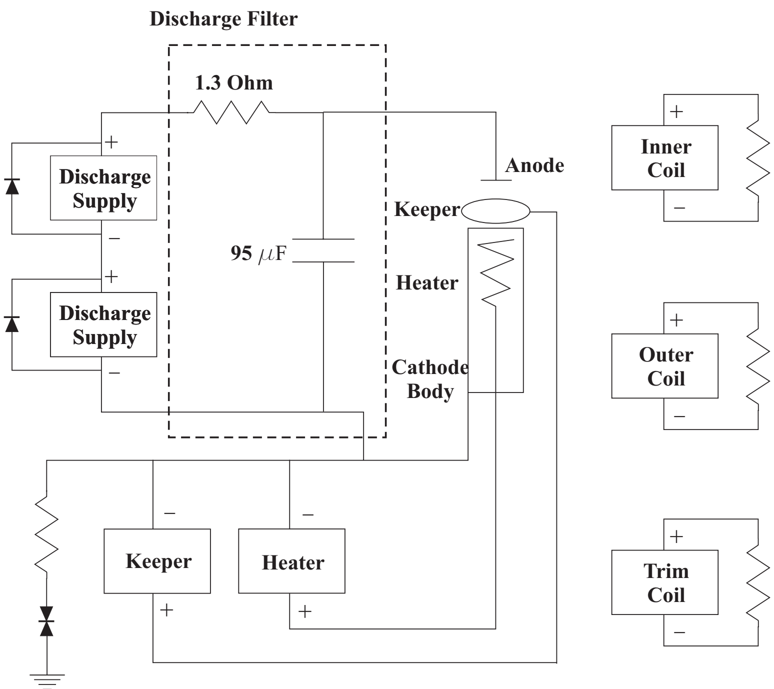

Figure 2-4. Schematic of the Hall Thruster Circuit

2.2.2 UM/AFRL P5

Although the vast majority of the presented results use the NASA-173Mv1 Hall thruster, performance measurements are also taken with the UM/AFRL P5. The UM/AFRL P5 appears in Figure 2-5.

Similar to the NASA-173Mv1 Hall thruster, the P5 has an outer diameter of 173 mm, discharge channel width of 25.4 mm, and a channel depth of 38 mm. The P5 has a nominal power rating of 5 kW. Unlike the NASA-173Mv1 Hall thruster, the P5 does not utilize a trim coil and only uses the standard inner and outer magnetic coils. A Moscow

Aviation Institute (MAI) laboratory-model cathode is located at the 12 o'clock position. The cathode orifice is located approximately 30 mm downstream from the outer front pole piece and the cathode body is oriented at angle of 45° below horizontal. This cathode orientation is consistent with work performed by Walker.[57] For all cases, the cathode flow rate is set to 10% of the anode flow rate. Similar to the investigation presented in this thesis, a detailed mapping of the plasma properties internal to the P5 has also been conducted by Haas.[58,59] A more detailed description of the P5 is covered by Haas.[58]

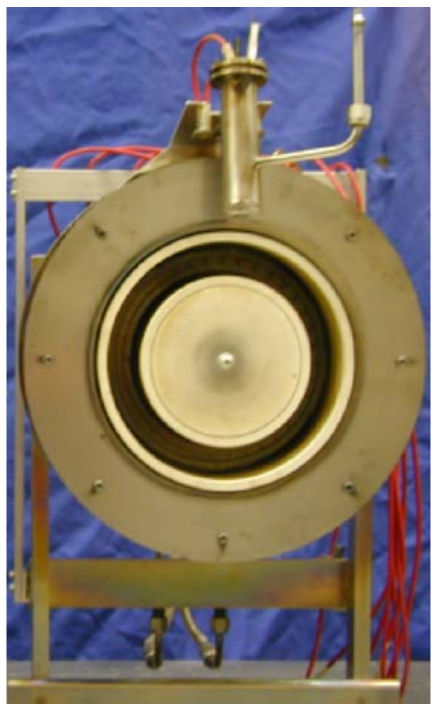

Figure 2-5. UM/AFRL P5 Hall Thruster

2.3 External Diagnostics

External diagnostics are defined as any sort of measurement device that can be used external to the thruster discharge channel. The diagnostics presented in this section measure thruster performance and plume properties.

2.3.1 Thrust Stand

Thrust measurements for this research are recorded using a null-type inverted pendulum thrust stand, the same thrust stand design used with the NASA-457M.[30,60] The thrust stand can be seen in Figure 2-6.

Figure 2-6. PEPL's Null Type Inverted Pendulum Thrust Stand

For the performance measurements, thruster operation is monitored in real-time by an Agilent data logger. The monitored properties include the magnet currents and voltages, discharge current, and thrust. The mass flow rate and discharge voltage are kept constant during the thruster tuning and therefore are inputted manually. Other than the discharge current, which is monitored via a current probe, currents are monitored by measuring the voltages across calibrated shunts. The magnet voltages are measured directly by the data logger. Thrust is measured by monitoring the thrust stand outputs and converting the voltage to thrust by a calibration curve. The shunts and current probe are calibrated before the experiments using a Fluke 77 III multimeter. The error associated with the multimeter is ±0.4% for DC voltage measurements and ±1.5% for DC current measurements. The current probe has approximately ±1.5% error.

The optimal efficiency is found for each operation point by monitoring Hall thruster conditions and thrust efficiency in real time. As the magnet currents are altered, the efficiency adjusts in response to the changing magnetic field and the peak efficiency is attained. An example of a typical optimization can be seen in Figure 2-7.

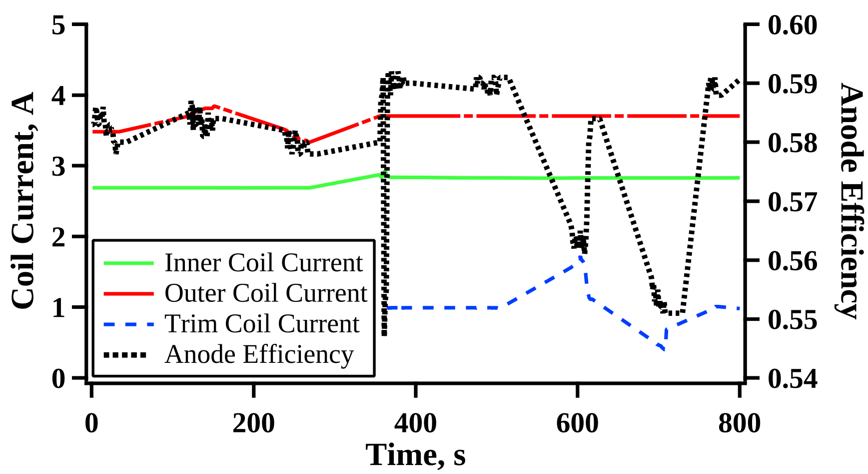

Figure 2-7. Real-Time Performance Optimization Example

Due to the thrust squared term in the efficiency equation, any error in the thrust measurement is especially damaging to the accuracy of efficiency measurements. For this reason a great deal of effort is spent in calculating the thrust for each data point. The thrust stand is calibrated by applying known weights and by monitoring the thrust stand output. Calibrations are taken hourly so that data points are always taken within thirty minutes of the closest calibration. Thrust can be calculated from the signal output and by using a calibration curve. Additionally, the plotter output is analyzed manually to double-check the thrust measurements.

Thrust, anode specific impulse, and anode thrust efficiency measurement uncertainties are found by accounting for all aforementioned errors. Thrust measurements have ±4.13 mN error, anode specific impulse measurements have approximately ±2.5% error, and anode efficiency measurements have a 5% relative error on average.[61] Anode specific impulse and anode efficiency are calculated using the standard form of the equations shown in Equs. 2-2 and 2-3.

$$I_{sp} = \frac{\tau}{\dot{m}_a g} \tag{2-2}$$

$$\eta_a = \frac{\tau^2}{2\dot{m}_a P_D} \tag{2-3}$$

2.3.2 E×B Probe

An E×B probe (or otherwise know as a Wien filter) is a commonly used tool for measuring ion species fractions.[57,62,63] The E×B probe uses the Lorentz force to select ions of a specific velocity for collection. This filtering is accomplished through crossed electric and magnetic fields that are mutually perpendicular to the ion velocity vector. Generally, a constant magnetic field is provided along with an applied variable potential between two parallel plates to create perpendicular fields. For a particular ion velocity (See Equ. 2-4), the Lorentz force vanishes and those ions can be collected by the probe. The E×B probe acts purely as a velocity filter and collects ions independent of mass and charge. While the E×B probe will not detect signatures due to charge exchange collisions, ions that have undergone elastic collisions will cause a broadening of the E×B probe traces.

$$v_{coll} = E / B \tag{2-4}$$

The ion charge-state can be determined by considering the relationship between ion energy-per-charge to the applied plate voltage. When the ion velocity (Equ. 2-5) is substituted into Equ. 2-4, by solving for the plate voltage, one arrives at the relation given in Equ. 2-6 in terms of acceleration potential and charge-state. Since the acceleration potential of all ion species is approximately equal[63] (refer to Section 3.4.2 for further discussion), multiply-charged species peaks will appear approximately at $Z_i^{1/2}$ times the probe voltage of the singly-charged peak.

$$v_{a,i} = \sqrt{2 Z_i e V_{a,i} / M_i} \tag{2-5}$$

$$V_{probe} = \sqrt{2 Z_i e V_{a,i} / M_i}\,(Bd) \tag{2-6}$$

The E×B probe used in this study was originally designed, built, and calibrated by Kim.[63] The E×B test section is 254 mm long. The magnetic field is supplied by four ceramic permanent magnets in the E×B test section and averages 0.162 Tesla with a variation along the section length of less than 10%.[63] The electric field is applied between two rectangular aluminum electrodes separated by a distance (*d*) of 1.90 cm. The entrance collimator is 152 mm in length and uses an entrance orifice of 1.5 mm in diameter. The exit collimator is 152 mm long and is connected to a 23-mm-diameter tungsten collector.

The dimensions of the E×B probe are identical to previous experiments[57,62,63] with the exception of the entrance orifice that is added to reduce the collected signal. Based on these dimensions, the half-cone acceptance angle is estimated to be 0.56 degrees and the probe resolution is estimated to be approximately 7% of the ion energy.[63] The E×B test section is located 1.5 m downstream on thruster centerline.

The electrodes in the E×B probe are biased at equal voltages above and below ground by a Keithley sourcemeter. A picoammeter records the current to the collector, which is given by Equ. 2-7. For the ion energies reported in this experiment, the secondary electron yield (γ_i) of tungsten is 0.058, 0.28, 0.78, and 1.75 for Kr^+, Kr^{2+}, Kr^{3+} and Kr^{4+}, respectively, and 0.018, 0.18, 0.69, and 1.46 for Xe^+, Xe^{2+}, Xe^{3+}, and Xe^{4+}, respectively.[64]

$$I_i = eZ_i n_i v_{a,i} A_c (1+\gamma_i) \qquad \text{(2-7)}$$

From the ion currents, the current fractions (Equ. 2-8) and species fractions (Equ. 2-9) are calculated. These values will be used in the analysis in the following sections.

$$\Omega_i = I_i \big/ \sum I_i \qquad \text{(2-8)}$$

$$\zeta_i = n_i \big/ \sum n_i \qquad \text{(2-9)}$$

Equations 2-5 and 2-7 are inserted into Equ. 2-9 to solve for the species fraction. Equations 2-5, 2-7, and 2-9 are then inserted into Equ. 2-8 to arrive at a new equation for ion current fractions in Equ. 2-10.

$$\Omega_i = \frac{Z_i^{3/2}\zeta_i(1+\gamma_i)}{\sum Z_i^{3/2}\zeta_i(1+\gamma_i)} \qquad \textbf{(2-10)}$$

The method used to measure the area under the separate species peaks is described below. First an ensemble average of three separate voltage sweeps is taken. The averaged data are then smoothed using a smoothing spline to reduce noise. Starting with the highest charge-state, a Gaussian curve fit is matched to these data and then the curve fit is subtracted from the lower charge-state species peaks. The process is then continued with the next highest charge-state and repeated until all charge-states have been analyzed. The current is subtracted to avoid double-counting the collected current. The process begins with the highest charge-state to avoid problems that can occur due to poor curve fits. Effort is taken to use only sections of the species peaks that are far enough away from neighboring peaks so the curve fits will not be affected by neighboring species peaks. An example of this method is shown in Figure 2-8. In this figure the solid black lines represent the Gaussian curve fits, the dotted black line is the summed curve fits, and the collected current from the E×B probe is given by the thin, grey line. Previous work has used the peak current and the full width half maximum (FWHM) to calculate the area under the curve.[62] When this method is compared to previous methods there is no significant difference in the species fraction calculations.

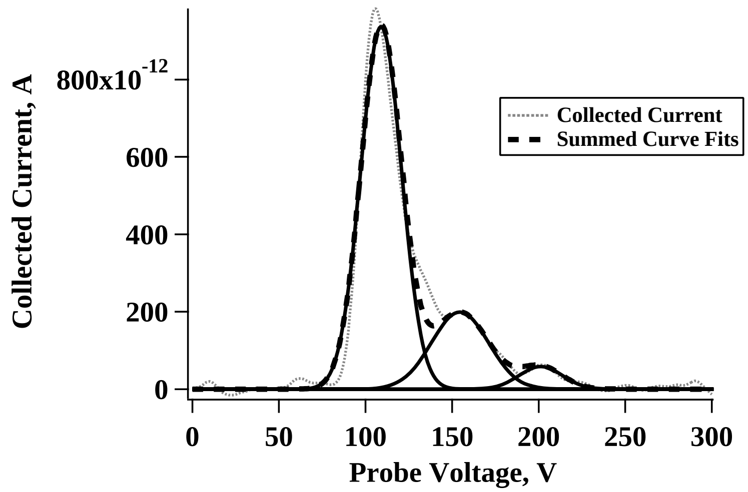

Figure 2-8. E×B Ion Current Integration Method

The error in the species fraction calculation is approximately 4%, 25%, 50% and 150% for Xe^{+}/Kr^{+}, Xe^{2+}/Kr^{2+}, Xe^{3+}/Kr^{3+}, and Xe^{4+}, respectively. These errors stem from a combination of voltage and current measurement inaccuracy, probe misalignment, probe resolution, loss of ions due to CEX collisions and variation of ion species velocity. The effect of particle buildup and collisions inside the probe was addressed by Kim[63] and found to be small negligible.

2.3.3 Magnetically Filtered Faraday Probe

Faraday probe data are collected using a magnetically filtered Faraday probe (MFFP).[57,65,66] For MFFP data collection the thruster is placed at thruster station 1. The MFFP is mounted on a 1-m-long radial arm that is attached to the theta table. This setup can be seen in Figure 2-9.

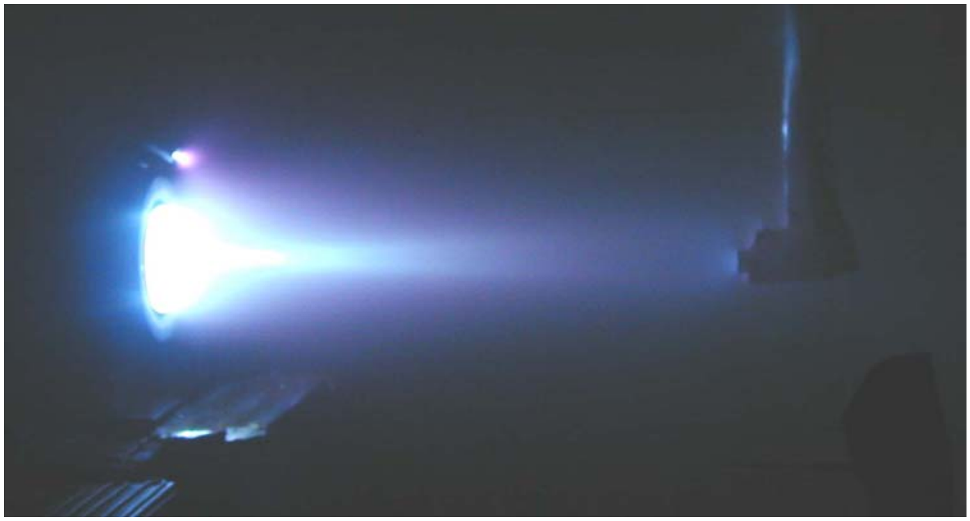

Figure 2-9. Faraday Probe and Retarding Potential Analyzer Data Collection at Station 1

Facility effects and high back pressure can result in inaccurate Faraday probe measurements. The predominant effect of high back pressure that manifests itself as artificially large current measurement is the charge exchange (CEX) ion produced in the plane. A CEX ion is produced when a "fast" ion interacts with a "slow" neutral by exchanging an electron. The result is a "fast" neutral and a "slow" ion. Low-energy ions are drawn to the negatively-biased collector and the Faraday probe is unable to distinguish between "fast" and "slow" ions. Because of this, standard current density measurements tend to over-predict the ion beam current. At large angles off centerline (>60 degrees), the measured current is largely CEX ions. The magnetically filtered Faraday probe has been shown to be very effective at excluding CEX ions. For this reason, the MFFP is chosen for the follow analysis.[65]

The MFFP incorporates a conventional Faraday probe collector located in an enclosure with a Helmholtz coil. The magnetic field alters the trajectory of ions such that ions with kinetic energies below 20 eV are deflected away from the collector. In addition, the enclosure surrounding the collector acts as a geometric collimator that further reduces CEX ion collection. This collimation acts to reduce the effective collection area of the probe[67] and the reported results are corrected accordingly. Thus, the enclosure and applied magnetic field result in dual-mode CEX ion filtration.

Due to the large inaccuracy in Faraday probe measurements, certain sources of error should be addressed. Secondary electron emission occurs when high-energy ions collide with the collector and a low-energy electron is released from the surface. Assuming that the plasma is predominantly singly-charged, the use of a tungsten collector greatly reduces the effect of secondary electron emission and this effect can be considered negligible.[64,68]

Another source of error connected to facility backpressure and high neutral density in the plume is plume attenuation. At high neutral densities, fewer ions are capable of reaching the collector without suffering a CEX collision. Attenuation is the decrease in beam current due to these collisions. By considering the one dimensional ion continuity equation and integrating over the path length z, one will arrive at the attenuation correction[69] in Equ. 2-11, where $j(\theta)$ is the beam current as each angular location, $j_{FP}(\theta)$ is the beam current collected by the Faraday probe, and the rest of the symbols have their usual meaning. The collector takes angular sweeps and is mounted 1 m downstream of the thruster. The operation pressure of the facility is approximately 3×10^{-6} torr and a neutral temperature of 300 K is assumed. The CEX collision cross sections for xenon and krypton are approximately 51 and 40 Å^2, respectively.[70,71] This result in a beam attenuation of approximately 5 and 4% for xenon and krypton, respectively.

$$j(\theta)/j_{FP}(\theta) = \exp(-n_n \sigma_{CEX} z) \qquad \textbf{(2-11)}$$

The beam current is calculated from these Faraday probe data by integrating from 0 to 90 degrees in spherical corrdinates.[72] The normalized current density function can be calculated by dividing the current density by the beam current. As is necessary with any filtering diagnostic with a characteristic transfer function, the MFFP has been calibrated.[65,66]

2.3.4 Retarding Potential Analyzer

The retarding potential analyzer[73-75] (RPA) diagnostic uses a series of grids to determine the ion energy distribution by selectively filtering ions on the basis of kinetic energy. The first grid is floating to minimize the perturbation of the sampled plasma, the second grid is negatively biased (-30 V) to repel effectively all plasma electrons, and the third grid is used to retard the ions so only ions with energy-to-charge ratios greater than the grid voltage can pass through the retarding grid and reach the collector. Retarding grid voltage is varied to determine the current-voltage characteristic. The derivative of the current-voltage characteristic is proportional to the ion energy distribution ($f(V)$) and can be seen in the idealized Equ. 2-12. It should be noted that since the RPA acts as a filter with a characteristic transfer function, it must be calibrated.[76] The schematic of the three-grid design appears in Figure 2-10 and the potential diagrams of the RPA can be seen in Figure 2-11.

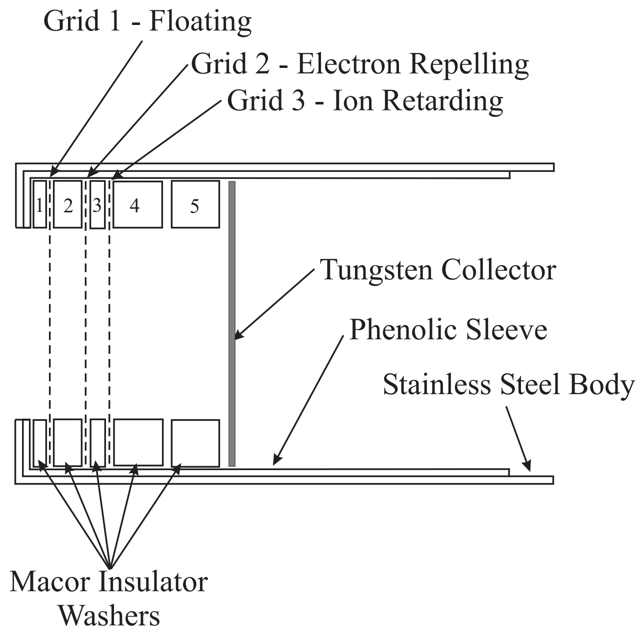

Figure 2-10. Retarding Potential Analyzer Schematic

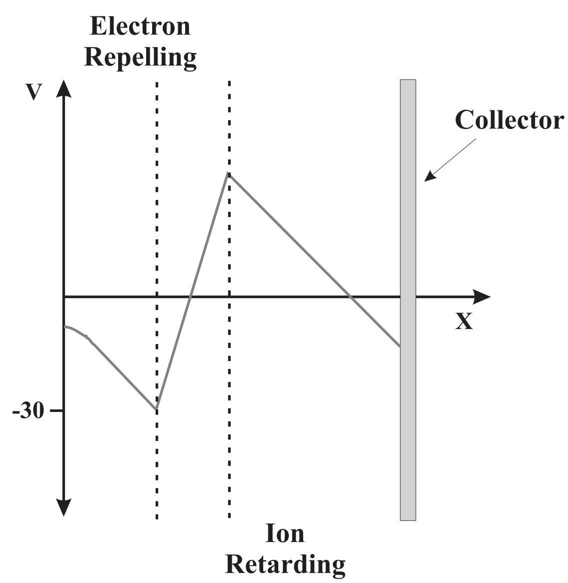

Figure 2-11. Retarding Potential Analyzed Potential Diagram

$$dI_p / dV_{probe} = \frac{-Z_i^{\,2} e^2 n_b A_c}{M_i} f(V) \qquad \textbf{(2-12)}$$

The outer body of the RPA is constructed of 316 stainless steel, which is held at ground potential. A phenolic sleeve placed inside the body provides electrical isolation of the grids. All grids are identical and are cut from 316 stainless steel, photochemically machined sheets with a thickness of 0.127 mm (0.005"). The grid apertures are 0.2794 mm (0.011") in diameter and the grids have an open area fraction of 38%. Grid spacing is achieved using Macor washers machined to provide the correct separation. The collector is a tungsten-coated stainless steel disc. A tungsten coating is used to reduce secondary electron emission from the collector. Electrical connections are accomplished by spot-welding stainless steel wire to each grid. The wires are then routed along the inner edge of the phenolic sleeve and through the rear of the RPA body. The washers and grids are compressed by a spring placed behind the collector and held in place by a rear cover.

During this investigation, RPA data are taken 1 meter downstream of the thruster exit plane from 30 to 90 degrees off centerline in 15-degree increments. Inside a 30-degree half-angle cone, the plasma density is often too high for proper RPA operation. RPA data as close as 20 degrees off centerline are possible for the operation points with lower discharge currents. Data collection on centerline is exceedingly difficult and attempts at data collection on axis resulted in RPA failure. It is shown in Section 3.4.3.2 that inside the cone half-angle of approximately 45 degrees, the most probable ion voltage is constant. Therefore, the lack of RPA measurements inside the 30-degree cone is not seen as a limitation for this investigation.

The RPA is used to provide estimates of the average ion acceleration kinetic energy. Due to difficulty in integrating the energy distribution function due to probe noise, the most probable voltage is used as an estimate of the average ion kinetic energy in electron volts. Since the ion retarding grid applies a voltage with respect to facility ground, it is necessary to correct the ion energy-per-charge distribution function for the plasma potential ($V_a=V_{mp}-V_p$). The plasma potential is measured using a Langmuir probe positioned at 1 m from the thruster exit plane at 30 degrees off centerline. The Langmuir probe measurements are conducted using ESPion from Hiden Analytical. The Langmuir probe is cylindrical in shape with a diameter and length of 0.1 mm and 15 mm, respectively. The same plasma potential correction is used for all RPA positions from 90 to 20 degrees off centerline. Gulczinski[77] found almost no plasma potential variation with angular position in the similar UM/AFRL P5 Hall thruster and Walker's[57] work with the P5 found plasma potential variation of no more than 4 V between 20 degrees and 90 degrees off centerline. The sources of error associated with the RPA result in an uncertainty in the most probable voltage of ±10 V.[34]

The current collected by the RPA is processed by using a smoothing spline[78] to reduce the signal noise. As shown in Equ. 2-12, the normalized ion energy-per-charge distribution function is found by taking the derivative of the current with respect to voltage using a central difference method. The collected current, spline smoothed collected current, and the resulting energy-per-charge distribution function is shown in Figure 2-12.

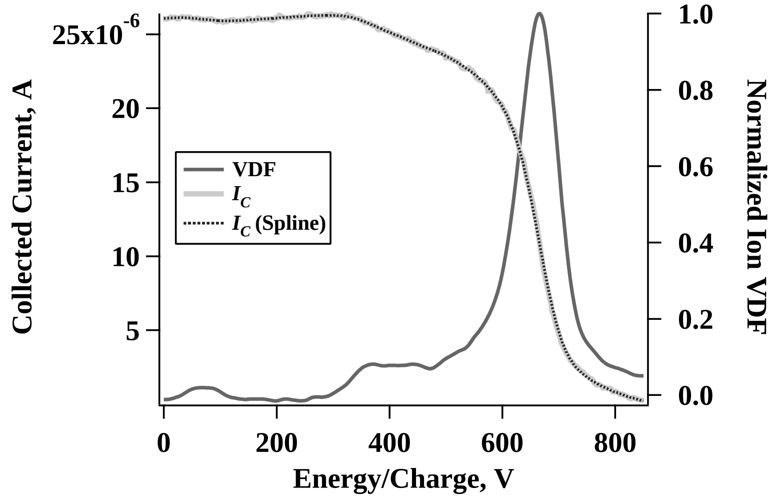

Figure 2-12. Retarding Potential Analyzer Data Processing Example

2.4 Internal Diagnostics

A large portion of this thesis focuses on the investigation of properties and processes internal to the Hall thruster. For these studies, the NASA-173Mv1 is mounted on two linear (radial and axial) tables that control the probe alignment and positioning. A series of diagnostics are mounted on the High-Speed Axial Reciprocating Probe (HARP) system and the diagnostics are then swept at high-speed into the Hall thruster discharge channel. The HARP system, is securely fixed downstream of the thruster to dampen any vibrations caused by the high-acceleration movement of the probe. The experimental setup can be seen in Figure 2-13 and a photograph of the probe insertion can be seen in Figure 2-14. The individual components are discussed in greater detail below.

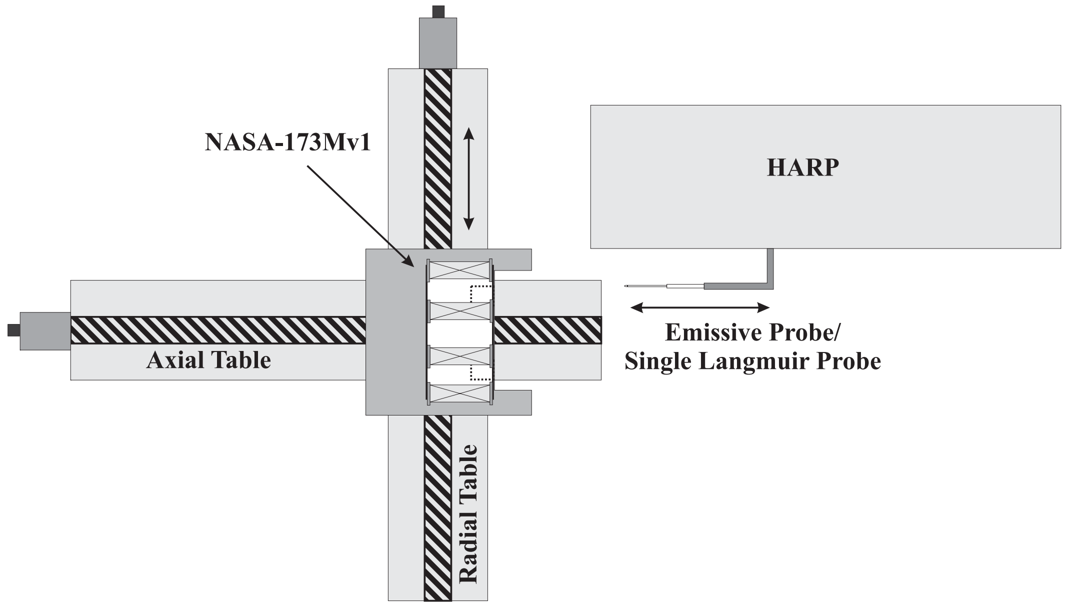

Figure 2-13. Internal Probe Experimental Setup

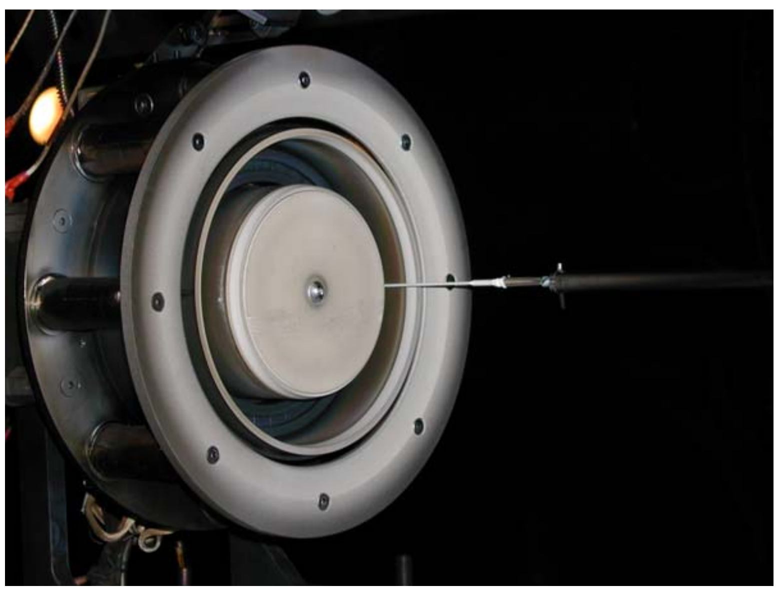

Figure 2-14. Discharge Channel Probe Insertion

2.4.1 High-Speed Axial Reciprocation Probe System

The HARP[58,79] (Figure 2-15) has a linear motor assembly providing direct motion at very high speed and large acceleration. The linear motor is an LM210 manufactured by Trilogy that has a three-phase brushless DC servomotor consisting of a linear, "U"-shaped magnetic track and a "T"-shaped coil moving on a set of linear tracks. A linear encoder provides positioning resolution of 5 microns. The table is covered by a stainless steel and graphite shroud to protect the HARP from excessive heating and high-energy ions. One side of the shroud has a thin slit running the length of the table through which a probe boom extends. The HARP is capable of moving small probes at speeds of 250 cm/s with linear accelerations of 7 g's.

Figure 2-15. High-Speed Axial Reciprocating Probe System

2.4.2 Floating Emissive Probe

In order to study the plasma potential structure internal to the Hall thruster, a floating emissive probe is utilized. Similar methods of characterizing the internal potential structure of Hall thrusters have been used by other researchers.[59,80-84] Haas[59] also mapped the entire discharge channel of the UM/AFRL P5 with this technique, which he pioneered. In addition to the plasma potential, the electron temperature and electric field maps are also extracted from these data.

The following review of floating emissive probe analysis and techniques is often critical and focuses on the error associated with the probe. With this said, there is no probe superior to the floating emissive probe in its simplicity of use and for measuring instantaneous plasma potential. Furthermore, the floating emissive probe has excellent heritage. The critical tone of this section is born from the desire to improve on existing measurement techniques.

2.4.2.1 Theory of Operation

The principle of floating emissive probe operation is fairly direct. As the probe is heated, electron emission increases. When the probe emission is low and the probe has a negative bias with respect to the local plasma potential, the electrons escape into the plasma. As emission increases, the probe bias will plateau at the plasma potential at which point emitted electron are returned back to the probe. The emitted electrons create an apparent ion current and the probe will float at the plasma potential. This idealized behavior is illustrated in Figure 2-16. In this figure, Point i indicates operation with insufficient emission.

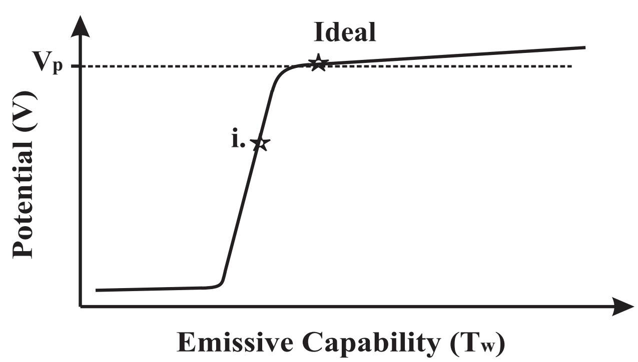

Figure 2-16. Ideal Characteristic Emissive Probe Curve

Chen[85] notes that in reality this ideal behavior cannot occur because of space-charge limitations. Due to the relatively low energy of the emitted electrons as compared to the hot plasma electrons, a double sheath will form. The potential well that forms reflects the emitted electrons back to the probe such that the probe is unable to reach plasma potential. In fact, the only case where the probe will float at plasma potential is when the emitted electron temperature is equal to the plasma electron temperature causing symmetry in the double sheath.[85]

2.4.2.2 Space-Charge Limited Sheath

Space-charge effects must be taken into account when analyzing emissive probe data in Hall thrusters. The space-charge limit is reached when the emitted electron current to collected electron current ratio (δ) reaches a critical ratio (δ_c) that is approximately equal to one. Hobbs and Wesson[86] present an equation for critical emission given in Equ. 2-13.

$$\delta_c = 1 - 8.3\left(m_e / M_i\right)^{1/2} \qquad \textbf{(2-13)}$$

As δ approaches δ_c, the electric field at the probe surface decreases and tends toward zero. Once δ becomes greater than δ_c, a potential well forms and emitted electrons are returned to the probe, creating a double sheath (solid line in Figure 2-17). Two other lines are also shown in Figure 2-17: i) $\delta < \delta_c$, insufficiency electron emission and iii) $\delta >> 1$, strong electron emission.[87] Due to the extreme frailty of the emissive probe inside the harsh Hall thruster discharge channel environment, the heater current is increased slowly until adequate filament heating is reached. Adequate heating is reached when the plasma potential profile no longer changes with increased electron emission. This heating method ensures that the probe is operating in the space-charge limited regime (regime ii).

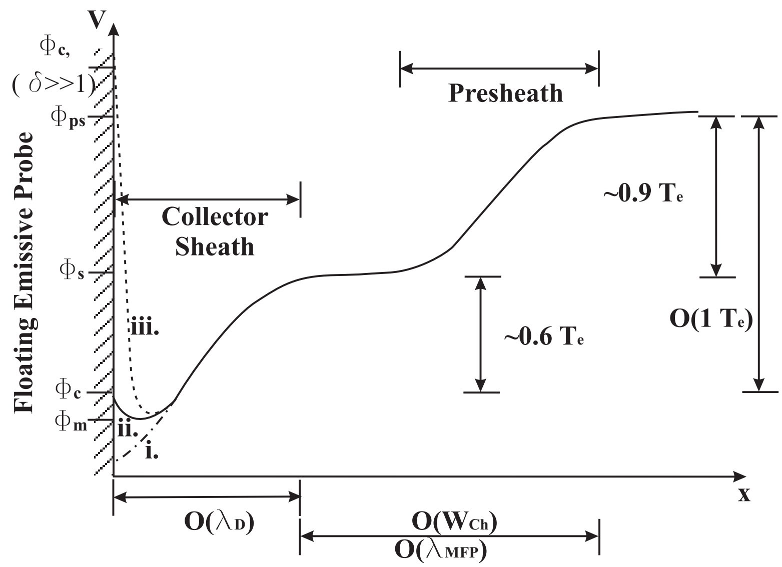

Figure 2-17. Emissive Probe Sheath. The different operation regimes are shown by dashed lines and are labeled accordingly. (Not to scale)

Adjacent to the emitting filament is the collector sheath. The collector sheath region is on the order of a Debye length in size and has been studied in great detail. Shwager[88] presents results that indicate the potential change in the collector sheath region to be 0.56 T_e for a D-T plasma with and ion-to-electron temperature ratio of 0.1. Hobbs and Wesson[86] present equations for cold ions, which Schwager solves exactly. For large ion to electron mass ratios, Schwager found the potential drop across the collector sheath region to asymptote to less than 0.6 T_e. Even for very different temperature and ion species, there is still relatively good agreement between these two results. The value for the potential drop across the collector sheath region is taken to be 0.6 T_e.

In addition to the collector sheath, there is a presheath separating the collector sheath and source plasma. A presheath forms in accordance to the Bohm criterion.[89,90]

In order for a stable sheath to form, the ions at the quasineutral sheath edge must be accelerated to the Bohm velocity in the presheath region. It is also necessary for the electric field to be close to zero at the edge of the sheath. The dimension of the presheath is typically on the scale of an ion mean free path (λ_{MFP}), which in our case is approximately as large at the Hall thruster discharge channel width (W_{ch}).[91] This fact presents difficulties that will be discussed later.

There has also been extensive work done to model the entire sheath (collector sheath and presheath) near a collecting and emitting wall. The total potential drop across the collector sheath and presheath is expected to be on the order of 1 T_e.[85] Schwager[88] suggests that the potential drop across the collector sheath and presheath should be approximately 1.5 T_e, a value that is commonly used by other researchers.[82,83,92-94] Stephens and Ordonez[95] offer an approximate expression to estimate the collector sheath and presheath potentials. For xenon plasma with an ion-to-electron temperature ratio of 0.2 and with an emission ratio (δ) equal to δ_c, the potential drop from the source plasma to the collector is approximately 1.35 T_e. For the current analysis, 1.5 T_e will be used for the potential drop across the collector sheath and presheath.

2.4.2.3 Space-Charge Limited Sheath Correction

Other experimenters[82,92,93] have augmented their floating emissive probe measurements by adding an electron temperature dependent correction term to the emissive probe measurements. This correction is used to account for the potential defect across the collector sheath and presheath in the space-charge limited case. The technique uses 1.5 T_e for the plasma potential correction term.

Unfortunately, this correction method can result in unusual behavior in the experimental results. Immediately upstream of the acceleration region, the electron temperature can be above 50 eV, which will result in a plasma potential correction of 75 V. This large voltage uncertainty leads to a large potential hump upstream of the acceleration region that is greater than the anode potential. This potential hump has not been observed experimentally.

The correction method for floating emissive probes is complicated by several other effects. Internal to a Hall thruster, the entire region consists of large interacting presheaths. With a highly non-uniform plasma and probe presheaths dimensions on the order of the discharge channel width,[91] it raises the question of how to most appropriately correct for the sheath potential defect while still maintaining a meaningful data resolution.

Aside from this, there are several other factors that complicate the space-charge limited sheath. Aforementioned models assume a large uniform plasma with a Maxwellian electron energy distribution, a situation that is not necessarily true inside the Hall thruster discharge channel. Most models assume a planer emitting surface, but the wire diameter is about equal to a Debye length, which places the probe between the thin sheath and orbital motion limited regimes. The magnetic field also changes the electron dynamics near the probe. A slight probe misalignment can have a large effect on the probe collection area.

Interestingly, there are cases when the emissive probe will operate ideally ($\delta > \delta_c$) due to charge exchange ions. When the CEX mean free path is on the same order as the plasma sheath potential structure, the slow moving ions fill the potential well and the sheath will not reach the space-charge limit.[87,88] The CEX mean free path is approximately of 3 cm (assuming n_n~5×10^{13} cm^{-3}). Keidar[91] suggests that the presheath is on the same order as the discharge channel (2.54 cm) whereas Intrator et al.[87] would suggest that total potential structure (collector sheath and presheath) is approximately 30-50 Debye lengths (0.3 cm). The effect of CEX ions on the space-charge limited sheath is not clear, but the behavior is worth considering.

To account for the inaccuracies in the measurement, the following correction is suggested and employed. The measured plasma potential is augmented by the collector sheath potential drop (0.6 T_e), which will give the instantaneous plasma potential local to the emissive probe. The collector sheath size (~O(λ_D)) internal to the Hall thruster is on the same order as the wire diameter, which is an order of magnitude smaller than the total emitting tip dimensions. Therefore, the desired resolution of approximately 1.5 mm is maintained. For reasons addressed previously, the effect from the probe presheath is more difficult to address and is considered a perturbation to the plasma. The presheath potential drop is used only to define error bars for the measurement. The corrected measurement should be accurate to within ±0.9 T_e. In addition to the presheath perturbation, one half of the potential drop across the floating heater power supply should also be included as uncertainty. Since the heater filament potential drop is 4 V, the total error associated with the plasma potential measurements is equal to ±0.9 T_e-2V. It is important to point out that for any of the aforementioned plasma potential corrections, the location and length of the acceleration zone will not be significantly affected.

Electron temperature can be calculated by assuming an isotropic Maxwellian and by using both "hot" and "cold" probe measurements. Although the electron energy distribution may depart from the Maxwellain assumption, the electron temperature measurements should represent an average electron energy. Equation 2-14 uses the potential drop across the total sheath to calculate the electron temperature. The error in this temperature calculation is -17%/+38%.[81]

$$V_p - V_f = -\frac{k_B T_e}{e} \ln\left(0.61\sqrt{\frac{2\pi m_e}{M_i}}\right) \tag{2-14}$$

Axial and radial electric fields at each location inside the thruster are also presented below. A central difference method is used with the plasma potential to calculate the electric field. The forward difference technique is used for the first point, and backward difference approach for the last point.

2.4.2.4 Emissive Probe Design

The emissive probe is based on the design used by Haas.[59] The emissive probe is composed of 1.5-mm-diameter double bore alumina insulator. The emitting filament is 1% thoriated tungsten with a diameter of 0.0127 cm. The electrical connection along the length of the probe is completed using 30 AWG copper leads that are slightly recessed into the alumina shaft. Additional short lengths of thoriated tungsten wire are inserted into the alumina tubing to provide a tight fit and guarantee good contact between the emitter and copper wires. The expected resolution of the emissive probe (1.5 mm) is the approximate size of the filament loop. A schematic of the emissive probe appears in Figure 2-18.

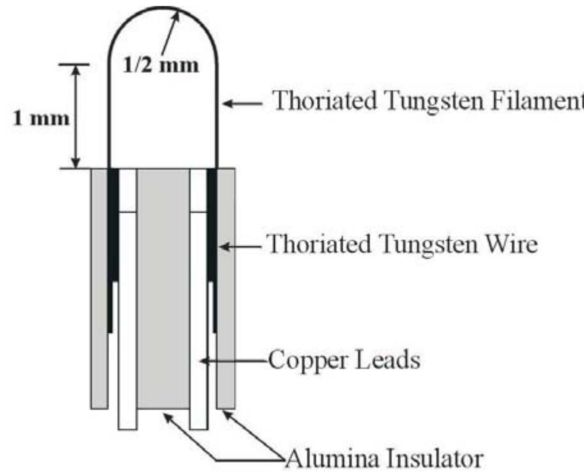

Figure 2-18. Emissive Probe Schematic

The diameter of the emitting filament is 0.0127 cm, which is much smaller than the electron cyclotron radius inside the Hall thruster. This condition is necessary for unmagnetized probe theory to be valid.[96,97] The filament size used in these measurements is of the same emitter diameter used by Haas[59] and similar to the emitter diameter used by Raitses et al.[81-83,92-94]

Another important consideration in the design of the emissive probe is the filament material. Kemp and Sellen[98] suggest an upper limit for plasma number density of 10^{12} cm^{-3}. Typical electron number densities internal to a Hall thruster are on the order of 10^{11}-10^{12} cm^{-3}.[58] Electron temperatures are expected to be as high as 50 eV at a discharge voltage of 500 V,[92] which will result in relatively high electron currents. However, the use of thoriated tungsten, which has a higher emissivity than pure tungsten, should insure sufficient emission. By comparing the Langmuir probe equation (Equ. 2-15) for electron saturation current and the Richard-Dushman's equation (Equ. 2-16) for electron emissivity, one can determine the maximum operation range for emissive probe measurements. Thoriated tungsten[87] has emissive properties of A_{em}=3 A/cm^{2}K^2 and a work function of Φ_w=2.65 eV. Tungsten[53] has emissive properties of A_{em}=60 A/cm^{2}K^2 and a work function of Φ_w=4.6 eV. As shown by Figure 2-19, assuming a constant electron number density of 5×10^{11} cm^{-3} and a constant electron temperature of 10 eV, pure tungsten will emit sufficient electron current at about 2900 K and thoriated tungsten will emit sufficient electron current at about 2000 K. Note that the melting point of tungsten is 3400 K. Given the delicate nature of emissive probe measurements, thoriated tungsten is the clear choice for filament material.

$$j_{es} = -n_e e\sqrt{\frac{k_B T_e}{2\pi m_e}} \tag{2-15}$$

$$j_{em} = A_{em} T_w{}^2 \exp\left(\frac{e\Phi_w}{T_w}\right) \tag{2-16}$$

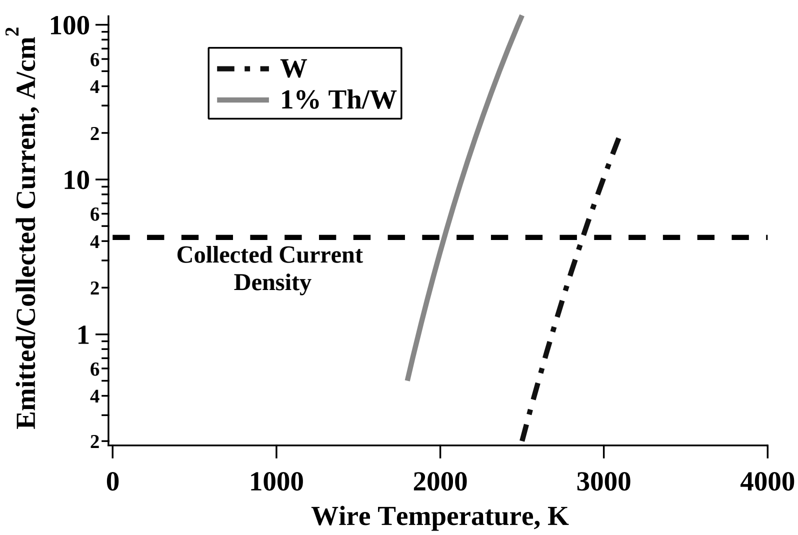

Figure 2-19. Emissive Capabilities of Pure and 1% Thoriated Tungsten

Plasma perturbations are in part caused by the alumina probe releasing secondary electrons into the discharge channel. Efforts were made to use a low secondary electron emitting (SEE) segmented coating[93] on the alumina shaft to reduce plasma perturbations.

A coating of 95% graphite paint is applied to the alumina in ringlets. The ringlets are approximately 1 mm in width with approximately 0.5 mm between the ringlets. A photograph of the emissive probe with low-SEE ringlets appears in Figure 2-20. Unfortunately, at high discharge voltage the graphite paint could not withstand the harsh environment internal to the thruster and for this reason, the graphite ringlets were not used for the data presented below. Even without the low secondary electron coating, the perturbations to the discharge current are below 10-20%.

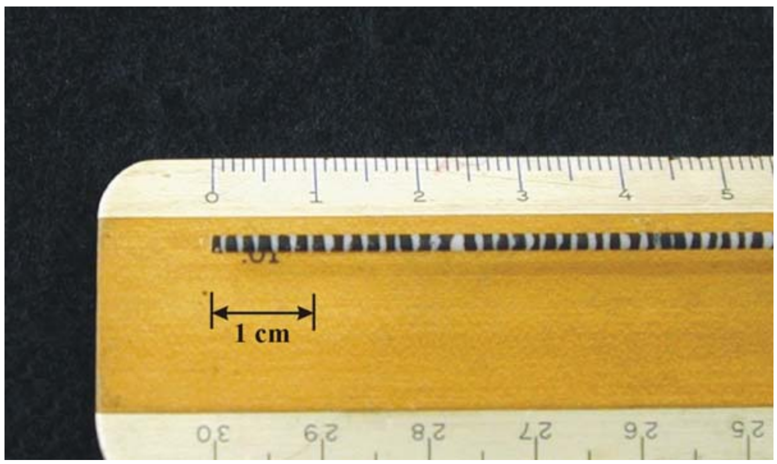

Figure 2-20. Photograph of the Low SEE Ringlets

2.4.2.5 Floating Emissive Operation

The floating emissive probe circuit consists of the emissive probe, an isolation amplifier, and a floating power supply capable of supplying enough current to heat the filament. The floating emissive probe circuit is shown in Figure 2-21. The sampling rate of the oscilloscope is dictated by the transit speed of the probe and is set to sample every 0.5 mm. This sampling speed is sufficient to easily capture the 1.5 mm resolution dictated by the probe dimensions. This sampling rate results in aliasing of the signal so that high frequency oscillations in the 10-30 kHz range, typical of the Hall thruster breathing mode, cannot be resolved. Therefore, these data constitute “time-averaged” measurements. The probe position and the perturbations to the discharge current and cathode potential are also recorded by the oscilloscope. During post processing, a gentle spline smoothing[78] is used to reduce the signal noise from the probe position and floating probe potential. An example of a typical data sweep is given in Figure 2-22, which shows the floating potential and the perturbations to the thruster as the probe is swept into the discharge channel. In this figure V_p is the plasma potential, V_k is the cathode potential and I_D is the discharge current.

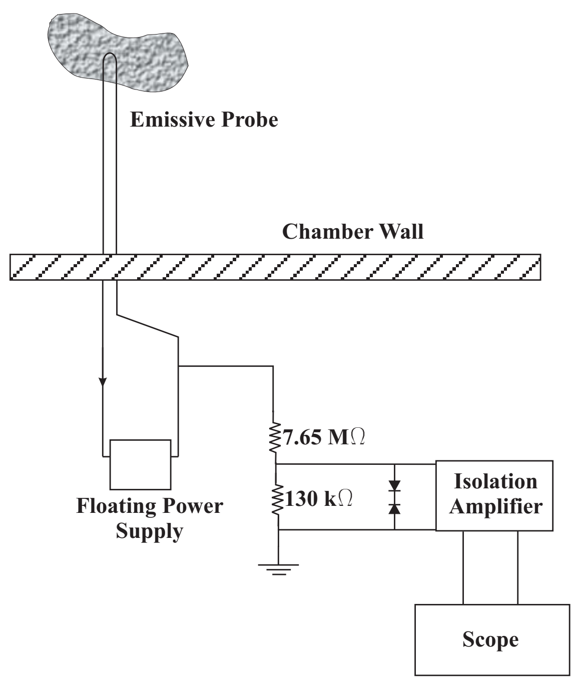

Figure 2-21. Floating Emissive Probe Circuit

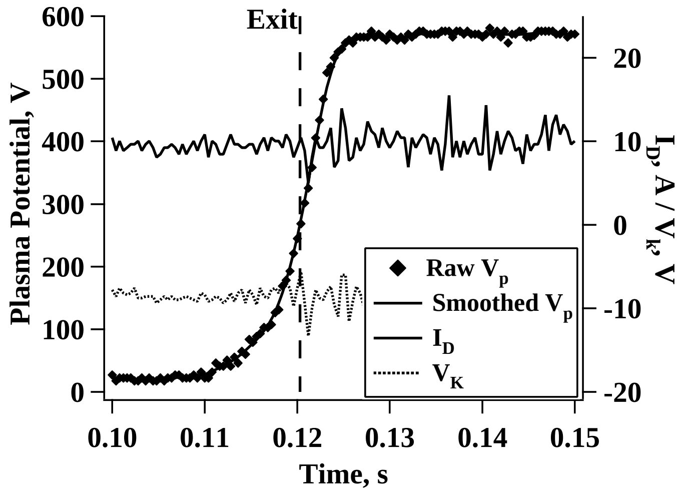

Figure 2-22. Emissive Probe Sweep Example

The area mapped by the emissive probes is displayed in Figure 2-23. The origin is taken to be the location where the inner wall meets the anode. Five axial sweeps spaced 5 mm apart are taken inside the Hall thruster discharge channel. The probe is aligned so that the filament tip travels from 137 mm to within 10 mm of the anode. However, in order to accentuate the areas of interest, the results section only shows the emissive probe findings in the region from 0 to 100 mm. The emissive probe is positioned so that the plane of the filament loop is normal to the thruster radial direction. For this experiment, the probe is swept at 150 cm/s and residence time inside the discharge channel is kept under 80 ms.

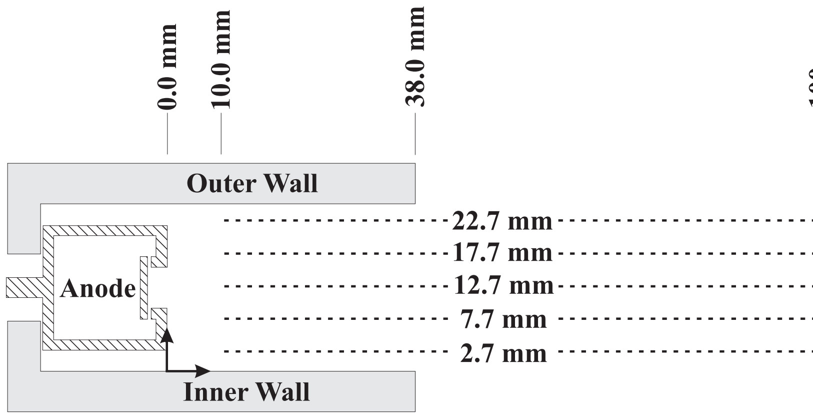

Figure 2-23. Region Mapped by the Floating Emissive Probe

2.4.3 Single Langmuir Probe

In conjunction with the internal emissive probe measurements, internal mapping with a single Langmuir probe is conducted. A single Langmuir probe is utilized to measure electron temperature and ion number density internal to the Hall thruster. A similar investigation on the UM/AFRL P5 Hall thruster has been conducted by Haas using a double Langmuir probe.[99] A single Langmuir probe is used in this investigation to improve the accuracy of the electron temperature measurements by avoiding the artificial electron saturation seen in double probe I-V characteristics. In recent years there has been extensive work mapping ion engine discharge chambers and near hollow cathodes using a similar technique.[100-105] With the combination of floating emissive probe measurement and Langmuir probe measurements, it should be possible to take a deep look at internal plasma processes.

2.4.3.1 Theory of Operation

Electrostatic probes are one of the most widely used diagnostics for determining plasma parameters. Due to the early work of Irving Langmuir, these electrostatic probes are often referred to as Langmuir probes.[106,107] The single Langmuir probe consists of an electrode connected to an electrical circuit allowing variation of probe voltage with respect to the local plasma, and the collection of current at each corresponding voltage. The current and voltage measurements create a current-voltage (I-V) characteristic from which properties including plasma potential, floating potential, electron temperature, and plasma density can be extracted. Although simple in operation, interpretation of the I-V characteristics is greatly complicated by a host of effects.

Langmuir probe operation can be divided into different probe regimes based on the two non-dimensional parameters: the Knudsen number (K_n) and Debye length (λ_D). The Knudsen number (Equ. 2-17) relates the ion or electron mean free path (λ_{MFP}) to the probe radius (r_p) and gives a relative measure of the number of ion or electron collisions as compared to the length scale of the probe. The Knudsen number also determines if the probe is in the collisionless or continuum plasma regimes. Since the mean free path of ions and electrons in the Hall thruster discharge channel is much larger than the probe radius, the Knudsen number is much greater than one and the probe operates in the collisionless regime.

$$K_n = \lambda_{MFP} / r_p \tag{2-17}$$

The next parameter used to determine the sheath analysis is the ratio of the Debye length (Equ. 2-18) to probe radius. The Debye length is proportional to the sheath width surrounding the probe and for this reason, this ratio can be used to determine the sheath regime. When $r_p/\lambda_D<3$ it is appropriate to use the orbital motion limited (OML) analysis and when $r_p/\lambda_D>10$ the thin sheath analysis is appropriate. Due to a range in electron temperature (5-60 eV) and plasma number density (10^{11}-10^{12} cm^{-3}), the Langmuir probe spans both of these sheath regimes. Selection of the proper sheath analysis is discussed in Section 2.4.3.4.

$$\lambda_D = \sqrt{\frac{k_B T_e}{4\pi n_e e^2}} \tag{2-18}$$

2.4.3.2 Langmuir Probe Design

For this investigation, a single cylindrical Langmuir probe is aligned with the axis of the thruster. The design of the Langmuir probe can be seen in Figure 2-24. The collector is a single tungsten wire routed through a 99.8% pure double bore alumina tube measuring a diameter of 1.5 mm in diameter and 100 mm in length. The length of the collector is 2 mm with a diameter of 0.254 mm. However, in the 300-V case, the tungsten collector is 1.5 mm long with a diameter of 0.102 mm. A 6.35-mm-diameter stainless steal tube is used to mount the probe and support the thin ceramic tube. The tungsten collector is connected to a bayonet Neill-Concelman (BNC) line through a pin connection and the stainless steel tube is connected to the BNC shield. Before and after the experiment, the probe is inspected under a microscope to verify probe dimensions and look for damage. There are several design and operational considerations that are used for the selection of these probe dimensions including probe survival, current signal strength, magnetic field effects, thruster perturbation, end effects, and data resolution.

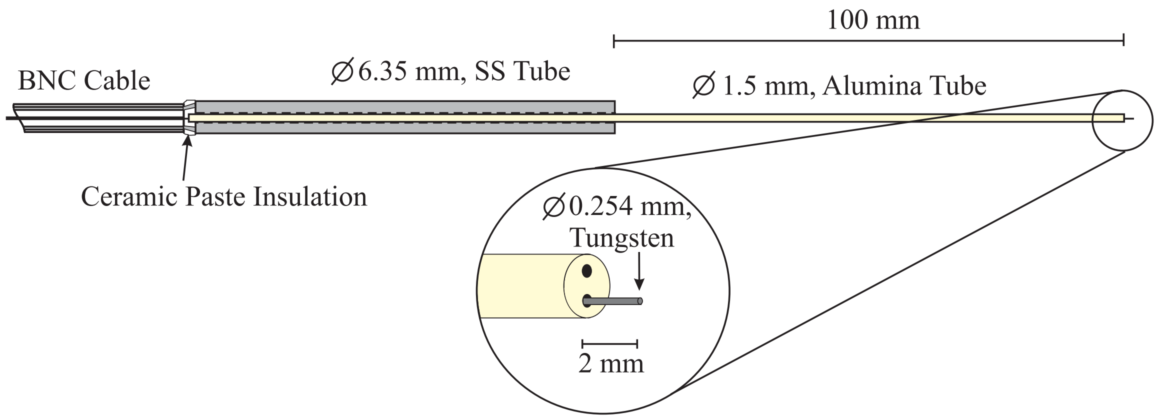

Figure 2-24. Single Langmuir Probe Design

A first concern in the design of the probe is robustness. The tungsten probe must be large enough to survive the energy flux from large, high-energy electron currents. The most extreme case occurs if there is a poorly timed probe bias pulse. A large tungsten collector also enables a strong, clean signal that greatly aids the analysis of these data. The drawback of increasing collector size is a reduction in spatial resolution. The alumina also needs to be robust in order to withstand the interaction with the Hall current for several successive sweeps. However, larger-diameter alumina tube results in greater discharge current perturbation.

2.4.3.3 Langmuir Probe Operation

For this experiment, the probe voltage oscillates at high-frequency during the HARP sweep to give a current-voltage curve corresponding to every spatial location. The probe voltage oscillates in a triangle wave pattern at 350 Hz. As the Langmuir probe is swept into the discharge channel, the floating potential (and plasma potential) increases several hundred volts over the length of a few millimeters. In order to capture sufficient data from the ion saturation and electron retarding regimes at every location, an offset voltage is superimposed on the voltage oscillation. This offset allows the probe bias voltage to always oscillate about the floating potential. To ensure that useful data are taken over the entire region, a second shallower set of sweeps is taken with a smaller bias voltage pulse. The voltage pulse is triggered by the HARP position. This probe bias pulsing is illustrated in Figure 2-25. In this figure, the plasma potential is shown in black and two bias voltage sweeps are labeled Bias Sweep 1 and 2. The location of the voltage pulse is determined from the internal emissive probe measurement.

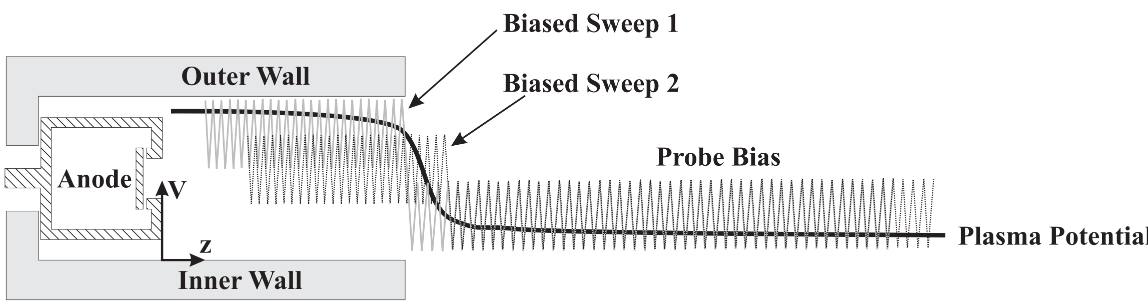

Figure 2-25. Probe Bias for Data Collection

In order to decrease the thruster perturbations it is necessary to increase the HARP speed, decrease the probe residence time, and decrease the probe size while keeping the probe large enough to ensure probe survival. However, in order to maximize the number of I-V characteristics per length, it is necessary to minimize the HARP speed and maximize the bias oscillation frequency while minimizing the stray capacitance associated with the rapid voltage oscillations. Probe resolution can be increased by decreasing the length of the probe tip at the cost of a weaker probe signal and a greater end effect. With all of these considerations in mind, the probe is operated in the following manner.

The probe is swept into the discharge channel nine times at a speed of 76 cm/s, keeping the probe residence time inside the discharge channel below 120 ms. The sweeps have a radial spacing of 2.5 mm (10% of the channel width). The HARP sweep length is set to 200 mm although data are only reported between 10 and 100 mm. After successive sweeps and exposure to the internal plasma, the alumina would begin to glow orange and eventually melt resulting in probe failure. To prevent this, 15 s are allowed between sweeps to allow the alumina to cool. The axial spatial resolution of the probe is assumed to be equal to the probe length; i.e., 2 mm for the 500-V cases and 1.5 mm for the 300-V case. The radial resolution is dictated by the error associated with manual alignment of the probe and any jitter during probe acceleration and results in a radial resolution of 0.5 mm. The voltage oscillation rate and the probe sweep speed yield an I-V curve every 1.09 mm of axial length. Figure 2-26 shows the region mapped by the HARP sweeps.

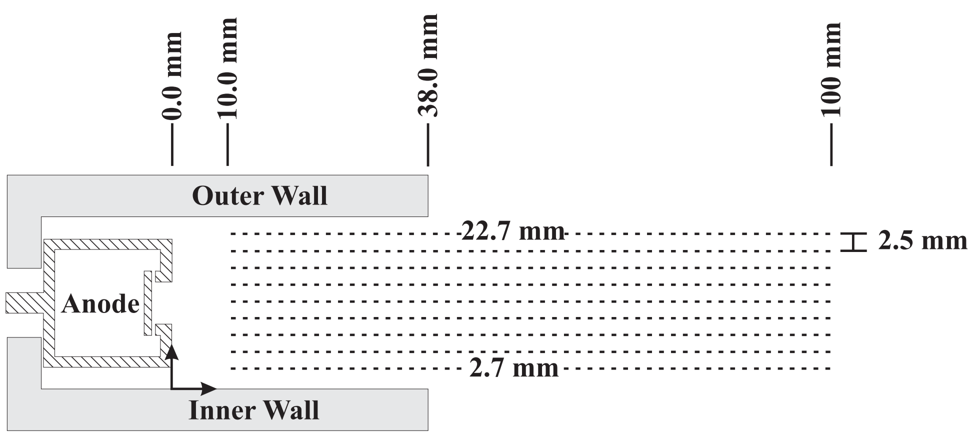

Figure 2-26. The Langmuir Probe Mapped Region

Due to the rapid voltage oscillation associated with the probe voltage sweep, stray capacitance becomes a concern. However, by characterizing the stray capacitance in a vacuum without the plasma, the classical trend where the capacitive current is equal to capacitance times the derivative of the voltage with respect to time ($I_{Cap}=C\ dV/dt$) can be easily observed, characterized, and accounted for. Therefore, raw data can be appropriately corrected and capacitive effects can be effectively removed. An example of the stray capacitance in the Langmuir probe circuit is shown in Figure 2-27.

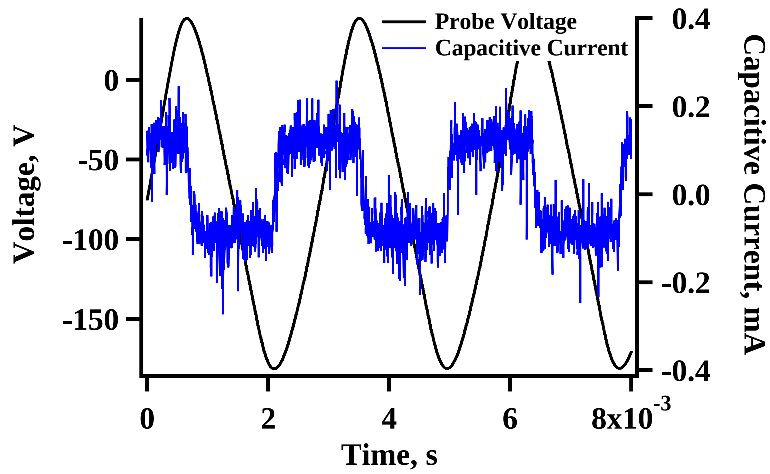

Figure 2-27. Stray Capacitance Causes by Voltage Oscillation

Another possible source of error is thermionic emissions from the probe. If the tungsten probe reaches very high temperatures, it is possible for the probe to emit electrons in the same manner as an emissive probe. When tungsten is heated to 2000 K, the emitted electron current equals 5% of the total ion saturation current. As the tungsten temperature continues to increase, the electron emission increases exponentially. In these cases, the emitted electron current will appear to be an increased ion current and the I-V characteristic will be shifted. Because the collected ion current is rather small, in comparison to the electron current, this effect is important. Although it is possible for the probe to gain significant heating due to the high-density, high-temperature electrons, very careful selection of the pulse location and modest probe bias voltages should prevent this behavior. A simple method to check for thermionic emission is to compare the floating potentials measured by the Langmuir probe with those measured with a cold emissive probe. This comparison suggests that the effects of thermionic emission can be ignored in this investigation.

A schematic of Langmuir probe circuit is shown if Figure 2-28. The triangle wave and square pulse are sent to a non-inverting summing amplifier, which then sends a signal to a bipolar power supply. This signal is amplified and sent to the Langmuir probe. The Langmuir probe current and voltage are monitored by two AD210 isolation amplifiers and their signals are monitored by a data acquisition system. The probe current, probe voltage, HARP location, and thruster discharge current are acquired at 100 kHz per channel. For each data sweep, 25,000 points are recorder per channel resulting in about 140 points per I-V curve.

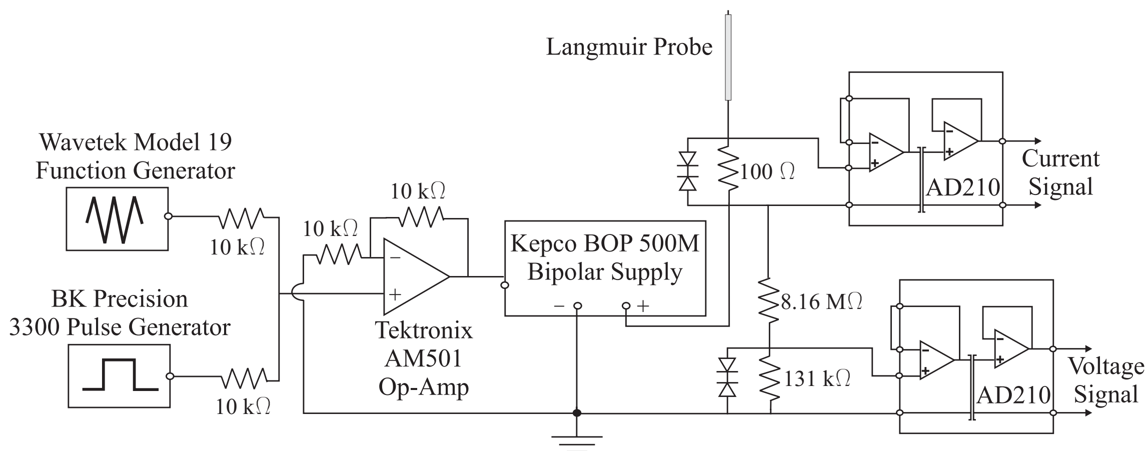

Figure 2-28. Langmuir Probe Circuit

For these data, the thruster discharge current perturbations reached a maximum of between 10 and 22%. Segmented graphite or tungsten coatings are used by other researchers[93] to reduce thruster perturbations by decreasing secondary electron emission from the alumina probe. However, for this experiment, due to the high-power and high-voltage of the Hall thruster operation, the high-temperature graphite paint is unable to withstand the extreme conditions in the discharge channel and no segmented coating is used.

2.4.3.4 Data Analysis

The magnetic field can affect Langmuir probe results by constraining the motion of charged particles (particularly electrons) and subsequently altering the I-V characteristic. As a result, sheath structures around probes are no longer symmetric and can become oblong. A magnetic field can most adversely affect the I-V characteristic by suppressing the electron saturation current. This effect makes it difficult to measure the electron number density and the plasma potential. The electron retarding region is also suppressed, giving rise to a smaller slope and corresponding an over predication in electron temperature. Since the ions are unmagnetized in the Hall thruster discharge chambers, and this study uses the ion saturation current to calculate the ion number density, the ion number density is unaffected by the magnetic field. Since the plasma potential is not the focus of these Langmuir probe measurements, magnetic field effects on plasma potential measurements are ignored. For a cylindrical probe, the effect of the magnetic field is minimized when the probe axis is perpendicular to the magnetic field lines. In the peak magnetic field region, the probe axis and magnetic field are very close to perpendicular. For all of the data presented the probe radius is smaller than the gyroradius by no less than a factor of 5 so the magnetic field effect is not significant in this problem.

The magnetic field can also cause anisotropy in the electron energy distribution function (EEDF), which can affect the electron temperature measurement. The magnetic field effects can be considered small based on the following argument. Passoth[108] determined that EEDF anisotropy depends upon the ratio B/p_o, where p_o is the pressure in the containment vessel. Aikawa[109] showed experimentally that EEDF anisotropy is negligible for $B/p_o < 2.5\times10^6$ G/torr. Assuming that the neutral temperature[110] and number density (see Section 5.4.7.2) are approximately 850 K and 4×10^{13} cm^{-3}, the pressure inside the discharge channel is 3.5×10^{-3} torr. With a maximum magnetic field on the order of 300 G, one finds a B/p_o ratio of 9×10^4 G/torr, which is well below the threshold value proposed by Aikawa.

When a cylindrical Langmuir probes is used in a flowing plasmas, one must consider end effects.[111] In this situation, an additional parameter becomes important: the probe length to Debye length ratio (l_p/λ_D). Chung, Talbot, and Touryan[111] offer the parameter given in Equ. 2-19 for the relative importance of end effects in the collisionless regime. When τ_l is much greater than unity, end effects are very small.

$$\tau_l = \frac{l_p}{\lambda_D}\frac{\left(k_B T_e / M_i\right)^{1/2}}{V_i} \tag{2-19}$$

In the prime area of interest, internal to the discharge channel, the ions have undergone little acceleration and the end effect is negligible. Consider, the worst case scenario, 100 mm downstream of the anode where the plasma number density and electron temperature are approximately 5×10^{11} cm^{-3} and 8 eV, respectively. Assuming that a propellant ion falls through 470 V of potential as it passes through the acceleration zone, and given the probe dimension in this experiment, the value of τ_l is greater than 6.

As the probe moves upstream into the region of interest, the value of τ_l increases to a value of a few hundred. In the center of the acceleration zone, τ_l is equal to approximately 20. Accordingly, the end effects have been neglected in the following analysis.

It is possible that aligning the probe parallel to the electric field may distort the I-V characteristic near the plasma potential by rounding the knee of the I-V curve.[108] However, this effect mostly affects the I-V characteristic near the plasma potential, and will have little influence on electron temperature and ion number density measurements. For this reason, this effect is not considered important and has been neglected.

The scientific graphing package Igor is used to analyze these data. The raw Langmuir probe data are first separated into current-voltage pairs resulting in approximately 4,000 I-V characteristics. Each I-V pair is analyzed separately and the extracted plasma properties are then reassembled into one output file. This output file is then plotted in contour maps.

Each I-V curve undergoes three passes with a three-point box smoothing algorithm to smooth the signal and increase the ease of analysis in difficult regions. The probe voltage range for each box is approximately 3-4 V. Internal to the discharge channel, the I-V characteristics sometimes become noisy due to the breathing mode instability creating an oscillation in the probe current. The breathing mode is a discharge current oscillation related to propellant ionization and is discussed in Section 4.1. An extreme case of this can be seen in Figure 2-29, which shows a breathing mode instability of 20 kHz. In this figure, one can see the raw I-V curve and the I-V curve after the smoothing. Also plotted is the discharge current versus time. The top and bottom axes

(Time and Probe Voltage, respectively) correspond point by point so it is possible to see the correlation between the discharge current and probe current. Due to this smoothing, the calculated plasma properties can be considered time averaged and any fluctuation in the ionization zone will be averaged in time accordingly.

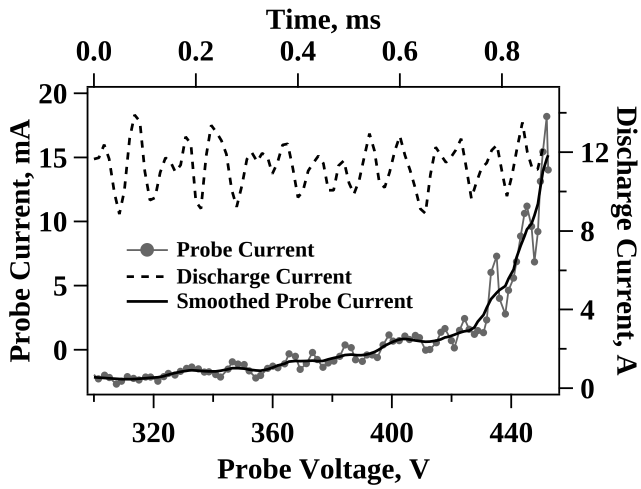

Figure 2-29. The Effect of the Breathing Mode on the I-V Characteristic

During the analysis of the I-V characteristic, the floating potential is first calculated and then if possible the plasma potential is measured by finding the maximum of the first derivative of the I-V characteristic. The electron population is assumed to be Maxwellian and the ion current is subtracted from the I-V curve. Theoretical Hall thruster models often assume a Maxwellian or bi-Maxwellian electron energy distribution, however there is no evidence of a bi-Maxwellian distribution from these Langmuir probe data. Based on the floating potential and plasma potential, the electron retarding region is defined and the electron temperature is calculated. The inverse slope of the natural log of electron current versus voltage gives the Maxwellian electron temperature.

The ion saturation current is then calculated. For consistency, the ion saturation current ($I_{i,sat}$) is always measured between a voltage range that varies relative to the floating potential. That is to say, if the floating potential is equal to 10 V, then the ion saturation current would equal the average of the ion current between -50 and 0 V. If the floating potential is 300 V, then the ion current would be averaged between 240 and 290 V. This range is chosen because it corresponds to a region where the I-V characteristic is roughly flat. Based on the ion saturation current and the electron temperature, the ion number density for the thin sheath assumption ($n_{i,thin}$) can be calculated by Equ. 2-20, where A_s is the probe collection area.

$$n_{i,thin} = \frac{I_{i,sat}}{0.61 A_s e}\sqrt{\frac{M_i}{k_B T_e}} \qquad \textbf{(2-20)}$$

The true probe collection area depends upon the thickness of the sheath surrounding the probe. For this reason, it is necessary to modify the probe collection area to calculate the true ion number density for the thin sheath assumption. Based on the calculated plasma properties, the new probe collection area is calculated and the iteration is continued until convergence is reached. Assuming quasineutrality for the calculation of the Debye length, the sheath thickness (δ_s) is calculated from Equ. 2-21 and the sheath collection area is calculated from Equ. 2-22.[112,113] In these equations, A_p is the physical probe surface area.

$$\delta_s = 1.02\lambda_D \left[\left(-\frac{1}{2}\ln\left(\frac{m_e}{M_i}\right)\right)^{1/2} - \frac{1}{\sqrt{2}}\right]^{1/2}\left[\left(-\frac{1}{2}\ln\left(\frac{m_e}{M_i}\right)\right)^{1/2} + \sqrt{2}\right] \qquad \textbf{(2-21)}$$

$$A_s = A_p\left(1 + \delta_s / r_p\right) \qquad \textbf{(2-22)}$$

The next step is to calculate the ion number density based on the OML assumption ($n_{i,OML}$). This regime is analyzed by the techniques developed by Laframboise[114,115] that assume a cylindrical probe immersed in a cold, collisionless, stationary plasma. In this case, the sheath dimensions are assumed to increase with probe bias such that the collected ion current is affected. In the OML regime, the number density for cylindrical probes is calculated from the slope of the ion current squared versus bias voltage according to Equ. 2-23.[85,115,116]

$$n_{i,oml} = \frac{1}{A_p}\sqrt{\frac{2\pi M_i}{1.27e^3}\left(\frac{dI_i^{\,2}}{dV}\right)} \tag{2-23}$$

Chen[85] suggests that the OML regime is entered when the ratio of probe radius-to-Debye length is less than approximately three. Whereas a probe radius-to-Debye length ratio of greater than ten indicates that the probe is in the thin sheath regime. Unfortunately, a great deal of these Langmuir probe data fall between the thin sheath and OML regimes. An example of the range in Debye lengths is illustrated in Figure 2-30. To account for these data, a weighted average (based on the Debye length to probe radius) is used to give smooth transition between these regimes. The analysis techniques used in this investigation have been used and documented by several researchers.[85,107,111,112,117-121]

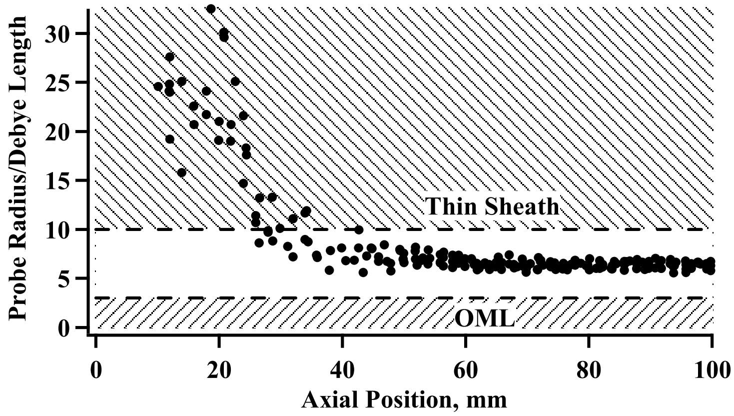

Figure 2-30. Probe Radius to Debye Length Ratio Along the Thruster Centerline

A traditional error estimate of 20% for electron temperature and 60% for ion number density are assumed in this experiment.[112] Although the magnitude of the error is somewhat large, the relative error from point to point should be consistent resulting in accurate relative trends.

Chapter 3.

Performance Study and Analysis

Chapter 3 includes a performance study based on the measurements from a series of external diagnostics. These results include efficiency optimization scaling analysis, performance results, a detailed efficiency analysis, and plume properties.

3.1 Efficiency Optimization Scaling

There have been several studies investigating Hall thruster performance using krypton propellant.[21,23,24,26-28,30,31,38] All investigations find krypton to have a performance gap ranging from marginal to significant. In general, the reason for this performance gap is related to propellant utilization. Although the focus of the scaling analysis is krypton ionization optimization, a similar analysis is applicable for xenon operation conditions where propellant utilization is low; e.g., low discharge voltages.

For efficient ionization, the neutral residence time should be longer than the time required for electron impact ionization. The time rate of change from neutrals to ions is equal to the total ionization collision rate (Equ. 3-1). Therefore, the characteristic ionization time is given by Equ. 3-2, which must be less than the neutral residence time. By approximating the residence time as the channel length (L_{ch}) divided by the neutral particle velocity, a relation for the ratio of times is given in Equ. 3-3.

$$\frac{dn_n}{dt} = -n_e n_n \left\langle Q_{i,n} V_e \right\rangle \qquad \textbf{(3-1)}$$

$$t_i = 1 \Big/ \left(n_e \left\langle Q_{i,n} V_e \right\rangle \right) \qquad \textbf{(3-2)}$$

$$\frac{t_{res}}{t_i} = \frac{L_{ch} n_e \left\langle Q_{i,n} V_e \right\rangle}{V_n} \qquad \textbf{(3-3)}$$

By assuming quasineutrality ($n_i \approx n_e$) to relate the electron number density to the ion flux, and assuming that the ion flux is proportional to and approximately equal to the total heavy particle flux through the anode, we can simplify the electron number density (Equ. 3-4). In this equation, K' is a constant of unspecified value. To first order accuracy, K' can be considered approximately equal for both propellants. In reality, due to the propellant utilization difference, the value of K' is approximately 10% higher for xenon as compared to krypton. Propellant utilization is approximately 90% for xenon and 80-86% for krypton (Section 3.4.3.5).

$$n_e \approx n_i \approx K' \big/ \left(A_{ch} V_i \right) \qquad \textbf{(3-4)}$$

By inserting standard relations for the neutral and electron velocities, relating ion velocity to the discharge voltage (V_D), and by noting that in the electron energy range of interest, the ionization collision cross section is approximately constant,[122] one can arrive at a simple expression for Hall thruster optimization (Equ. 3-5).

$$\frac{t_{res}}{t_i} = \frac{K \left[M_i Q_{i,n} \right] \dot{v}_a L_{ch}}{A_{ch}} \sqrt{\frac{T_e}{T_n V_D}} \qquad \textbf{(3-5)}$$

When Equ. 3-5 is maximized, ionization efficiency is optimized. Again, K is a constant of unspecified value. For the same reasons as K', K is about 10% higher for xenon as compared to krypton, but can be considered approximately equal for both propellants. Anode volumetric flow rate ($\dot{v}_a$) is used because it is a measure of the total propellant atoms injected into the discharge channel and because of it is a more fundamental quantity than total thruster flow rate for understanding ionization processes.

Equation 3-5, which is effectively the same scaling relation found by Kim et al.,[26] suggests that propellant utilization will be improved for increased anode flow rate, channel length, and electron temperature. The propellant utilization will also improve when neutral temperature and channel area (A_{ch}) for a given anode flow rate are reduced. Discharge dimensions can indeed be exploited to optimize krypton efficiency, but for the current discussion the discharge channel dimensions are fixed. It is also possible that the neutral temperature can be managed by active or passive thermal control of the anode and discharge channel walls. Although this suggests a new important design consideration, this experimental setup is incapable of Hall thruster thermal control. The most obvious factor that improves propellant utilization is anode flow rate, which is the focus of the later discussion.

Equation 3-5 would appear to suggest that as discharge voltage increases, ionization efficiency decreases, but in fact the opposite is true. Ionization efficiency improves at high voltages due to changes in the electron temperature and thus the ionization collision cross section. At low discharge voltages, electron temperatures increase linearly (due to Joule electron heating) with discharge voltage.[81,123,124] Moreover, the ionization collision cross section for krypton also increases nearly linearly below an electron temperature of approximately 40 eV.[122] However, with discharge voltages between approximately 400-700 V, the electron temperature saturates[81,123,124] near 50-60 eV, which results in a plateau in ionization efficiency.

The behavior of the bracketed constant in Equ. 3-5 is worth exploring. Figure 3-1 shows that above an electron temperature of about 30 eV (approximate discharge voltage of 300 V as shown in Sections 4.2.2.1 and 4.3.2) the ratio of krypton-to-xenon total electron impact ionization collision cross section is almost constant at 0.68. If the Hall thruster is operating above a discharge voltage of 300 V with xenon and krypton, the bracketed coefficient given in Equ. 3-5 ($M_i Q_{i,n}$) will be 2.3 times lower for krypton, which shows the difficulty in operating krypton efficiently. At electron temperatures below 30 eV (discharge voltages below ~300 V), it is probably nearly impossible for krypton to rival xenon in performance with conventional Hall thruster designs.

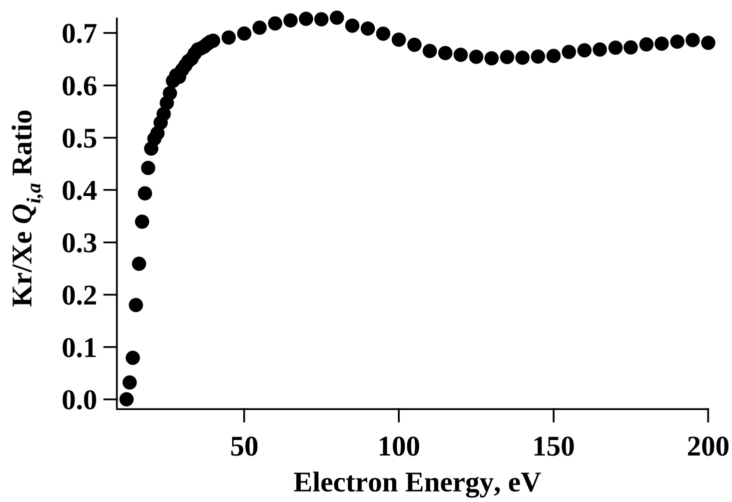

Figure 3-1. Ratio of Krypton to Xenon Total Electron-Atom Impact Ionization Collision Cross Section versus Electron Energy

It should be possible to determine a scaling constant that indicates the point at which efficient ionization is reached. Equation 3-6 gives this constant is a function of discharge channel dimension and anode flow rate. This constant should be consistent for a large range of thruster sizes assuming that different thrusters are operating at similar conditions (e.g. matched discharge voltage, electron temperature, and thruster thermal temperature). Each propellant will have its own unique value of α_V. Krypton's value of α_V is expected to be approximately twice as high as xenon's α_V value.

$$\alpha_V = \dot{v}_a \frac{L_{ch}}{A_{ch}} \tag{3-6}$$

Equation 3-6 is analogous to the relation found by Morozov and Melikov[125] and Bugrova et al.,[126] which is shown in Equ. 3-7. In Equ. 3-7, volumetric flow rate is replaced with mass flow rate and channel length is replaced by the channel width (b). Channel width is chosen for their scaling constant because they assert that channel width is characteristic of the region with significant electric fields. According to Kim,[127] discharge channel length and width scale proportionally, so either choice for scaling is likely equivalent. Bugrova et al.[126] suggest that the value of α is approximately constant at 0.02 mg/(mm-s) and is similar for both krypton and xenon.[23] For reasons discussed previously, krypton's α value is expected to be as much as 50% higher than xenon's α value. The use of mass flow rate instead of volumetric flow rate reduces the difference in the α value for krypton and xenon due to the difference in atomic mass. There is not enough information about the electron energy distribution to give a conclusive statement as to the difference in the value of α between krypton and xenon. To be consistent with previous work, the value of α derived by Bugrova et al. will be used in the following analysis.

$$\alpha = \dot{m}_a \frac{b}{A_{ch}} \tag{3-7}$$

3.1.1 Discussion of Optimization Design Consideration

This optimization scaling offers a series of operation and design conditions to improve krypton performance in Hall thrusters. A few of these considerations require deeper discussion and these will be covered in this section.

3.1.1.1 Discharge Channel Dimensions

Due to the simple nature of Equ. 3-5 it is very easy to misinterpret the findings. A particular point of possible confusion is the discharge channel dimensions. Both channel area and channel length appear in Equ. 3-5 and both deserve some discussion. It should be noted that Raitses, Ashkenazy, and Guelman studied the effect of discharge channel dimension on propellant utilization and found conclusions that agrees with this optimization scaling.[128]

It could be reasoned that ionization zone length is more appropriate than chamber length in this scaling argument. However, to make this substitution would incorporate magnetic field design and would defeat the purpose of the first order optimization. The effects of magnetic field topology will be handled in Chapter 6. It is important to note that by increasing the channel length, it would be effectively increasing the scale of the thruster. Not only would the channel length change, but accordingly so would the magnetic field topology and the ionization zone resulting from a particular topology.

The discharge channel area also appears in the Equ. 3-5. The author wishes to note that it is the neutral flow to channel area that is important, not the channel width alone.

3.1.1.2 Neutral Temperature

Although it is a topic that has had little discussion in the past, the control of the neutral number density through active or passive thermal control is an intriguing one. The little previous work that exists is reviewed below.

Researchers from Michigan Technological University have experimented with a Hall thruster using a shim anode.[129] The shim anode is an auxiliary anode separate from the traditional propellant injecting anode and is used to split the discharge current between the two anodes. By splitting the discharge current between these two anodes they are able to control the temperature of the propellant injector. This design was studied for use with a Bismuth Hall thruster where thermal management is extremely important. It is shown that by modifying the shim current, they are able to decrease the propellant injector temperature by about 10% in the rear of the propellant injector.[110] It is unclear what the temperature of the propellant injector is on the surface exposed to plasma. Kieckhafer et al. showed that by increasing the shim current and hence decreasing the anode temperature, the plume centerline beam current increases. Kieckhafer et al. briefly suggested that the reason for this result may be related to propellant utilization.

Active thermal control in ion engines was also studied by Wilber and Brophy.[130] In similar fashion, they hoped to decrease the ion engine wall temperature as a way to decrease neutral velocity and improve thruster performance. Wilber and Brophy found significant performance improvements as the thruster was cooled from 500 to 90 K.

3.1.1.3 Cold Anode Experiment

Following this theory of decreasing neutral temperature as a means to increase propellant utilization, the following experiment was conducted. In an attempt to cool the neutral atoms entering the discharge channel a "cold anode" was designed and tested in the LVTF. A photograph of the cold anode is shown in Figure 3-2 and a schematic of the anode appears in Figure 3-3. Water flows through the rear portion of the anode and actively controls the anode temperature.

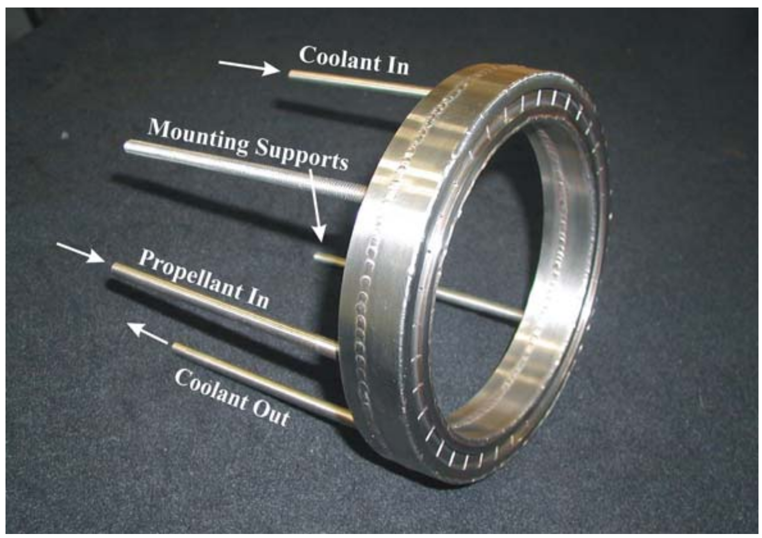

Figure 3-2. The Water Cooled Anode for Active Thermal Management

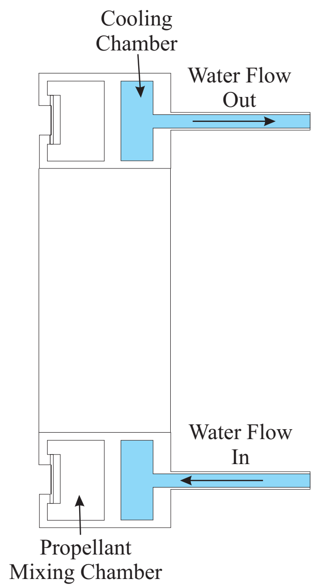

Figure 3-3. Water Cooled Anode Schematic (Not to scale)

The experimental setup for the cold anode experiment can be seen in Figure 3-4. The coolant water is supplied by a recirculation chiller. Deionized water is used and the water lines are isolated from the cold anode by two water breaks. The total resistance between the anode and ground was 5 MΩ. The thruster used in this experiment was a UM/AFRL P5 Hall thruster.

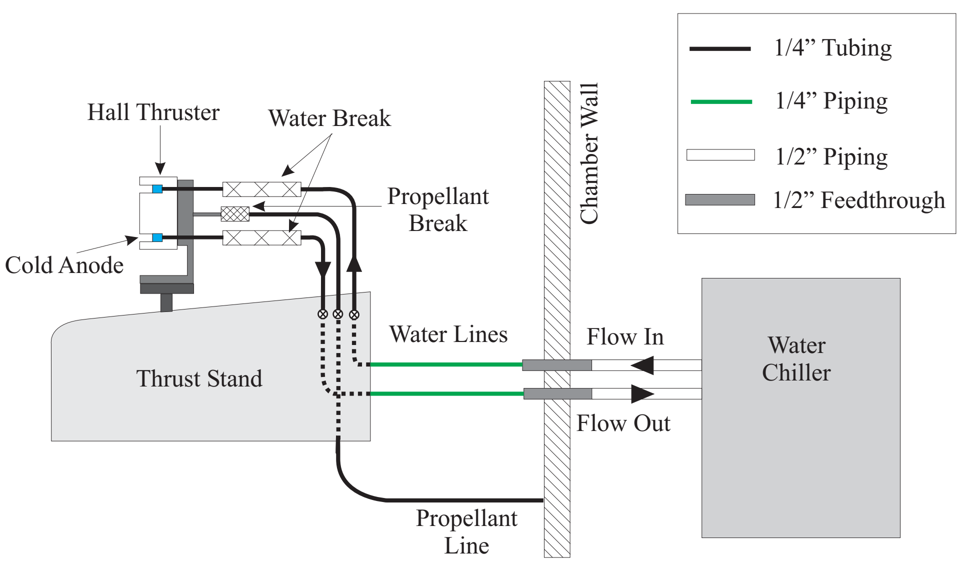

Figure 3-4. Cold Anode Experimental Setup

Unfortunately, the thruster failed to operate properly in this configuration. The thruster, while able to establish a glow discharge, was unable to establish a standard thruster plume. It is possible that the cooling water created a conductive path to ground and reduced the anode potential. The experiment failed when the thruster anode shorted to ground. This shorting took place at a discharge voltage of only 150 V and shorted though several layers of fiberglass and fusion electrical tape. Previous to the experiment, the anode was biased to over 1000 V without shorting.

3.2 Performance Results

All of these data presented below are taken using the NASA-173Mv1 Hall thruster unless otherwise noted. A table of the performance results for the NASA-173Mv1 can be seen in Appendix A. Although little focus is given to the UM/AFRL P5 Hall thruster performance using krypton propellant, for completeness tabulated performance data can be seen in Appendix B.

3.2.1 Specific Impulse Trends

Although an efficiency gap does exist between xenon and krypton, Figure 3-5 shows the superior anode specific impulse of krypton. This figure illustrates the advantage of reducing the efficiency gap between xenon and krypton. Krypton could potentially, broaden the range of mission applications for Hall thrusters. The points presented in Figure 3-5 operate at discharge voltages ranging from 300 to 800 V and discharge currents ranging from 5-16 A.

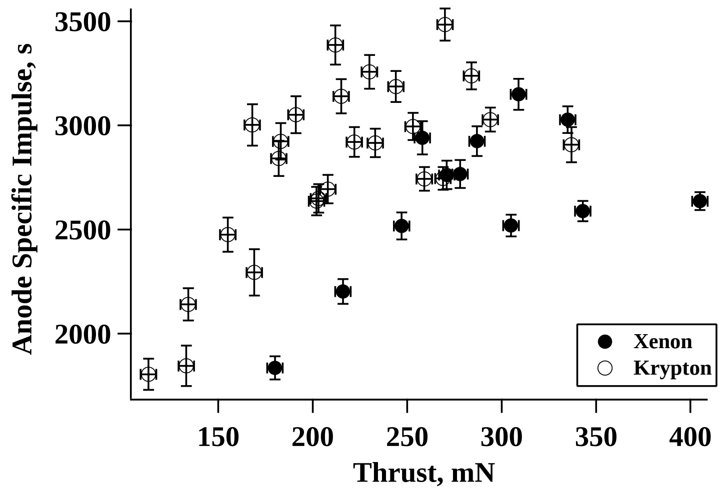

Figure 3-5. Krypton and Xenon Anode Specific Impulse versus Thrust

3.2.2 High-Voltage Krypton Operation

Figure 3-6 shows the performance results for the NASA-173Mv1 operating with krypton at 1200 V discharge voltage. The anode efficiency ranges between 54-59% and the specific impulse is greater than 4100 s with a maximum specific impulse of 4300 s. Both the thruster anode efficiency and anode specific impulse decrease with increasing power. The decrease in thruster efficiency is probably related to the extreme operating conditions and overheating of the thruster. The discharge channel walls visibly glow orange when the thruster is operated at such high voltage. The glowing walls indicate very high electron-wall collisions and the reduced efficiency is likely due to increased near-wall conductivity.

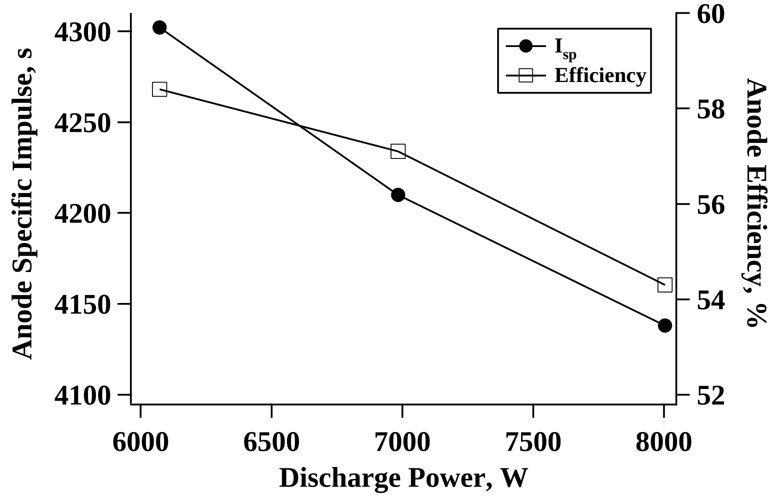

Figure 3-6. NASA-173Mv1 Performance at a Discharge Voltage of 1200 V with Krypton Propellant

3.2.3 Voltage Trends

Anode efficiency versus discharge voltage at a constant flow rate of 102.4 sccm is shown in Figure 3-7. There are three curves in this figure: one xenon curve, a krypton curve matching xenon volumetric flow rate, and a krypton curve matching xenon power. Krypton efficiency improves and the efficiency gap between xenon and krypton narrows with increasing discharge voltage. At low voltage, the absolute anode efficiency gap is approximately 15% and as voltage is increased the efficiency gap is reduced to 2%. Also, the krypton efficiency improves with increased anode flow rate. The power matched flow rate curve has higher anode efficiency than the flow rate matched curve and has approximately 25% higher anode flow rate. There is a peak in xenon efficiency located at a discharge voltage of 500 V. This peak may be due to increased discharge current associated with the hotter electrons and increased near wall conductivity. Although the krypton power matched line shows a similar peak at 500 V, this trend is much less clear in the krypton lines because of the dominant role that propellant utilization plays.

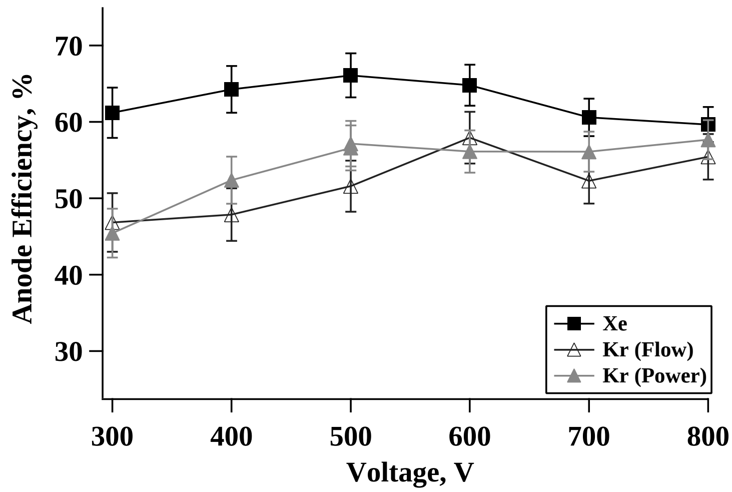

Figure 3-7. Anode Efficiency versus Discharge Voltage for the NASA-173Mv1

The flow rate and voltage trends shown in Figure 3-7 indicate that propellant utilization is likely responsible for the efficiency gap. Increasing krypton anode flow rate increases the neutral number density and the ionizing collision frequency. As discharge voltage increases, the electron temperature increases and plateaus at around 50-60 eV.[81,123,124] It is shown in Sections 4.2 and 4.3 that the maximum electron temperature for both xenon and krypton does fall in this range, however krypton's electron temperature is slightly higher. This is expected since many researchers believe that main contributor to the electron temperature saturation is losses to the wall in a space-charge limited sheath.[81,123,124] This figure suggests that krypton efficiency plateaus in the electron saturation regime (approximately 400-700 V) and krypton efficiency is optimized above discharge voltages of 500 V.

Similarly, the anode efficiency versus voltage for the UM/AFRL P5 Hall thruster is shown in Figure 3-8. Just as in Figure 3-7, the anode flow rate is set equal to 102.4

sccm and the discharge voltage is varied from 150 to 700 V. Again, anode efficiency increases with discharge voltage and seems to plateau above 500 V. As the discharge voltage increases, the efficiency gap appears to decrease. The efficiency gap between xenon and krypton reaches a minimum of 6.1% at 600 V. The krypton efficiency appears to plateau at and above 600 V and would probably only increase by a few percent with further increase in discharge voltage. Unfortunately, data are not taken at higher voltages since the P5 is not designed for high voltage operation. Although the trends seen with the P5 are similar to the trends seen with the NASA-173Mv1, the NASA-173Mv1 performance is clearly superior to the P5's.

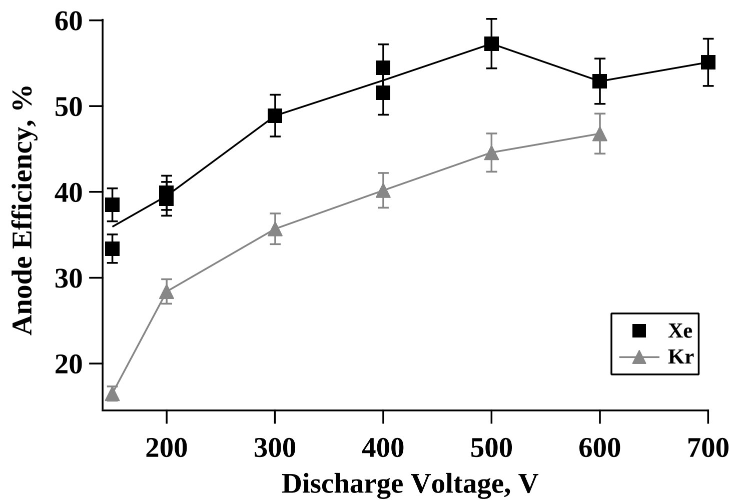

Figure 3-8. Anode Efficiency versus Discharge Voltage for the UM/AFRL P5 with 102.4 sccm Anode Flow Rate

3.2.4 Flow Rate Trends

To improve the krypton efficiency further, it is important to focus on efficiency trends at different anode flow rates. Figure 3-9 shows anode efficiency versus anode flow rate for krypton at 500, 600, and 700 V. These voltages are in the electron saturation regime discussed earlier and also fall above the suggested voltage minimum for optimized krypton efficiency. At low flow rates, krypton efficiency greatly improves with anode flow rate. However, the anode efficiency plateaus between 55 and 60% as anode flow rate continues to increase. Two linear fits are applied to the low anode flow rate and high anode flow rate sections. The intersection of these lines is located at 114 sccm and defines the point at which the anode efficiency plateau begins. This suggests that in the electron saturation regime, optimum krypton efficiency is reached when α is equal to or greater than 0.015 mg/(mm-s). This corresponds to a current density and flow rate density of approximately 80 mA/cm^2 and 1 sccm/cm^2, respectively. This criterion should give the necessary neutral number density for efficient krypton operation for a broad range of Hall thruster sizes.

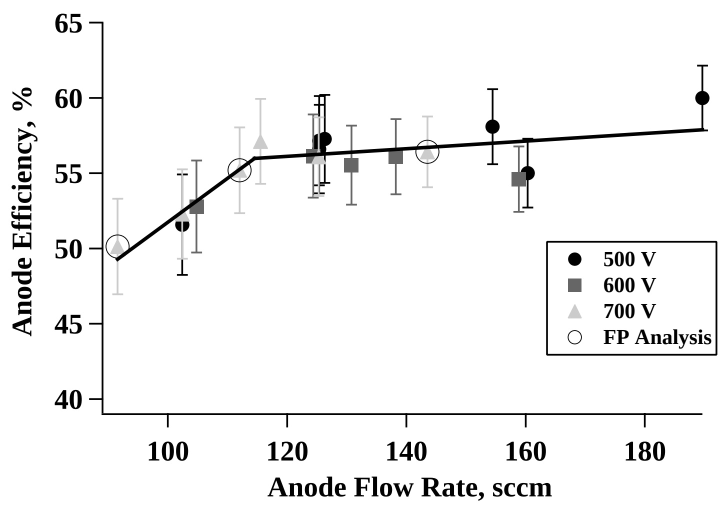

Figure 3-9. Krypton Anode Efficiency versus Anode Flow Rate

3.3 Faraday Probe Measurement of Propellant Utilization

The MFFP is used to estimate the propellant utilization and identify trends in the performance results. Propellant utilization is the ion mass flow out of the thruster as compared to the total anode flow rate. The beam current is calculated from the Faraday probe data by integrating from 0 to 90 degrees in spherical corrdinates.[72] It is then possible to calculate propellant utilization efficiency by using Equ. 3-8, where $\dot{m}_b$ is the total ion mass flow rate, I_b is the beam current, and all other symbols have been defined previously.[34,73] Species fraction results, which are presented in Section 3.4.3.3 are incorporated to calculate propellant utilization. Although the propellant utilization magnitude is somewhat imprecise, the relative trends between these data points are expected to be much more accurate.

$$\eta_p = \frac{\dot{m}_b}{\dot{m}_a} = \frac{M_i I_b}{\dot{m}_a e} \sum \frac{\Omega_i}{Z_i} \qquad \text{(3-8)}$$

Faraday probe results are presented for the four operation points given in Table 3-1: xenon operation at 700 V and 6 kW, and three krypton conditions that match the xenon volumetric flow rate, xenon power, and xenon mass flow rate. The anode efficiency and propellant utilization for these points also appear in Figure 3-10. The krypton points fall above, below, and on the knee of the efficiency optimization curve and are circled in Figure 3-9. The relative error associated with calculating propellant utilization from the Faraday probe measurements is estimated as 9%.

Table 3-1. Operation Points of Interest for the Faraday Probe Analysis

Point #	Propel.	V_D, V	I_D, A	Discharge Power, W	Anode Flow, mg/s (sccm)	Cathode Flow, mg/s	Inner Coil, A	Outer Coil, A	Trim Coil, A	Thrust, mN	I_{SP}, s	Anode Effic., %	Propel. Util., %
1	Xe	700	8.57	5999	8.94 (91.59)	0.90	2.81	2.95	-1.48	258	2940	62.0	86.5
2	Kr	700	11.42	7994	8.94 (143.52)	0.89	2.20	2.52	-0.51	284	3237	56.4	78.7
3	Kr	700	8.57	5999	6.98 (112.03)	0.70	2.32	2.94	-0.51	215	3140	55.2	78.2
4	Kr	700	7.05	4935	5.70 (91.56)	0.57	2.20	2.25	-0.57	168	3002	50.1	75.3

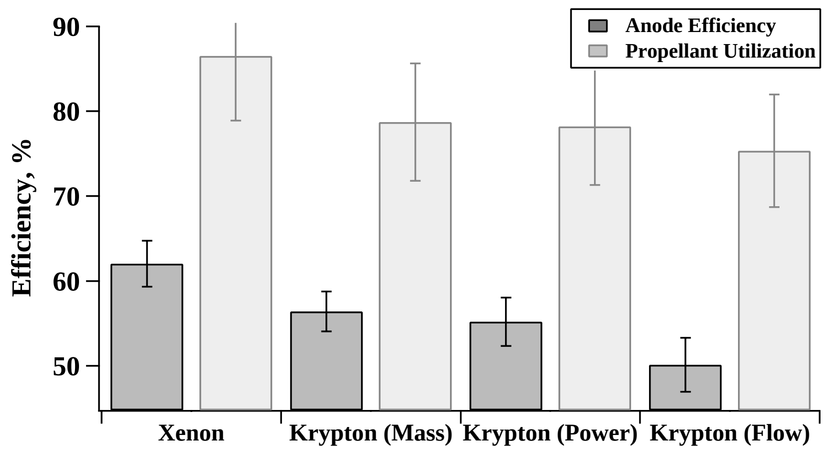

Figure 3-10. Anode Efficiency and Propellant Utilization Efficiency Comparison

The anode efficiency compared to xenon is relatively 10% lower (absolute difference of about 6-7%) for krypton operating at and above the anode efficiency knee, and below the efficiency knee, the relative difference in anode efficiency is 19%. Above the efficiency knee, the propellant utilization efficiency for krypton has a relative difference of 9% below xenon. Below the efficiency knee the relative propellant utilization efficiency gap increases to 13%. These trends confirm the theory that the efficiency gap for krypton is strongly related to the propellant utilization efficiency.

3.4 Detailed Efficiency Analysis

The next step in reducing the efficiency gap between xenon and krypton is to more precisely pinpoint the reasons for this gap. Although, performance and Faraday probe measurements go a long way in understanding the link between propellant utilization and the performance gap, a detailed efficiency analysis is necessary to fully characterize the problem.

This section presents a series of experimental results using the NASA-173Mv1 Hall thruster. The diagnostics used include a thrust stand, RPA, E×B probe, cylindrical Langmuir probe, and MFFP. These measurements are then applied to a modified performance model first presented by Hofer[34,73] to isolate the efficiency differences between krypton and xenon. The efficiency analysis separates the anode efficiency into separate components, which allows one to evaluate the specific performance differences between krypton and xenon, define a direction for further investigation, and improving krypton efficiency in future thrusters.

3.4.1 Phenomenological Performance Model

A phenomenological performance model developed by Hofer[34,73] separates the Hall thruster anode efficiency into four separate terms: the charge utilization; the propellant utilization; the current utilization; and the voltage utilization. With these efficiencies separated, it is possible to create distinctions in the importance of the individual efficiencies. In the case of krypton operation, it should be possible to pinpoint the different features that lead to the efficiency gap.

Total Hall thruster efficiency is a combination of anode efficiency (η_a), cathode efficiency (η_c), and electromagnetic coil efficiency (η_{Mag}). The anode efficiency can be further broken down into the four aforementioned partial efficiencies. Equation 3-9 shows the total efficiency whereas Equ. 3-10 gives the equation for anode efficiency.

$$\eta_T = \eta_c \eta_{Mag} \eta_a \tag{3-9}$$

$$\eta_a = \tau^2 / \left(2 \dot{m}_a P_D\right) = \eta_b \eta_p \eta_q \eta_v \tag{3-10}$$

The partial efficiencies are defined as follows. Current utilization efficiency is the amount of ion current as compared to the discharge current and is given in Equ. 3-11. Voltage utilization efficiency is the measure of the amount of the discharge voltage (potential energy) that is converted into axial ion kinetic energy and is defined in Equ. 3-12. Propellant utilization is the amount of neutral anode flow that is converting into ion flow and is given in Equ. 3-13 (and in a slightly different form in Equ. 3-8). Finally, charge utilization is the measure of the overall charge state of the beam ions (Equ. 3-14). Based on a series of diagnostic measurements, values for these separate efficiencies can be calculated.

$$\eta_b = I_b / I_D \tag{3-11}$$

$$\eta_v = V_{a,eff} \big/ V_D = 1 - V_l \big/ V_D \tag{3-12}$$

$$\eta_p = \frac{\dot{m}_b}{\dot{m}_a} = \frac{M_i I_D}{\dot{m}_a e} \eta_b \sum \frac{\Omega_i}{Z_i} \tag{3-13}$$

$$\eta_q = \left(\sum \frac{\Omega_i}{\sqrt{Z_i}} \right)^2 \Bigg/ \sum \frac{\Omega_i}{Z_i} \tag{3-14}$$

Based on probe measurement uncertainty, the charge utilization efficiency has a relative error of less than 1% for krypton and less than 2% for xenon. The propellant utilization efficiency and current utilization efficiency can be calculated based on the diagnostic measurements and the other efficiency calculations. The relative errors are 3.1% and 4.4% for current utilization and propellant utilization efficiency, respectively (for both xenon and krypton). Voltage utilization efficiency error will be covered in the next section.

3.4.2 Acceleration and Beam Divergence Efficiency

The assumptions used in the derivation of acceleration and beam divergence efficiency are summarized below. These assumptions are covered in greater detail in the text.

1. The average acceleration voltage is equal for all ion species.
2. The average acceleration voltage is constant at all angular positions in the beam.
3. The species fractions along centerline are a good representation of the species fractions in the entire thruster plume.
4. The species fractions are approximately constant at different angular positions in the plume.

While the Hofer performance model is extremely useful for conducting a detailed study of Hall thruster performance, a modification can be applied to measure the voltage utilization efficiency more accurately. The problem in the existing method of measuring the voltage utilization is not a flaw in the theory, but in the application of the theory. Previously,[73] the voltage utilization has been calculated by taking an RPA measurement to calculate the average ion kinetic energy. While being able to capture the average kinetic energy of the ions, RPA measurements are incapable of capturing the entire voltage utilization efficiency.

Voltage utilization efficiency is a measurement of the effective axially directed ion kinetic energy in electron volts as compared to the thruster discharge voltage. The energy loss is mainly a combination of spread in the energy-per-charge distribution function (dispersion efficiency), failure of the plasma to drop to cathode potential, and radial beam divergence. The energy loss is also affected by the ionization potential of the propellant, wall losses, and ion charge-state. The correct calculation of the average axial ion energy requires a mass-weighted average of the ion energy over the entire angular range of the thruster plume (See Equ. 3-15). Furthermore, this analysis should take into account the effects of multiply-charged species. Voltage utilization can be broken into two measurable components: acceleration efficiency; and beam divergence efficiency. The acceleration efficiency is a way of quantifying the average ion kinetic energy and the beam divergence efficiency is a measure of the divergence loss in the beam. Hofer's voltage utilization efficiency (given in Equ. 3-12) is broken into the acceleration and divergence components in Equs. 3-16 and 3-17, respectively.

$$\eta_v = \eta_{acc}\eta_{div} = \frac{\langle \dot{m}_i(\theta) V_z(\theta) \rangle}{\dot{m}_b V_D} \tag{3-15}$$

$$\eta_{acc} = \frac{V_a}{V_D} \tag{3-16}$$

$$\eta_{div} = \frac{\langle \dot{m}_i(\theta) V_z(\theta) \rangle}{\dot{m}_b V_a} \tag{3-17}$$

Using a combination of RPA, Faraday probe, and E×B measurements, a more rigorous analysis of the voltage utilization efficiency can be conducted. This study shows that the beam divergence efficiency is between approximately 75-90% for xenon and krypton. Previous studies that neglected the beam divergence efficiency[73] have under-predicted the current and propellant utilizations by approximately 5-15%. Note that effort has been made to be consistent with Hofer's original model and the original model should be referenced as a guide to some of the finer details in this derivation.[34] In this derivation the subscript "*, i*" indicates the ith ion species.

Similar to Hofer's work, the average exit velocity of each species at angle θ is:

$$\langle v_{a,i}(\theta)\rangle = \sqrt{\frac{2Z_i eV_{a,i}(\theta)}{M_i}}\,. \tag{3-18}$$

To account for the axially directed thrust power produced, the axial component of ion velocity for each ion species is given in Equ. 3-19. However, in terms of performance, the average axial accelerating voltage for each ion species is the important variable, and is given in Equ. 3-20.

$$\langle v_{z,i}(\theta)\rangle = \langle v_{a,i}(\theta)\rangle \cos(\theta) \tag{3-19}$$

$$V_{z,i}(\theta) = M_i/(2eZ_i)\langle v_{z,i}(\theta)\rangle^2 = V_{a,i}(\theta)\cos^2(\theta) \tag{3-20}$$

The current density of all ion species at angle θ is

$$j(\theta) = \sum n_{i,i}(\theta) q_i \langle v_i(\theta)\rangle = \sqrt{2/M_i}\, n_b(\theta) e^{3/2} \sum \zeta_i(\theta) Z_i^{3/2} \sqrt{V_{a,i}(\theta)}\,. \tag{3-21}$$

The ion mass flux for all species at angle θ is given in Equ. 3-22.

$$\Gamma_i(\theta) = M_i \sum n_{i,i}(\theta)\langle v_i(\theta)\rangle = n_b(\theta)\sqrt{2eM_i} \sum \zeta_i(\theta) Z_i^{1/2} \sqrt{V_{a,i}(\theta)} \tag{3-22}$$

By solving Equ. 3-21 for n_b and combining it with Equ. 3-22, the ion mass flux equation reduces to:

$$\Gamma_i(\theta) = \frac{M_i}{e} j(\theta) \frac{\sum \zeta_i(\theta) Z_i^{1/2} \sqrt{V_{a,i}(\theta)}}{\sum \zeta_i(\theta) Z_i^{3/2} \sqrt{V_{a,i}(\theta)}}\,. \tag{3-23}$$

The average acceleration voltage of the different ion species may vary by a few volts. Kim[63] and King[131] both observe that the difference of these voltage potentials is on the order of the ionization potentials.[132] Due to the fact that the RPA measures energy-to-charge ratio of the ions, the measured most probable kinetic energy is an average acceleration voltage over all species. In addition to this, singly-charged ions account for a vast majority of the ion species in the plume. For these reasons, the average acceleration voltage is assumed to be equal for all ion species. A comprehensive discussion of this assumption is covered in Hofer's thesis.[34] With this assumption, Equ. 3-23 becomes:

$$\Gamma_i(\theta) = \frac{M_i}{e} j(\theta) \frac{\sum \zeta_i(\theta) Z_i^{1/2}}{\sum \zeta_i(\theta) Z_i^{3/2}}. \qquad (3\text{-}24)$$

The total ion mass flow rate in the beam can be calculated by Equ. 3-25.

$$\dot{m}_b = 2\pi z^2 \int_0^{\pi/2} \Gamma_i(\theta) \sin(\theta) d\theta \qquad (3\text{-}25)$$

Assuming that the species fraction measurement along centerline is a good representation of the species fractions in the entire thruster plume, the total ion beam mass flow rate can be given in the much simpler form shown in Equ. 3-26. Since the large majority of the beam mass flow rate will fall near the centerline of the thruster, this assumption is a good one.

$$\dot{m}_b = \frac{I_b M_i}{e} \left[\sum \Omega_i / Z_i \right]_{CL} \qquad (3\text{-}26)$$

To calculate the average mass-weighted axial acceleration voltage, the mass flux multiplied by the axial acceleration voltage is integrated from 0 to 90 degrees (Equ.

3-27). For this analysis, it will be necessary to make one more assumption; the species fractions are constant at different angular positions in the plume. Kim[63] did see species variation at different angular positions off thruster axis. If the multiply-charged species are formed in a multi-step process (as opposed to a single ionizing collision) they would begin accelerating farther down-stream, which would result in a larger divergence angle for multiply-charged species. Although Kim found species fraction variation at different angular positions, the above mentioned assumption will be necessary to proceed further with our analysis. Since such a large majority of the beam is located near the centerline of the thruster in a region of little species fraction variation, the error associated with this assumption will remain small. Additionally, the species fraction effects are of second order, so this assumption will still yield reliable results. Note that if E×B data are taken at all angular positions, this assumption would not be needed.

We are now able to solve for the voltage utilization efficiency. The new expression for voltage efficiency is given in Equ. 3-28.

$$\left\langle \dot{m}_i(\theta) V_z(\theta) \right\rangle = 2\pi z^2 \int_0^{\pi/2} \Gamma_i V_z(\theta) \sin(\theta) d\theta \tag{3-27}$$

$$\eta_v = \frac{2\pi z^2}{V_D \left[\sum \frac{\Omega_i}{Z_i} \right]_{CL}} \int_0^{\pi/2} V_a(\theta) g(\theta) \frac{\sum \zeta_i(\theta) Z_i^{1/2}}{\sum \zeta_i(\theta) Z_i^{3/2}} \cos^2(\theta) \sin(\theta) d\theta \tag{3-28}$$

$$g(\theta) = \left[j(\theta) / I_b \right] \tag{3-29}$$

The term $g(\theta)$ is the ion current density term divided by the beam current term, which gives particular advantages to the presented analysis. Faraday probes are well known to have a relatively moderate degree of error and are often only reliable in identifying relative trends. The advantage of dividing the current density by the total beam current measured by the Faraday probe is to remove this magnitude error. With this normalized current density function, the beam can be integrated using only the relative current density change, and the true beam current is left undetermined to be calculated later in the efficiency analysis. For this analysis it is advantageous to use a Faraday probe that filters charge exchange ions (e.g. a MFFP[65]) since, CEX ions contribute a large portion of the beam at large angles off centerline.

In the Hall thruster plume, the voltage for the primary beam ions is constant for a vast majority of the beam. This result is shown in the results Section 3.4.3.2. Experimental results show that elastic collision ions and CEX ions become a significant portion of the beam current only outside of the 95% cone half-angle (~60 degrees off centerline). For this reason, it is a safe to assume that the average acceleration voltage is constant at all angular positions in the beam. In fact, the difference in beam efficiency is less than one half of one percent with this assumption. This assumption further simplifies Equ. 3-28, which becomes Equ. 3-30 accordingly. The beam divergence efficiency is given in Equ. 3-31 and requires only one E×B measurement on centerline and one Faraday probe sweep.

$$\eta_v = \frac{V_a}{V_D} \frac{\sum \zeta_i Z_i^{1/2}}{\left[\sum \frac{\Omega_i}{Z_i}\right] \sum \zeta_i Z_i^{3/2}} \left[2\pi z^2 \int_0^{\pi/2} g(\theta)\cos^2(\theta)\sin(\theta)d\theta\right] \tag{3-30}$$

$$\eta_{div} = \frac{\sum \zeta_i Z_i^{1/2}}{\left[\sum \frac{\Omega_i}{Z_i}\right] \sum \zeta_i Z_i^{3/2}} \left[2\pi z^2 \int_0^{\pi/2} g(\theta)\cos^2(\theta)\sin(\theta)d\theta\right] \tag{3-31}$$

The relative error in the accelerating voltage efficiency is calculated from the RPA uncertainty and is equal to 1.6%. The beam divergence efficiency is calculated by analyzing a large number of MFFP measurements and comparing the results to nude Faraday probe data. The variance of the beam divergence efficiency is then calculated and is used to arrive at a conservative estimate for the beam divergence error. The relative error of the beam divergence efficiency is 2.5%. This method is conservative because the nude Faraday probe is well known to vastly over-predict the beam current at large angles off centerline and can be considered the worst case scenario. At last, the relative error of the voltage utilization efficiency is equal to 3%.

3.4.3 Efficiency Analysis Results

3.4.3.1 Operation Points of Interest

The operation points of interest and performance values for each are given in Table 3-2. Xenon data are taken at 700 V, 6 and 8 kW with and without the trim coil. The xenon points are lightly shaded in all of the tables in this section. There are two corresponding krypton points for each xenon point. One krypton point matches the volumetric flow rate of the analogous xenon case, and the other matches the power of the xenon case. Krypton propellant would most likely be chosen over xenon for a particular mission because of its superior specific impulse. For this reason, operation points with large discharge voltages are chosen. The choice of 700 V discharge voltage also has the benefit of minimizing the krypton-xenon efficiency deficit. The krypton efficiency is optimized for high anode flow rates and at high discharge voltages. This finding is expected since previous work[21,26] and the results from the performance analysis suggests that the krypton efficiency gap is largely due to deficient propellant utilization efficiency.

Table 3-2. Operating Conditions for the 700 V, 6 and 8 kW Cases

Point #	Propel.	Power/ Flow Matched	V_k, V	I_D, A	P_D, kW	Anode Flow, mg/s	Current, IC, A	Current, OC, A	Current, TC, A	Thrust, mN	I_{sp}, s	Total Effic., %
3.1	Xe	N/A	-11.1	11.43	8.00	11.38	2.95	2.93	0.00	334	2991	61.2
3.2	Xe	N/A	-11.2	11.43	8.00	11.28	3.00	3.12	-1.54	335	3028	62.2
3.3	Kr	Power	-13.6	11.43	8.00	8.47	2.56	2.92	0.00	273	3287	55.0
3.4	Kr	Power	-14.2	11.42	8.00	8.94	2.24	2.57	-0.51	284	3237	56.4
3.5	Kr	Flow	-14.0	9.75	6.83	7.26	2.31	2.79	0.00	225	3160	51.1
3.6	Kr	Flow	-14.2	9.19	6.43	7.20	2.56	2.78	-1.14	230	3257	57.1
3.7	Xe	N/A	-11.3	8.57	6.00	8.74	2.74	2.73	0.00	248	2893	58.7
3.8	Xe	N/A	-12.2	8.57	6.00	8.94	2.86	3.01	-1.49	258	2940	62.0
3.9	Kr	Power	-13.7	8.57	6.00	6.61	2.06	2.87	0.00	199	3067	49.9
3.10	Kr	Power	-13.9	8.57	6.00	6.98	2.36	3.00	-0.51	215	3140	55.2
3.11	Kr	Flow	-14.7	7.30	5.11	5.59	2.13	2.30	0.00	164	2992	47.1
3.12	Kr	Flow	-15.4	7.05	4.94	5.70	2.24	2.29	-0.57	168	3002	50.1

3.4.3.2 Retarding Potential Analyzer Results

An example of the RPA measurements appears in Figure 3-11. As seen by other experimentalists,[133] the RPA identifies three species of ions in the energy-per-charge distribution curves: the primary beam ions, ions that have undergone elastic collisions, and CEX ions. Interestingly, within the 90% beam divergence half-angle (found to be approximately 50 degrees in the MFFP results), the ions are almost solely primary beam ions and the most probable velocity is roughly constant. Near the 95% beam divergence half-angle (~60 degrees) the current collected from ions that have undergone elastic collisions are on the same order as the beam ions. Beyond the 95% beam divergence half-angle, the CEX ions are the dominant ion species.

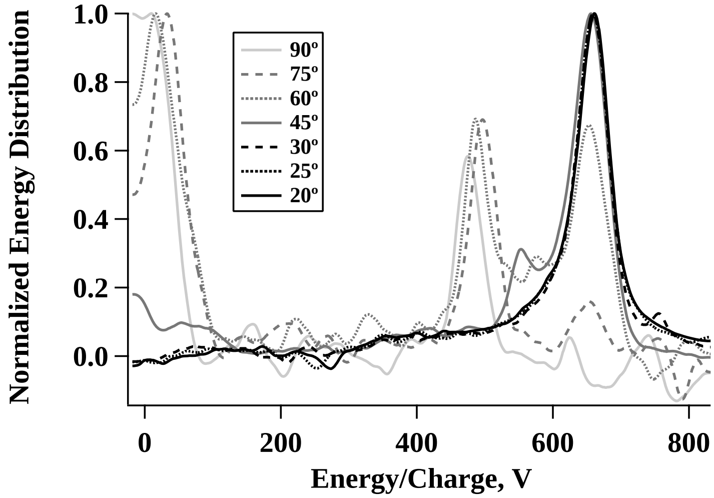

Figure 3-11. Normalized Voltage Distribution Function for Operation Point 12

The most probable voltage is given by the dominant peak in energy-per-charge distribution function. This value is taken to be the average beam voltage (ion kinetic energy in eV). It is shown in Figure 3-11, that the most probable voltage is constant inside of the 30-degree cone of the Hall thruster plume. For this reason, the average ion kinetic energy inside the 30-degree cone is used in the acceleration efficiency and is given in Table 3-3. The most probable beam voltage and the FWHM of the beam voltage distribution function are also given in the following table.

Table 3-3. RPA Results for the 700 V, 6 and 8 kW Operation Points

Point #	Most Probable Voltage, V	Voltage Loss, V	Voltage Spread FWHM, V	Acceleration Efficiency, %
3.1	652	48	92.6	93.1
3.2	662	38	79.4	94.6
3.3	651	49	69.0	93.0
3.4	664	36	59.8	94.9
3.5	653	47	68.6	93.3
3.6	663	37	58.4	94.7
3.7	656	44	92.9	93.7
3.8	670	30	87.2	95.7
3.9	656	44	79.0	93.7
3.10	654	46	68.8	93.4
3.11	657	43	68.3	93.9
3.12	662	38	57.6	94.6

The most probable voltage is approximately the same for xenon and krypton. One might expect the most probable voltage to be marginally lower for krypton because of its higher ionization potential. However, this effect is negligible for these operation points. The trim coil does increase the most probable ion voltage by around 1%. The acceleration efficiency is then calculated by simply measuring the average ion voltage (kinetic energy).

The dispersion efficiency characterizes the effect of the spread in ion velocities in the Hall thruster plume[13] (Equ. 3-32). An example of the spread in ion energy-per-charge at 30 degrees off centerline is displayed in Figure 3-12. Xenon appears to have approximately a 25% larger FWHM in the ion beam voltage distribution function than krypton. This trend is also observed by Marrese et al.[27] This effect counteracts any voltage loss due to krypton's higher ionization potential. These results suggest that more of the ionization occurs upstream of the acceleration zone in the krypton case. This is confirmed by the internal Langmuir probe results in Section 4.3. The trim coil reduces the ion velocity spread by approximately 13%, which leads to improved acceleration. Although the ion velocity spread is important, the dispersion efficiency is difficult to calculate and the average ion voltage is more simply calculated from the most probable voltage.

$$\eta_d = \langle v_a \rangle^2 \Big/ \langle {v_a}^2 \rangle \qquad \textbf{(3-32)}$$

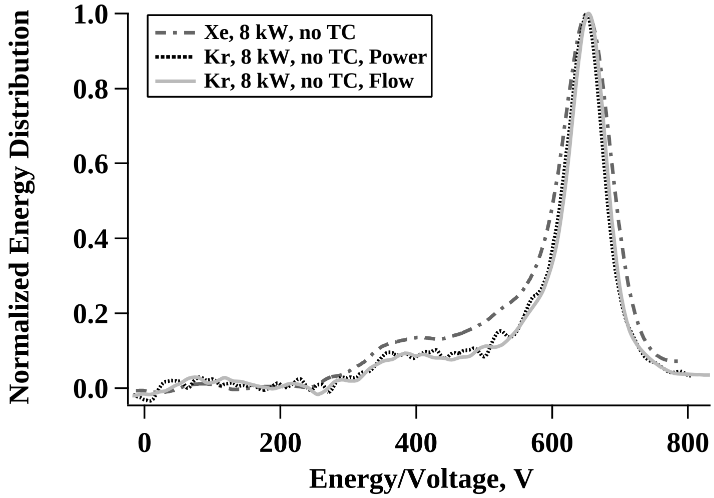

Figure 3-12. Voltage Energy Distribution Comparison for Xenon and Krypton at 8 kW without the Trim Coil

3.4.3.3 E×B Probe Results

The E×B results are shown in Table 3-4. Although Xe^{+4} is clearly visible in the xenon data sweeps, only charge states up to and including Kr^{+3} could be resolved for the krypton measurements. Due to higher ionization energies, it is not surprising that krypton displays fewer multiply-charged species. Accordingly, the charge utilization is approximately 2% higher for krypton.

Table 3-4. E×B Results for the 700 V, 6 and 8 kW Operation Points

Point #	Ω_1	Ω_2	Ω_3	Ω_4	Xe^{+}/Kr^{+} Fraction	Xe^{2+}/Kr^{2+} Fraction	Xe^{3+}/Kr^{3+} Fraction	Xe^{4+} Fraction	Charge Util. Eff., %
3.1	0.6268	0.2219	0.1152	0.0361	0.8832	0.0954	0.0188	0.0026	96.0
3.2	0.5938	0.1793	0.1612	0.0657	0.8855	0.0816	0.0279	0.0051	95.1
3.3	0.6741	0.2346	0.0913	0	0.8951	0.0910	0.0139	N/A	97.0
3.4	0.7522	0.1818	0.0660	0	0.9254	0.0653	0.0093	N/A	97.6
3.5	0.7161	0.2054	0.0785	0	0.9121	0.0765	0.0114	N/A	97.3
3.6	0.7478	0.2048	0.0474	0	0.9197	0.0736	0.0067	N/A	97.7
3.7	0.6286	0.1956	0.1349	0.0408	0.8903	0.0845	0.0222	0.0030	95.79
3.8	0.6565	0.1624	0.1215	0.0597	0.9078	0.0685	0.0195	0.0043	95.7
3.9	0.8219	0.1257	0.0525	0	0.9506	0.0425	0.0069	N/A	98.2
3.10	0.8036	0.1362	0.0602	0	0.9451	0.0468	0.0081	N/A	98.0
3.11	0.7840	0.1697	0.0463	0	0.9346	0.0591	0.0063	N/A	98.0
3.12	0.7344	0.2171	0.0485	0	0.9141	0.0790	0.0069	N/A	97.7

3.4.3.4 Magnetically Filtered Faraday Probe Results

The beam current and beam divergence half-angles from the MFFP results are given in Table 3-5. The MFFP data are used in conjunction with E×B and RPA results to solve for the beam divergence efficiency given in Equ. 3-31. The ion current density for the 8 kW no trim coil data points are given in Figure 3-13. The krypton operation points have greater beam divergence half-angles than the xenon points (~6 degrees). This trend is consistent with other researchers findings.[24] The trim coil does not appear to have a significant effect on beam divergence for these experimental conditions. The calculated beam divergence efficiencies are given in the following section.

Table 3-5. Magnetically Filtered Faraday Probe Results for the 6 and 8 kW Operation Points

Point #	Beam Current, A	95 % Beam Div., degrees	90 % Beam Div., degrees
3.1	9.21	53.0	42.0
3.2	9.33	54.5	44.5
3.3	8.44	60.0	49.0
3.4	8.87	60.5	50.5
3.5	7.57	61.5	50.5
3.6	7.62	60.5	50.0
3.7	7.14	57.5	46.0
3.8	7.20	57.5	47.0
3.9	6.74	63.5	52.5
3.10	6.79	61.5	50.5
3.11	5.56	63.5	52.5
3.12	5.76	62.5	51.5

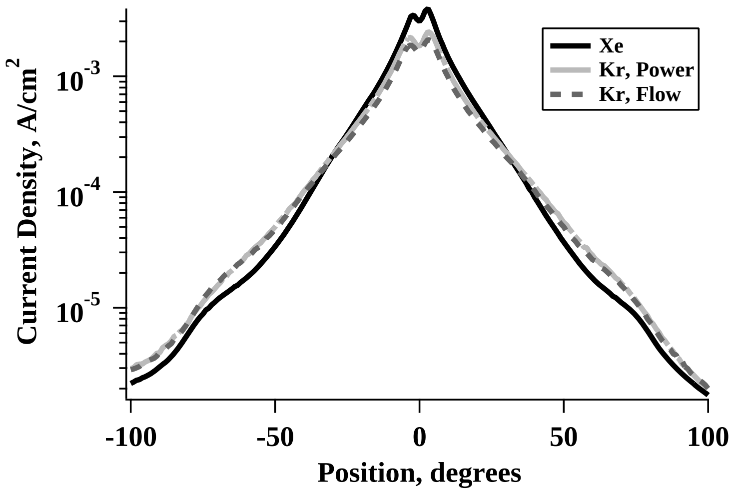

Figure 3-13. Ion Current Density Comparison of the 8 kW Case without the Trim Coil

3.4.3.5 Efficiency Analysis: Current, Propellant, and Beam Divergence Efficiency

A complete table of the efficiencies for the 6 and 8 kW operation points is given in Table 3-6. As expected from the performance measurements, the propellant utilization is a dominant factor in determining the efficiency gap between xenon and krypton. More interestingly, the beam divergence accounts for a loss equally as important as propellant utilization.

Table 3-6. The Complete Efficiency Analysis for Krypton and Xenon Operation Points

Point #	Propell.	Power/ Flow Matched	Trim Coil Used?	Total Anode Eff., %	Charge Util., %	Accel. Eff., %	Diverg. Eff., %	Voltage Util. Eff., %	Current Util. Eff., %	Propellant Util. Eff., %
3.1	Xe	N/A	No	61.2	96.0	93.1	89.2	83.1	84.3	91.1
3.2	Xe	N/A	Yes	62.2	95.1	94.6	88.8	84.0	86.2	90.3
3.3	Kr	Power	No	55.0	97.0	93.0	82.0	76.3	87.5	85.0
3.4	Kr	Power	Yes	56.4	97.6	94.9	80.1	76.0	88.7	85.8
3.5	Kr	Flow	No	51.1	97.3	93.3	80.8	75.4	83.7	83.2
3.6	Kr	Flow	Yes	57.1	97.7	94.7	80.1	75.8	89.3	86.4
3.7	Xe	N/A	No	58.7	95.8	93.7	86.6	81.2	84.7	89.1
3.8	Xe	N/A	Yes	62.0	95.7	95.7	85.8	82.1	87.0	90.7
3.9	Kr	Power	No	49.9	98.2	93.7	78.4	73.4	82.3	84.2
3.10	Kr	Power	Yes	55.2	98.0	93.4	79.9	74.6	88.8	85.1
3.11	Kr	Flow	No	47.1	98.0	93.9	78.3	73.5	80.4	81.3
3.12	Kr	Flow	Yes	50.1	97.6	94.6	78.9	74.6	86.1	80.0

The beam divergence efficiency is between 78% and 89% for the listed operation points. Xenon has a beam divergence efficiency about 8% larger than the krypton points. This divergence is a significant contributor to the krypton efficiency gap and results in a voltage utilization efficiency deficit of about 8%.

The propellant utilization for xenon is approximately 90% and between 80% and 86% for krypton. The trim coil appears to have very little effect on propellant utilization for xenon and krypton. The high krypton efficiency results seen with the NASA-457M[30,60] and the NASA-400M[31] experiments are connected to propellant utilization optimization. These thrusters have a large discharge channel that increases krypton residence time and hence the probability of ionization.

Current utilization is approximately the same for the krypton and xenon points. However, the trim coil appears to improve the electron dynamics inside the Hall thruster, which can be seen in the current utilization. The current utilization (shown in Table 3-6) is between 80% and 89% for these operation points. The current utilization is improved by 1 to 6.5% when the trim coil is in use. This improved current utilization can be explained by the magnetic mirroring effect that theoretically is focusing the electrons toward the center of the discharge channel. This effect may reduce electron wall collisions and near-wall conductivity.[14,134]

Several trends can be observed from these tabulated data when plotted versus anode flow rate. As anode flow rate increases, several performance components are improved, including anode efficiency, propellant utilization, current utilization, and beam divergence. Charge utilization is decreased slightly by increased anode flow rate. The acceleration efficiency is not strongly affected.

The anode efficiency is given in Figure 3-14. As the anode flow is increased 50 sccm, krypton anode efficiency increases by as much as 10%. Xenon performance is largely unaffected by the increased anode flow rate. The finer points of this efficiency improvement are captured in the propellant utilization, charge utilization, and beam divergence efficiency calculations.

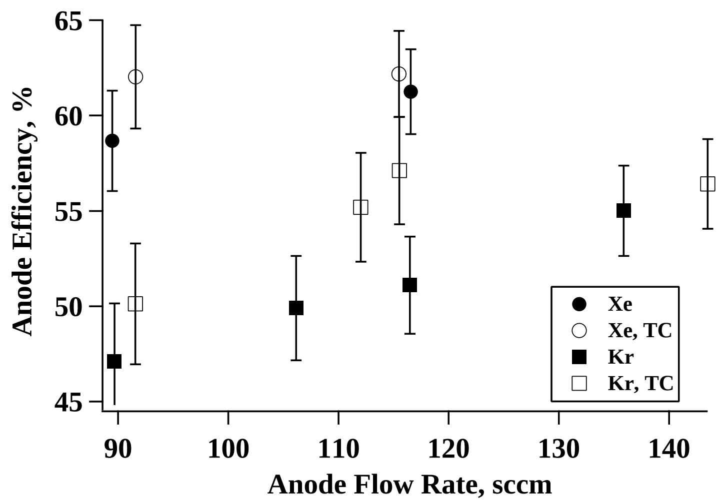

Figure 3-14. Anode Efficiency versus Anode Flow Rate

Propellant utilization efficiency versus anode flow rate is given in Figure 3-15. Propellant utilization is increased by almost 7% as anode flow rate increases and plateaus to around 85%. This finding is not surprising since a larger anode flow rate will increase the neutral number density and concurrently the rate of ionizing collisions. Xenon propellant utilization is approximately constant (~90%) for all flow rates. The xenon propellant utilization is already maximized and nothing is gained by increasing anode flow rate. Following the same lines of thought, this trend explains the slight decrease in charge utilization efficiency with increased anode flow rate. That is, the larger neutral number density results in more ionizing collisions and therefore more multiply-charged species.

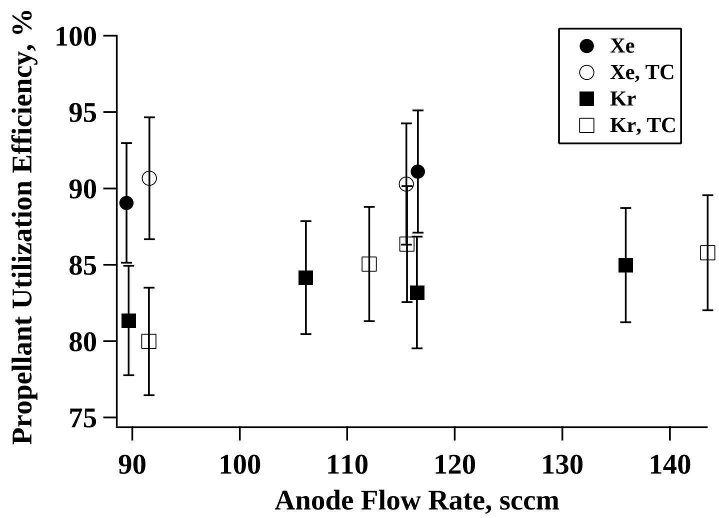

Figure 3-15. Propellant Utilization Efficiency versus Anode Flow Rate

The peak propellant utilization is about 5% higher for xenon and the charge utilization efficiency is approximately 2% better for krypton. This suggests that there may always be a relative efficiency gap of about 4% between xenon and krypton. It is conceivable that a two-stage Hall thruster, which separates the ionization and the acceleration, could improve propellant utilization. One example is the helicon Hall thruster currently being studied.[135-138]

Current utilization efficiency is shown in Figure 3-16. For krypton, the current utilization efficiency increases by almost 9%. For the trim coil case, current utilization appears to plateau at around 90% as flow rate increases. This result may seem counter-intuitive since the increasing neutral and plasma density should result in more electron-particle collisions, which should increase the electron cross-field mobility. However, as flow rate increases, ion production increases, which in turn increases the beam current. This result may also suggest that the dominant mode of axial electron transport is near-wall conductivity. The reason for the improved current utilization is not clear although the limiting current utilization behavior seen in the krypton trim coil case suggests that there are competing factors at work. Xenon again is largely unaffected by the increased flow rate.

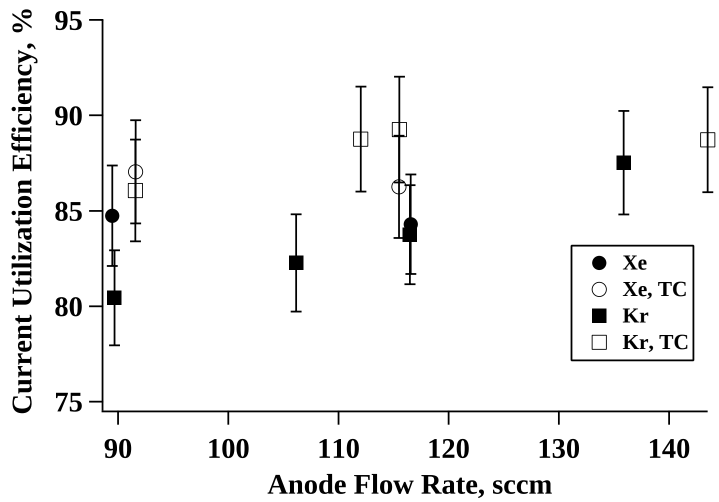

Figure 3-16. Current Utilization Efficiency versus Anode Flow Rate

Beam divergence efficiency (Figure 3-17) is shown to improve slightly for both propellants as anode flow rate is increased. The beam divergence efficiency is improved by about 3 and 4% for xenon and krypton, respectively. A possible explanation is that as the anode flow rate increases, the ionization rate increases and the ionization zone moves upstream. As the ionization zone is moved farther upstream, ions are able to begin their acceleration earlier in the acceleration zone and more likely in the axial direction. Also, the higher flow rate requires a stronger magnetic field to control and direct the plasma. The stronger magnetic field improves the beam divergence. This is discussed in greater detail in Section 6.5.

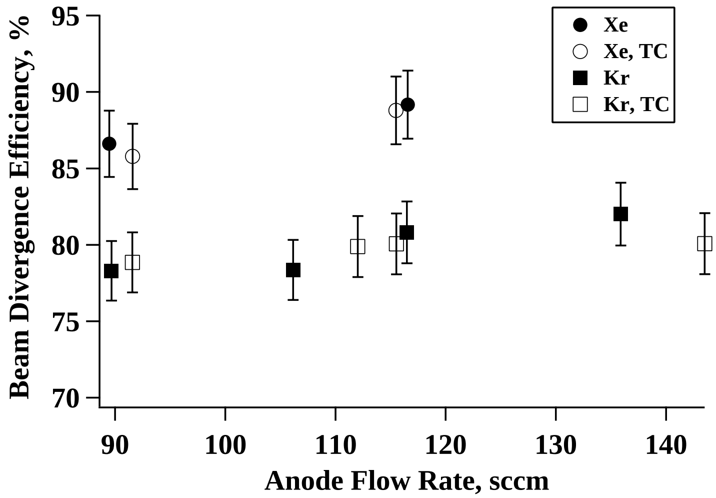

Figure 3-17. Beam Divergence Efficiency versus Anode Flow Rate

Chapter 4.

Internal Experimental Results

In order to better understand and reduce the efficiency gap between xenon and krypton, it will be necessary to conduct a detailed study of krypton propellant in Hall thrusters. In order to fill the remaining gaps in the krypton Hall thruster performance puzzle, it will be necessary to collect more information about the plasma properties internal to the Hall thruster. Internal emissive probe and internal Langmuir probe results are presented in this Chapter.

4.1 Perturbation Analysis

Much can be learned from simply observing the trends in the thruster perturbations. Due to the high-speed data acquisition used in the internal Langmuir probe experiment, the discharge current perturbations can be studied in great detail. The statistics of the discharge current are calculated during each I-V characteristic and the results are mapped in Figure 4-1, which shows results from the 500-V xenon case with the trim coil (Point 4, Table 4-2). The discharge current perturbation is calculated by averaging the discharge current during each I-V characteristic sweep and comparing it to the unperturbed discharge current. Similarly, the discharge current standard deviation is calculated at each spatial location. For every spatial location, a fast Fourier transform of the discharge current is taken to find the dominant current oscillation. This current oscillation, which is referred to as the breathing mode, is also mapped. Superimposed on Figure 4-1 are the magnetic field pathlines. The magnetic fields have been calculated using the 3D magnetostatic solver Magnet 6.0 by Infolytica. Additionally, the boundary of the acceleration zone, which appears in Figure 5-27, Section 5.6.1, is overlaid using black circles. These boundaries were found from the internal emissive probe measurements.

The largest perturbation to the thruster is approximately 22% and occurs near the center of the discharge channel and just upstream of the Hall current and acceleration zone (see Figures 5-20b and 5-35b). However, the standard deviation of the discharge current is the highest in the Hall current region and it is also slightly increased near the channel walls. By monitoring the discharge current and with this very simple analysis, one can find important information about the location of the acceleration zone and the Hall current.

The breathing mode frequency also decreases in the area of high perturbation although the breathing mode intensity remains mostly unchanged. When the probe tip is upstream of the Hall current the typical breathing mode oscillation (~22 kHz) decreases to approximately 12 kHz.

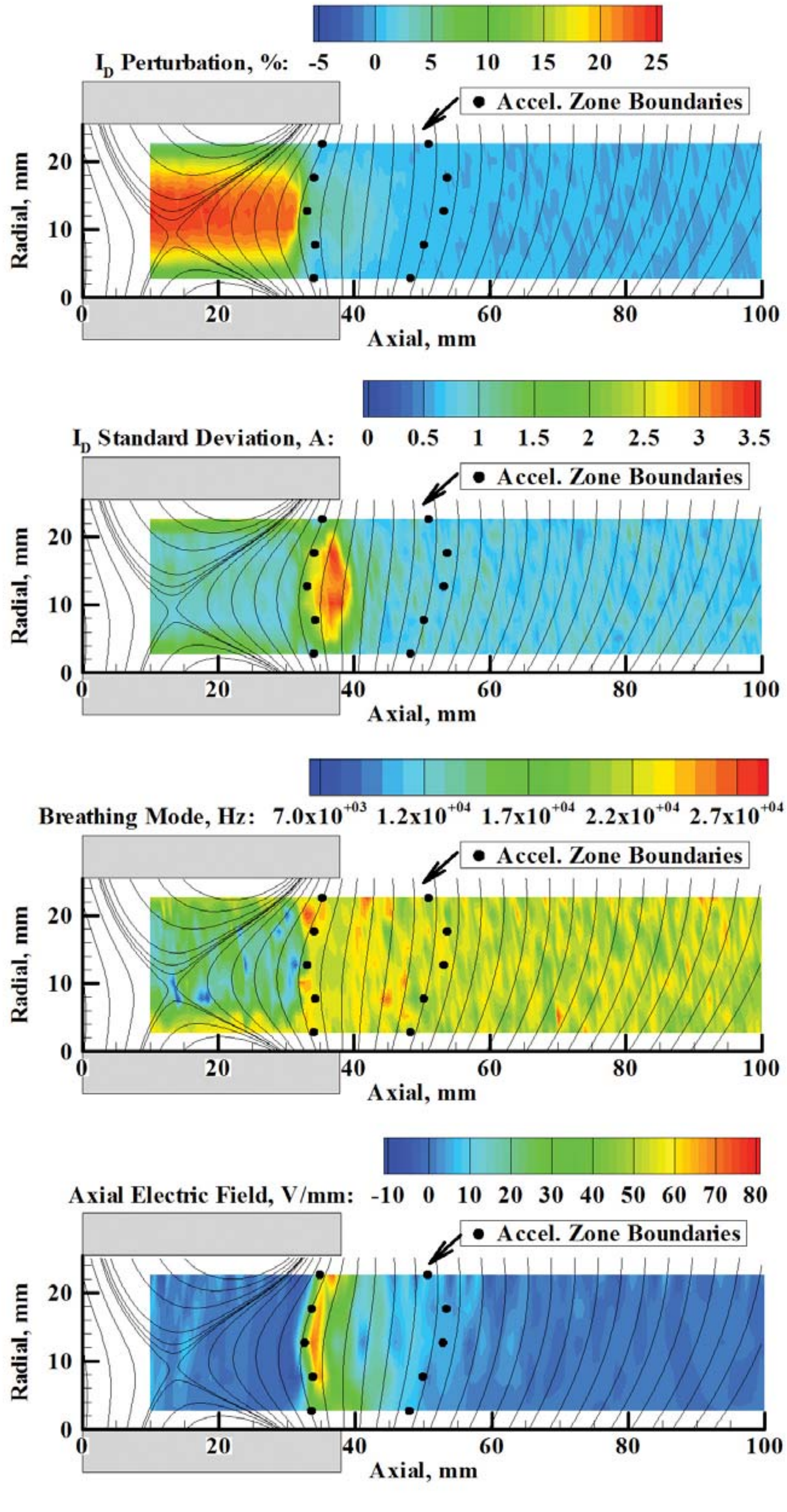

Figure 4-1. Probe Induced Perturbations for the 500 V, Xenon Case

The breathing mode[139,140] is a low-frequency discharge current instability related to predator-prey relation between the electron and neutral propellant atoms. Due to the large magnetic field near the channel exit, the electron conductivity is low, resulting in a large electric field in this region, and a high ionization rate that acts to deplete the neutral density. The front of the neutral flow retreats upstream to a region where the ionization rate is low. As the front of the neutral flow once again moves downstream into the region of high electric field, the neutral density is replenished and the ionization rate increases, thus the process is repeated. This behavior results in an oscillation in the location of the ionization zone and an oscillation in the electric field. Fife et al.[141] offer a simple predator-prey model that gives the relation for the breathing mode frequency shown in Equ. 4-1, where L_i is the length of the ionization zone, and V_n is the neutral velocity.

$$f_B = \sqrt{V_i V_n} / 2\pi L_i \tag{4-1}$$

As the tip of the probe passes through the Hall current, the ionization process is disturbed, resulting in greater oscillation in the electric field and the ionization zone location. However, these increased thruster oscillations do not increase the discharge current and cross-field electron mobility, which would be expected from a Bohm type anomalous diffusion. Since the discharge current is not increased, the ionization and acceleration zone are probably not strongly perturbed by the presence of the probe tip in this region.

As the tip continues to move upstream of the acceleration zone, the probe shaft interacts with the Hall current. The presence of the alumina probe shaft increases the electron collisions, resulting in increased cross-field mobility and hence increased electron flow to the anode, which manifests as an increased discharge current. Moreover, the high secondary electron emission from the electron-alumina interaction further increases the electron flow toward the anode. This enhanced electron conductivity in the Hall current region, decreases the magnitude of and broadens the high-electric field region. At least local to the probe, this effect acts to decrease the ionization rate and increase the length of the ionization zone since the ionization rate is inversely proportional to the ionization zone length.[141] The increase in ionization zone length results in the decreased breathing mode frequency observed in Figure 4-1. Another possible explanation is that due to the probe shaft obstructing the flow of the Hall current, a great deal of energy is deposited into the alumina shaft. This energy loss in the plasma (cooling) decreases the ionization rate and increases the ionization zone length. Again, this decrease in ionization rate and increase in the ionization zone length decreases the breathing mode frequency.

Because the Hall current is so focused in the center of the discharge channel, there is very little perturbation when the probe is swept near the walls. Near the center of the channel, it is difficult to tell how damaging the thruster perturbations are to the Langmuir probe results. Most of the thruster perturbation is caused in the Hall current region, when the probe collector is upstream of the Hall current. Since the probe collector is not located in this region of high disturbance, it is conceivable that the plasma measurements are less affected by these perturbations than feared. Due to the low perturbation in the acceleration region, measurements in the acceleration zone are probably fairly accurate.

4.2 Internal Emissive Probe Results

An internal floating emissive probe is used to map the structure internal to the NASA-173Mv1 discharge channel using xenon and krypton propellant. In addition to the plasma potential, the electron temperature and electric field maps are also extracted from these data.

This section is broken into two sections: a study into the magnetic field topological effects in the Hall thruster and a comparison between xenon and krypton propellant. These sections will outline the experimental results of the emissive probe mapping and identify major trends in these data.

4.2.1 Internal Emissive Operation Points

The internal plasma potential mapping is discussed for seven operation points (See Table 4-1). Data are taken for xenon at discharge voltages of 300, 500, and 600 V at an anode flow rate of 10 mg/s. The 300 and 500 V xenon conditions are taken with and without trim coil operation. Krypton points are show for 2 cases at 500 and 600 V both with the trim coil. The krypton operation points have the same power as the corresponding xenon operation points. High-voltage operation is chosen because a krypton Hall thruster would most likely operate in a way that decreases krypton's performance gap and maximize krypton's superior specific impulse. For each operation point, performance was optimized in the performance analysis section. Additional emissive probe maps for other operating conditions can be seen in Appendix C.

Table 4-1. Operation Points for Internal Plasma Potential Mapping

Point #	Propel.	V_k, V	V_D, V	I_D, A	Anode Flow, mg/s	Cathode Flow, mg/s	IC Current, A	OC Current, A	TC Current, A	Thrust, mN	Anode Effic., %
1	Xe	-10.5	300	9.17	10.00	1.00	1.89	2.21	0.00	179	57.9
2	Xe	-10.9	300	8.95	10.00	1.00	1.88	2.21	-0.51	180	61.2
3	Xe	-11.5	500	9.35	10.00	1.00	2.90	2.67	0.00	243	61.6
4	Xe	-11.7	500	9.27	10.00	1.00	2.90	2.87	-0.87	247	66.1
5	Xe	-12.3	600	9.59	10.00	1.00	3.17	3.42	-1.08	271	64.8
6	Kr	-14.4	500	9.27	7.77	0.78	1.79	2.27	-0.43	203	57.2
7	Kr	-13.3	600	9.59	7.80	0.78	1.98	2.18	-0.46	222	56.1

For each operating condition the corrected plasma potential, electron temperature, axial electric field, and radial electric field are mapped. In each map, the magnetic field topology pathlines are overlaid with the plasma properties. Line plots for plasma potential, electron temperature, and axial electric fields are given along the discharge channel centerline for each operating condition.

4.2.2 Magnetic Field Topology Trends

The magnetic field has been shown to have a strong effect on the overall Hall thruster efficiency.[34,55,56] The focus of this section is to study the effect that magnetic field topology has on the internal plasma potential structure of Hall thrusters. The equipotential structure internal to the UM/AFRL P5 has been well characterized by Haas,[58,59] however with improvements in magnetic field topological design in the past years, the re-examination of the internal Hall thruster phenomena is a worthy pursuit. Also, since both the UM/AFRL P5 and the NASA-173Mv1 have the same discharge channel dimensions, a comparison between these thrusters is important because it shows the effect that a different magnetic field topology has on similar sized thrusters at similar operating conditions.

An important magnetic field topological feature in any state-of-the-art Hall thruster is what is commonly referred to as a plasma lens.[13,34,142-146] A plasma lens uses curved magnetic field lines that create electric fields that focus ions toward the center of the discharge channel. This phenomena can be explained because, to first order, the magnetic field lines chart the equipotential lines inside a Hall thruster.[144,145] The NASA-173Mv1 Hall thruster utilizes a plasma lens topology, which has been shown to improve beam focusing, ion acceleration processes, and internal electron dynamics (See Section 3.4.3).[34,55,56]

Notable investigations of the internal plasma properties by Bishaev and Kim[147] and Haas[58,59] show at best a weak correlation between the magnetic field lines and the equipotential lines. Haas noticed strong defocusing equipotential lines in the UM/AFRL P5 at a discharge voltage and current of 300 V and 10 A, respectively. The internal plasma potential mapping for the UM/AFRL P5 is shown if Figure 4-2. Keidar[148] shows that this behavior is related to a change in the electron mobility due to the magnetic field gradient and due to a radial electron temperature gradient.

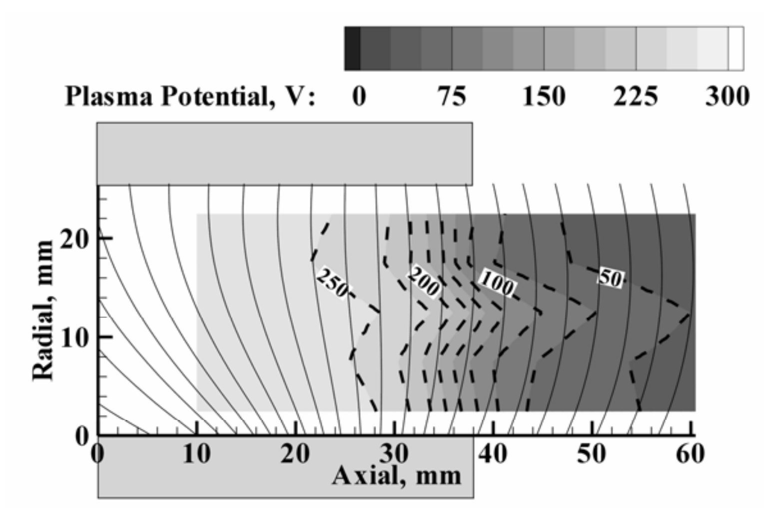

Figure 4-2. Plasma Potential Map for the UM/AFRL P5 Hall Thruster operation at 10 A and 300 V (Ref. 59)

A plasma lens magnetic topology leads to an additional effect of creating a magnetic mirror. A magnetic mirror results in a magnetic field magnitude near the discharge channel walls which is large in comparison to the channel centerline. This creates a force that acts to focus the electrons toward the center of the discharge channel. Keidar studied the effect of a magnetic mirror on potential structures inside the discharge channel.[149] In traditional thinking, the thermalized potential should match the magnetic field lines. Keidar shows that a radial magnetic field gradient may result in deviation between the electric potential and the thermalized potential, which acts to increase the potential in regions of high magnetic field. Furthermore, this study showed that a focusing potential structure could be obtained even in regions with primarily radial magnetic fields.

4.2.2.1 300-V Operation

The internal mappings for the 300-V cases with and without the trim coil are shown in Figures 4-3 to 4-6. These plots correspond to Points 1 and 2 on Table 4-1. The mapped regions for the magnetic field comparison have been reduced to 0-60 mm in order to focus on the internal region. When the trim coil is energized, the thrust increases by 1 mN and the discharge current decreases by 0.22 A. This suggests a decrease in the electron current to the anode. The case without the trim coil shows a slight defocusing of the equipotential lines downstream of the acceleration region and a focusing in the main acceleration region. The slight asymmetry in the acceleration zone can be explained by the asymmetry in the magnetic field lines. The trim coil case shows greater equipotential focusing in the regions upstream and downstream of the acceleration zone. This result can be explained by the stronger plasma lens focusing of the trim coil. The agreement between the equipotential lines and magnetic field lines is not as strong in the acceleration zone due to the high electron temperature. This focusing behavior has also been predicted by Keidar[149] for a thruster using a magnetic mirror.

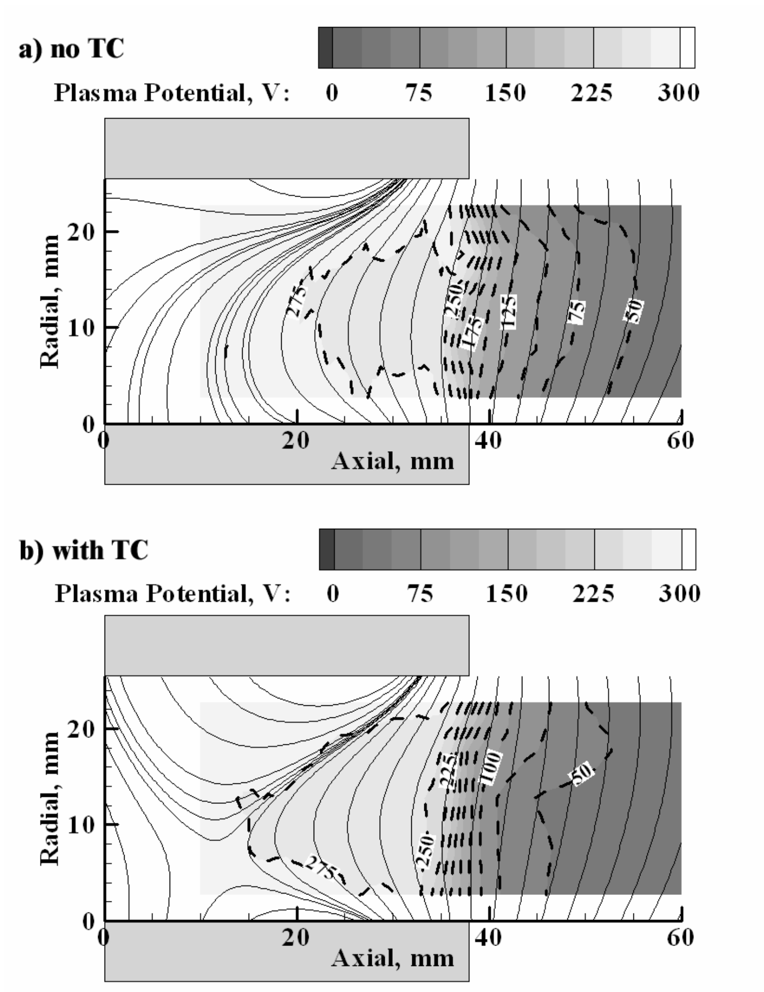

Figure 4-3. Plasma Potential Map for the 300-V Cases (a) without and (b) with the Trim Coil

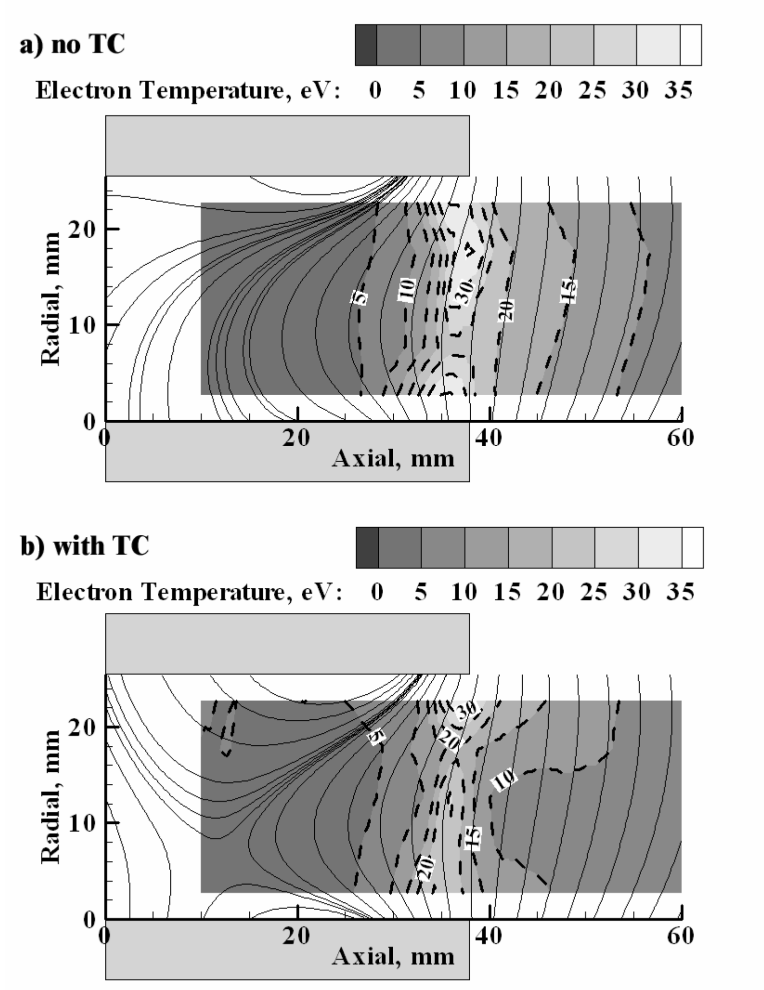

Figure 4-4. Electron Temperature Map for the 300-V Cases (a) without and (b) with the Trim Coil

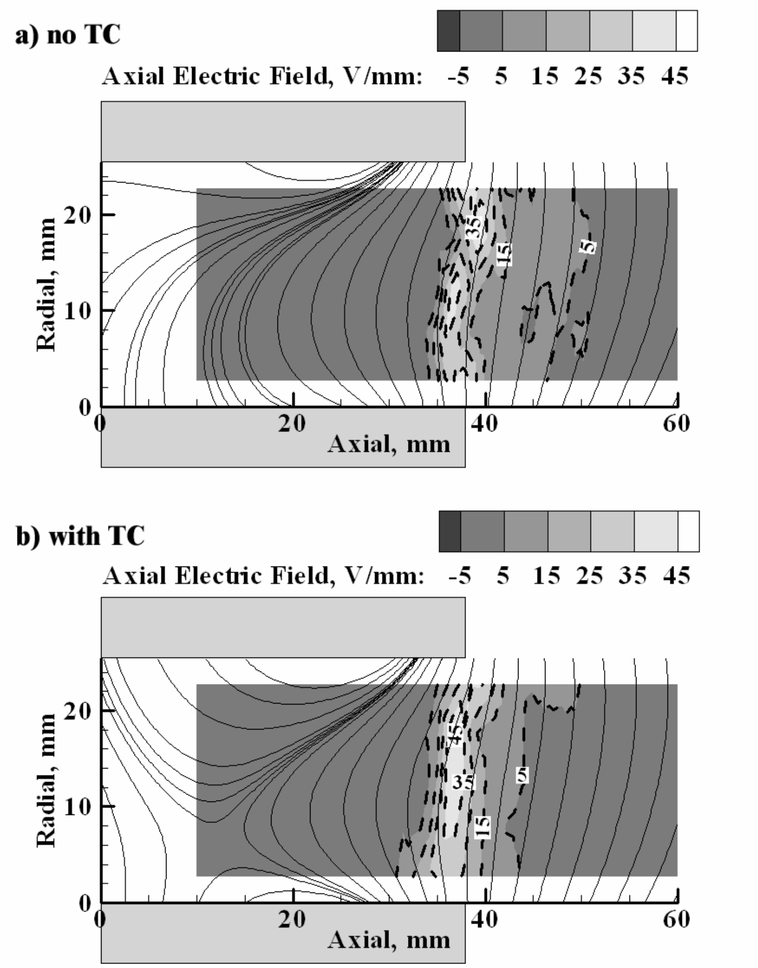

Figure 4-5. Axial Electric Field for the 300-V Cases (a) without and (b) with the Trim Coil

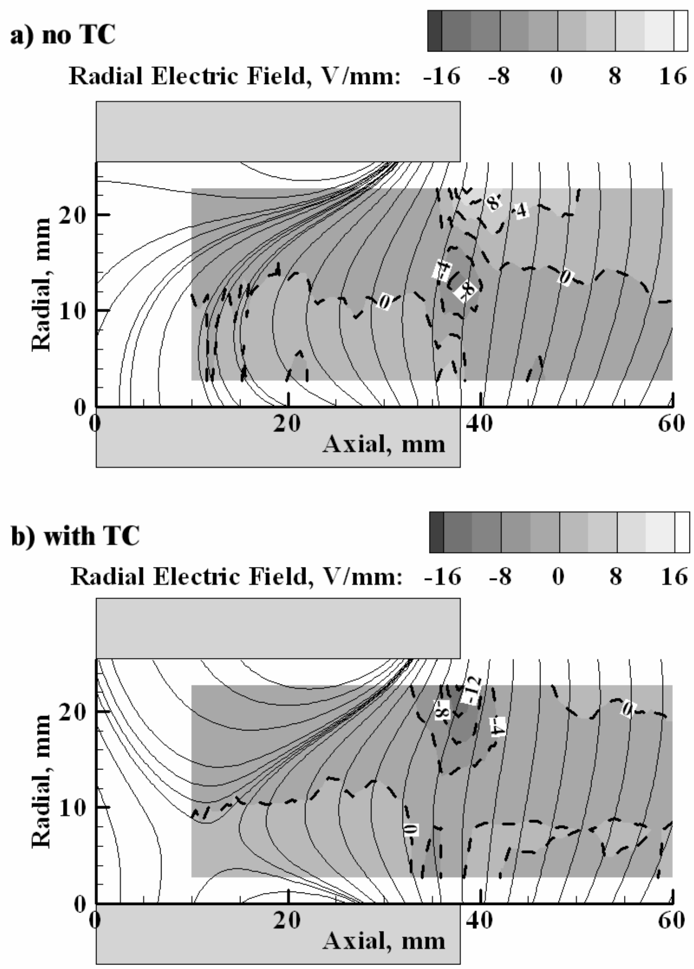

Figure 4-6. Radial Electric Field Map for the 300-V Cases (a) without and (b) with the Trim Coil

The location of maximum electron temperature begins just upstream and continues to the center of the acceleration zone for both the case with and without the trim coil. The maximum electron temperature is approximately 35 eV for the case without the trim coil. For the trim coil case, the electron temperature reaches a maximum of approximately 27 eV for most of the discharge channel, although it does reach an electron temperature of 34 eV on the outer wall. Both 300-V cases have a maximum axial electric field of approximately 45 V/mm.

Centerline plasma properties are shown in Figure 4-7. The acceleration zone is located further upstream for the 300-V trim coil case. For the trim coil case there is a slow decrease in plasma potential between 26 and 35 mm. This slow decrease then transitions into the rapid decline in plasma potential that is similar to the non-trim coil case. The difference in these two potential structures is not well understood, however the trim coil case does not have a larger magnetic field than the non-trim coil case.

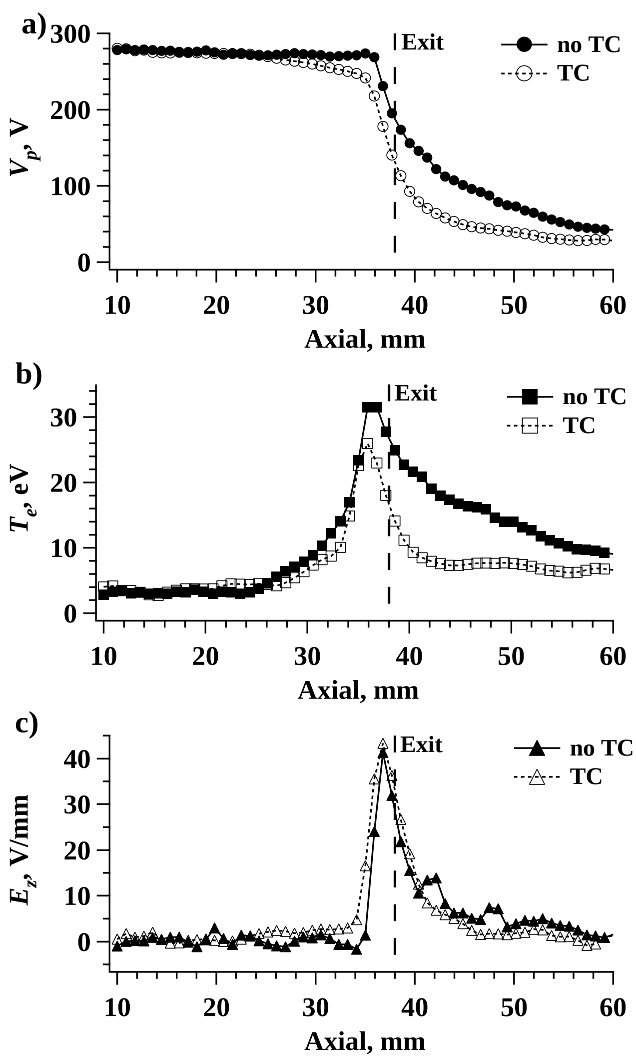

Figure 4-7. Centerline Plasma Properties for the 300-V Non-Trim Coil and Trim Coil Conditions

4.2.2.2 500-V Operation

The internal emissive probe mappings for the 500-V cases with and without the trim coil are given in Figures 4-8 to 4-11. These plots correspond to Points 3 and 4 on Table 4-1. The use of the trim coil results in an increase in thrust of 5 mN or 1.6% and a decrease in discharge current of 0.08 A. The increase in thrust is likely due to the improvement in beam focusing. These cases show a remarkable correlation between the focusing magnetic field lines and the plasma potential. The non-trim coil case has an equipotential asymmetry that can be explained by an asymmetry in the magnetic field lines. The trim coil case has a strong focusing in the equipotential lines that is due to the focusing effect of the magnetic lens. Even the defocusing magnetic field lines downstream of the discharge channel correspond to defocusing equipotential lines. The ion focusing is clearly shown by the radial electric fields in Figure 4-11. The radial electric fields focus the ions into the center of the discharge channel and are approximately 12-18 V/mm while the axial electric field reaches a maximum of about 70 V/mm in the trim coil case. Similarly, the axial electric field reaches a maximum of approximately 80 V/mm in the non-trim coil case.

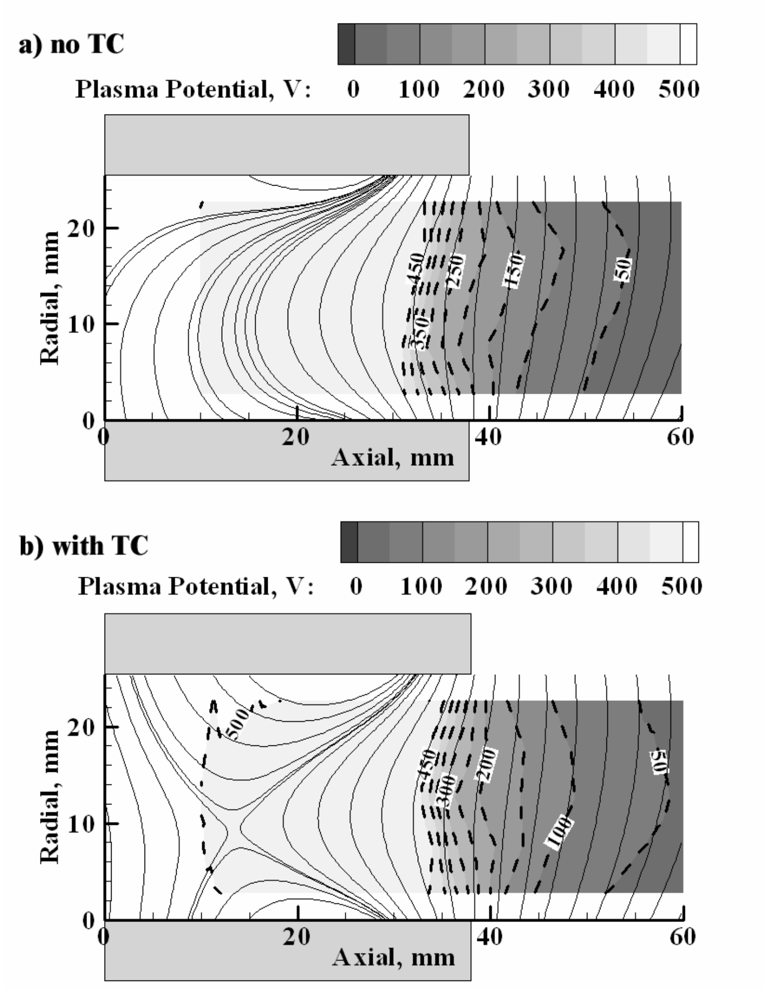

Figure 4-8. Plasma Potential Map for the 500-V Cases (a) without and (b) with the Trim Coil

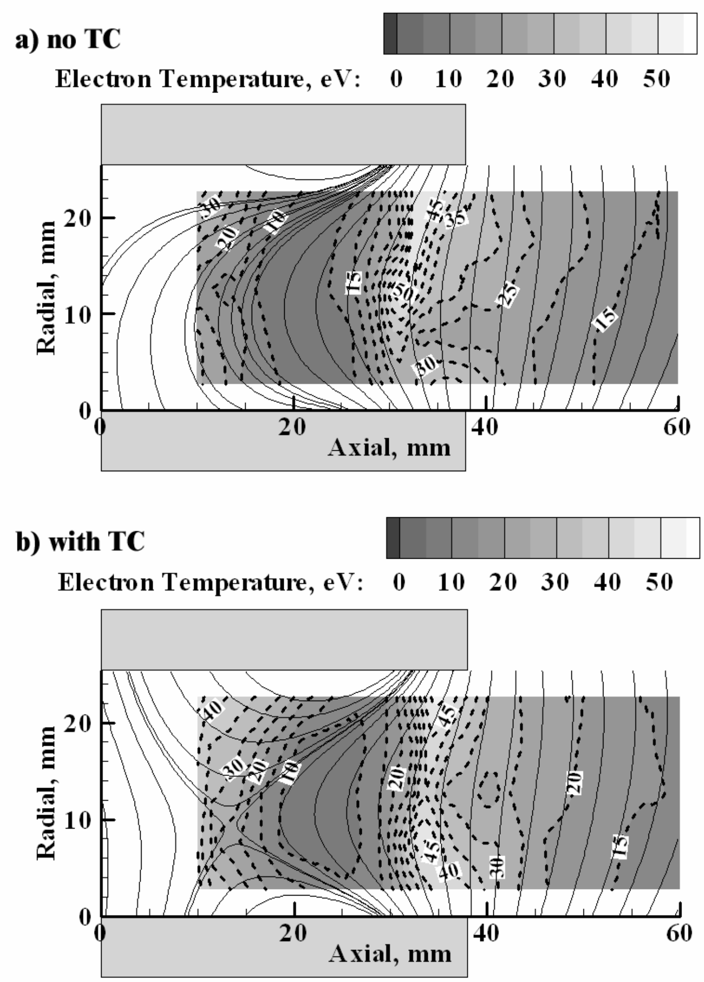

Figure 4-9. Electron Temperature Map for the 500-V Cases (a) without and (b) with the Trim Coil

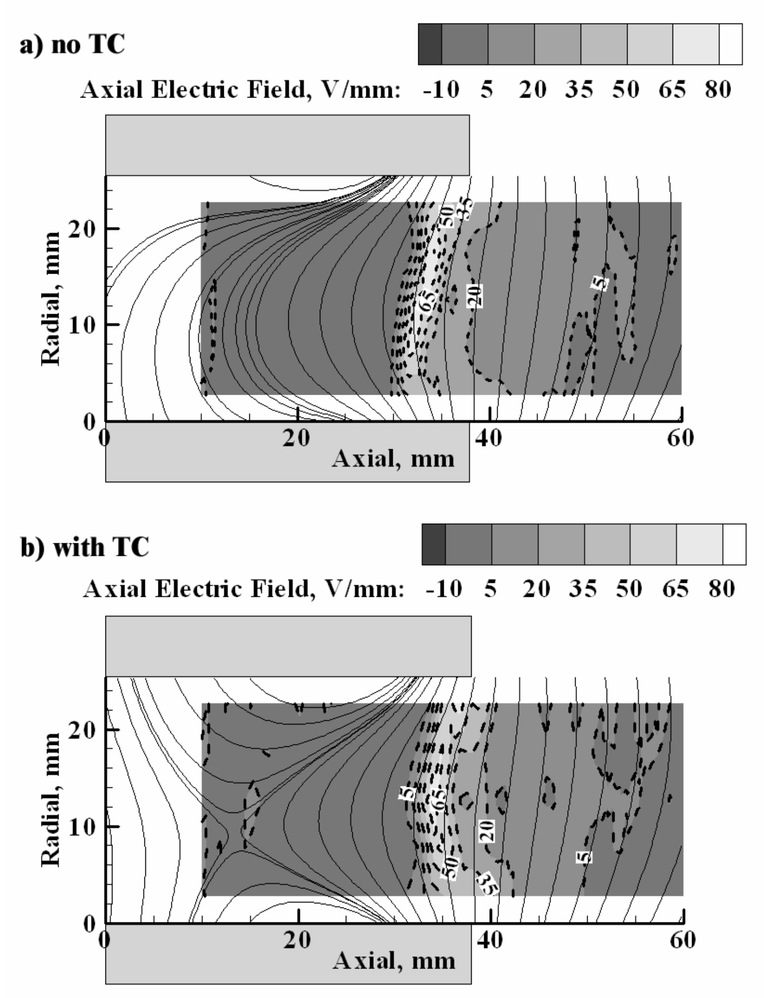

Figure 4-10. Axial Electric Field Map for the 500-V Cases (a) without and (b) with the Trim Coil

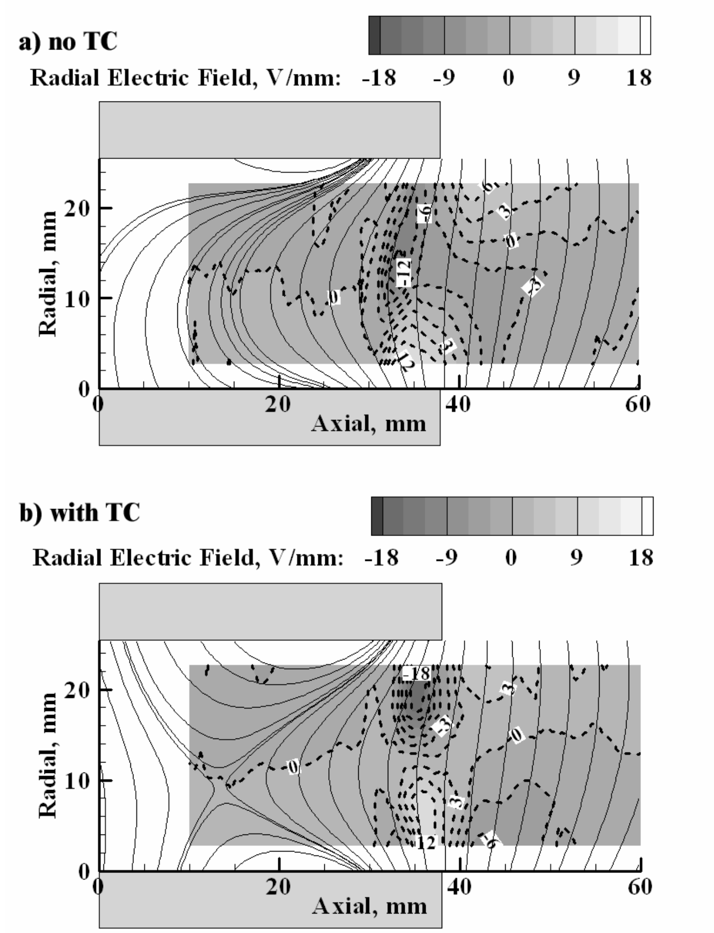

Figure 4-11. Radial Electric Field Map for the 500-V Cases (a) without and (b) with the Trim Coil

A possible explanation of the improved ion focusing at higher voltage is due to electron temperature saturation. Electron temperature saturation is a behavior that has been both predicted computationally[123,124] and observed experimentally.[81,82] Since thermalized potential follows the magnetic field lines, the equipotential lines should differ from the magnetic field line by roughly the electron temperature. As discharge voltage increases past 400 V, the electron temperature is shown to saturate to 50-60 eV.[81,82] This saturation results in a greater ratio of plasma potential to electron temperature and the equipotential lines follow the magnetic field lines more closely. This larger plasma potential to electron temperature ratio is shown by Langmuir probe measurements for these operation conditions presented in the next section. The Langmuir probe results show a maximum electron temperature for the 300 and 500-V trim coil cases of 40 and 50 eV, respectively. The electron temperature measurements from the Langmuir probe results are expected to be more accurate than the emissive probe measurements. Consistent with this observed trend, in the Bishaev and Kim[147] experiment where they observed weak correlation between equipotential lines and magnetic field lines, the thruster was operated at a discharge voltage of only 200 V. Unfortunately, this explanation is purely conjecture and additional measurements over a large range of discharge voltages are necessary to confirm this theory.

Similar to the 300-V cases, both 500-V cases show a region of high electron temperature immediately upstream of the acceleration zone that continues into the acceleration zone. The electron temperature of both trim coil and non-trim coil cases reaches a maximum of 45-50 eV. As a result of increased Joule electron heating,[81,82,123,124] the electron temperature is higher for the 500-V cases than the 300-V cases (27-35 eV). The higher voltage operation points also display an additional region of increased electron temperature near the anode that is comparable to the "hot" region near the acceleration zone. This near-anode hot zone is unusual although a similar trend is observed by Meezan et al.[80] Internal Langmuir probe measurements show that this near-anode hot zone probably does not exist and may be an artifact of the floating emissive probe technique for calculating the electron temperature. The cold probe measurements used to calculate the electron temperature (Equ. 2-14) measured an artificial drop in floating potential not observed in the Langmuir probe measurements. The source of this near-anode hot zone is not entirely clear, although the magnetic field can cause a significant change on the probe collection area and the electron dynamics near the probe. The near-anode hot zone is extremely well correlated with decreased magnetic field strength and magnetic field lines that are predominantly axial. When the magnetic field strength approaches zero gauss, the electron current appears to be enhanced resulting in a decreased floating potential measurement. However, this error in electron temperature is only a concern near the anode and the electron temperatures elsewhere in the discharge channel are considered more reliable.

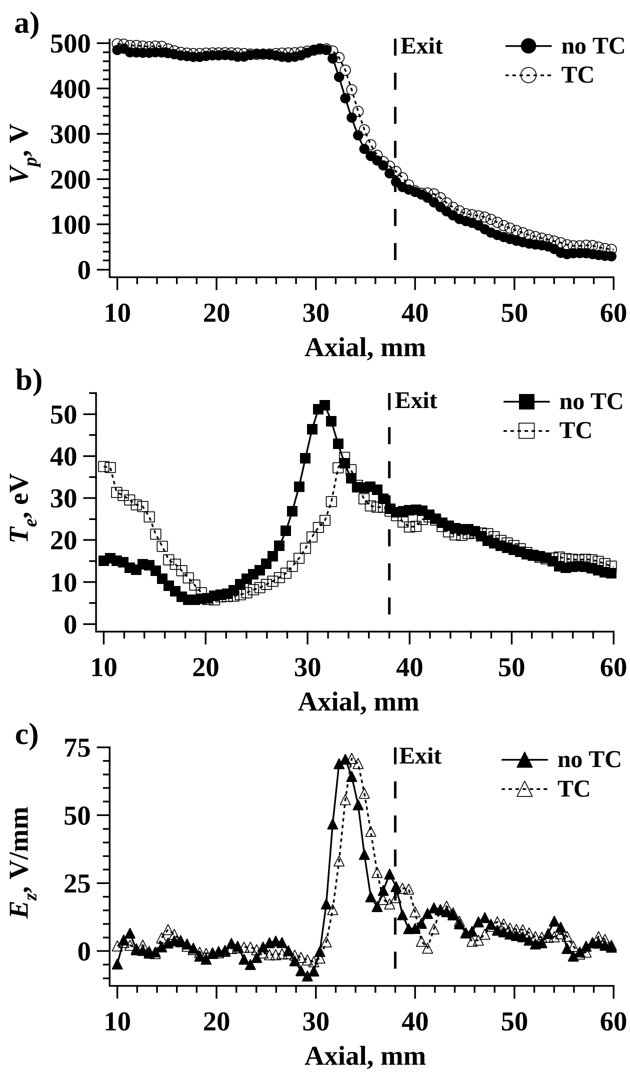

Figure 4-12. Centerline Plasma Properties for the 500-V Non-Trim Coil and Trim Coil Conditions

Centerline plasma properties are shown in Figure 4-12. These plots show that the location of acceleration zone for the trim coil and non-trim coil cases are very similar and that the trim coil has little effect on the acceleration zone.

4.2.3 Krypton-Xenon Comparison

This section will compare the internal plasma potential structure of xenon and krypton. An interesting feature of the detailed efficiency analysis presented in the previous chapter is that beam divergence is a significant contributor to the krypton-xenon efficiency gap. Internal emissive probe measurements are a logical step in understanding this phenomenon.

As mentioned earlier, each operation point has its own unique and optimized magnetic field topology. However, both operation points have the same location of peak magnetic field. It should be noted that the magnetic field topology strongly affects internal features such as the acceleration zone location and dimensions, and the location of the maximum electron temperature. For this reason, any differences in internal features between xenon and krypton operation will always be strongly tied to the different magnetic field topologies. With this said, the focus of this experiment is to study optimized xenon/krypton performance not to match the magnetic field topology.

4.2.3.1 500-V Comparison

This operation points discussed in this section correspond to Points 4 and 6 is Table 4-1. The internal plasma potential map for xenon and krypton at 500 V is shown in Figure 4-13. These cases show a strong correlation between the magnetic field lines and the plasma potential. The xenon case displays a strong focusing in the equipotential lines that is due to the plasma lens established by the magnetic circuit. This behavior is also demonstrated computationally by Keidar.[149] However, the krypton equipotential lines have less of a concave shape and are actually defocusing in the acceleration zone. This result is consistent with the finding that krypton has a larger beam divergence than xenon. The differences in the shape of xenon and krypton equipotential lines are strongly related to their different magnetic field topologies. Krypton operation requires lower magnet currents to achieve optimum efficiency and utilizes a weaker plasma lens. Efficiency optimization for the krypton data points are strongly connected to maximizing propellant utilization. With propellant utilization being such an important focus of optimization, other efficiency components (such as beam divergence) suffer.

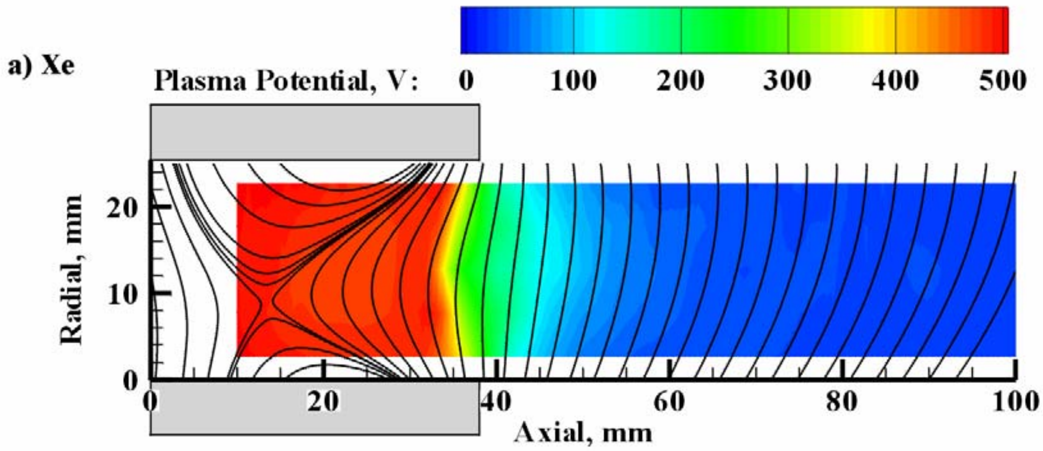

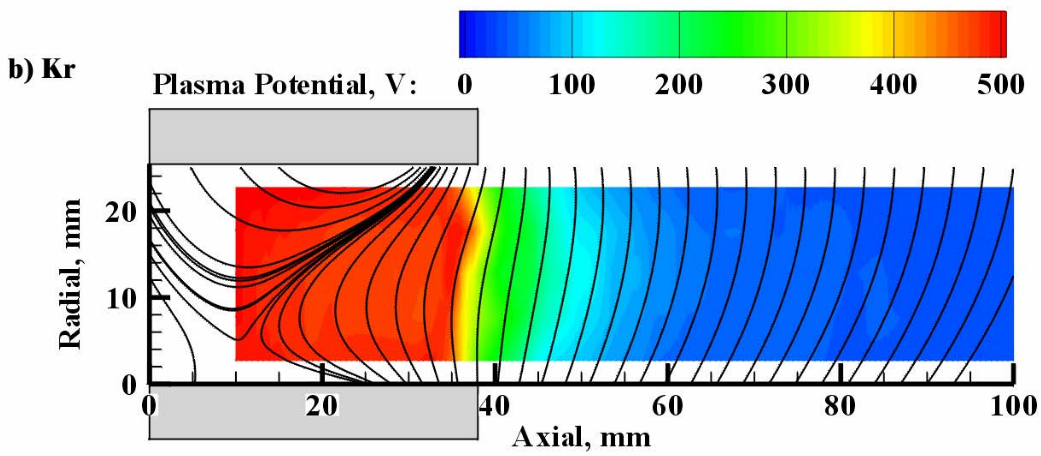

Figure 4-13. Plasma Potential Map for (a) Xenon and (b) Krypton at a Discharge Voltage of 500 V

Electron temperature mapping for the 500-V cases are shown in Figure 4-14. There is a region of high electron temperature that begins immediately upstream of the acceleration zone and continues into the acceleration zone. This region is similar in dimension and magnitude for both propellants, although in the krypton case the acceleration zone starts slightly farther downstream. The maximum electron temperature of both xenon and krypton cases reaches approximately 50 eV, although there is one "hot" spot in the krypton case that reaches 60 eV. There is high electron temperature near the anode for these operating conditions. As mentioned in the previous section, this anode heating region is not seen in the internal Langmuir probe measurements and is suspect.

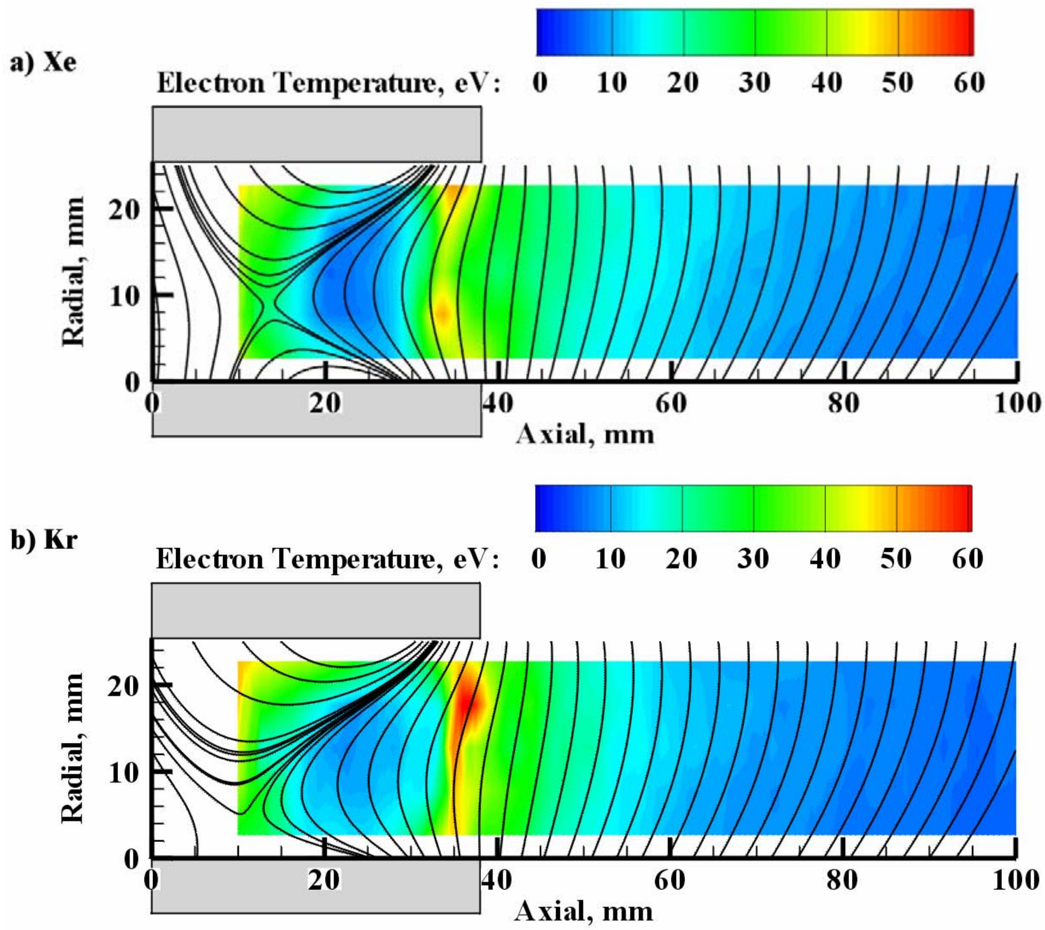

Figure 4-14. Electron Temperature Map for (a) Xenon and (b) Krypton at a Discharge Voltage of 500 V

Axial electric fields for the 500-V xenon and krypton cases are shown in Figure 4-15. For xenon, the maximum electric field reaches approximately 70 V/mm. For krypton, the maximum axial electric field is also approximately 70 V/mm, but extends over a thin region in the acceleration zone. Figure 4-15 also shows that both cases display a potential well downstream of the main acceleration zone. This can be seen as a dark spot in the middle of the mapped area between the axial locations of 40-45 mm. This potential well has also been observed by other researchers.[59,92,150]

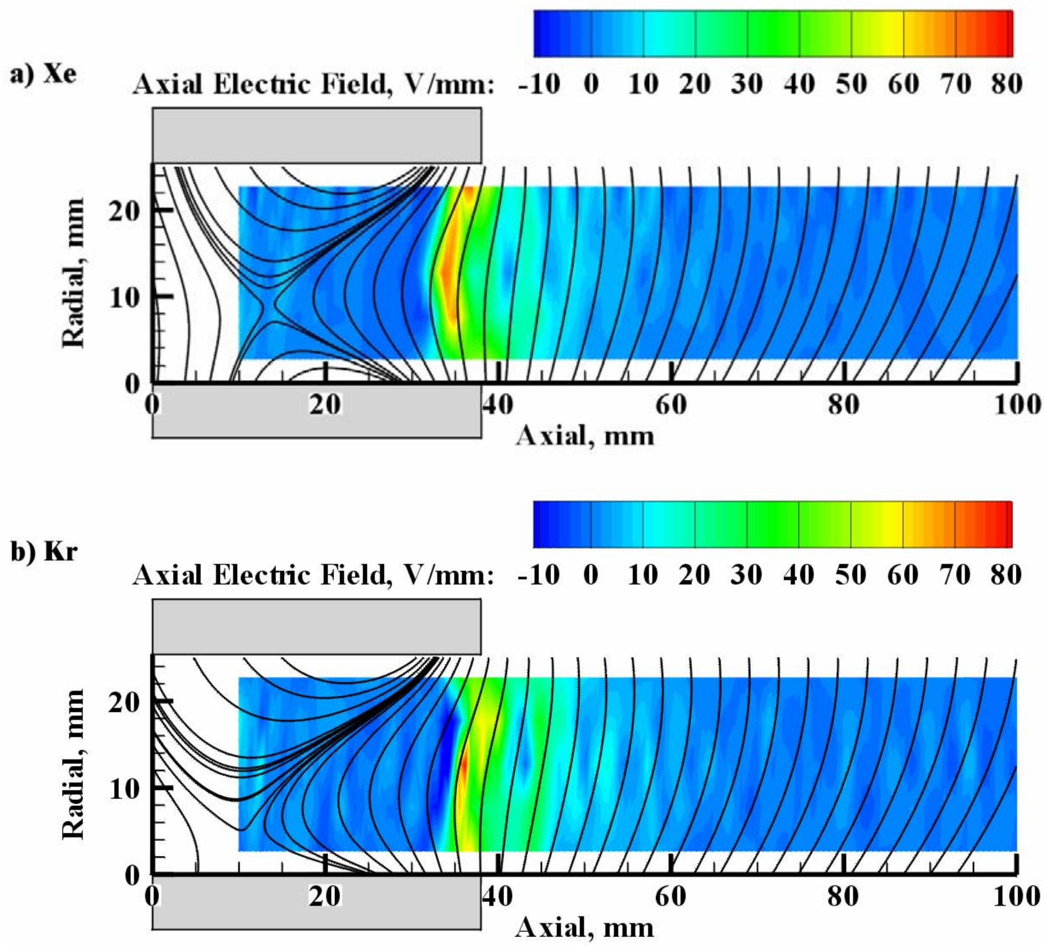

Figure 4-15. Axial Electric Field Map for (a) Xenon and (b) Krypton at a Discharge Voltage of 500 V

Radial electric fields can be seen in Figure 4-16. Xenon's beam focusing and krypton's defocusing are well illustrated by the compression and expansion points near the channel walls and exit. The maximum radial electric fields are approximately 20% of the maximum axial electric field for both xenon and krypton. The xenon focusing occurs just inside the discharge channel, but the krypton defocusing begins at the exit and continues downstream. The findings suggest that there may not be an appreciable difference in wall losses and erosion for krypton and xenon.

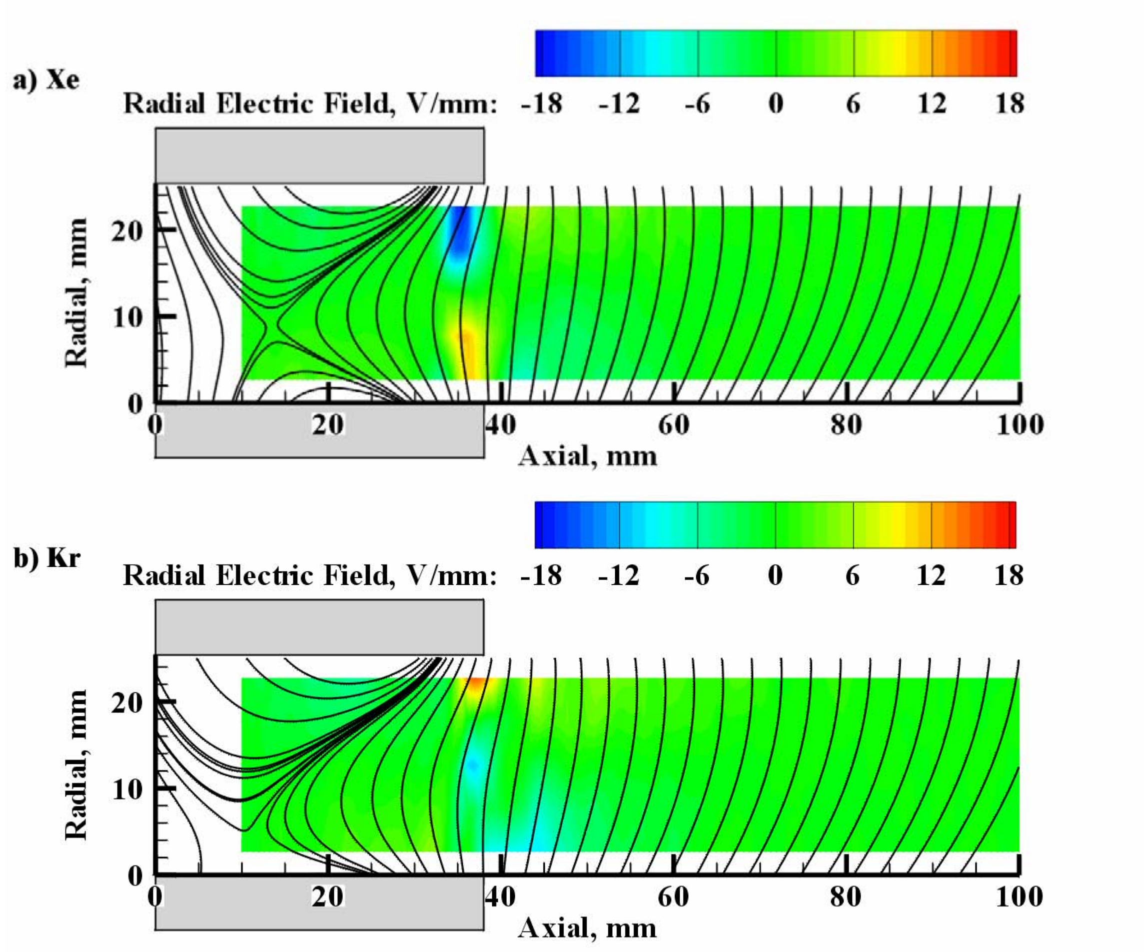

Figure 4-16. Radial Electric Field Map for (a) Xenon and (b) Krypton at a Discharge Voltage of 500 V

The centerline properties for the 500-V xenon and krypton operation points are shown in Figure 4-17. One can easily see how the acceleration zone begins a few millimeters further downstream in the krypton case.

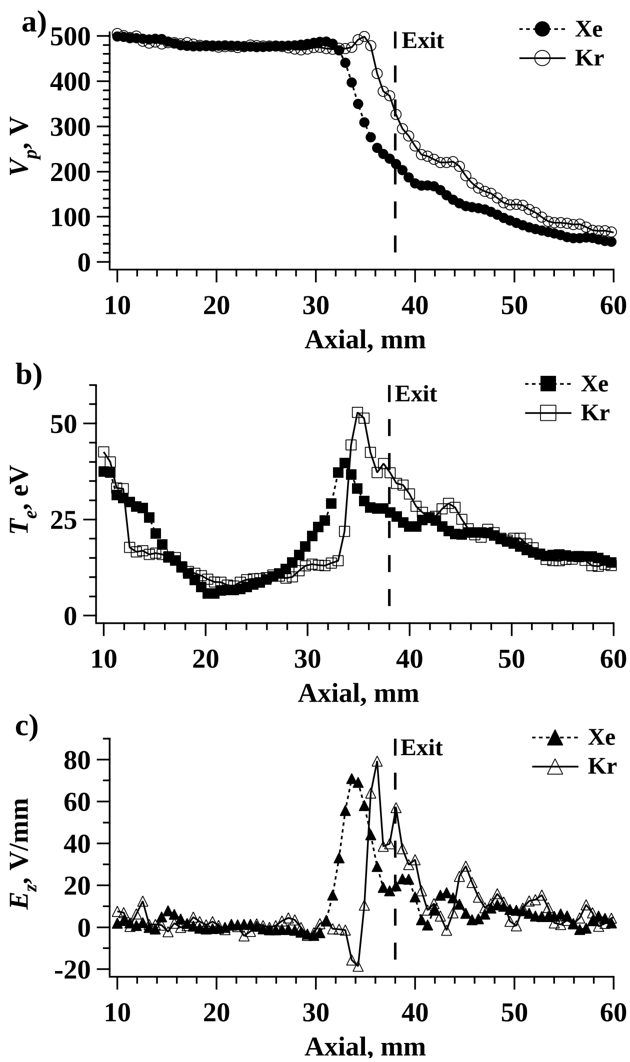

Figure 4-17. Centerline Emissive Probe Results for Xenon and Krypton at a Discharge Voltage of 500 V

4.2.3.2 600-V Comparison

This operation points discussed in this section correspond to Points 5 and 7 is Table 4-1. As in the 500-V cases, the 600-V measurements show an excellent correspondence between the magnetic field pathlines and the equipotential lines (Figure 4-18). Again, this correlation between equipotential lines and magnetic field pathlines results in strong focusing for the xenon case and defocusing in the krypton case.

Interestingly, the 600-V case also shows a weak "plasma jet" behavior that has also been observed by Haas (Figure 4-2).[59] This behavior is visible in the area downstream of the main acceleration zone where the magnetic field pathlines are slightly convex.

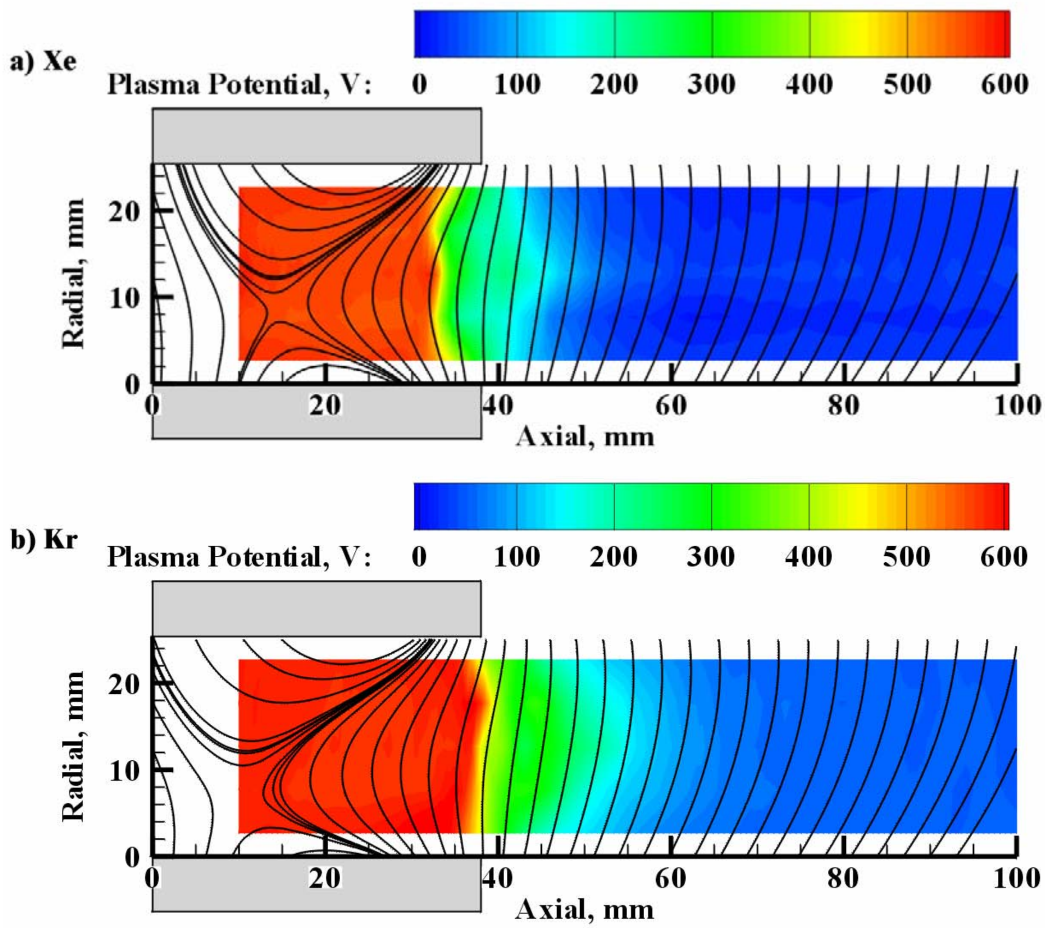

Figure 4-18. Plasma Potential Map for (a) Xenon and (b) Krypton at a Discharge Voltage of 600 V

Figure 4-19 shows the electron temperature map for the 600-V cases. The same high electron temperature regimes exist in the 600-V case as in the 500-V case, although the "anode heating" zone is not captured in the 600-V krypton data. In the xenon case, the maximum electron temperature is about 47 eV. In the krypton case, the maximum electron temperature is between 50 and 60 eV in most of the discharge channel, although there is an unusual "hot spot" on the inner discharge channel wall that reaches 85 eV.

The electron temperature on the inner wall is extremely high, although given the relatively large error bars for electron temperature, this measurement is not unreasonable for high-voltage operation. With this said, the maximum electron temperature measured in the rest of the discharge channel is probably more representative of the true electron temperature. The high electron temperature regions are similar in dimension for the xenon and krypton cases although the krypton case is located slightly farther downstream. The fact that the maximum electron temperatures are similar in the 600-V and the 500-V cases is expected since the electron temperature is anticipated to saturate near 50-60 eV due to discharge channel wall interactions.[81,82,123,124]

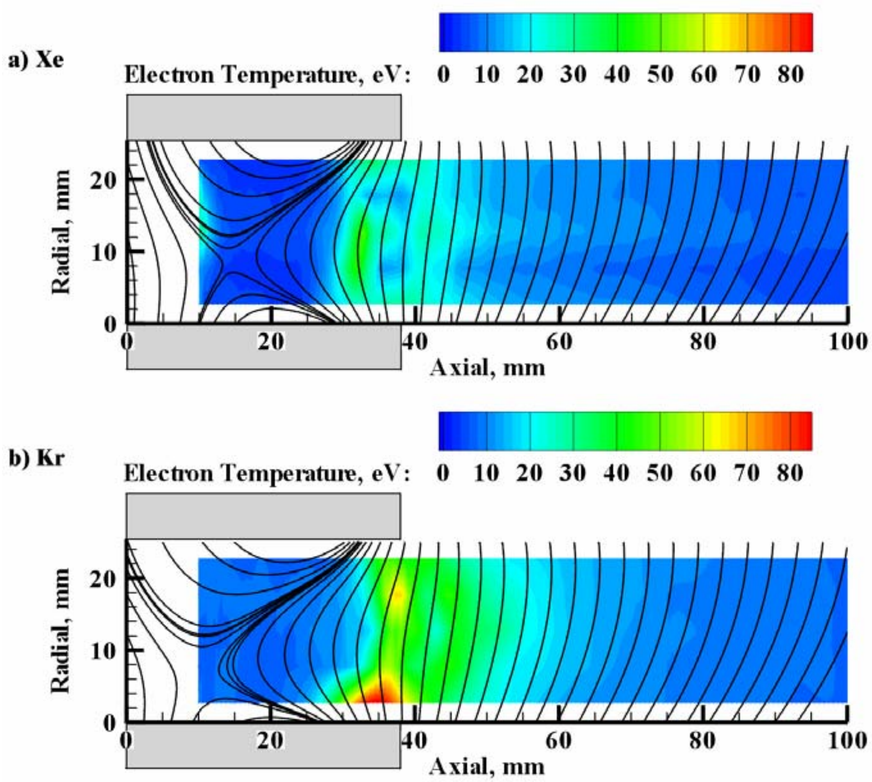

Figure 4-19. Electron Temperature Map for (a) Xenon and (b) Krypton at a Discharge Voltage of 600 V

The axial electric fields are shown in Figures 4-20. Figure 4-20 illustrates that krypton's acceleration zone is longer and located farther downstream than the xenon case. The maximum axial electric fields are 150 V/mm and 115 V/mm in the xenon and krypton cases, respectively. Also visible in Figure 4-20 is the potential well located between the axial locations of 40 and 45 mm.

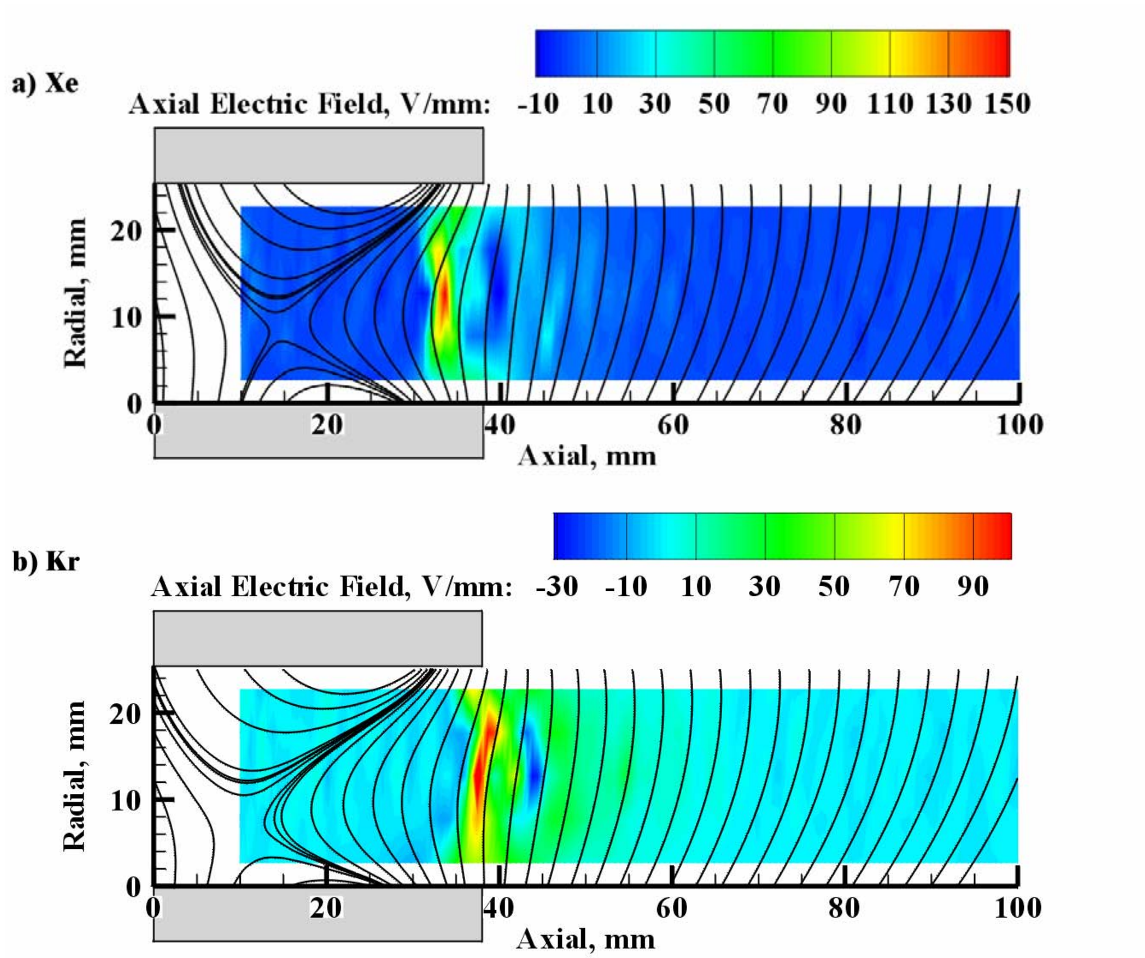

Figure 4-20. Axial Electric Field Map for (a) Xenon and (b) Krypton at a Discharge Voltage of 600 V

From these results a few statements can be made about the acceleration zone in the xenon and krypton cases. Although both xenon and krypton have a significant portion of their acceleration outside the discharge channel, the acceleration zone with krypton extends much farther than the xenon acceleration zone. Since the krypton acceleration zone starts farther downstream, is longer, and is almost entirely located outside of the discharge channel, it is not surprising that krypton has a larger beam divergence than xenon. The krypton ions that are accelerated away from the discharge channel centerline will have less of a chance to collide with the channel wall and therefore will accelerate freely to high angles off thruster centerline.

The dispersion efficiency characterizes the effect of the spread in ion velocities in the Hall thruster plume and is given by Equ. 3-32. With a longer acceleration length, one might expect krypton to have greater ion velocity dispersion than xenon. However, retarding potential analyzer measurements (Section 3.4.3.2) indicate that krypton actually has a smaller spread in ion velocity than xenon cases. Since ion velocity dispersion is dictated by the ionization zone, this finding indicates that the majority of the krypton ionization must be occurring upstream of the acceleration zone, a result that has been shown by Langmuir probe measurements (Section 4.3.4). This dispersion trend also makes sense because the krypton acceleration zone is located slightly farther downstream than xenon's acceleration zone.

The radial electric fields shown in Figure 4-21 demonstrate the strong focusing and defocusing seen in the xenon and krypton cases, respectively. The maximum radial electric field is 36 V/mm for the xenon case and 28 V/mm in the krypton case, which are both greater than 20% of the maximum axial electric field. The maximum radial electric field is just upstream of the discharge channel exit in the xenon case and begins at the exit for the krypton case. Accordingly, severe wall erosion and wall losses are not expected due to this krypton defocusing.

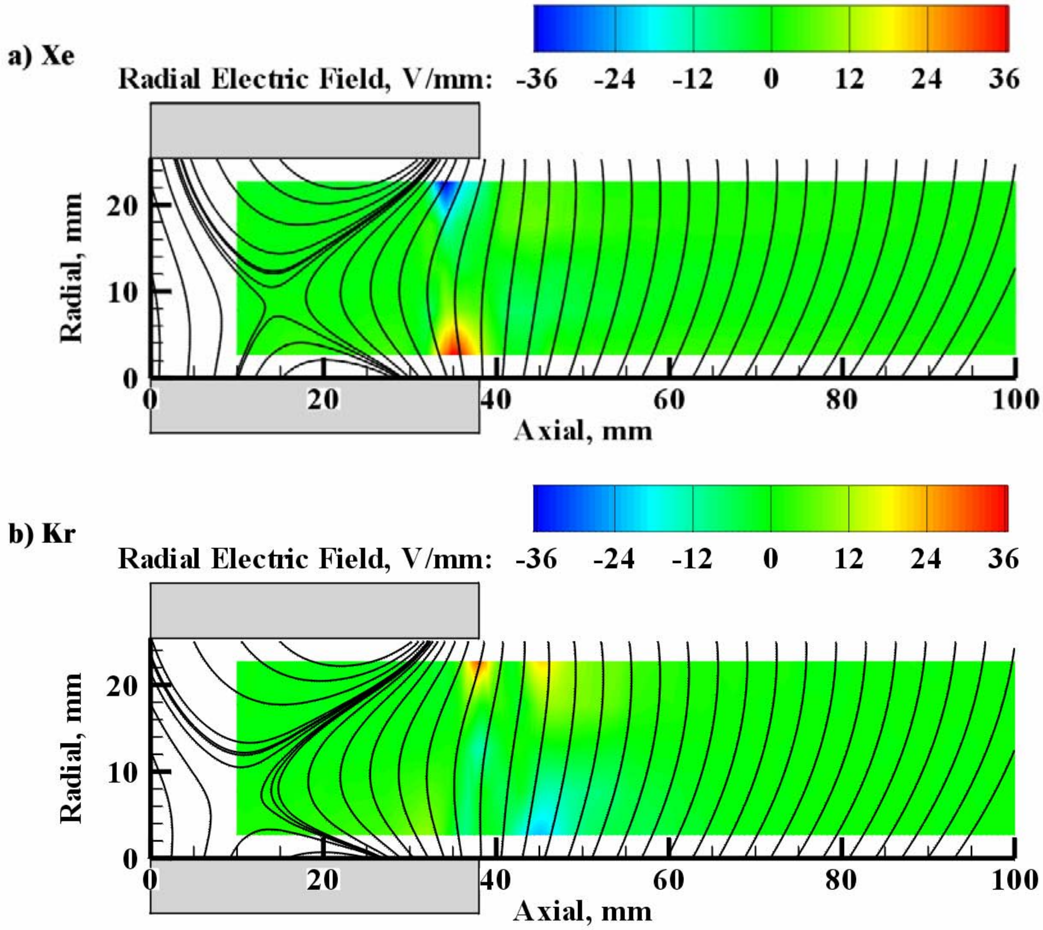

Figure 4-21. Radial Electric Field Map for (a) Xenon and (b) Krypton at a Discharge Voltage of 600 V

The centerline properties for the 600-V xenon and krypton operation points are shown in Figure 4-22. Again, it can be seen that krypton acceleration zone begins further downstream and the region of high electron temperature is much wider in the krypton case. The potential well is also well illustrated by part a) in Figure 4-22.

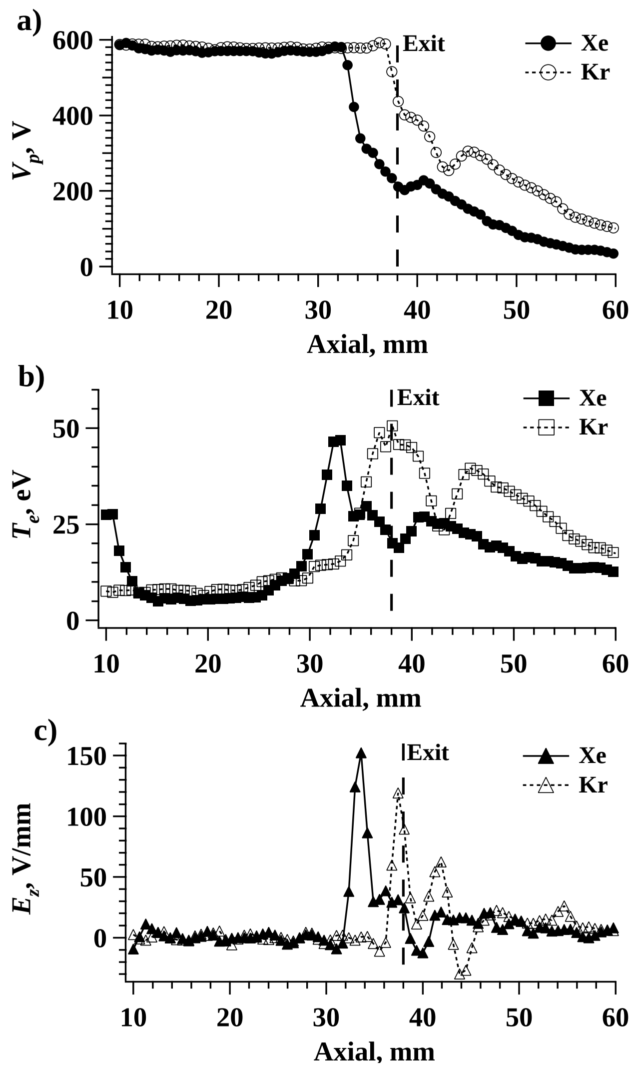

Figure 4-22. Centerline Emissive Probe Results for Xenon and Krypton at a Discharge Voltage of 600 V

4.3 Internal Langmuir Probe Results

In conjunction with the internal emissive probe investigation of krypton propellant, the internal mapping of the NASA-173Mv1 with a single Langmuir probe is conducted. The measured properties include ion number density and electron temperature.

The following section will outline the experimental results of the internal Langmuir probe mapping and identify major trends in these data. This section is broken into three sections: 300-V xenon operation, a comparison of magnetic field topology, and a xenon-krypton comparison. Detailed analyses will be reserved for the Internal Analysis chapter.

4.3.1 Internal Langmuir Operation Points

A list of the operating conditions appears in Table 4-2. These points are identical to some of the points presented in the internal emissive probe section and are numbered accordingly. Point 2 uses xenon propellant and operates at 300 V and 10 mg/s anode flow rate. Points 3 and 4 compare xenon with and without the trim coil at 500 V and anode flow of 10 mg/s. Point 6 uses krypton propellant and operates at 500 V and matches Point 4's discharge power. Point 8 is identical to the 500-V krypton point (6) except that it is operated using the same magnetic coil settings as the 500-V xenon point (4). The internal mapping is not conducted for krypton at 300 V due to the relatively poor performance of krypton at low voltages. For each operation point the electron temperatures and ion number densities are shown. The magnetic coil settings for these operation points were found in the performance analysis section.

Table 4-2. Thruster Operating Conditions for the Internal Langmuir Probe Mapping

Point #	Propel.	V_k, V	V_d, V	I_d, A	Anode Flow, mg/s	Cathode Flow, mg/s	Inner Coil, A	Outer Coil, A	Trim Coil, A
2	Xe	-12.8	300	8.54	10.00	1.00	1.88	2.21	-0.51
3	Xe	-11.5	500	9.25	10.00	1.00	2.90	2.67	0.00
4	Xe	-12.9	500	9.44	10.00	1.00	2.90	2.87	-0.87
6	Kr	-15.1	500	9.44	7.89	0.79	1.79	2.27	-0.43
8	Kr	-15.7	500	10.15	7.89	0.79	2.90	2.87	-0.87

4.3.2 300-V Xenon Operation

To be consistent with emissive probe data and work done by Haas with the UM/AFRL P5, 300-V xenon mapping is presented in this section. The ion number density and the electron temperature for the 300-V xenon case are shown in Figure 4-23. The centerline properties appear in Figure 4-24. The maximum ion density is 2.5×10^{12} cm^{-3}. Upstream of the ion acceleration zone, the ions are confined in the center of the discharge channel by the magnetic field. One can also see the ion focusing downstream of the acceleration zone.

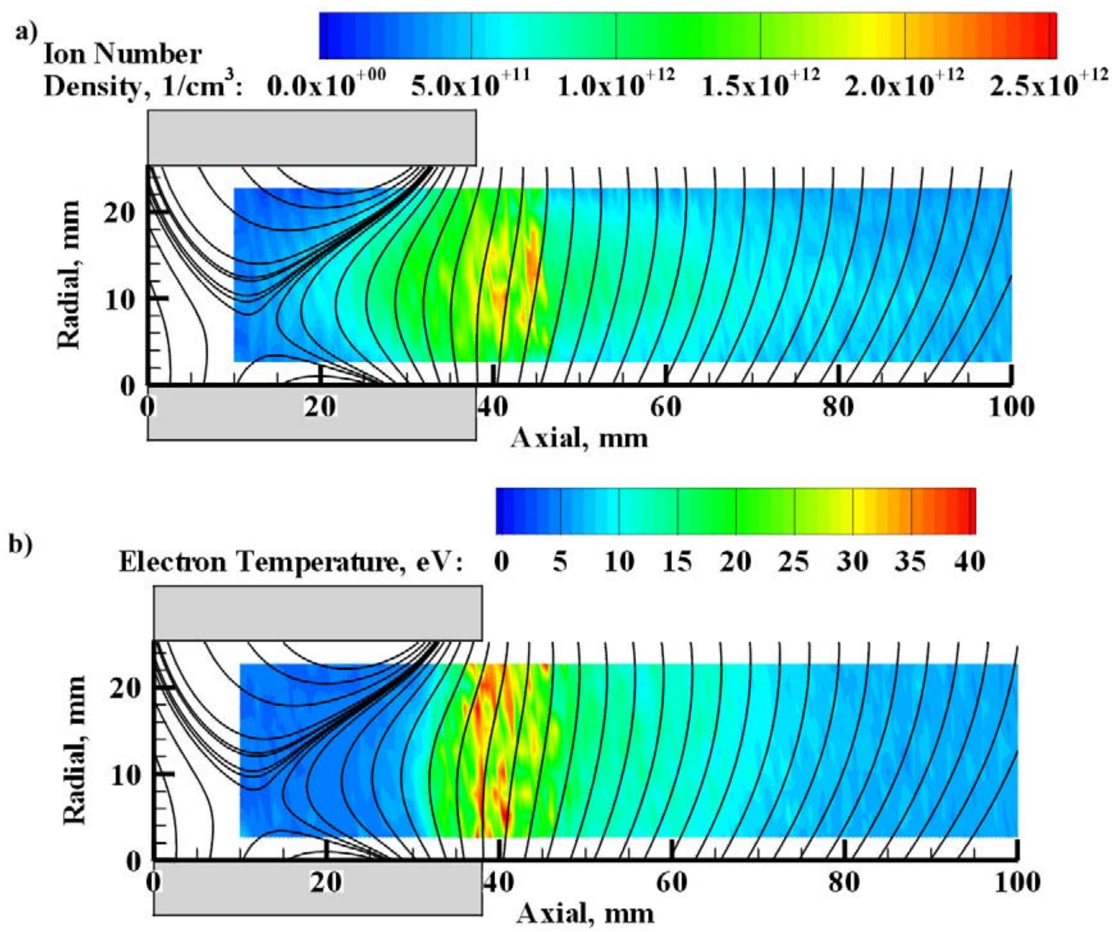

Figure 4-23. Internal Langmuir Probe Results for 300-V Xenon Operation with the Trim Coil (Point 2)

The electron temperature increases in the acceleration zone and reaches a maximum of 40 eV which is located near the beginning of the acceleration zone. Electron temperature is strongly tied to the magnetic field lines, which appear to be approximately isothermal in electron temperature as expected. This finding is true in the entire mapped region and is no surprise since the electrons should diffuse freely along the B-field lines.

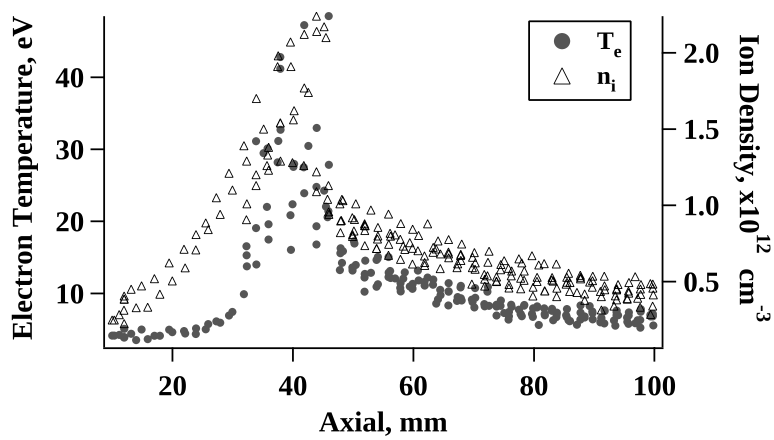

Figure 4-24. Centerline Langmuir Probe Results for Xenon Operation at a Discharge Voltage of 300 V, with the Trim Coil (Point 2)

Although more discussion of the ionization zone will be covered in Section 5.6.2, a few conclusions can be made based on the information learned from these raw internal data. There is high ion density in the center of the discharge channel and begins between 20-25 mm downstream of the anode. This high number density continues to around 47 mm. This extends past the beginning of the acceleration zone measured by the internal emissive probe measurements (Figure 4-3, b and Figure 4-7, a). This indicates a high ionization rate in the Hall current region.

Another interesting feature of the internal Langmuir probe data are the radial striations in plasma properties. This is related to the operation of the Langmuir probe and is not a physical phenomenon.

4.3.3 Magnetic Field Topology Trends

One interesting difference between the 300 and 500-V cases is the location of high ion number density. The region of high ion density begins upstream of the mapped region in the 500-V trim coil case. If one compares this to the 300-V trim coil case (Figure 4-23), this upstream region of ionization is not observed at the lower discharge voltage. This is most likely due to the higher electron temperature at higher voltages. Consistent for all xenon operation cases is the trend of high ion density in the acceleration region. This suggests that xenon ionization is strongly linked to the Hall current.

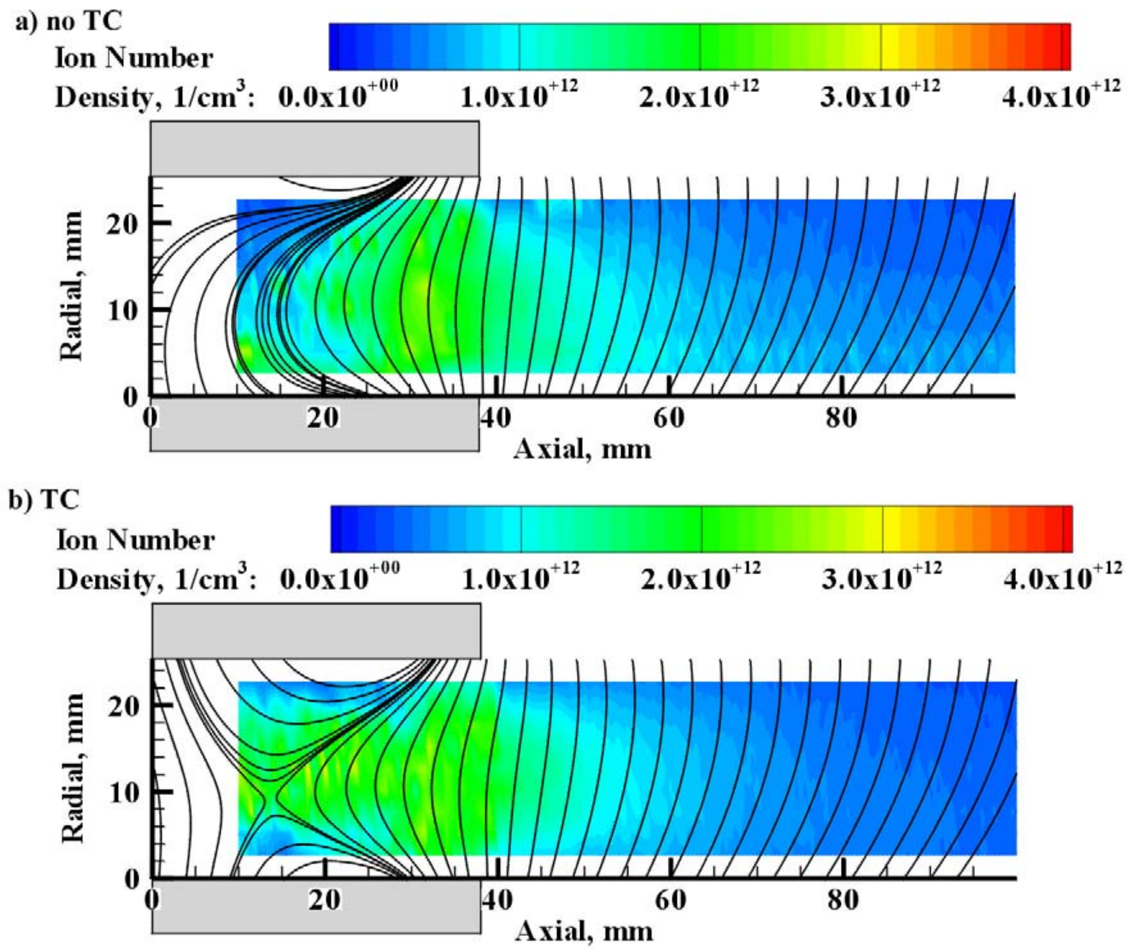

Figure 4-25. Ion Number Density Map for 500-V Xenon Operation without (a) and with the Trim Coil (b)

Interestingly, the upstream ionization is smaller in the 500-V non-trim coil case. This upstream ionization is connected to the trim coil and could be related to a few phenomena. The highest plasma density is located in the center of the discharge channel near the anode in a region where the magnetic mirror (or "magnetic bottle") is particularly strong. This finding is not entirely surprising since the magnetic mirror acts to confine the electrons and increase the electron number density in the center of the "bottle". The increased electron density increases the ionization collision rate and hence dictates the location of the ionization zone.

Another explanation for this high ionization is discussed by Fructman.[151] Fructman suggests the ionization will be enhanced in the unmagnetized region which results from the use of the trim coil. This correlation between magnetic field topology and ion production is an interesting trend and an area for future study.

The electron temperature mapping for the 500-V non-trim coil and trim coil cases are shown in Figure 4-26. The maximum electron temperature exceeds 40 eV in the bulk of the discharge channel and reaching a maximum of 50 eV. The region of high electron temperature is clearly outlined by the magnetic field lines, which is expected since the electrons freely move along the B-field lines and are impeded across the field lines. Just as in the 300-V case, the electrons are very close to isothermal along the B-field lines. These trends are more easily observed in the trim coil case. Finally, the region of high electron temperature extends farther up and downstream for the higher voltage case. This due to the larger electron temperature and hence the larger electron pressure which force the high temperature region upstream.

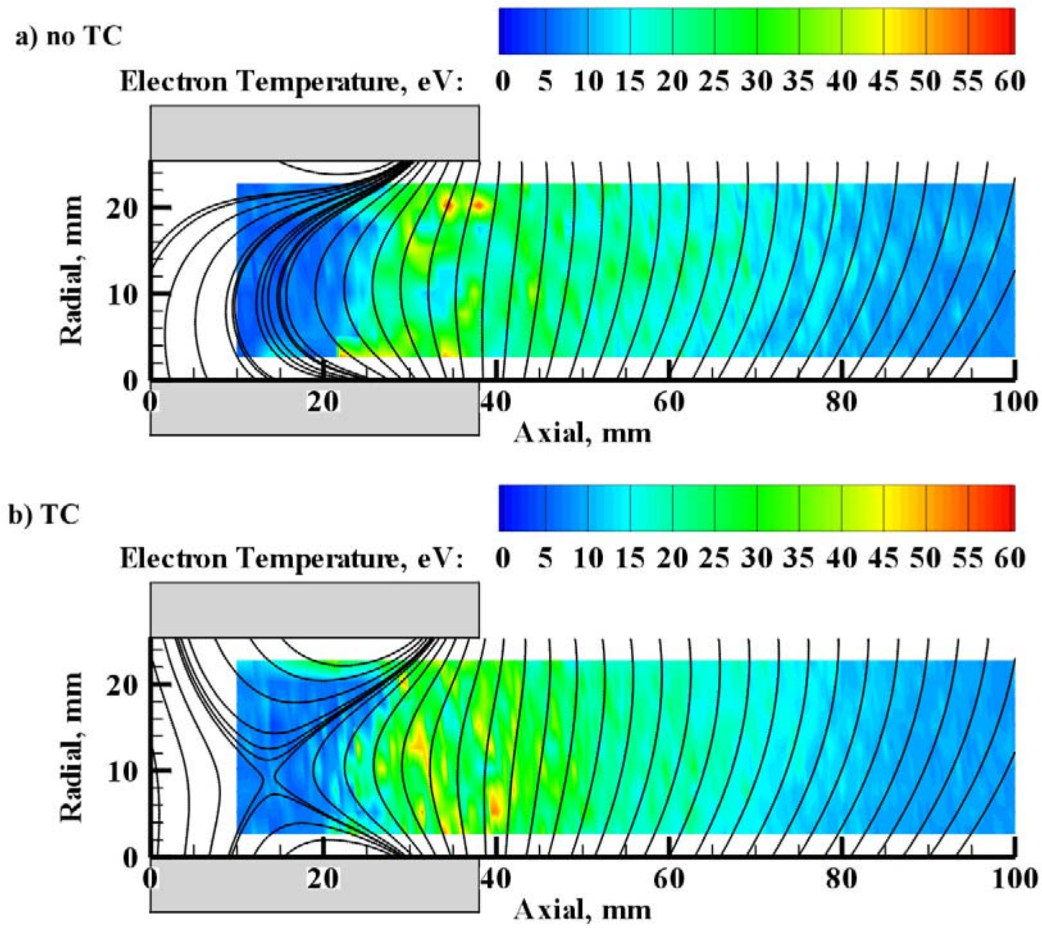

Figure 4-26. Electron Temperature Map for 500-V Xenon Operation without (Point 3) and with the Trim Coil (Point 4)

Centerline properties with non-trim coil and trim coil operation appear in Figure 4-27. Downstream of the thruster exit, the ion number densities and electron temperatures closely match for the trim coil and non-trim coil cases. This is expected since the acceleration zones are very similar for both cases (Section 4.2.2.2). The peak ion number density and electron temperature are slightly lower for the non-trim coil case. Due to the chaotic nature of the high-voltage internal Langmuir probe measurements, there is some spread in these data. However, this spread is on the order of the experimental error and when these data is viewed in bulk such as in a contour plot, trends are more easily observed.

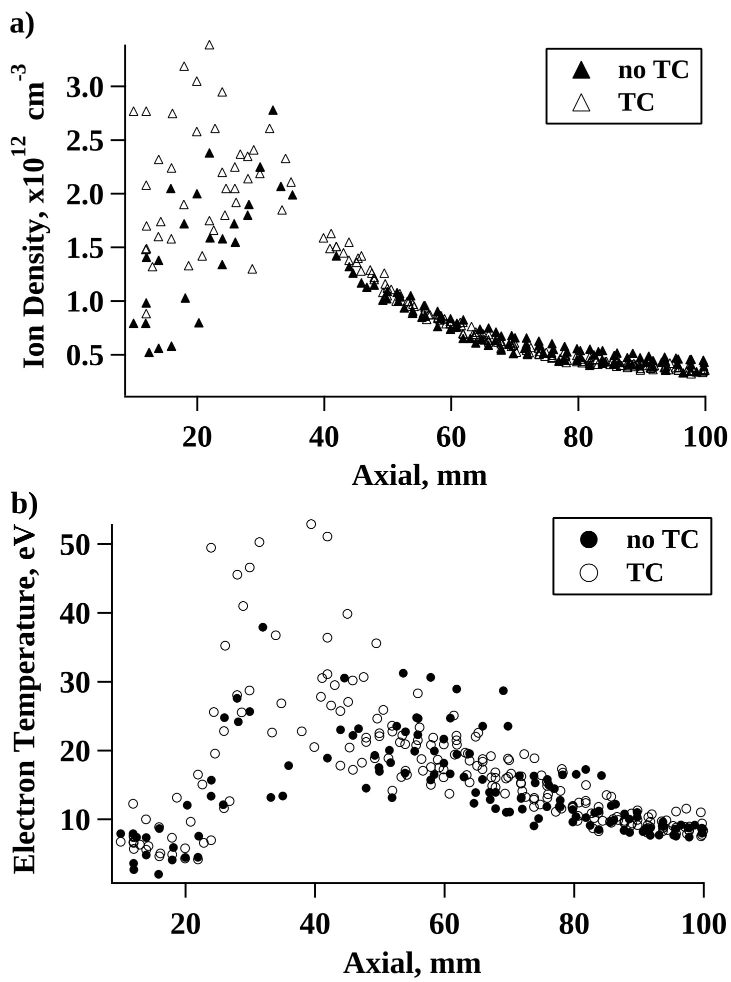

Figure 4-27. Centerline Langmuir Probe Results for 500-V Non-Trim Coil (Point 3) and Trim Coil (Point 4) Conditions

4.3.4 Krypton-Xenon Comparison

Figure 4-28 shows the ion number density measurements for the 500-V xenon (Point 4, Table 4-2) and krypton (Point 6, Table 4-2) operation. For the krypton case, the maximum ion number density reaches 4×10^{12} cm^{-3}, which is larger than the xenon operation points. Given the large relative error in Langmuir probe measurements, it is unclear if this difference has any significance. Downstream of the acceleration zone, the ion number densities contours show a slight focusing toward the centerline of the thruster as opposed to predominantly axially as seen in the xenon case. This result is consistent with the focusing effects shown by the internal emissive probe results.

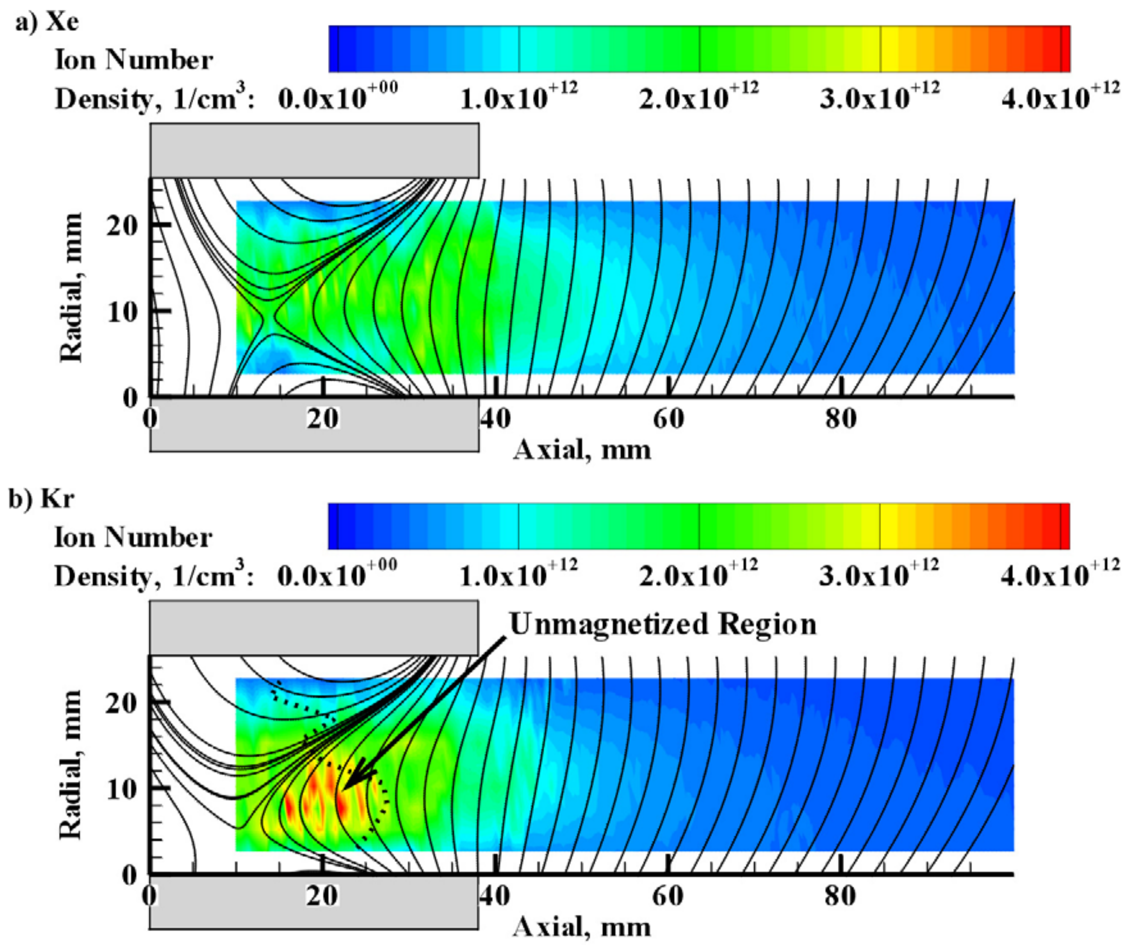

Figure 4-28. Ion Number Density Map for Xenon (Point 4) and Krypton (Point 6) at a Discharge Voltage of 500 V

For the krypton case, the region of high plasma density is located almost entirely upstream of the acceleration zone, unlike the xenon cases which have high ionization in the Hall current region. The low ionization rate in the Hall current region is likely due to the krypton's high ionization potential and low residence time. It is unclear what role the magnetic field topology plays in influencing this behavior. Although the location of the krypton ionization zone may be unexpected, its location is consistent with retarding potential analyzer measurements, which indicate that the krypton ion velocity dispersion is lower than xenon's (Section 3.4.3.2).

As discussed in the previous section, the ion density is highest at the center of a strong magnetic mirror. These results may suggest that the ionization is related to the magnetic mirror. To further study this phenomenon, the region of magnetized plasma is defined as the region where the cyclotron radius (Equ. 4-2) is much smaller than the discharge channel width (r_c<15 b). In Equ. 4-2, electron temperature has units of eV, magnetic field has units of Gauss, and the cyclotron radius has units of meters. Overlaid on top of Figure 4-28 b is a line marking the dividing line separating the magnetized and unmagnetized region inside the discharge channel. Upstream of this line the plasma is unmagnetized.

$$r_c = 0.0238 \frac{T_e^{1/2}}{B} \tag{4-2}$$

The border of magnetization very clearly outlines the region of high ion density. It seems that ionization may indeed be enhanced in the region of unmagnetized plasma, although the magnetic mirror argument can not be dismissed. A magnetic mirror that is unmagnetized in the center will be unable to confine electrons and will not operate ideally, however the magnetic pressure force should still focus electrons away from the walls and into center of the bottle. The high ionization region is probably due to a combination of magnetic field topology effects.

Electron temperature comparison can be seen in Figure 4-29. This electron temperature for krypton is slightly higher than the electron temperature in the xenon case.

For krypton, the electron temperature reaches a maximum of 60 eV near the outer wall of the discharge channel and is around 45 eV in the bulk of the discharge channel. the electron temperature in the xenon case peaks between 40-50 eV. Inside and downstream of the acceleration zone, the magnetic field pathlines again appear to approximately match electron isothermal lines.

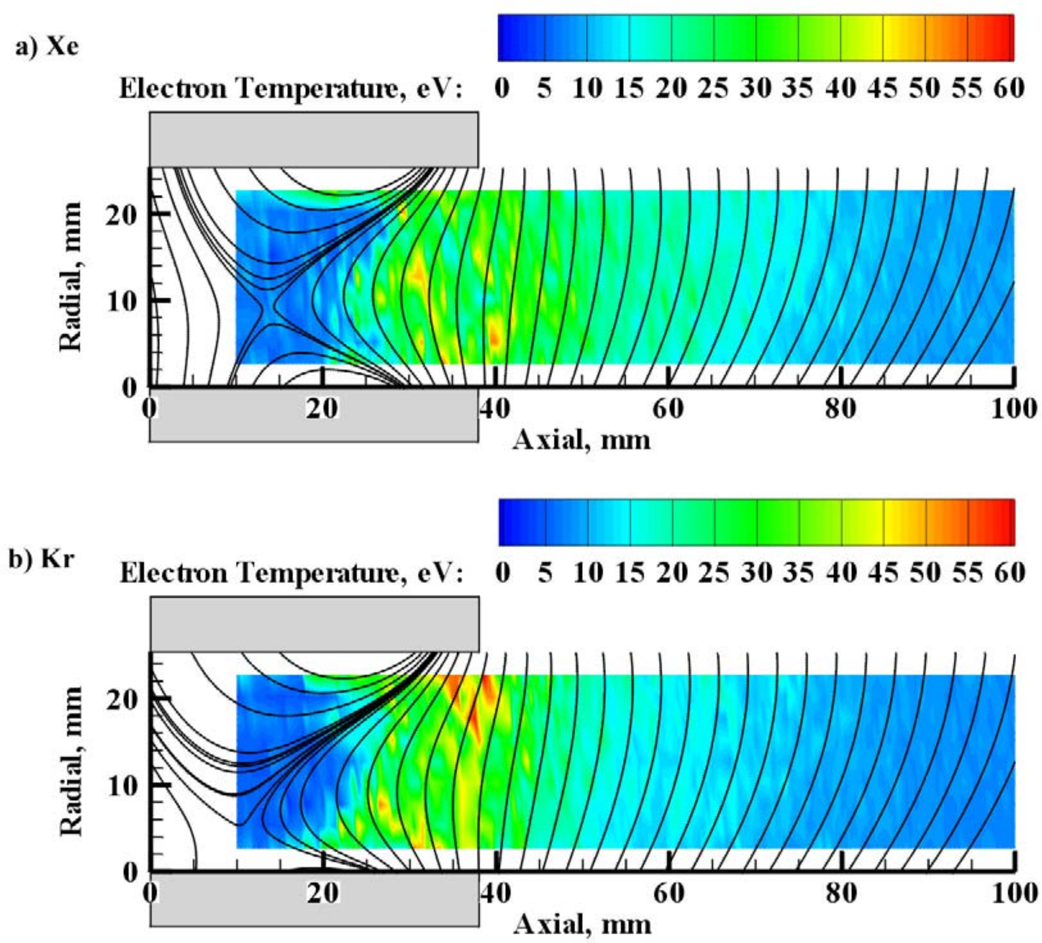

Figure 4-29. Electron Temperature Map for Xenon (Point 4) and Krypton (Point 6) at a Discharge Voltage of 500 V

Krypton's slightly larger maximum electron temperature is consistent with krypton's low number density in the acceleration zone. Since the ion production in the acceleration zone is lower in the krypton case, the electrons energy loss to ionization is small resulting in a slightly higher maximum electron temperature. With this said, the difference in electron temperature in the krypton and xenon case is not significant, which may indicate that ionization is not the dominant electron energy loss term. Another explanation is that since the region of high radial electron mobility (See Figure 5-17) is located largely outside of the discharge channel in the krypton case, there are fewer electron-wall losses and therefore the electron temperature is higher.

Centerline properties comparing 500-V xenon and krypton operation appear in Figure 4-30. Downstream of the exit, krypton centerline electron temperatures are a bit higher than xenon's. Ion number densities are higher in the xenon case downstream of the exit. This is a consequence of the high xenon ionization rate in the Hall current region. Upstream of the exit, ion densities and electron temperatures are approximately equal and peak at the same location. Electron temperature peaks near the thruster exit and ion number density peaks near 20-25 mm from the anode.

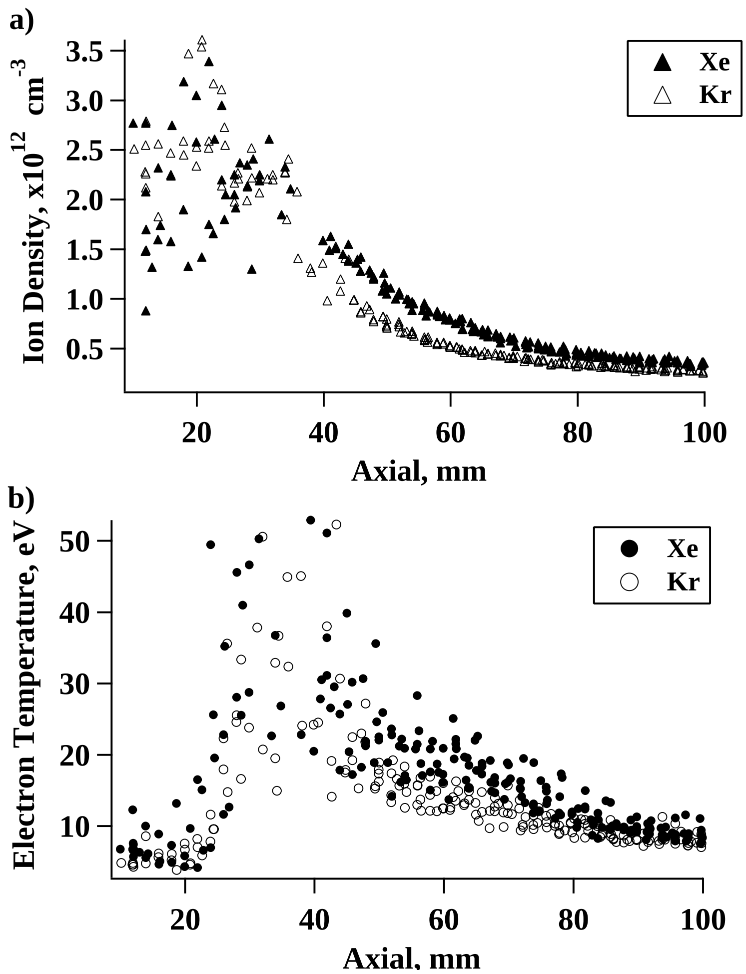

Figure 4-30. Centerline Langmuir Probe Results for Xenon (Point 4) and Krypton (Point 6) at a Discharge Voltage of 500 V

4.3.4.1 500-V Krypton Case with Matched B-Field

The results from the Langmuir Probe investigation for krypton operation with the same magnetic field topology as the 500-V xenon case are shown in Figure 4-31. Just as in the power-matched krypton case (Table 4-2, Point 6); the B-field matched case has a maximum number density of 4×10^{12} cm^{-3}. By following the lines of constant density, it can be seen that the ions are accelerated more along the center of discharge channel than in the power-matched krypton case. Consequently, it appears that the beam divergence may be improved for the B-field matched case. Similar to the power-matched case, the ion number density is highest in the middle of a strong magnetic mirror in the center-rear of the discharge channel.

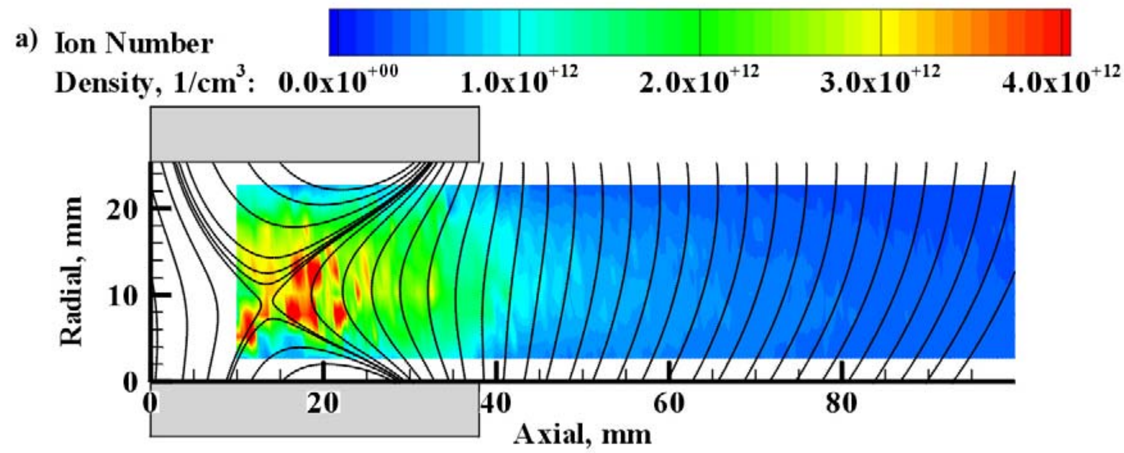

Figure 4-31. Internal Langmuir Probe Results for 500-V Krypton Operation with Matched B-field (Point 8)

The electron temperatures are approximately 45 eV on average and reach a maximum of 60 eV upstream of the acceleration zone. Data collected at this condition are more erratic than the other data sets due to the large discharge current oscillations associated with Point 8 operation. Nevertheless, this supports the major trends found in the power-matched krypton case.

As discussed in Section 4.1, the discharge current can be analyzed to study the Hall current and acceleration region. The standard deviation of discharge current is shown in Figure 4-32. This figure demonstrates the very large discharge oscillations with these non-optimized magnet settings. Just as in Figure 4-1, the acceleration zone boundaries from the 500-V xenon case (Point 4) are overlaid on the contour plot. Again, the region of highest current oscillation indicates the location of the Hall current. This figure shows that for this krypton case, the Hall current and acceleration zone locations are very similar to the xenon case, which implies that the magnetic field alone is enough to match the acceleration zone regardless of the propellant. However, because of the different ionization properties of krypton, the ionization is not stable, resulting in large current oscillations and lower thruster performance. In other words, the different properties of krypton and xenon mandate that the thruster operate with different magnetic field topologies to optimize the performance of each propellant.

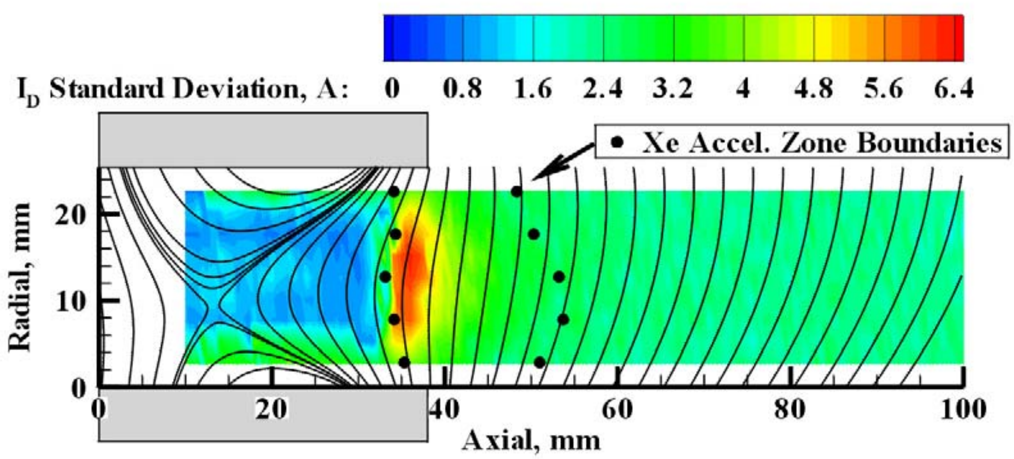

Figure 4-32. Probe Induced Perturbations for the 500-V Krypton Case with Matched B-field (Point 8)

In Figure 4-33, a fast Fourier transform (FFT) is taken for krypton and xenon at a discharge voltage and current of 500 V and 9.44 A, respectively (Table 4-2, Points 4, 6). Additionally, there is the operation point with krypton operating with the same magnetic field topology as xenon (Point 8). For the tuned setting the krypton oscillations are smaller than the xenon case, however when the magnetic field is matched to the xenon case, the oscillations increase significantly.

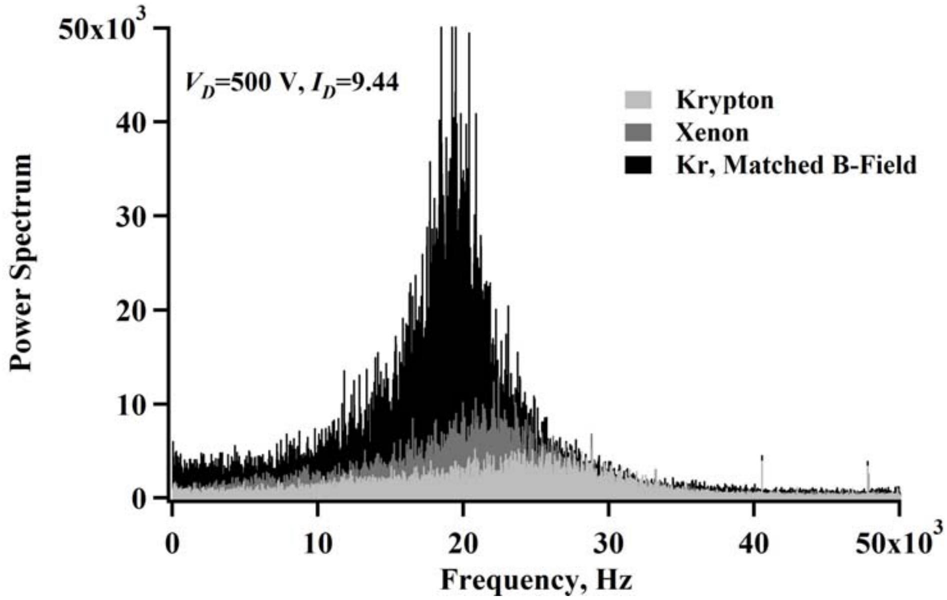

Figure 4-33. Comparison between Xenon and Krypton Discharge Current Oscillations

4.4 Comparison of Electron Temperature Measurements

The previous sections reported electron temperature measurements from both a floating emissive probe and a single Langmuir probe. Based on these presented results a few general trends can be observed. A comparison of these results will be briefly discussed here.

Both probes measure electron temperatures of approximately the same magnitude. However, the shape of the high electron temperature regions had little in common. The Langmuir probe electron temperature seems to follow the B-field lines and seem to be equipotential along the B-field lines. No such trends can be seen in the emissive probe temperature measurements.

There is more spread in the Langmuir probe data, which is not surprising given the nature of the diagnostic. The Langmuir probe data is based on 10's of data points whereas the emissive probe measurements are based on two data points. Since the emissive probe electron temperature measurements have a linear dependence on plasma potential, the electron temperature is expected to be as "smooth" as the plasma potential results.

Figure 4-34 shows a comparison of the electron temperature measurements taken for the 500-V xenon (Point 4) and krypton (Point 6) operation points both with the trim coil. The agreement between the emissive and Langmuir probe measurement can range between relatively good to poor.

Another disturbing trend in the internal emissive probe measurements is the artificial electron temperature increase near the anode. This is discussed in some detail in Section 4.2.2.2 and is circled in Figure 4-34. This brings the robustness of the emissive probe method into question.

In summary, single Langmuir probe electron temperature measurements while imperfect are preferred over emissive probe measurements. Because the emissive probe measurements are only based on two data points and often produce questionable results, they should be considered less robust than Langmuir probe measurements. However, the emissive probe does produce seemingly accurate magnitude results and can be a useful tool when yielded carefully and with healthy speculation. For these reason the Langmuir probe electron temperature measurements will be used in the Internal Analysis section.

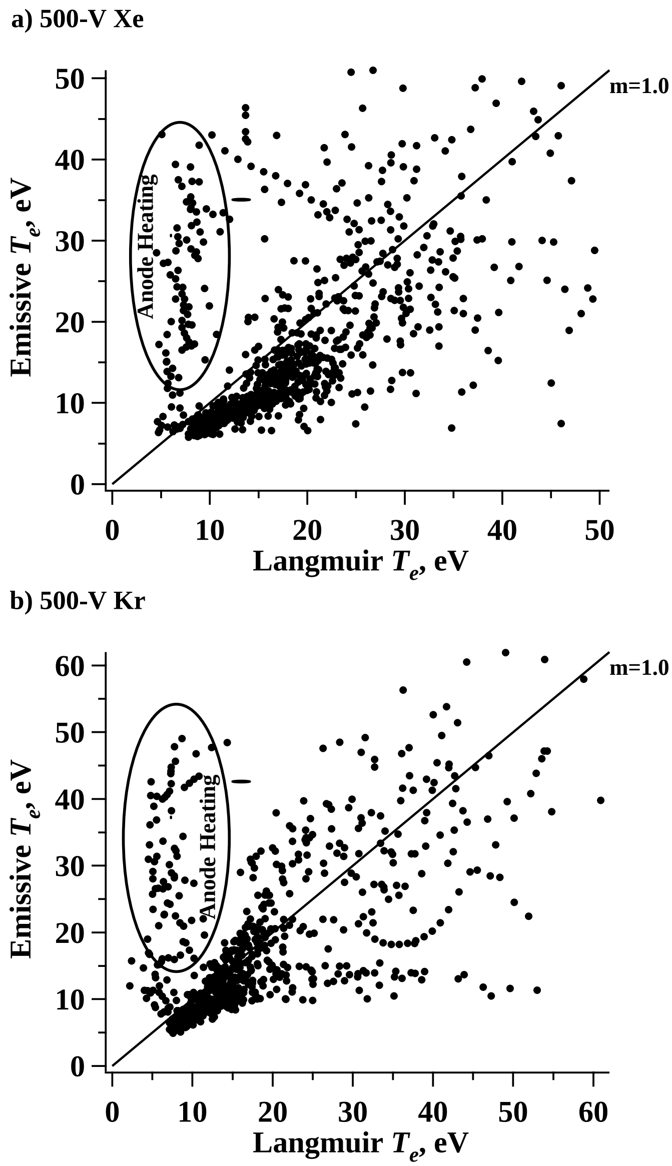

Figure 4-34. Comparison of Emissive Probe and Langmuir Probe Electron Temperature Measurements

Chapter 5.

Internal Analysis

In order to better understand the phenomena internal to the Hall thruster discharge channel, a thorough internal analysis is conducted. The results from these analyses should elucidate many of the remaining pieces of the krypton performance puzzle and result in a cogent analysis of the problem. This will additionally help to further understand the benefits of the trim coil. The analysis will focus on studying the electron motion, electron energy, ionization process, acceleration process, and the Hall parameter. The points of major consideration are 500-V, xenon operation with and without the trim coil, and 500-V krypton operation with the trim coil (Points 3, 4, and 6). For completeness, results for the 300 and 600-V xenon operation are also included in certain sections.

5.1 Internal Electron Temperature Gradients

It has long been suggested electron temperature is linearly dependent on plasma potential. Zharinov and Popov[152] modeled the potential profile in the discharge channel ignoring the wall effects and found a linear dependence between electron temperature and plasma potential equal to 0.4 eV/V. Using the similar emissive probe method as presented in this paper, Staack, Raitses, and Fisch[83] measured this linear dependence and found a slope between 0.08-0.14 eV/V. Using emissive probe techniques, similar results have been found by other experiments.[80,153] However, internal work using a double Langmuir probe does not observed the same linear trends.[58,99]

It should be noted that the equation used for calculating electron temperature has a linear dependence on plasma potential (seen in Equ. 2-14), so a linear relation between electron temperature and plasma potential may be a result of the analysis technique. This may explain why the internal work using a different probe technique returns different results. Result from the internal Langmuir and emissive probe are shown below.

Figure 5-1 show electron temperature versus plasma potential for 500-V xenon and krypton operation. Both of these cases are operated with the same discharge power and both use the trim coil. These plots show the assembled results from 5 axial sweeps. All cases with either emissive or Langmuir probe show a roughly linear dependence of electron temperature with plasma potential. A linear fit is applied to the temperature gradient and the equation for the curve fit is given.

Since the emissive probe recorded both plasma potential and electron temperature, the Langmuir probe is expected to have more noise and have greater spread in these data. This noise varies from relatively little to quite extreme. Given the high voltage, high density plasma, the internal measurements look fairly good.

For xenon, the emissive probe results are linear; however the Langmuir probe results are less clear. The Langmuir probe electron temperature measurements increases linearly until around 250 V, at this point there seems to be a decrease in electron temperature after which the linear increase seems to continue. This trend could be from error in these data or from enhanced ionization in this region. The slope of the temperature gradient is between 0.07 and 0.08 eV/V.

The krypton results are linear for both emissive probe and Langmuir probe results. The slope is between 0.08-0.095 eV/V. The steeper slope in the krypton case indicates that the krypton case has fewer electron energy losses. This may be related to fewer ionizing collision in the Hall current region or due to fewer wall losses in the region of high radial mobility region.

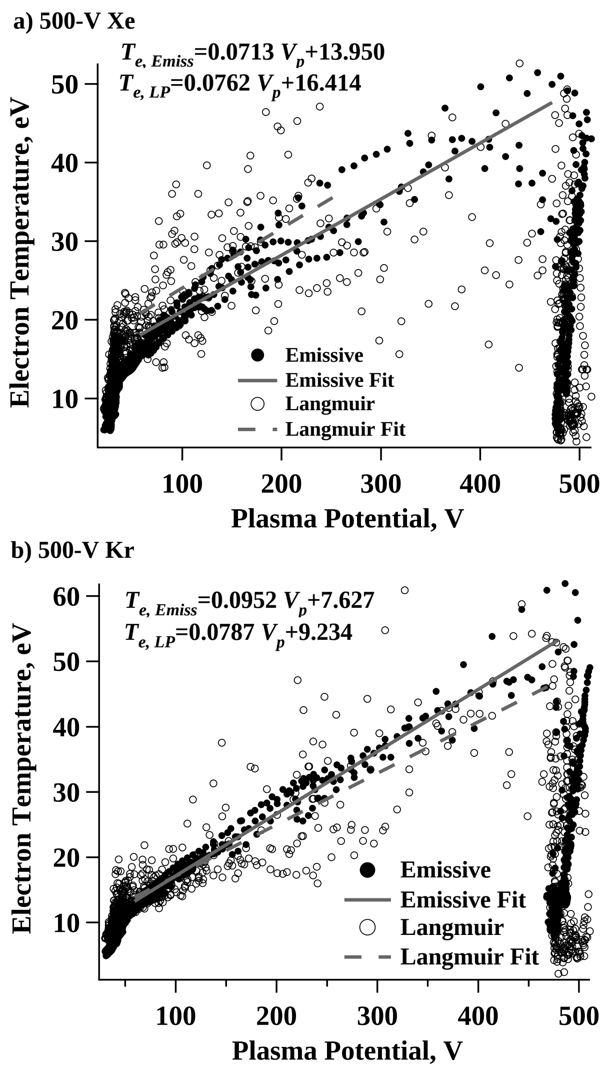

Figure 5-1. Electron Temperature versus Plasma Potential for a) 500-V Xenon Operation and 500-V Krypton Operation

The rapid decrease in electron temperature upstream of the acceleration zone may be due to high ionization. It also may be due to the low magnetic field and high neutral number density. In this upstream region, the magnetic field is much lower and for this reason the hottest electrons are poorly confined and stream easily toward the anode. Additionally, the high neutral density will increase electron-neutral collisions, hence enhancing the classical mobility and electron energy loss.

5.2 Thermalized Potential

Given the importance of the beam focusing trends shown in the emissive probe section, for completeness it is necessary to discuss the thermalized potential. Morozov[144] first suggested that to the first order, the magnetic field lines should predict the equipotential lines inside the Hall thruster. More accurately, assuming that the electron pressure is negligible, the thermalized potential should follow the magnetic field lines. The thermalized potential is defined in Equ. 5-1. In this equation, n_o is a reference number density equal to 1×10^{12} cm^{-3} and the other symbols have their normal meaning. The electron temperature and plasma number density (assuming quasineutrality) are taken from internal Langmuir probe measurements for these operating condition. The thermalized potential for the 300-V and 500-V xenon cases and the 500-V krypton cases (Points 2, 4, and 6), are shown in Figure 5-2. These points are presented to be consistent with the emissive probe experimental results section. It should be noted that in Figure 5-2 the electron temperature measured from the Langmuir probe is used for the emissive probe correction. The thermalized potential is well correlated with the magnetic field lines in and upstream of the acceleration zone.

$$V_p^{\ *} = V_p + T_e \ln\left(\frac{n_e}{n_o}\right) \qquad (5\text{-}1)$$

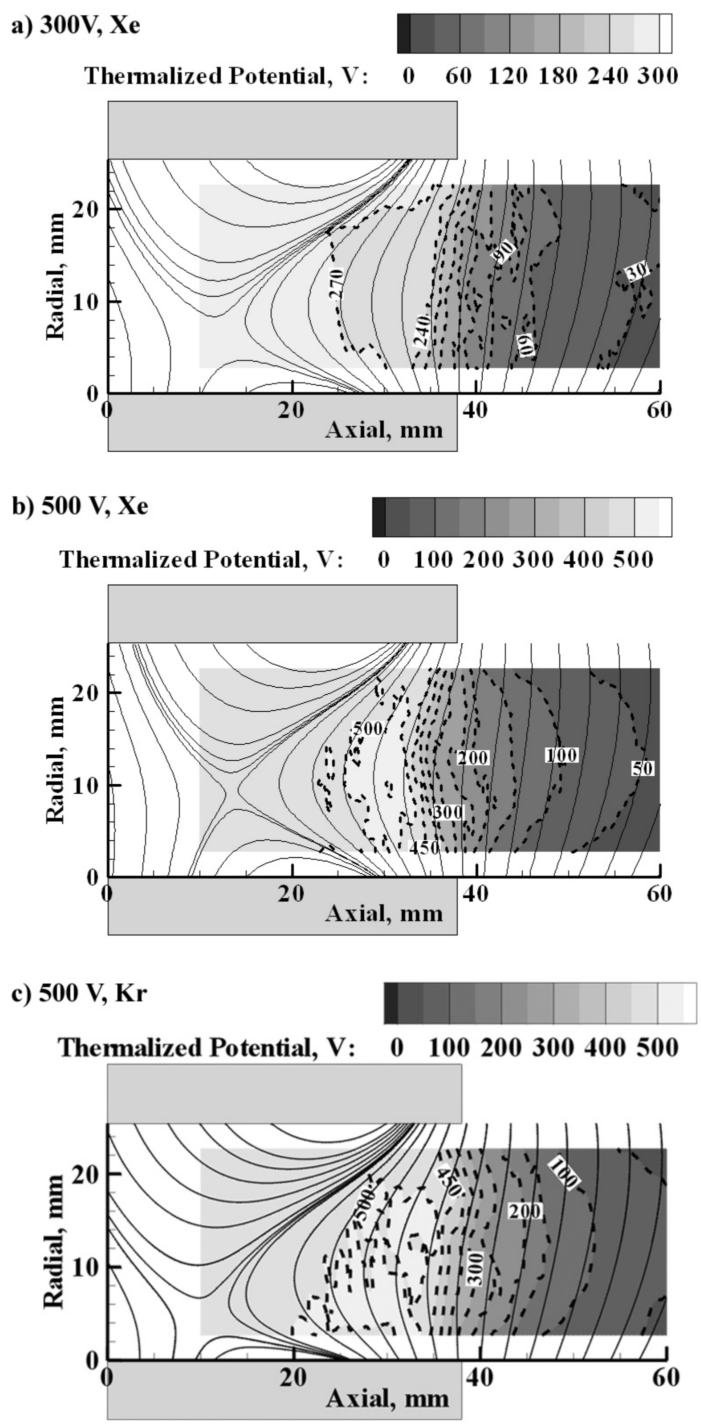

Figure 5-2. Thermalized Potential Maps for the a) 300-V and b) 500-V Xenon Cases, and c) 500-V Krypton case (all with the Trim Coil)

5.3 Ion Particle Trajectories

In this section, a simple method is employed to estimate the ion trajectories inside the discharge channel. The ion velocity is assumed to be uniform and purely axial at 10 mm from the anode. The axial velocity is uniform and determined by the half Maxwellian assuming an ion temperature of 0.1 eV, which is consistent with temperatures used by Hall thruster modelers.[154] The ions are assumed to be unmagnetized, collisions are neglected, and the ion pressure is neglected. Assuming that the axial ion velocity is significantly larger than the radial ion velocity and based on the ion momentum equations, equation for the axial and radial ion velocities are shown in Equs. 5-4 and 5-3.

$$V_{iz}(z)^2 = \sum_{i=0}^{i=z} \frac{2e}{M_i}\left(V_{p,i-1} - V_{p,i}\right) + \left(V_{iz,10mm}\right)^2 \qquad \textbf{(5-2)}$$

$$V_{ir,i}(z) = V_{ir,i-1} + \frac{eE_r \Delta z}{M_i V_{iz,i}} \qquad \textbf{(5-3)}$$

The ion trajectories are compared for the 500-V xenon and krypton operation points with the trim coil (Points 2 and 6) and the results can be seen in Figure 5-3. This figure clearly shows the focusing effect of the plasma lens. The xenon case is strongly focusing ions toward the center of the discharge channel. Although the acceleration zone is divergent in the krypton case, the focusing equipotential lines in the region upstream of the acceleration zone results in significant beam focusing. The krypton case is focusing ions toward the thruster axis as opposed to directly out of the discharge channel. These results are also supported by the internal Langmuir probe results (Section 4.3).

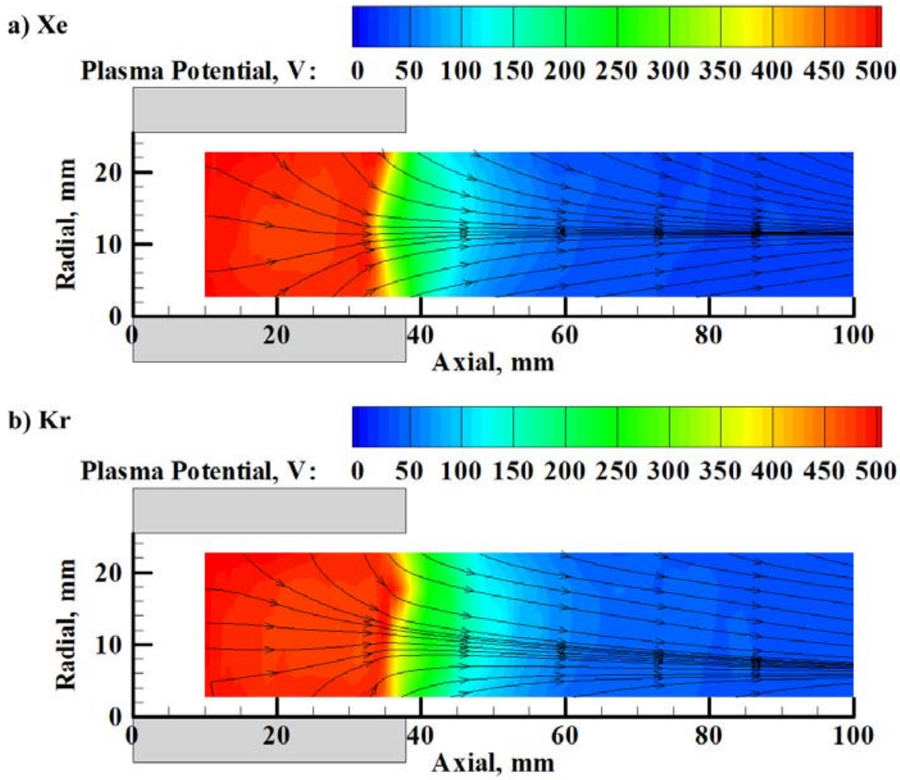

Figure 5-3. Ion Particle Trajectories for the 500-V Xenon and Krypton Cases with the Trim Coil

5.4 Numerical Fluid Model

5.4.1 Description of Model

In order to study the flow of heavy particles in the discharge channel, a time-marching technique[155,156] is used to solve the steady-state solution of the flow. This is a method where an initial guess is assumed and then the flow field is advanced in time by using the Taylor series expansion (Equ. 5-4). In this equation, U is any conserved quantity. The physics of the problem are given by the governing equations and enter the equations in the form of the time derivatives. The continuity and momentum equations are applied to a small control volume and the equations are relaxed to the steady-state solution. After a large enough number of time steps, the changes in the flow field become negligibly small and the flow is considered converged.

$$U(t+\Delta t) = U(t) + \left(\frac{\partial U}{\partial t}\right)_{avg} \Delta t + \ldots \qquad \textbf{(5-4)}$$

This analysis is unique in that it uses a combination of experimental results and the governing equation to solve the flow field. The experimental result from the floating emissive probe and single Langmuir probe are used to partially solve the equations and help drive the equations to convergence. One continuity equation is partially solved and the energy equations are solved by the probe measurements. The ion energy equation is not needed due to the known electric fields, which were found by the emissive probe. The ion continuity equation can be solved to find the ionization rate at each time step and also can be used to define the ion pressure term.

A fluid dynamics approach is used to solve the flow field. For this analysis, a fluid description is appropriate because single particle effects can be considered much less important that the collective effects of the plasma. A rough criterion to show this is by comparing the collisions frequency (ionization frequency is on the order of 100 kHz) to the much larger ion plasma frequency (approximately 13 MHz).

5.4.2 Axisymmetric Finite Volume Formulation

The conservative form of the continuity and momentum equations for the ion and neutral flow can be seen in Equs. 5-5 to 5-8.

$$\frac{\partial n_i}{\partial t} + \nabla \cdot (n_i \vec{V}_i) = \left\langle Q_{i,n} V_e \right\rangle n_i n_n \qquad \textbf{(5-5)}$$

$$\frac{\partial n_n}{\partial t} + \nabla \cdot (n_n \vec{V}_n) = -\langle Q_{i,n} V_e \rangle n_i n_n \qquad (5\text{-}6)$$

$$\frac{\partial \left(n_i \vec{V}_i\right)}{\partial t} + \nabla \cdot \left(n_i \vec{V}_i \vec{V}_i\right) = \frac{e n_i}{M_i}\left(\vec{E} + \vec{V}_i \times \vec{B}\right) - \frac{1}{M_i}\nabla P_i + \langle Q_{i,n} V_e \rangle n_i n_n \vec{V}_{MT} \qquad (5\text{-}7)$$

$$\frac{\partial \left(n_n \vec{V}_n\right)}{\partial t} + \nabla \cdot \left(n_n \vec{V}_n \vec{V}_n\right) = -\frac{1}{M_i}\nabla P_n - \langle Q_{i,n} V_e \rangle n_i n_n \vec{V}_{MT} \qquad (5\text{-}8)$$

The first step in this analysis is to put the governing equations into vector form (Equ. 5-9). In this equation, *U* is the array of conserved quantities, *G* is the source term, *F* are the flux terms across each of the control volume faces, and the subscripts 1-3 indicate the direction normal to the surface faces.

$$\frac{\partial U}{\partial t} + \frac{\partial \vec{F}}{\partial \vec{x}} = \frac{\partial U}{\partial t} + \frac{\partial F_1}{\partial x_1} + \frac{\partial F_2}{\partial x_2} + \frac{\partial F_3}{\partial x_3} = G \qquad (5\text{-}9)$$

By using the Gauss's Theorem these equations can be applied to a finite volume (Equ. 5-10).

$$\iiint_V \frac{\partial U}{\partial t} dV + \iint_S \vec{F} \cdot \hat{e}\, dS = \iiint_V G dV \qquad (5\text{-}10)$$

Where *U*, *F* and *G* are given in Equ. 5-11.

Error! Objects cannot be created from editing field codes.

$$G=\begin{pmatrix} \left\langle Q_{i,n}V_e\right\rangle n_i n_n \\ -\left\langle Q_{i,n}V_e\right\rangle n_i n_n \\ \frac{en_i}{M_i}\left(E_1+V_{i2}B_3-V_{i3}B_2\right)+\left\langle Q_{i,n}V_e\right\rangle n_i n_n V_{MT1} \\ \frac{en_i}{M_i}\left(E_2+V_{i3}B_1-V_{i1}B_3\right)+\left\langle Q_{i,n}V_e\right\rangle n_i n_n V_{MT2} \\ \frac{en_i}{M_i}\left(E_3+V_{i1}B_2-V_{i2}B_1\right)+\left\langle Q_{i,n}V_e\right\rangle n_i n_n V_{MT3} \\ -\left\langle Q_{i,n}V_e\right\rangle n_i n_n V_{MT1} \\ -\left\langle Q_{i,n}V_e\right\rangle n_i n_n V_{MT2} \\ -\left\langle Q_{i,n}V_e\right\rangle n_i n_n V_{MT3} \end{pmatrix} \tag{5-11}$$

Before continuing the derivation, the ions are assumed to be unmagnetized. This assumption greatly simplifies the length of the derivation by canceling the source terms related to the magnetic field.

From this point on derivation of the axisymmetric finite volume formulation is similar to the derivation done by Nompelis.[157] In order to use an axisymmetric formulation of the finite volume method it is necessary to first convert the Cartesian coordinates to cylindrical coordinates. In this case the x-y plane is the cylindrical plane given by θ=0.

To covert from Cartesian to cylindrical coordinates the transformation matrix (Equ. 5-12) is used.

$$\begin{pmatrix} V_1 \\ V_2 \\ V_3 \end{pmatrix}=\begin{pmatrix} 0 & 0 & 1 \\ \cos\theta & -\sin\theta & 0 \\ \sin\theta & \cos\theta & 0 \end{pmatrix}\begin{pmatrix} V_r \\ V_\theta \\ V_z \end{pmatrix} \tag{5-12}$$

This results in transforming Equ. 5-11 into Equs. 5-13 to 5-15:

$$U=\begin{pmatrix} n_i \\ n_n \\ n_i V_{iz} \\ n_i\left(V_{ir}\cos\theta - V_{i\theta}\sin\theta\right) \\ n_i\left(V_{ir}\sin\theta + V_{i\theta}\cos\theta\right) \\ n_n V_{nz} \\ n_n\left(V_{nr}\cos\theta - V_{n\theta}\sin\theta\right) \\ n_n\left(V_{nr}\sin\theta + V_{n\theta}\cos\theta\right) \end{pmatrix} \tag{5-13}$$

$$F_1=\begin{pmatrix} n_i V_{iz} \\ n_n V_{nz} \\ n_i V_{iz}{}^2 + \dfrac{P_i}{M_i} \\ n_i V_{iz}\left(V_{ir}\cos\theta - V_{i\theta}\sin\theta\right) \\ n_i V_{iz}\left(V_{ir}\sin\theta + V_{i\theta}\cos\theta\right) \\ n_n V_{nz}{}^2 + \dfrac{P_n}{M_i} \\ n_n V_{nz}\left(V_{nr}\cos\theta - V_{n\theta}\sin\theta\right) \\ n_n V_{nz}\left(V_{nr}\sin\theta + V_{n\theta}\cos\theta\right) \end{pmatrix},\ F_2=\begin{pmatrix} n_i\left(V_{ir}\cos\theta - V_{i\theta}\sin\theta\right) \\ n_n\left(V_{nr}\cos\theta - V_{n\theta}\sin\theta\right) \\ n_i V_{iz}\left(V_{ir}\cos\theta - V_{i\theta}\sin\theta\right) \\ n_i\left(V_{ir}\cos\theta - V_{i\theta}\sin\theta\right)^2 + \dfrac{P_i}{M_i} \\ n_i\left(V_{ir}\cos\theta - V_{i\theta}\sin\theta\right)\left(V_{ir}\sin\theta + V_{i\theta}\cos\theta\right) \\ n_n V_{nz}\left(V_{nr}\cos\theta - V_{n\theta}\sin\theta\right) \\ n_n\left(V_{nr}\cos\theta - V_{n\theta}\sin\theta\right)^2 + \dfrac{P_n}{M_i} \\ n_n\left(V_{nr}\cos\theta - V_{n\theta}\sin\theta\right)\left(V_{nr}\sin\theta + V_{n\theta}\cos\theta\right) \end{pmatrix},$$

$$F_3=\begin{pmatrix} n_i\left(V_{ir}\sin\theta + V_{i\theta}\cos\theta\right) \\ n_n\left(V_{nr}\sin\theta + V_{n\theta}\cos\theta\right) \\ n_i V_{iz}\left(V_{ir}\sin\theta + V_{i\theta}\cos\theta\right) \\ n_i\left(V_{ir}\cos\theta - V_{i\theta}\sin\theta\right)\left(V_{ir}\sin\theta + V_{i\theta}\cos\theta\right) \\ n_i\left(V_{ir}\sin\theta + V_{i\theta}\cos\theta\right)^2 + \dfrac{P_i}{M_i} \\ n_n V_{nz}\left(V_{nr}\sin\theta + V_{n\theta}\cos\theta\right) \\ n_n\left(V_{nr}\cos\theta - V_{n\theta}\sin\theta\right)\left(V_{nr}\sin\theta + V_{n\theta}\cos\theta\right) \\ n_n\left(V_{nr}\sin\theta + V_{n\theta}\cos\theta\right)^2 + \dfrac{P_n}{M_i} \end{pmatrix} \tag{5-14}$$

$$
G = \begin{pmatrix}
\left\langle Q_{i,n} V_e \right\rangle n_i n_n \\
-\left\langle Q_{i,n} V_e \right\rangle n_i n_n \\
\frac{e n_i}{M_i}\left(E_z\right) + \left\langle Q_{i,n} V_e \right\rangle n_i n_n V_{MTz} \\
\frac{e n_i}{M_i}\left(E_r \cos\theta - E_\theta \sin\theta\right) + \left\langle Q_{i,n} V_e \right\rangle n_i n_n \left(V_{MTr} \cos\theta - V_{MT\theta} \sin\theta\right) \\
\frac{e n_i}{M_i}\left(E_r \sin\theta + E_\theta \cos\theta\right) + \left\langle Q_{i,n} V_e \right\rangle n_i n_n \left(V_{MTr} \sin\theta + V_{MT\theta} \cos\theta\right) \\
-\left\langle Q_{i,n} V_e \right\rangle n_i n_n V_{MTz} \\
-\left\langle Q_{i,n} V_e \right\rangle n_i n_n \left(V_{MTr} \cos\theta - V_{MT\theta} \sin\theta\right) \\
-\left\langle Q_{i,n} V_e \right\rangle n_i n_n \left(V_{MTr} \sin\theta + V_{MT\theta} \cos\theta\right)
\end{pmatrix} \tag{5-15}
$$

To continue we must to handle the surface integrals over the finite volume. First we will need to relate the derivatives in Equ. 5-9 to the new axisymmetric coordinate system. This is shown in the following set of transformation equations.

$$
\begin{aligned}
x_1 &= z \\
x_2 &= r\cos\theta \\
x_3 &= r\sin\theta \\
r^2 &= {x_2}^2 + {x_3}^2 \\
\tan\theta &= \frac{x_3}{x_2}
\end{aligned} \tag{5-16}
$$

From these we can relate the derivatives in the two different coordinates systems. Later, the axisymmetric assumption will be applied and θ will be set to zero, at which point these equations will simply as shown in Equ. 5-17.

$$
\begin{aligned}
\frac{\partial}{\partial x_1} &= \frac{\partial}{\partial z} \\
\frac{\partial}{\partial x_2} &= \cos\theta\frac{\partial}{\partial r} - \frac{\sin\theta}{r}\frac{\partial}{\partial \theta} = \frac{\partial}{\partial r} \\
\frac{\partial}{\partial x_3} &= \sin\theta\frac{\partial}{\partial r} + \frac{\cos\theta}{r}\frac{\partial}{\partial \theta} = 0
\end{aligned} \tag{5-17}
$$

Now Equ. 5-10 can be rewritten as is shown in Equ. 5-18. At this point the surface integral of the axisymmetric domain can be calculated over the six surfaces of the volume. The axisymmetric control volume can be seen in Figure 5-4. These surface integrals can be broken into two pieces. In the cases where the fluxes are integrated over the faces normal to the radial and axial directions, the process is fairly straight forward. However, additional attention is given to the integral of the surface normal to the θ-direction.

$$\iiint_V \frac{\partial U}{\partial t} dV + \iint_{S_r} \vec{F} \cdot \hat{e}_r ds_r + \iint_{S_z} \vec{F} \cdot \hat{e}_z ds_z + \iint_{S_\theta} \vec{F} \cdot \hat{e}_\theta ds_\theta = \iiint_V G dV \quad \textbf{(5-18)}$$

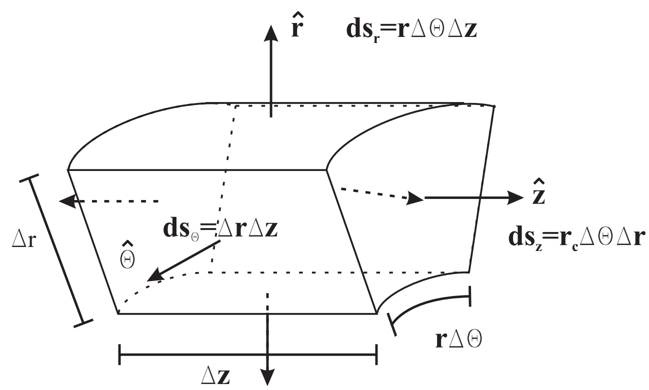

Figure 5-4. The Axisymmetric Control Volume

By evaluating the θ-normal surfaces at angles $\pm\theta_o$ ($\Delta\theta = 2\theta_o$), one can evaluate these integrands for each face as:

$$\vec{F} \cdot \hat{e} = \vec{F}\Big|_{\pm\theta} \cdot \left(-\sin\theta\,\hat{j} + \cos\theta\,\hat{k}\right) = -F_2 \sin\theta\Big|_{\pm\theta_o} + F_3 \cos\theta\Big|_{\pm\theta_o}. \quad \textbf{(5-19)}$$

When expanding the terms and summing the contributions from both faces one arrives at Equ. 5-20.

$$\iint_{S_\theta} \vec{F} \cdot \hat{e}_\theta \, ds = \Delta r \Delta z \begin{pmatrix} 0 \\ 0 \\ 0 \\ -2V_{i\theta}{}^2 n_i \sin\theta_o - 2\dfrac{P_i}{M_i}\sin\theta_o \\ 2V_{ir}V_{i\theta}n_i \sin\theta_o \\ 0 \\ -2V_{n\theta}{}^2 n_n \sin\theta_o - 2\dfrac{P_n}{M_i}\sin\theta_o \\ 2V_{nr}V_{n\theta}n_n \sin\theta_o \end{pmatrix} \tag{5-20}$$

By completing the integral over the other surfaces, each term can be rewritten as appears in Equ. 5-21 (Refer to Figure 5-4).

$$\begin{gathered} \iiint_V \frac{\partial U}{\partial t} dV = r_c \Delta z \Delta r \Delta\theta \left(\frac{\partial U}{\partial t}\right) \\ \iint_{S_z} F_1 \cdot \hat{e}_z ds_z = r_c \Delta r \Delta\theta \sum F_1 \cdot \hat{e}_z \\ \iint_{S_r} F_2 \cdot \hat{e}_r ds_r = \Delta z \Delta\theta \sum r F_2 \cdot \hat{e}_r \\ \iiint_V G dV = r_c \Delta z \Delta r \Delta\theta (G) \end{gathered} \tag{5-21}$$

Plugging these terms back into Equ. 5-18 and dividing both sides by the volume ($V=r_c\Delta\theta\Delta r\Delta z$) and then taking the limit as θ_o goes to zero one arrives at the simplified form of the integral. Where, r_c is the radius of the centroid.

$$\frac{\partial U}{\partial t} + \frac{1}{\Delta z}\sum F_1 \cdot \hat{e}_z + \frac{1}{r_c \Delta r}\sum r F_2 \cdot \hat{e}_r + \frac{1}{r_c}\begin{pmatrix} 0 \\ 0 \\ 0 \\ -V_{i\theta}{}^2 n_i - \dfrac{P_i}{M_i} \\ V_{ir}V_{i\theta}n_i \\ 0 \\ -V_{n\theta}{}^2 n_n - \dfrac{P_n}{M_i} \\ V_{nr}V_{n\theta}n_n \end{pmatrix} = G \tag{5-22}$$

Now that the general form of the equations is written, it is the appropriate time to reduce these equations for this particular problem. These can be simplified to a 2-D problem in cylindrical coordinates. Since there are no source terms in the θ-momentum equation, there is only the trivial solution and $V_{i\theta}$ and $V_{n\theta}$ are zero everywhere. As mentioned earlier, the plane of investigation is the plane in which θ is zero.

We can also assume that the flow is axisymmetric. This removes the theta momentum equation, simplifies the flux term across the θ-normal face, and reduces the equations. The pressure terms found by taking the surface integral over the θ-normal surfaces create effectively a source term, which are included in the G term.

The new conserve quantities, flux terms, and source terms for the axisymmetric finite volume heavy particle analysis appear in Equ. 5-23.

$$U=\begin{pmatrix} n_i \\ n_n \\ n_iV_{iz} \\ n_iV_{ir} \\ n_nV_{nz} \\ n_nV_{nr} \end{pmatrix}, F_1=\begin{pmatrix} n_iV_{iz} \\ n_nV_{nz} \\ n_iV_{iz}^{\ 2}+\dfrac{P_i}{M_i} \\ n_iV_{iz}V_{ir} \\ n_nV_{nz}^{\ 2}+\dfrac{P_n}{M_i} \\ n_nV_{nz}V_{nr} \end{pmatrix}, F_2=\begin{pmatrix} n_iV_{ir} \\ n_nV_{nr} \\ n_iV_{iz}V_{ir} \\ n_iV_{ir}^{\ 2}+\dfrac{P_i}{M_i} \\ n_nV_{nz}V_{nr} \\ n_nV_{nr}^{\ 2}+\dfrac{P_n}{M_i} \end{pmatrix}, G=\begin{pmatrix} \langle Q_{i,n}V_e\rangle n_in_n \\ -\langle Q_{i,n}V_e\rangle n_in_n \\ \dfrac{en_i}{M_i}E_z+\langle Q_{i,n}V_e\rangle n_in_nV_{MTz} \\ \dfrac{en_i}{M_i}E_r+\dfrac{P_i}{r_cM_i}+\langle Q_{i,n}V_e\rangle n_in_nV_{MTr} \\ -\langle Q_{i,n}V_e\rangle n_in_nV_{MTz} \\ \dfrac{P_n}{r_cM_i}-\langle Q_{i,n}V_e\rangle n_in_nV_{MTr} \end{pmatrix} \tag{5-23}$$

5.4.3 Numerical Method

A predictor-corrector setup is used in this analysis. This method calculates the time derivative in the Taylor expansion (Equ. 5-4) at a half time step and then the entire time step is completed using the half-values. This can be seen in Equ. 5-24.

$$U_{n+1/2} = U_n + \frac{\Delta t}{2}\left(-\frac{1}{\Delta z}\sum F_1 \cdot \hat{e}_z - \frac{1}{r_c \Delta r}\sum rF_2 \cdot \hat{e}_r + G \right)_n$$
$$U_{n+1} = U_n + \Delta t\left(-\frac{1}{\Delta z}\sum F_1 \cdot \hat{e}_z - \frac{1}{r_c \Delta r}\sum rF_2 \cdot \hat{e}_r + G \right)_{n+1/2} \qquad \textbf{(5-24)}$$

The time step is determined by the CLF (Courant, Friedrichs, and Lewy) condition. That is to say, the time step is less than the cell length divided by the characteristic wave speed. This prevents a wave from passing two adjacent grid points in one time step.

These experimental data are interpolated to create a cell size of 0.5 mm square. Near the wall, the radial length of the cells is increased to 2.95 mm. This is dictated by the resolution and location of these experimental data.

An upwind differencing technique is used in this time-marching technique. This approach is appropriate since the ions are supersonic in the great majority of the flow field. The upwind differencing technique has the added benefit of adding implicit dissipation in order to control numerical instability. This implicit dissipation is especially useful due to the nature of this application. These experimental data can be very irregular causing stability to be the key concern for such a problem. These experimental data receive a 3-point box smoothing before it is inputted into the numerical code.

Because of the stability issues associated with this problem, the highly dissipative Lax-Friedrich Method is also tested. While this method is extremely stable the dampening is too great to achieve meaningful results.

5.4.4 Boundary Conditions

The boundary conditions are assigned as follows. From 0-38 mm axially, the discharge channel walls are treated as normal walls with zero flux. The wall pressure is assigned assuming a zero radial gradient in number density.

Beyond 38 mm axially, ions and neutrals are allowed to cross the radial faces. A constant gradient exit boundary condition is used. Therefore, the spatial derivatives are constant and values are extrapolated to the boundaries.

At the anode, the entering flow is assumed to have an ionization fraction of zero with a uniform neutral density and velocity. The radial neutral and ion velocity are set to zero and the axial velocities are dictated by the half-Maxwellian function. The neutral number density at the anode is found by solving the continuity equation. The ion temperature is 0.1 eV[154] and the neutral temperature is 850 K[110] everywhere in the flow.

5.4.5 Initializations

The ion and neutral velocities and number densities are initialized in order to accelerate convergence of the numerical code. The neutral and ion radial velocity is set equal to zero and the axial neutral velocity is set to be constant and equal to the anode velocity. The ion number density is known from the Langmuir probe measurements.

Axial ion velocity is calculated from a simple one-dimensional energy equation. All ions are assumed to start at 10 mm from the anode with a uniform velocity given by the half-Maxwellian. As the ions move axially downstream, they fall though the acceleration zone and gain the kinetic energy form the potential drop. A simple equation explaining the initialization is shown in Equ. 5-2. In this equation V_{iz} is the axially directed ion velocity and V_p is the plasma potential.

Neutral number density is initialized by solving the neutral and ion continuity equation, assuming the radial velocities are equal to zero and the neutral velocity is constant. This method simply solves the one-dimensional heavy particle continuity equation (Equ. 5-25).

$$n_{n,i,j} = \frac{1}{V_{nz,i,j}}\left(n_i V_{iz}\big|_{i-1,j} + n_n V_{nz}\big|_{i-1,j} - n_i V_{iz}\big|_{i,j} \right) \tag{5-25}$$

5.4.6 Assumptions

5.4.6.1 Ionization Rate Source Term

As discussed before, the flow field is solved using Equs. 5-23 and 5-24. However, there is one feature that is handled a bit differently. Since the ion number density is known from the experimental results, the ion continuity can be solved separately in order to calculate the ionization rate source term prior to every iteration. In Equ. 5-5, the time derivative is canceled and the remaining equation is rearranged to solve for ionization rate as shown in Equ. 5-26.

$$\left\langle Q_{i,n} V_e \right\rangle n_i n_n = \frac{1}{\Delta z} \sum n_i V_{iz} \cdot \hat{e}_z + \frac{1}{r_c \Delta r} \sum r n_i V_{ir} \cdot \hat{e}_r \tag{5-26}$$

5.4.6.2 Ion Number Density Modification

One of the plasma properties with the largest experimental error is ion number density (±60%). Since the same probe takes all experimental measurements, relative trends in the ion number density are expected to be much more accurate than the absolute trends. This is also a concern because ion number density is the only conserved quantity that is not determined from the continuity and momentum equations. As a correction for this error, the beam current is monitored downstream of the acceleration region and the ion number density is multiplied by a constant in order to make the maximum beam current equal a specified value. The target beam current is calculated using Equ. 5-27. In this equation, anode flow rate is specified during thruster operation. The propellant utilization is assumed to be 90 and 85% for xenon and krypton, respectively (see Section 3.4.3.5). The ion species fraction are assumed to be 93/6/1% for Xe^{+1}, Xe^{+2}, and Xe^{+3} and 97/3% for Kr^{+1} and Kr^{+2}, respectively (see Section 3.4.3.3).[158]

$$I_b = \frac{\dot{m}_a \eta_p e}{M_i} \frac{1}{\sum \Omega_i / Z_i} \tag{5-27}$$

5.4.6.3 Radial Electric Field

The radial electric field is assumed to be equal to zero. The radial electric field, while important, is poorly captured by the internal emissive probe results. The internal emissive probe only takes 5 axial sweeps with 5 mm spacing. This is insufficient to capture the complex behavior inside the discharge channel and the radial electric field measurements are too sparse for use in the numerical code.

5.4.6.4 Momentum Transfer Due to Ionization/Recombination

One of the most difficult parts of this analysis is the momentum transfer due to ionization/recombination reactions. In a normal computational model, the ionization process can be captured in a number of ways and the physics associated with recombination can be neglected since it is highly unlikely to occur internal to the Hall thruster and in the thruster plume. However, in the case where ionization is determined through experimental measurements and given the noise associated with experimental measurements, momentum exchange during ionization/recombination can be a significant contributor to error in this numerical analysis.

When an ionization/recombination occurs, not only does the heavy particle change species, it also transfers its momentum to the new species. In most computational models that use a fluid approach to study Hall thrusters,[124,148,149,154,159,160] the momentum transfer due to ionization is equal to the momentum transfer from one neutral particle. In the case of recombination, the momentum of one ion should be subtracted from the ion fluid and added to the neutral fluid. This matter is further complicated since the degree of elasticity in these ionization/recombination collisions is not clear.

Much of this recombination is probably unphysical; however it can cause unusual behavior in the flow. If the ionization rate is too high in a region downstream of the acceleration zone, the ion fluid will gain a significant number of low-speed ions resulting in low bulk ion velocity, which is not observed in the RPA measurements. When recombination occurs, the neutral fluid can gain significant momentum and reach unrealistically high velocities. However, experiments have shown that the neutral velocities increase through the discharge channel.[80,161]

The goal of this analysis is to arrive at reasonable estimates of neutral number density and ionization rate. For this reason, it is essential to model the ion and neutral velocities as accurately as possible. This unusual numerical problem requires an unconventional solution to prevent the solution from blowing up. To address this problem, the momentum exchange during recombination and ionization downstream of the acceleration zone are ignored.

This is an inconsistency in the code that must be pointed out to the reader. However, given the peculiarity of the problem, such steps must be taken to arrive at reasonable results. With this said, the electric field source term is orders of magnitude larger than the momentum exchange due to collisions. This suggests that the solution will be approximately correct.

5.4.7 Discussion of Results

The two major goals of this analysis are to calculate the ionization rate and neutral number density. An overview and discussion of these results will be given below. All of the results are shown for 500-V xenon operation with the trim coil (Point 4).

5.4.7.1 Ionization Rate

The ionization rate as calculated by Equ. 5-26 can be seen in Figure 5-5. Figure 5-5 show a high ionization rate at the beginning of the acceleration zone in the Hall current region. Upstream of this region, no discernable trends can be seen. One unusual result is the region of recombination on the downstream side of the acceleration zone. There is a thin region of high recombination beginning around 40 mm and a weak recombination in the center of the investigated region, which continues to past 65 mm.

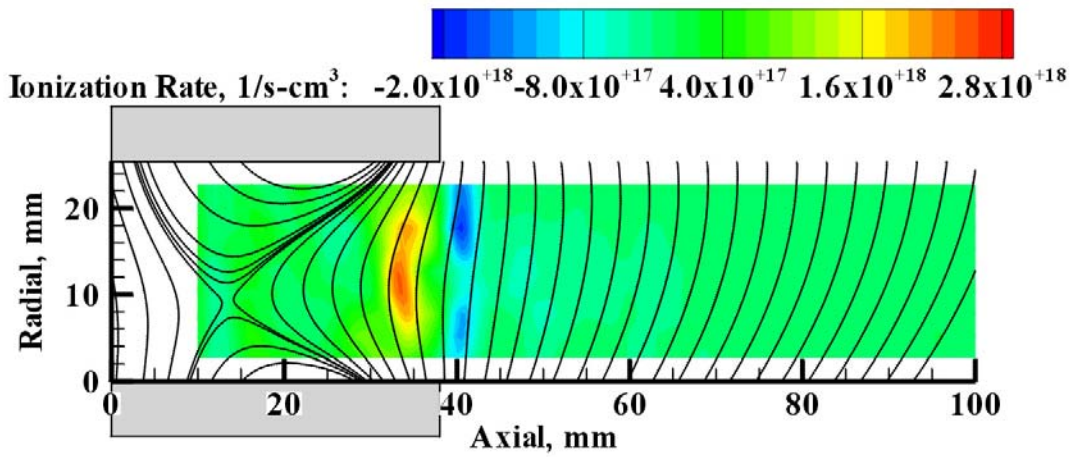

Figure 5-5. Ionization Rate from the Numerical Model

The most likely cause of this behavior is due to probe heating internal to the Hall thruster. This would result in electron emissions and would appear to be an increase in ion current. This would result in over-prediction of ion number densities inside the discharge channel. To account for the drop in ion number densities, there must be a region of recombination downstream of the acceleration zone. A comparison of floating potential measurements from emissive and Langmuir probes indicate that electron emission from the probe is small. Although the electron emission will remain small below temperatures of 2700 K, the ion saturation current can be significantly altered at tungsten temperatures as low as 2000 K.

Another possible cause of this recombination zone is due to misalignment in the probe measurements. The ion number density appears to be shifted too far down stream. This could be caused by imperfect spatial resolution in these probe data or due to shifting in the chamber during pump down. However, this is difficult to prove since any significant misalignment would have resulted in probe collision with the thruster and instant experiment failure. Also, many trends in these experimental data match up almost perfectly in the Langmuir probe and emissive probe measurements. As a check for this hypothesis, the ion number density is shifted 5 mm upstream and the shifted properties are input into the numerical code. The ionization zone calculated from the shifted ion number density is shown in Figure 5-6.

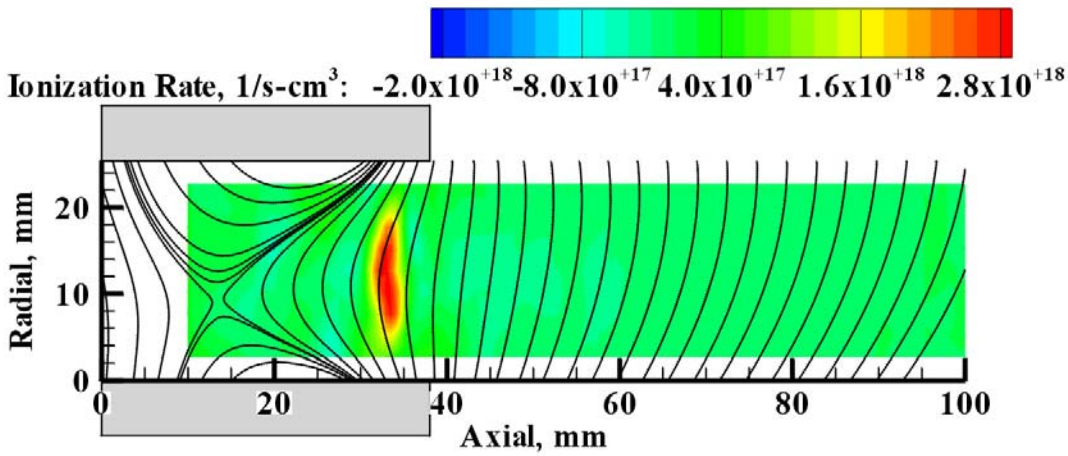

Figure 5-6. Ionization Rate from the Numerical Model with 5 mm Shifted Ion Number Density

With the ion number density shifted, the region of high recombination disappears. Another important result is that although the recombination region disappears, shifting of these data has almost no effect on the location of the calculated ionization. Although subtle, the weak recombination, which extends to 65 mm downstream, can still be observed even with these shifted data. Since the likelihood of recombination is very small, this observed behavior is probably CEX collisions. The CEX mean free path of ions can range from a few centimeters to tens of centimeters throughout the investigated region. This collision type is highly likely in this region and this could explain the increased neutral velocity observed in laser-induced fluoresence measurements.[80,161] It is suggested that the neutral velocity increases due to the depletion of low velocity neutrals which increases the average neutral velocity. However, the CEX collision is another plausible mechanism for neutral acceleration and strongly supported by these results.

The main goal of this investigation is to find the ionization region, and Figure 5-6 shows that this is possible without shifting these experimental data. The region of high ionization is the same regardless of the spatial shift. With this said, the complete discussion of the ionization zone will be reserved until Section 5.6.2.

5.4.7.2 Neutral Number Density

The neutral number density calculated from the numerical model for the 500-V xenon case with xenon is shown in Figure 5-7. As expected, the neutral density is depleted in the region of high ionization. However, these results show that due to the high recombination rate region, the neutral number density climbs extremely quickly at the end of the acceleration region. While the recombination region did relatively little damage to the ionization rate analysis, the neutral number density is too irregular to be physical and has limited use in future analyses.

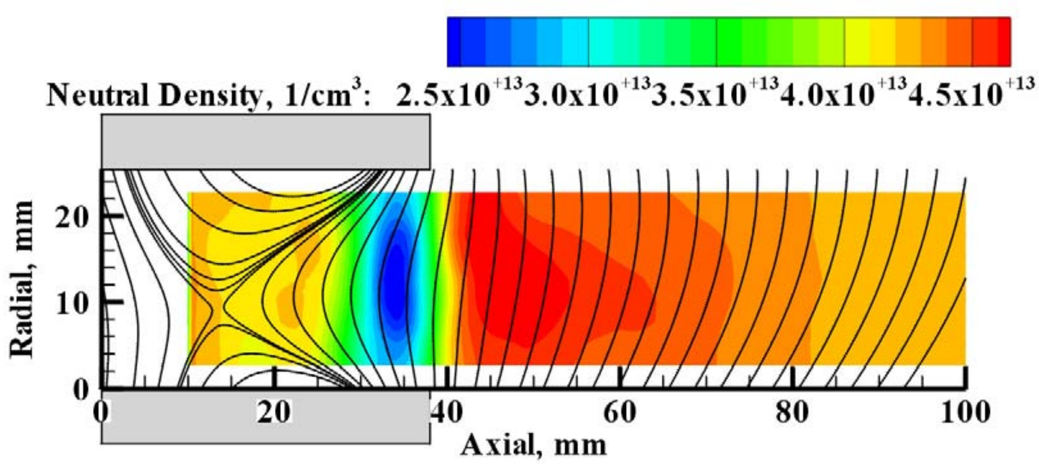

Figure 5-7. Neutral Number Density Calculated from the Numerical Model

As a point of reference, let's compare these neutral density results to the simple one-dimensional heavy particle continuity analysis used to initialize the neutral number density (Equ. 5-25). Figure 5-8 shows the results from the one-dimensional neutral density calculation. Similar to the neutral density results from the numerical model; this predicts a large depletion of ions in the Hall current region. Continuing downstream, the neutral number density again increases suggesting that recombination is occurring and that CEX collisions are significant in this problem.

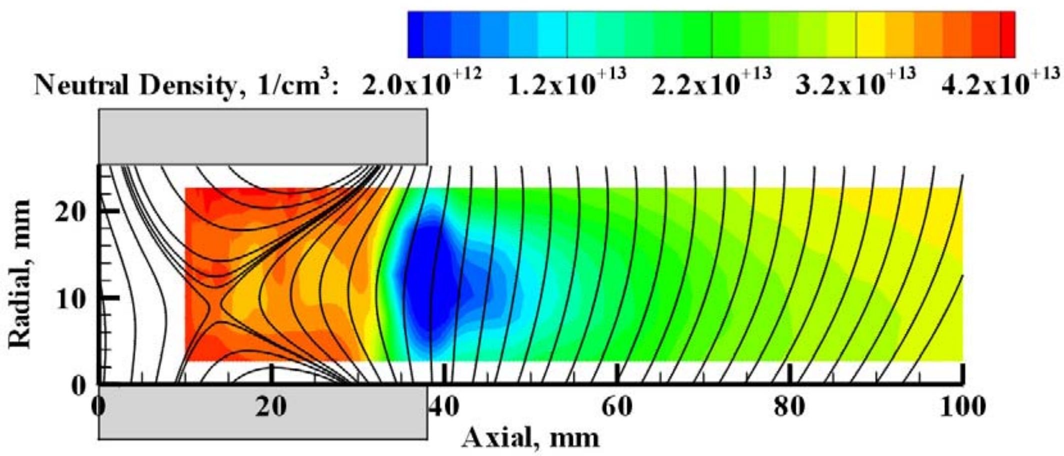

Figure 5-8. Neutral Number Density Calculated from the 1-Dimensional Analysis

Although less robust than a full numerical model, the one-dimensional neutral number density calculation makes more physical sense and produces relatively accurate result. Although the neutral velocity is expected to increase as neutrals moves farther downstream, the assumption of constant velocity can't be avoided. For some of the analyses, which appear later in this chapter, neutral number density from this one-dimensional method will be employed.

5.4.8 Evaluation of the Model

The use of a numerical model that uses experimental measurements in combination with hydrodynamic equations is a progressive step in the analysis of internal Hall thruster phenomena. However, the use of experimental data with margins of error and experimental uncertainty create several complications.

The greatest difficulty is in the stability of the code. These experimental data are noisy by nature. This noise and uncertainty drives the numerical model to be highly unstable and effectively poisons the code. Only by using a dissipative technique, carefully selecting grid spacing and time steps, and by carefully monitoring these experimental data, is it possible to reach convergence.

Since experimental data drives the numerical code, failure to capture all of the physics inside the discharge channel can yield results that are difficult to explain. Particularly, there is a whole host of complex collisions that are insufficiently captured by the code.

The data resolution that internal experimental measurement can capture is relatively very sparse. At best, the data resolution can only be on the order of a few millimeters, which is too large for the numerical model. Particularly near the discharge channel walls this is a problem. The boundary conditions near the wall are poorly captured and can result in errors in the code. Furthermore, probe measurements can only be taken within approximately 10 mm of the anode. There can be a great deal occurring inside this upstream region, which cannot be captured by the code.

In conclusion, with the large error and perturbation to the thruster the experimental error may be too flawed to apply such an exact analysis. This method may be too ambitious because the exact analysis can only be as good as these experimental data and the stability of the numerical algorithm. Flaws in these experimental data can produce unusual behaviors that are not necessarily physical. A better plan of attack may be to use these experimental data as convergence criteria in a normal Hall thruster computational code. It may also be possible to solve the energy equation using experimental data while leaving ion number density unspecified to be solved by the code. This would require an additional equation to include the effect of the CEX collisions and ionization. The ionization rate can be calculated as a function of electron temperature. Although the current method is not perfect, several interesting trends could be observed that can help to improve understanding of internal discharge channel physics.

5.5 Electron Motion

At this time, internal electron behavior is one of the greatest mysteries in Hall thruster physics. This section will address this electron motion by using a combination of experimental results and theory to study this phenomenon.

5.5.1 Fluid Equations of Motion

For this analysis a fluid description of the electron motion inside the discharge channel is used. A rough criterion for the importance of single particle effects as opposed to collective effects is the plasma parameter (Equ. 5-28). For the plasma typical for a Hall thruster discharge channel, the plasma parameter is approximately 2×10^5. Therefore, the fluid description is selected since the single particle effects are much less important than the bulk plasma trends. King has done interesting work focusing on the single particle electron dynamics inside the NASA-173Mv1.[162]

$$\Lambda = \frac{4}{3}\pi n_i \lambda_D{}^3 \approx \frac{\omega_e}{\nu_c} \tag{5-28}$$

Let us begin with the electron fluid momentum equation shown in Equ. 5-29.[163] Before continuing, it is assumed that the bulk electron motion is in steady state and the inertial term can be neglected. The four terms that remain on the right hand side of the equation are the contribution due to the Lorentz force, the electron pressure term, and the momentum exchange due to collisions. The curvature drift can be included in this analysis by adding a centrifugal force term to the right hand side of the fluid equation of motion.[163] However, the centrifugal force is negligibly small in this analysis. The grad-B drift and the nonuniform electric field drift are more difficult to address in the fluid plasma description. These drifts will be discussed in Section 5.5.4 and both are found to be negligibly small.

$$m_e n_e \left(\frac{d\vec{V}_e}{dt} + \left(\vec{V}_e \cdot \nabla\right)\vec{V}_e \right) = -en_e\left(\vec{E} + \vec{V}_e \times \vec{B}\right) - \nabla(P_e) - m_e n_e \vec{V}_e \nu_{e,\,tot} \tag{5-29}$$

In Equ. 5-29, P_e is the electron pressure and is given in Equ. 5-30. In the collision term, the heavy particle velocity is assumed to be negligible compared to the electron velocity, and $\nu_{e,tot}$ is the total momentum exchange collision frequency.

$$P_e = n_e k_B T_e \tag{5-30}$$

In order to simplify the electron motion analysis, the coordinate systems is changed to be relative to the magnetic field lines. This transformation can be seen in

Figure 5-9 and described by Equs. 5-31 and 5-32. In these equations, the *i*-direction is perpendicular to the magnetic field, the *j*-direction is parallel to the magnetic field, and the *k*-direction is in the azimuthal direction. Also in these equations, ϕ is the angle of rotation.

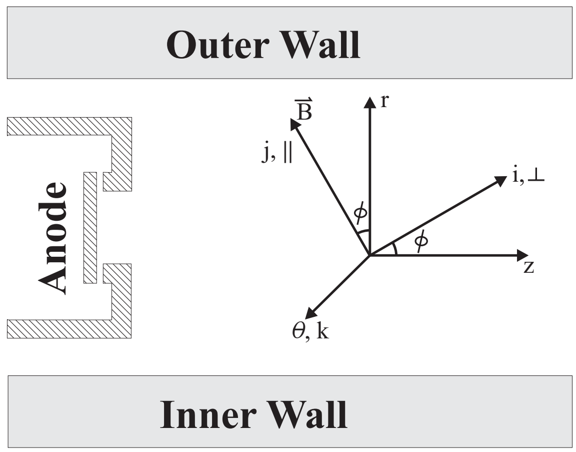

Figure 5-9. Coordinate Transfer Relative to the Magnetic Field

$$\begin{pmatrix} \hat{e}_i \\ \hat{e}_j \\ \hat{e}_k \end{pmatrix} = \begin{bmatrix} \cos\phi & \sin\phi & 0 \\ -\sin\phi & \cos\phi & 0 \\ 0 & 0 & 1 \end{bmatrix} \begin{pmatrix} \hat{e}_z \\ \hat{e}_r \\ \hat{e}_\theta \end{pmatrix} = \overline{\overline{T}} \begin{pmatrix} \hat{e}_z \\ \hat{e}_r \\ \hat{e}_\theta \end{pmatrix} \tag{5-31}$$

$$\tan\phi = \frac{B_z}{B_r} \tag{5-32}$$

Now we are able to rewrite Equ. 5-29 into its separate components as shown in Equs. 5-33 to 5-35. For this analysis, the azimuthal component of magnetic field is negligible and the plasma is assumed to be axisymmetric. The last term on the right hand side of Equ. 5-34 is the effect of the magnetic mirror.[149,164]

i:
$$0 = -en_e E_i + en_e V_{ek} B - \frac{\partial P_e}{\partial i} - m_e n_e V_{ei} \nu_{e,tot} \tag{5-33}$$

j: $$0 = -en_e E_j - \frac{\partial P_e}{\partial j} - m_e n_e V_{ej} \nu_{e,tot} - \frac{n_e k_B T_e}{B}\frac{\partial B}{\partial j} \tag{5-34}$$

k: $$0 = -en_e V_{ei} B - m_e n_e V_{ek} \nu_{e,tot} \tag{5-35}$$

At this point we will introduce several new parameters. The electron cyclotron frequency and the Hall parameter are given and Equs. 5-36 and 5-37, respectively. Where ω_c is in units of Hz and B is in units of gauss. The definitions of mobility appears in Equ. 5-38 and the definition of diffusivity appears in Equ. 5-39. The classical electron mobility and classical electron diffusivity perpendicular to the magnetic field lines appears in Equs. 5-40 and 5-41, respectively.

$$\omega_c = \frac{eB}{m_e} = 2.8 \times 10^6 B \left[\frac{1}{s}\right] \tag{5-36}$$

$$\Omega_e = \frac{\omega_c}{\nu_{e,tot}} \tag{5-37}$$

$$\mu = \frac{e}{\nu_{e,tot} m_e} \tag{5-38}$$

$$D = \frac{k_B T_e}{\nu_{e,tot} m_e} \tag{5-39}$$

$$\mu_\perp = \mu\left(\frac{1}{1+\Omega_e^{\ 2}}\right) \tag{5-40}$$

$$D_\perp = D\left(\frac{1}{1+\Omega_e^{\ 2}}\right) \tag{5-41}$$

Now we are able to solving Equs. 5-33 to 5-35 for electron velocity. The electron pressure term is expanded using Equ. 5-30 and electrons are assumed to be isothermal along the magnetic field streamlines. The electron velocities for each direction are given in Equs. 5-42 to 5-44. For clarity, the *i* and *j* subscripts have been replaced by perpendicular and parallel symbols, respectively. These equations will be used in the following sections, but before moving on each of these equations will be discussed briefly.

i:

$$V_{e\perp} = -\mu_\perp E_\perp - \frac{D_\perp}{n_e}\frac{\partial n_e}{\partial x_\perp} - \frac{D_\perp}{T_e}\frac{\partial T_e}{\partial x_\perp} \qquad \textbf{(5-42)}$$

j:

$$V_{e\|} = -\mu E_\| - D\frac{\nabla_\| n_e}{n_e} - D\frac{\nabla_\| B}{B} \qquad \textbf{(5-43)}$$

k:

$$V_{ek} = \frac{\Omega_e^{\,2}}{1+\Omega_e^{\,2}}\left(\frac{E_\perp}{B} + \frac{k_B T_e}{eBn_e}\frac{\partial n_e}{\partial x_\perp} + \frac{k_B}{eB}\frac{\partial T_e}{\partial x_\perp}\right) \qquad \textbf{(5-44)}$$

The first equation (Equ. 5-42) is the electron velocity perpendicular to the magnetic field. Because of the reduced mobility across the field lines the mobility is highly dependent on the Hall parameter. The electrons should be trapped on the magnetic field lines and this behavior is observed with the internal Langmuir probe measurements.

The electron motion along the field lines (Equ. 5-43) is very different. The electrons move relatively freely due to a random diffusion process and a balance between the electric field, the pressure forces, and the magnetic mirror force. The mobility and diffusivity are much higher than the mobility across the field lines. With exception to the magnetic mirror force term, this is the classic form of the equation for unmagnetized electrons.

Equation 5-44 shows the electron velocity in the azimuthal direction. On the right hand side, the first term is the E×B drift and the second two terms are the diamagnetic drift. These drifts will be studied in Section 5.5.3.

5.5.2 Hall Parameter and Electron Mobility

The Hall parameter is one of the major values describing the electron motion inside a Hall thruster. By definition, the Hall parameter is a ratio between the electron cyclotron frequency and the total electron collision frequency (Equ. 5-37). Physically, the Hall Parameter characterizes the number of azimuthal orbits that an electron completes before undergoing a particle collision, which results in cross-field migration and eventually the loss of electrons to the anode.

It can be shown very easily from Equs. 5-42 and 5-44 that the Hall parameter is a ratio between the azimuthal and perpendicular electron velocities. This is shown in Equ. 5-45.

$$\Omega_e = -\frac{V_{e\theta}}{V_{e\perp}} \tag{5-45}$$

This electron cross-field migration is affected by any process that increases the electron mobility. A number of different electron transport mechanisms are commonly used by modelers to explain this complex phenomenon. In order to apply the summed effects of these mechanisms, an effective electron collision frequency can be modeled as shown by Equ. 5-46.

$$\nu_{e,tot} = \nu_{Classical} + \nu_{Wall} + \nu_{Bohm} \qquad \textbf{(5-46)}$$

The simplest form of electron mobility is called classical mobility. It can be inferred from Equs. 5-42 to 5-44 that without collisions, electrons would not be able do diffuse across magnetic field line and will continue to gyrate about their lines of force. However, when an electron undergoes a momentum transfer collision with a heavy particle it will begin a random-walk process with step sizes on the order of a Larmor radius. While logical and straight-forward, this process under-predicts the electron mobility inside the Hall thruster. Another phenomenon is necessary to explain the anomalous cross-field mobility.

One explanation of this anomalous behavior is Bohm mobility. The equation describing collisions due to Bohm mobility can be seen in Equ. 5-47. Bohm mobility stems from the turbulent fluctuations in the electric field and plasma density. This case is analogous to enhanced diffusion due to turbulent fluctuations in general fluids. Evidence of this anomalous Bohm mobility has observed experimentally[80] and is often necessarily imposed in order to match computational models to experimental results.

$$\nu_{Bohm} = \alpha_B \omega_c \qquad \textbf{(5-47)}$$

Typically the coefficient (α_B) used to model the Bohm collision frequency is 1/16. Obviously, this is a gross simplification of a complex problem and as it turns out enormously over-predicts the electron cross-field mobility in the acceleration zone. For this reason, this type of anomalous mobility is often only applied in specific regions of the Hall thruster model ("Mixed mobility" model)[140] and the typical value of 1/16 is modified.[165-167] Fife[166] found that a value of a coefficient of 1/107 yields the necessary amount of cross-field mobility and Ahedo[168] also found a value of 1/100 to be appropriate.

Another source of this anomalous cross-field electron transport is near-wall conductivity and was first proposed by Morozov.[134,169-171] This theory proposes that electron collisions with the walls enhance electron cross-field mobility and in this way the walls act like a macro-particle. This effect is enhanced due to high secondary electron emission from the walls and particularly in the case of space-charge saturated wall sheaths.[124,172] Due to the potential fall in the wall sheath and the low energy emitted electrons, the walls can act like gutters for electron cross-field mobility. There have been several investigations that suggest the importance of near-wall conductivity.[124,172-174] Unfortunately, these experimental data presented in this thesis are not well suited to study near-wall conductivity since the closest measurements are 2 mm from the wall.

In reality, the cross-field mobility is likely a combination of these effects and many modelers account for all of these electron transport mechanisms. In the following sections, the classical mobility will be measured as well as an experimentally determined mobility.

5.5.2.1 Classical Analysis

In the classical concept of cross-field electron mobility, electrons can cross magnetic fields when they undergo a momentum exchange collision. By far the predominant momentum exchange collision that occurs is between electrons and neutrals;[140] however, to a lesser degree electron-ion collisions can enhance electron mobility. The total momentum exchange collision frequency is equal to the sum of the electron-ion and electron-neutral as shown Equ. 5-48. Where in this equation, V_e is the electron velocity given in Equ. 5-49. The ion number density and neutral number density are known from the Langmuir probe measurements and the one-dimensional neutral number density calculation (Section 5.4.7.2).

$$\nu_{Classical} = \nu_{en} + \nu_{ei} = n_n \langle Q_{en} V_e \rangle + n_i \langle Q_{ei} V_e \rangle \quad (5\text{-}48)$$

$$V_e = \sqrt{\frac{8 k_B T_e}{\pi m_e}} \quad (5\text{-}49)$$

The collision cross-section for the electron-neutral momentum exchange is based on a number of accumulated references.[175-178] These combined measurements are merged and then used to define the collision cross-sections for this analysis. These merged data are shown in Figures 5-10 and 5-11 and the fit applied to these data points is used in the remainder of the analysis.

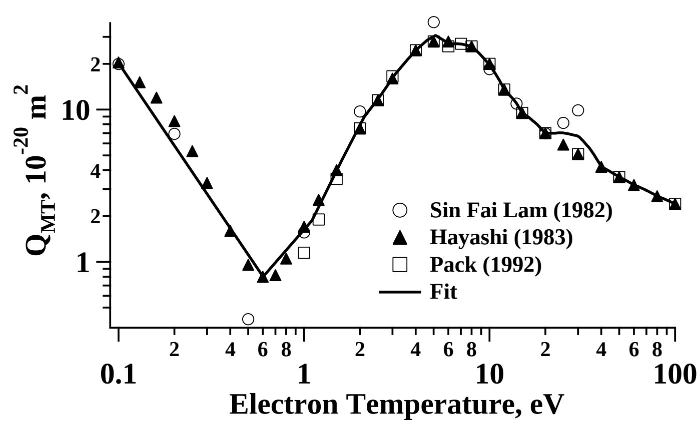

Figure 5-10. Electron-Neutral Momentum Exchange Collision Cross-Sections for Xenon

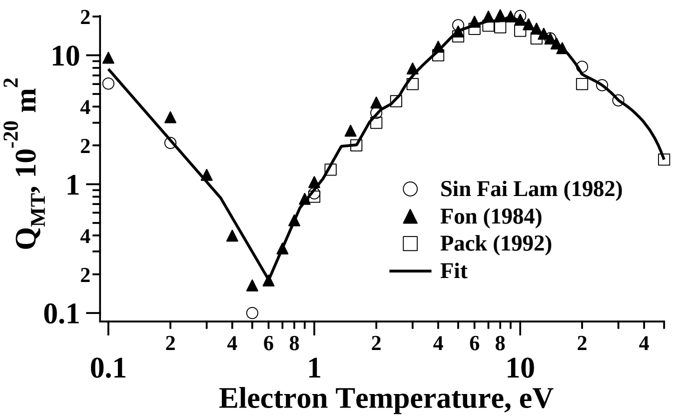

Figure 5-11. Electron-Neutral Momentum Exchange Collision Cross-Sections for Krypton

The electron-ion interaction is taken to be Coulombic and collision cross section and given by Equ. 5-50.[163] In this equation, Λ is the plasma parameter and is give in Equ. 5-28.

$$Q_{ei} = 2.988 \times 10^{-18} \frac{Z \ln \Lambda}{T_{eV}^{\ 2}} \left[m^2 \right] \tag{5-50}$$

5.5.2.2 Experimental Analysis

Assuming that the fluid description of the electron motion is appropriate, then Equs. 5-42 to 5-44 should tell everything about the electron motion inside the discharge channel. Almost all of the terms on the right hand side of the equations can be calculated from the experimental data and only one more assumption must be made to close these equations.

In order to close the equations the axial electron flow toward the anode is considered. It is assumed that the current density is uniform and the electron current is evenly distributed at each axial location in the discharge channel. Since the ion current density and the discharge current are known, the electron current can be estimated by Equ. 5-51. The ion velocity is easily calculated from a simple energy balance given in Equ. 5-2. This analysis is somewhat similar to the analysis conducted by Meezan et al.[80] Unfortunately, this assumption does not account for near wall conductivity.

$$J_{eZ}(z) = \frac{I_D - \int_{A_{ch}} e n_i V_{iz}\big|_z \, dA}{A_{ch}} \qquad (5\text{-}51)$$

5.5.2.3 Collision Rate Results

The collision rate for electron cross-field transport is measured with the classical approach using Equ. 5-48. The experimentally collision rate is determined by using Equ. 5-37 and the experimentally determined Hall Parameter. To illustrate some basic trends, the centerline collision rates for the 500-V xenon case with and without the trim coil and the 500-V krypton case with the trim coil can be seen in Figure 5-12.

The experimentally determined collision rate ranges mostly between 10^7 and 10^8 Hz although in the peak acceleration zone the collision rate drops to approximately 10^6 Hz. This range of collision frequency has also been observed in many computational codes.[140,168] The classical collision rate follows a similar shaped trend as the experimental collision rate although the classical collision rate is in the rage between 10^6-10^7 Hz in the bulk of the channel and hits a minimum of about 10^5 Hz in the acceleration zone. Again, this range in classical collision frequency is predicted by computational Hall thruster models.[58,139] These results also agree with Haas's experimental results.[58]

The Bohm collision rate has a very differently shaped trend as compared to the classical and experimental data and agreement is extremely poor in the acceleration zone.

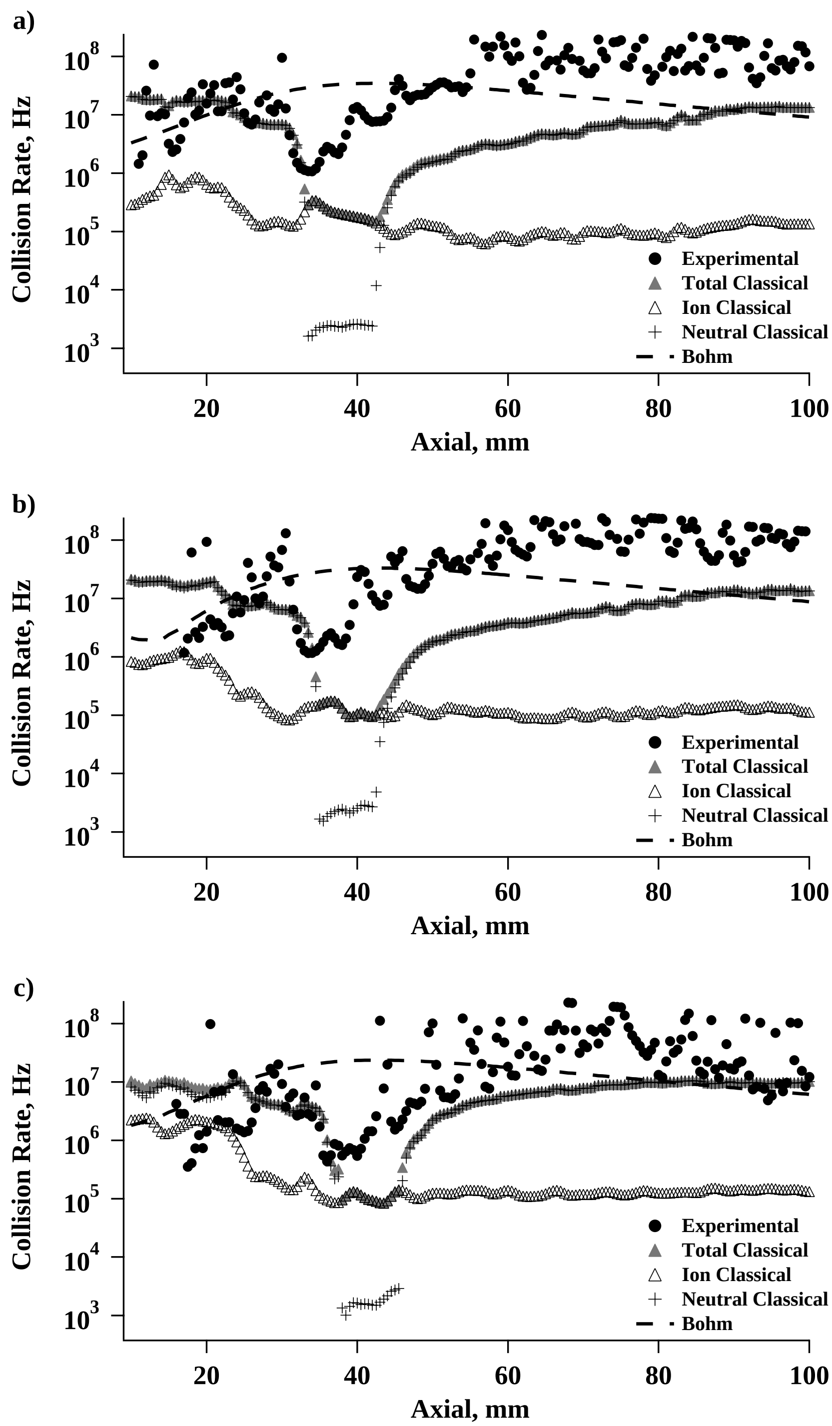

Figure 5-12. Centerline Collision Rates for the 500-V Xe and Kr Cases. a) 500-V xenon without the trim coil, b) 500-V xenon with the trim coil, and c) 500-V krypton with the trim coil.

The effect of the ion-electron collision rate is approximately one to two orders of magnitude smaller than the electron-neutral collision rate except in the Hall current region where there is a depletion of neutrals. This depletion is expected although it may be enhanced due to probe heating or poor alignment in experimental data and the use of a simple 1-D analysis to predict neutral number density.

Upstream of the acceleration zone, the experimental collision rate agrees well with both Bohm and classical collision rates. This is particularly true for case a), which does not use the trim coil and has predominantly radial the magnetic field. In the trim coil cases (b and c), the collision rates are slightly lower than either the Bohm or the classical collision rates. For the trim coil cases, the magnetic field lines are largely axial and the electron can move freely and few collisions are necessary for electron migration toward the anode. Near the exit of the thruster between 25 and 38 mm from the anode, the experimental collision rate seems to match the classical collision rate closely.

In the acceleration zone, the experimental collision rate is much lower, although classical collisions are insufficient to account for the electron mobility. The Bohm mobility is particularly poor in the acceleration zone and this illustrates the true weakness of the Bohm mobility assumption. Either a more robust description of the Bohm-like mobility is needed or the anomalous mobility in this region is due to near wall conductivity.

Downstream of the acceleration zone, the experimental mobility is greater than either the classical or the Bohm mobility alone. The downstream mobility is likely a combination of classical and Bohm-like effects.

5.5.2.4 Hall Parameter Results

The Hall parameter can be experimentally determined from Equ. 5-45. The perpendicular electron current is determined from Equ. 5-51 and transformed to the magnetic field coordinate system. The azimuthal electron velocity is determined from Equ. 5-44. Notice that the Hall parameter coefficient in this equation becomes completely negligible for Hall parameters greater than approximately 10. The classical Hall parameter can be determined from Equs. 5-37 and 5-48. The classical and experimental Hall parameters for the 500-V xenon and krypton cases can be seen mapped in Figures 5-13 and 5-14, respectively.

Both the experimental and classical Hall parameters follow a similar trend in shape although the classical Hall parameter under-predicts the electron mobility. The classical Hall parameter increases in the acceleration zone to a few thousand. The experimental Hall parameter peaks in the same location although it reaches a maximum of only a few hundred. These classical and experimental values are consistent with work done by Haas,[58] Choueiri,[139] and Meezan et al..[80]

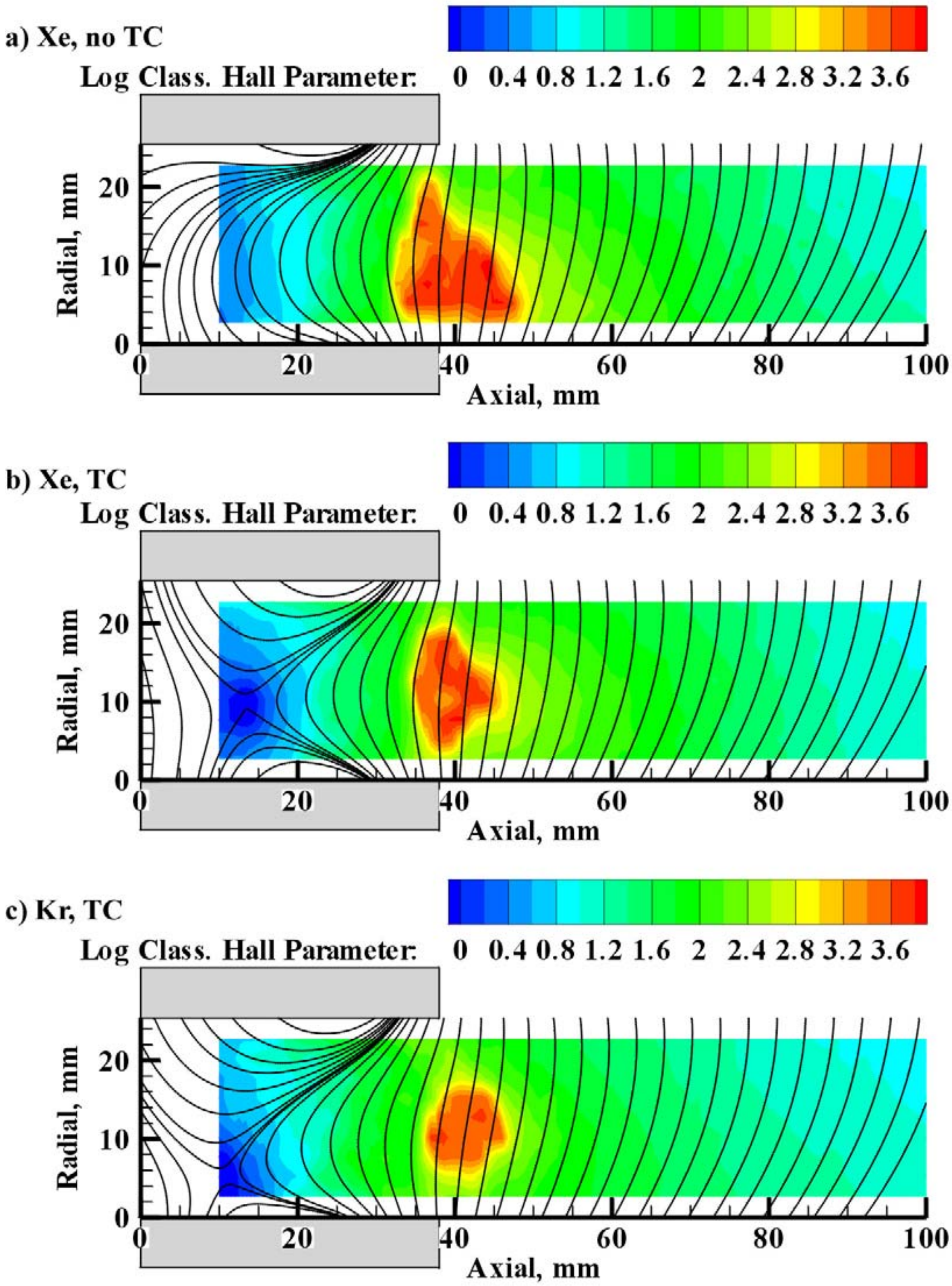

Figure 5-13. Classical Hall Parameter for the 500-V Xenon and Krypton Cases

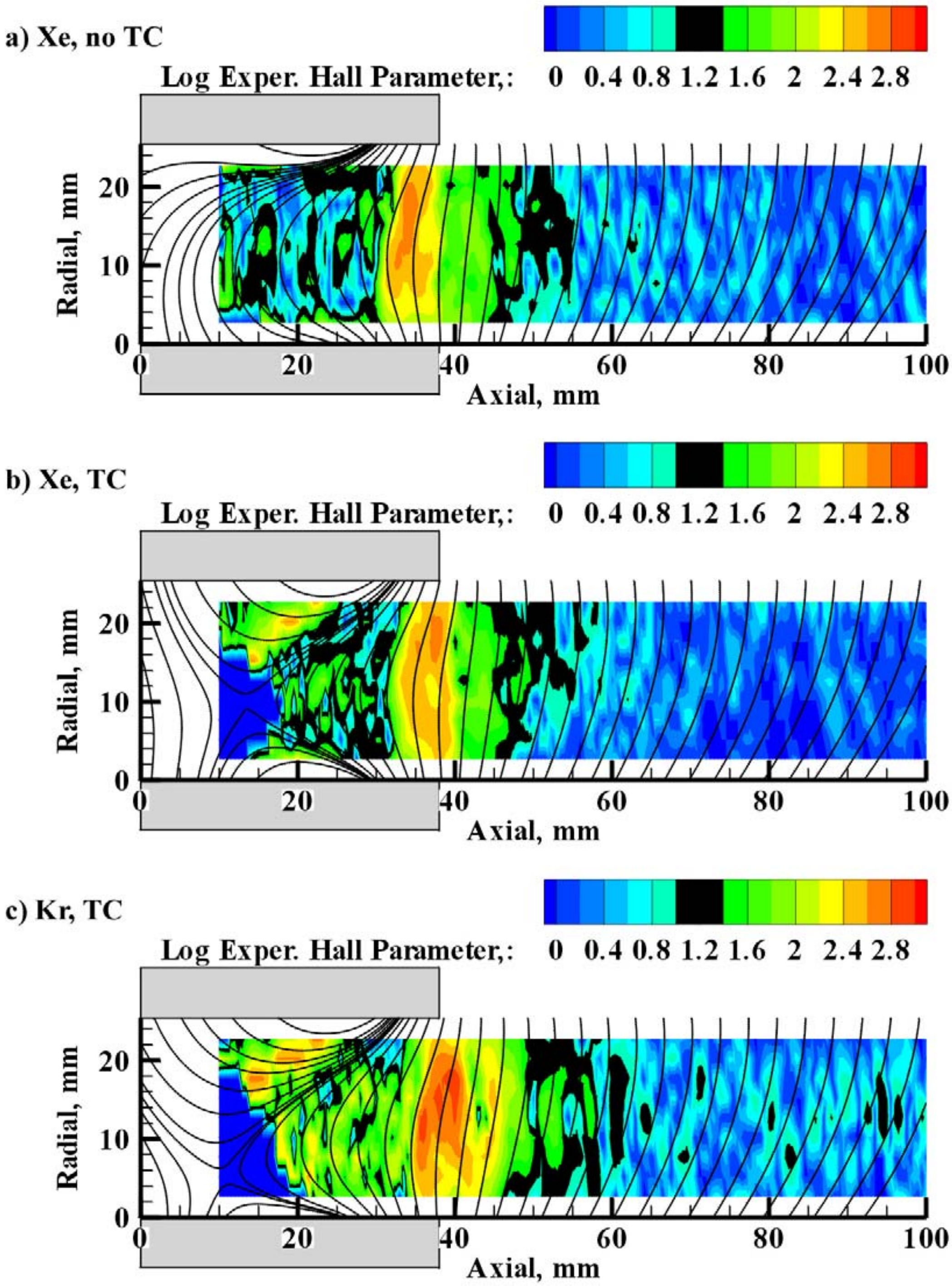

Figure 5-14. Experimental Hall Parameter for the 500-V Xenon and Krypton Cases

In the experimental Hall parameter contour plots, Bohm-like Hall parameter is outlined by the black bar. Bohm mobility appears to closely agree with the experimental

Hall parameter in the near anode region. In the downstream region, Bohm mobility alone is insufficient to predict the experimental Hall parameter.

It should be noted that in the upstream region of the trim coil cases, the plasma is unmagnetized so the azimuthal current is set to zero and the Hall parameter is set to one. This can be seen as the dark blue block on the upstream side of the Figure 5-14. These points with unmagnetized plasma are excluded from Figure 5-15.

More specific trends can be seen plotting the centerline Hall parameters and this is shown in Figure 5-15. In the near anode region the Hall parameter is on the order of tens and is approximately equal to both the Bohm and the classical Hall Parameters. Between approximately 25 and 38 mm, the experimental Hall parameter matches the classical value closely. In the Hall current region, the classical approach over-predicts the Hall parameter and the Bohm approach grossly under-predicts the Hall parameter. From approximately 55 mm on, in the downstream region, the experimental Hall parameter is less than 10. This suggests that a combination of classical and Bohm like mobility are required to match the experimental Hall parameter.

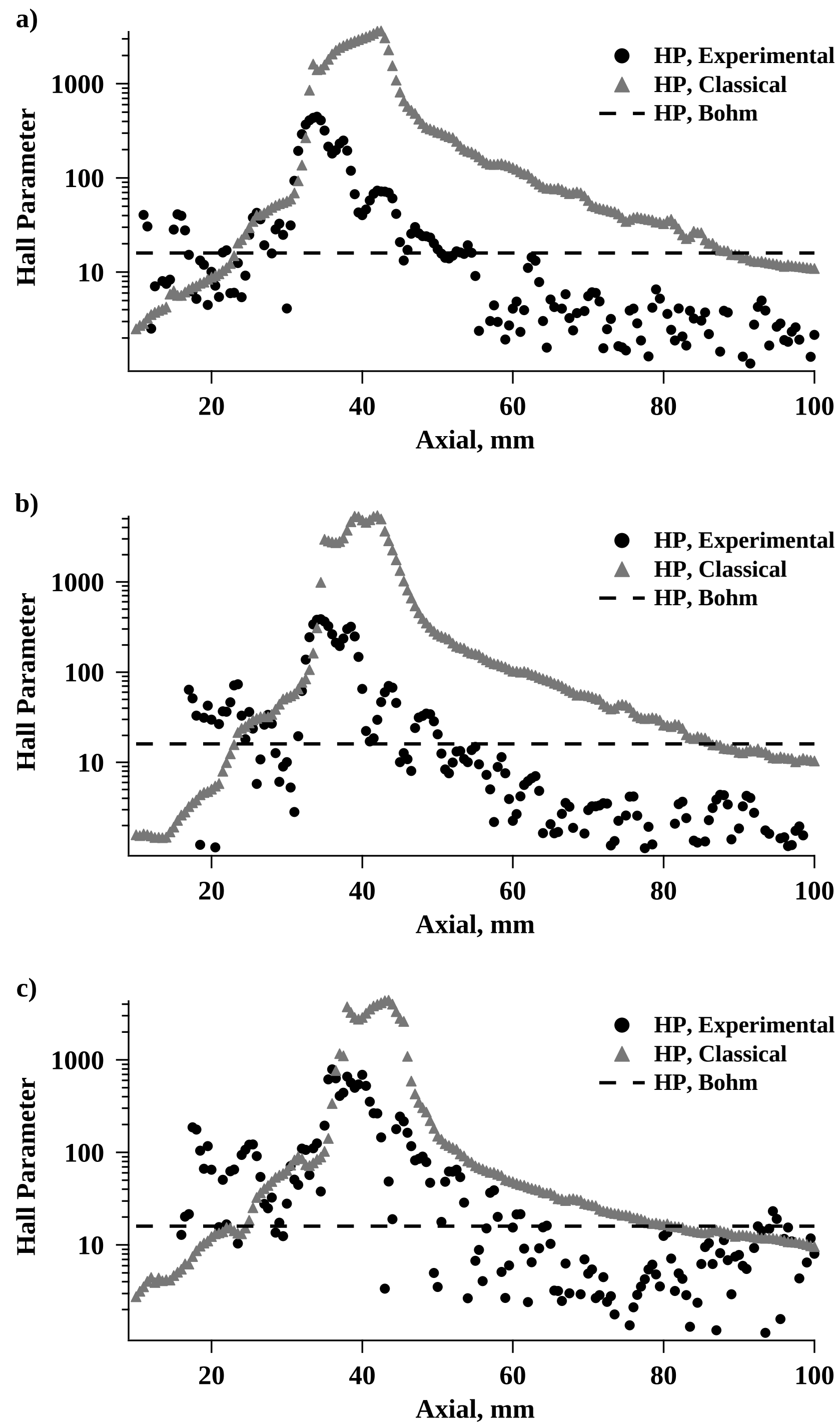

Figure 5-15. Centerline Hall Parameters for the 500-V Xenon and Krypton Cases. (a) 500-V xenon without the trim coil, b) 500-V xenon with the trim coil, and c) 500-V krypton with the trim coil)

Other researchers have studied Hall parameter using similar techniques with a range of different conclusions. Meezan et al.[80] found the Hall parameter to be close to classical near the anode where Haas[58] and Choueiri[139] found the near anode region to be closer to Bohm mobility. Meezan et al. suggest using a Bohm-like mobility at and downstream of the peak magnetic field region although by doing so, the model fails to capture the high Hall parameter region observed in their data. Although others suggest using a Bohm mobility in the downstream region.[139,147] Haas saw that classical mobility is closer to predicting the Hall parameter in the downstream of the acceleration zone.

5.5.2.5 Electron Mobility Results

With the classical collision frequency it is possible to calculate the mobility parallel and perpendicular to the magnetic field lines (Equs. 5-38 to 5-41). Since the electron mobility is really a tensor, it is necessary to transform the electron mobility from magnetic field coordinates to thruster coordinates. The transformation can be done by using Equ. 5-52. In this equation, the transformation matrix is given in Equ. 5-31. At this point the axial and radial mobility can be studied.

$$\overline{\overline{\mu}}_{Thruster} = \begin{bmatrix} \mu_z & \mu_{zr} & 0 \\ \mu_{rz} & \mu_r & 0 \\ 0 & 0 & \mu_\vartheta \end{bmatrix} = \overline{\overline{T}}^T \overline{\overline{\mu}}_B \overline{\overline{T}} = \overline{\overline{T}}^T \begin{bmatrix} \mu_\perp & 0 & 0 \\ 0 & \mu_\parallel & 0 \\ 0 & 0 & \mu_k \end{bmatrix} \overline{\overline{T}} \qquad \textbf{(5-52)}$$

Experimental values of axial, radial, and R-Z mobility are shown in Figures 5-16 to 5-18. The axial mobility is enhanced in the regions of axial magnetic fields and reaches a maximum on the order of 10^5-10^6 C-s-kg^{-1}. The R-Z mobility has peak values on the order of 10^5 C-s-kg^{-1}.

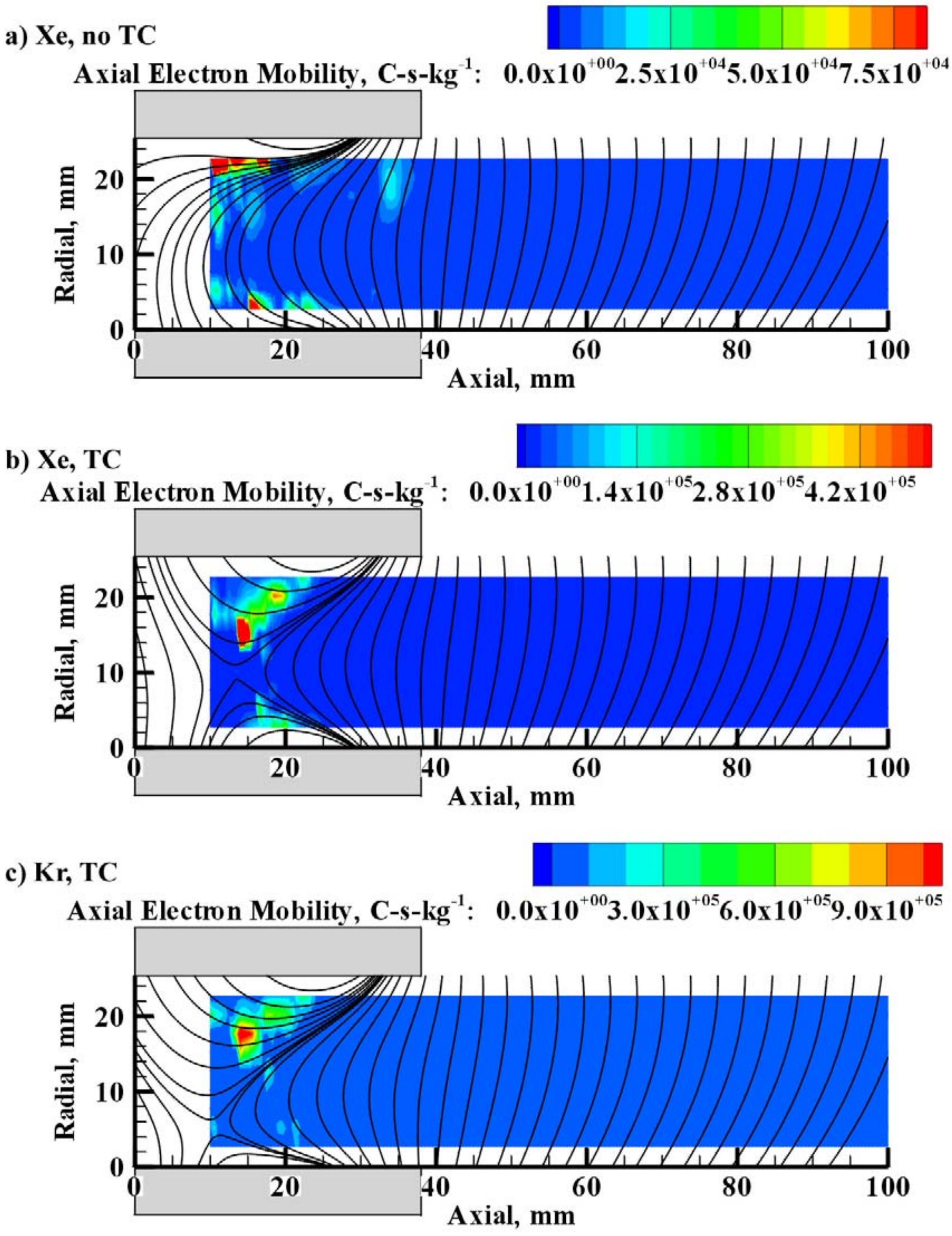

Figure 5-16. Axial Electron mobility for the 500-V Xenon and Krypton Cases

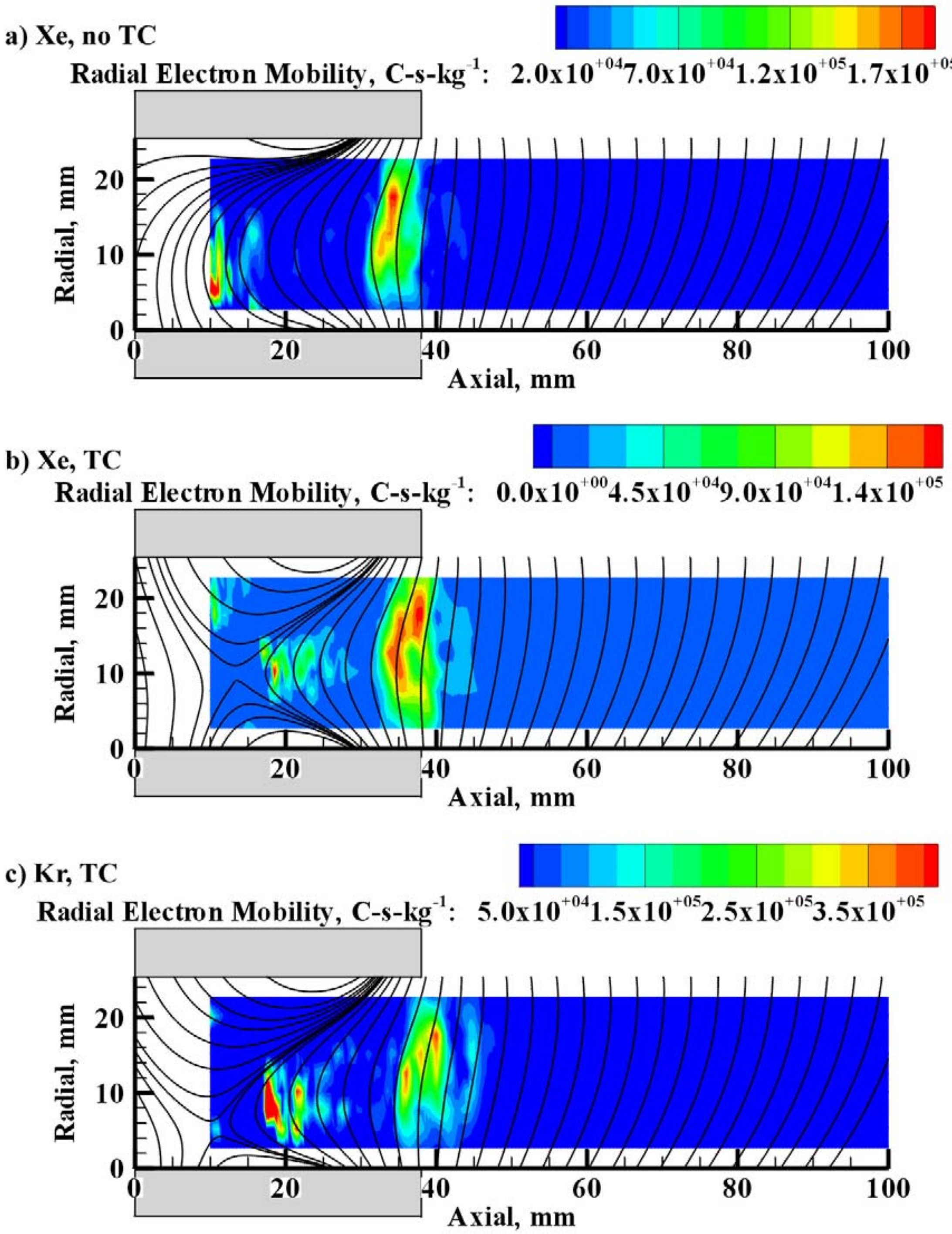

Figure 5-17. Radial Electron mobility for the 500-V Xenon and Krypton Cases

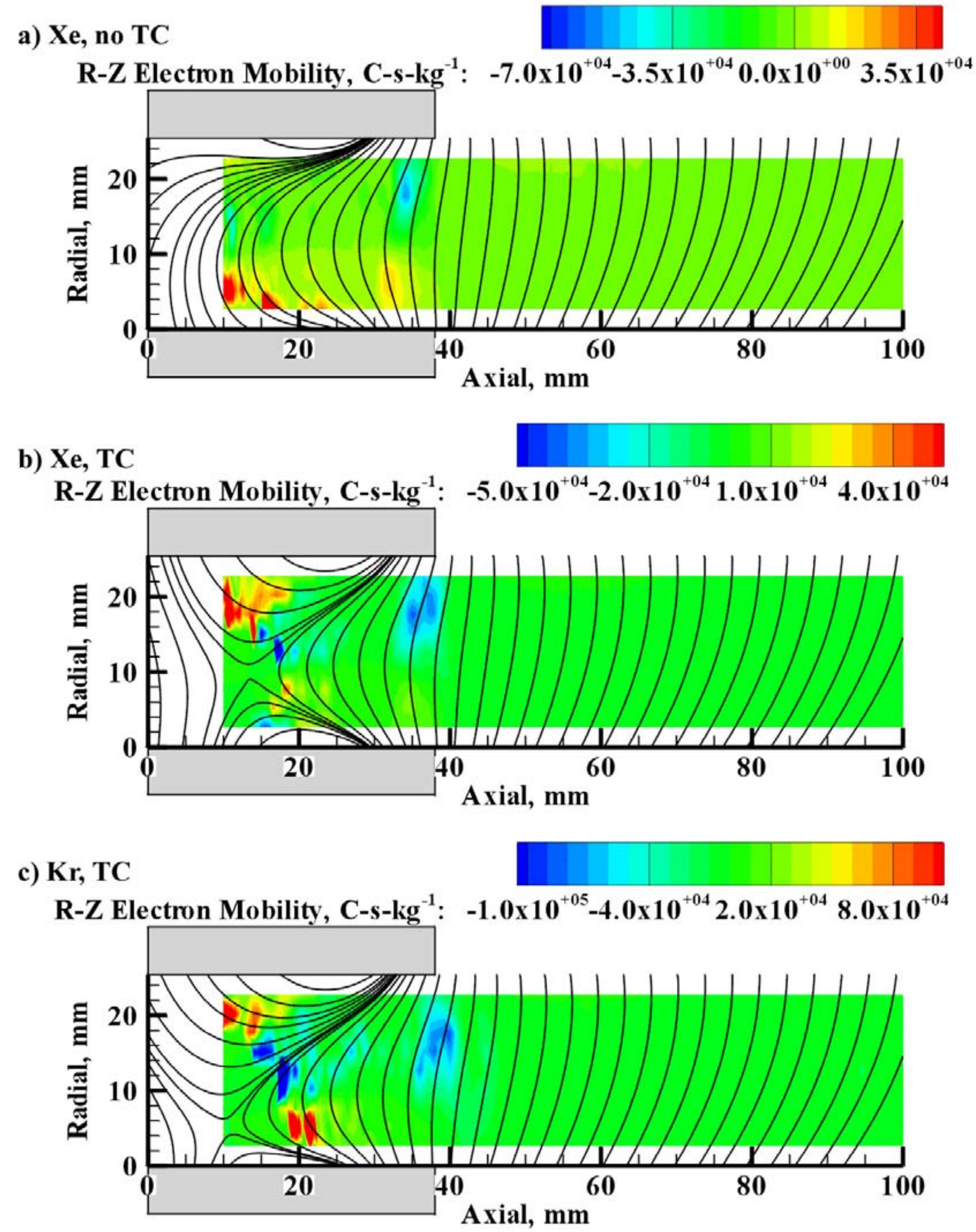

Figure 5-18. R-Z Electron mobility for the 500-V Xenon and Krypton Cases

The radial mobility reaches a maximum around 10^5 C-s-kg^{-1}. The radial mobility is highest in the region of high electron temperature and when the magnetic field lines are radial. This clearly illustrates where the electron-wall collision rate is highest. Notice that in the krypton case, this region of high radial mobility is largely outside the discharge channel. Hence, the near wall conductivity may be reduced for the krypton case.

5.5.3 Azimuthal Current

5.5.3.1 Electron Fluid Drifts

Equation 5-44 is used to describe the azimuthal electron velocity in the Hall thruster discharge channel. The azimuthal electron velocity can be broken into two components: the E×B drift and the diamagnetic drift. These velocities are converted into electron currents by assuming quasineutrality and multiplying the velocities times the ion number density and the elementary charge. The experimental Hall parameter is used in the coefficient of Equ. 5-44, although it is a very safe assumption to set this coefficient to one. Where the cyclotron radius is much smaller than the discharge channel width (r_c<15b), the electrons are considered to be unmagnetized and the azimuthal current is set to zero. A comparison of the relative importance of these electron drifts can be seen in Figure 5-19. These currents correspond to the 300-V xenon case with the trim coil (Point 2).

This figure shows that the E×B current is by far the most significant portion of the azimuthal current. The maximum diamagnetic current is approximately 20% of maximum E×B current. Therefore, the diamagnetic current is a second-order effect although it is still significant. Although the Hall current normally only refers to the E×B current, for the remainder of this thesis "total Hall current" will refer to the summed current from the of E×B and the diamagnetic.

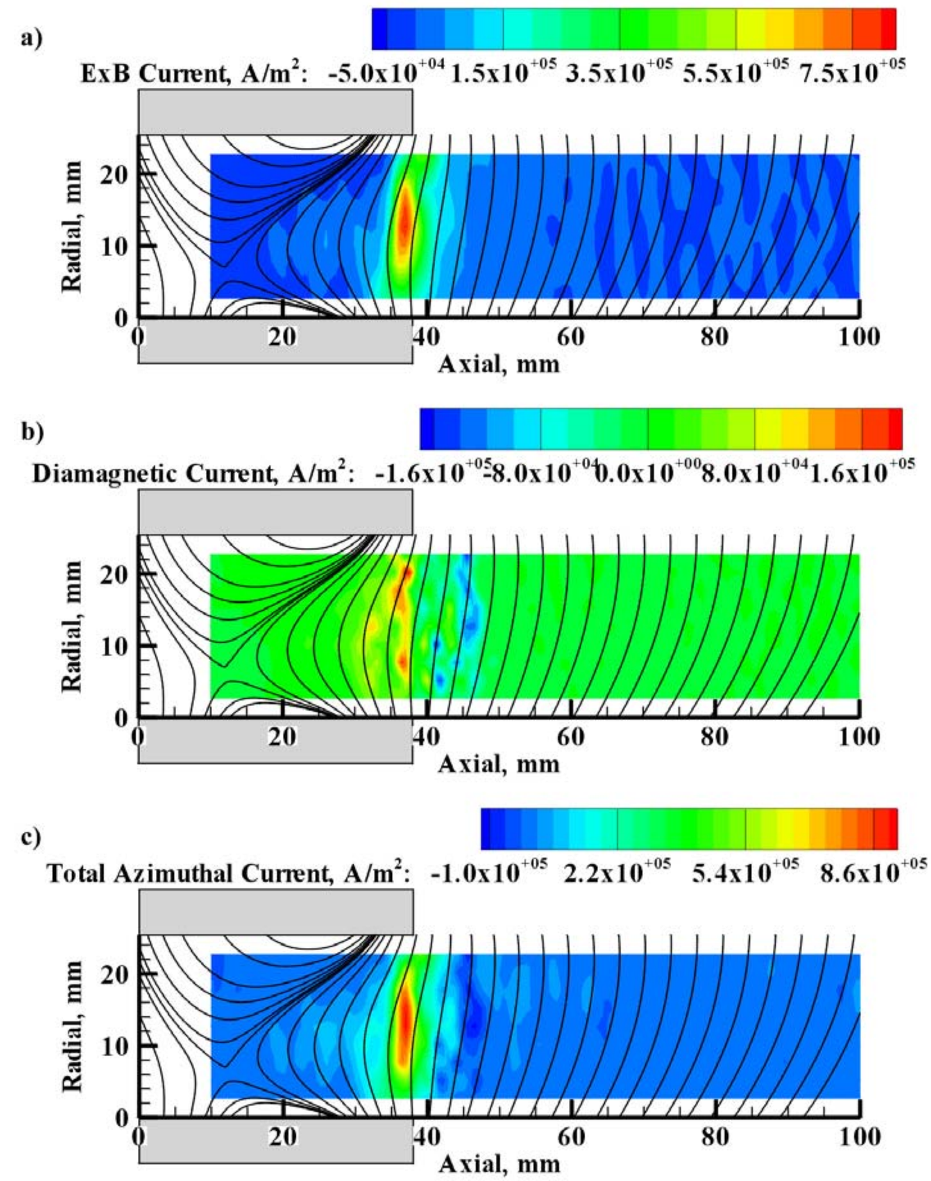

Figure 5-19. Azimuthal Electron Currents for the 300-V Xenon Case with the Trim Coil

5.5.3.2 Total Hall Current

The total Hall currents including the E×B and the diamagnetic drifts are shown in Figure 5-20. The cases shown are the 500-V xenon point with and without the trim coil and the 500-V krypton point with the trim coil.

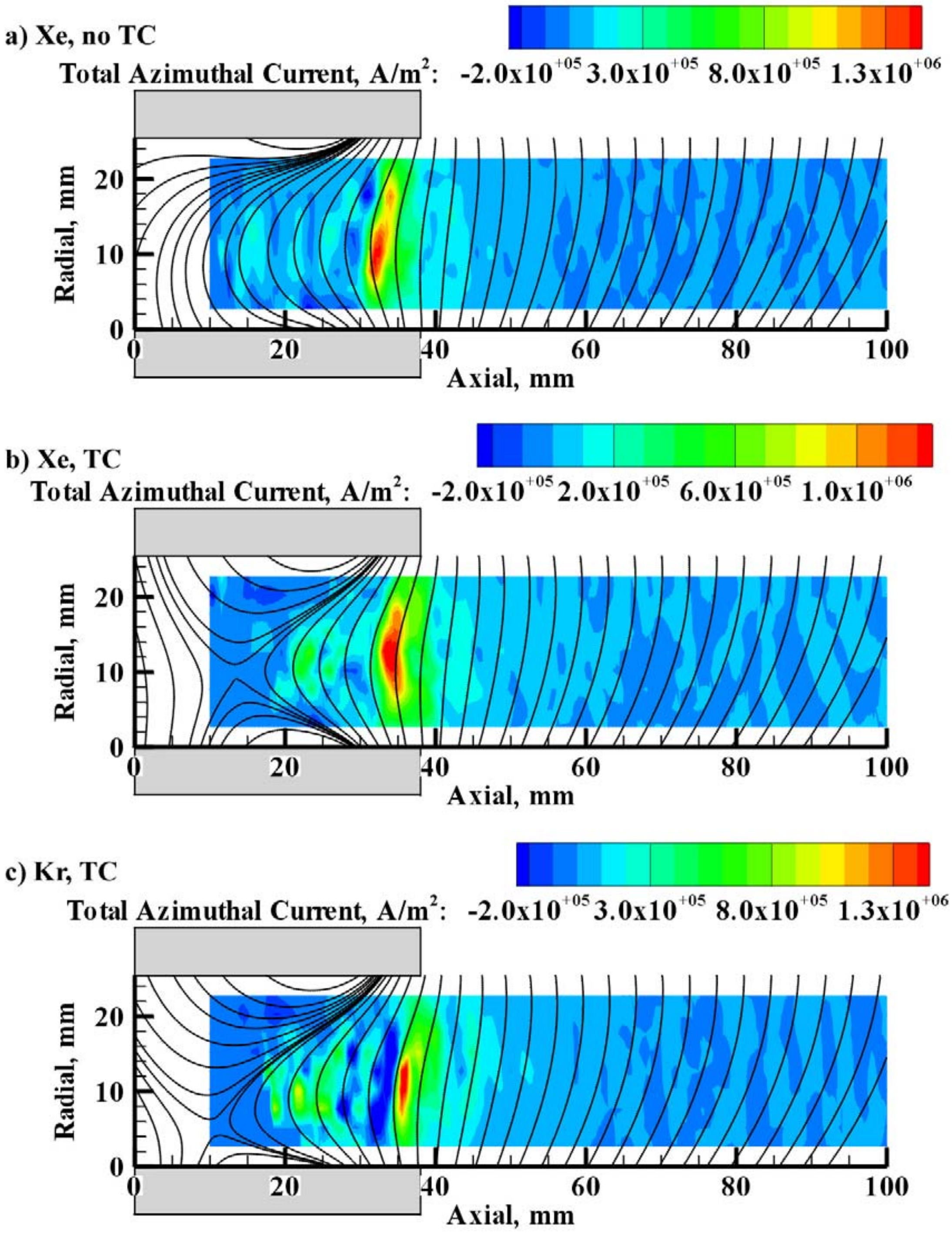

Figure 5-20. Total Hall Current for the 500-V Xenon and Krypton Cases

We can see in this figure that the trim coil is acting to focus the Hall current into the center of the discharge channel due to the magnetic mirror effect. Both xenon cases with and without the trim coil have the same maximum magnitude of approximately 1.3×10^6 A/m^2. The location of the peak Hall current is located at 32 mm and 34 mm for the non-trim coil can trim coil cases, respectively.

Krypton also has a similar maximum Hall current peak located in the center of the discharge channel. The krypton case however peaks over a much smaller region in discharge channel located at approximately 36 mm from the anode. This lower Hall current is due to the lower plasma density in the acceleration zone.

5.5.3.3 Electron Drift Energy

The azimuthal electron velocity is converted into electron drift energy and the results can be seen in Figure 5-21. As always, these points correspond to the 500-V xenon and krypton points. The black band that appears in all of the figures shows the point at which the electron drift energy surpasses the first ionization potential of each propellant. The first ionization potentials of xenon and krypton are 12.1 and 14 eV, respectively.

The krypton case has a peak electron energy of approximately 70 eV whereas both xenon cases have a peak energy of 60 eV. This shows the importance of the ionization process in the Hall current region. The region enclosed by the black band is also slightly larger for the krypton case despite krypton's high ionization potential. This larger electron drift energy is related to the lower magnetic field necessary for krypton operation. This helps to partially understand why krypton requires lower magnetic field for stable and efficient operation. Although the electrons have a higher drift energy, krypton still has a lower ionization rate in the acceleration zone than xenon. This is likely due to krypton's higher ion speed.

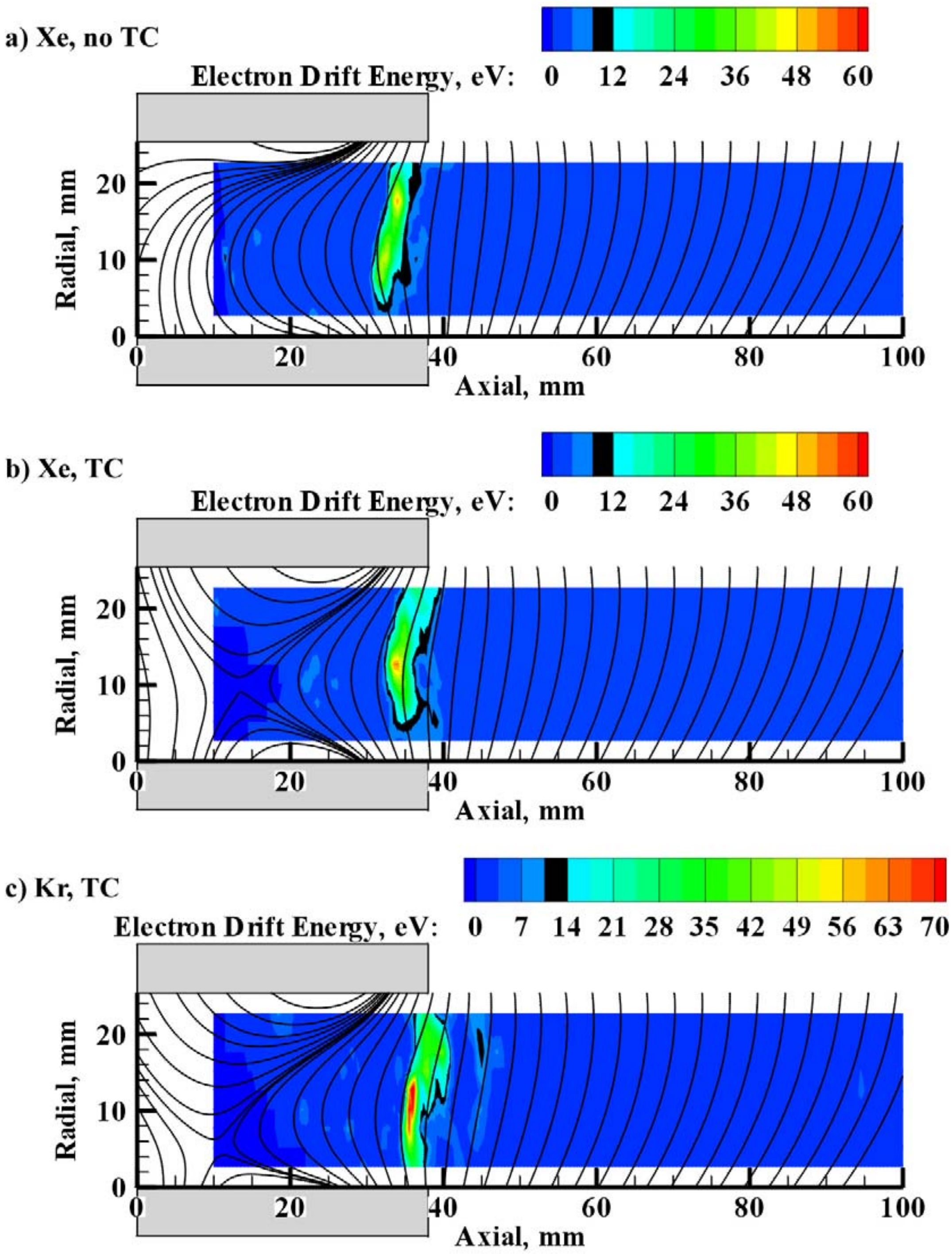

Figure 5-21. Electron Drift Energy for the 500-V Xenon and Krypton Points

5.5.3.4 Global Current Trends

Global current trends for the 500-V xenon and krypton operation can be seen in Table 5-1. This table contains the discharge current, the integrated Hall current, the beam current, and the electron current to the anode. The Hall current is calculated by integrating the total Hall current from 10 to 55 mm from the anode. This captures the bulk of acceleration zone in all of these cases. The beam current is calculated using Equ. 5-27. The anode current is just the discharge current minus the beam current.

The Hall current is approximately the same for all of the 500-V cases. The total Hall current ranges between 33 and 36 A and is approximately 3.5 to 4 times the discharge current. The anode current decreases when the trim coil is energized and krypton has a smaller anode current than either xenon case. This may be due to the fact that krypton's region of high radial electron mobility is largely outside of the thruster. This means there will be fewer electron-wall collisions and less near-wall conductivity.

Table 5-1. Global Current Trends for the 500-V Xenon and Krypton Points

Point #	Propell.	TC used?	Discharge Current, A	Hall Current, A	Beam Current, A	Electron Current to Anode, A
3	Xe	no	9.59	34.73	7.34	2.25
4	Xe	yes	9.23	33.71	7.34	1.89
6	Kr	yes	9.23	36.12	7.93	1.30

5.5.4 Particle Drifts

By taking a fluid approach to studying the electron motion inside the discharge channel certain particle drifts are ignored. Electron drifts sometimes behave differently depending on if a fluid or particle description is applied. For instance, the diamagnetic drift does not exist in the particle sense and is sometimes referred to as a "fictitious" drift.[163] A study of a few particle drifts, which were ignored in the fluid description, will be covered in this section. A detailed look at the electron motion inside the NASA-173Mv1 has been studied by King using a guiding center particle approach.[162]

The E×B drift is not covered in this section because for Hall parameters greater than 10, the fluid and particle descriptions are indistinguishable. All of the drifts presented in this section correspond to the 300-V xenon point with the trim coil (Point 2, see Figure 5-19).

5.5.4.1 Nonuniform Electric Field Drift

In regions of nonuniform electric fields a particular type of drift can results. The nonuniform electric field drift is a finite-Larmor-radius effect and related to the electron gyration about its guiding center. When the spatial variation of electric field is significant as compared to the cyclotron radius, it is necessary to correct the E×B drift for this effect. It is often very difficult to reconcile the fluid and particle descriptions of this drift and the two descriptions in fact have opposite signs.[163] The particle description of this drift is shown in Equ. 5-53. In this equation, the first term is the E×B drift and the second term is called the finite-cyclotron-radius effect.[163] This finite-cyclotron radius effect is converted to current density and plotted in Figure 5-22.

$$\vec{V}_E = \left(1 + \frac{1}{4} r_c{}^2 \nabla^2\right) \frac{\vec{E} \times \vec{B}}{|B|^2} = \vec{V}_{E\times B} + \frac{1}{4} r_c{}^2 \left(\frac{\partial^2 \vec{V}_{E\times B}}{\partial r^2} + \frac{1}{r} \frac{\partial \vec{V}_{E\times B}}{\partial r} + \frac{\partial^2 \vec{V}_{E\times B}}{\partial z^2} - \frac{\vec{V}_{E\times B}}{r^2} \right) \tag{5-53}$$

The peak magnitude of the nonuniform electric field current density is between 5×10^4 and 10^5. This is roughly an order of magnitude smaller than the E×B drift current density and occurs in a small region in the acceleration zone. This drift is relatively unimportant and can be neglected.

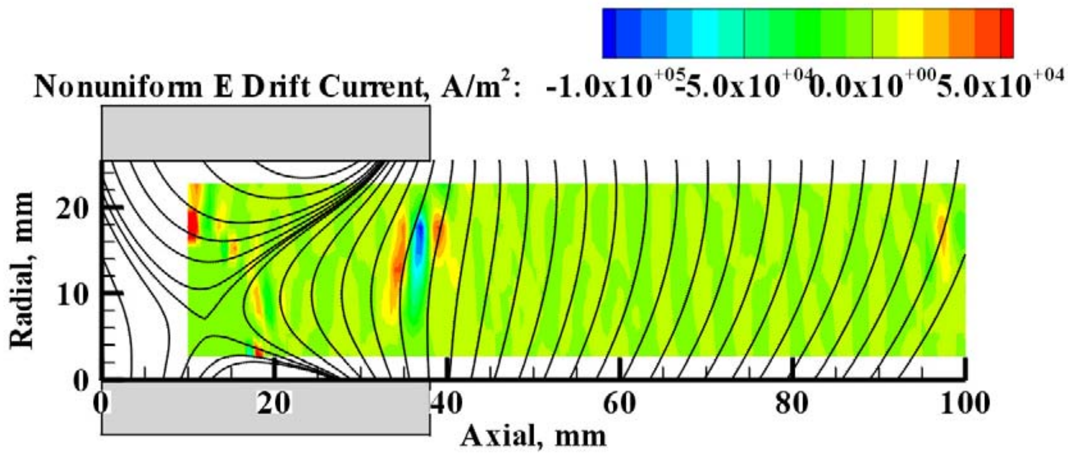

Figure 5-22. Nonuniform Electric Field Drift Current for the 300-V Xenon Case with the Trim Coil

5.5.4.2 Curvature Drift

Curvature drift arise in regions with curved magnetic filed lines. As the particles travel along the lines of force, they experience a centrifugal force and a drift orthogonal to the radius of curvature and the magnetic field line results. The equation for the curvature drift is given in Equ. 5-54, where the radius of curvature (R_c) is given in Equ. 5-55. By assuming the electron temperature is isotropic, the curvature force term is simplified to the term shown on the right hand side of Equ. 5-54.

$$\vec{V}_R = -\frac{m_e V_\parallel^2}{e}\frac{\vec{R}_c \times \vec{B}}{|R_c|^2|B|^2} = -\frac{k_B T_e}{e}\frac{\vec{R}_c \times \vec{B}}{|R_c|^2|B|^2} \qquad (5\text{-}54)$$

$$\vec{R}_c = \frac{\left(1+\left(\frac{dy}{dx}\right)^2\right)^{3/2}}{\left|\frac{d^2y}{dx^2}\right|} \qquad (5\text{-}55)$$

The curvature drift is converted to a current and can be seen in Figure 5-23. The peak curvature drift is only on the order of a few percent of the maximum E×B drift for this case. Because of this, the curvature drift can be considered negligible.

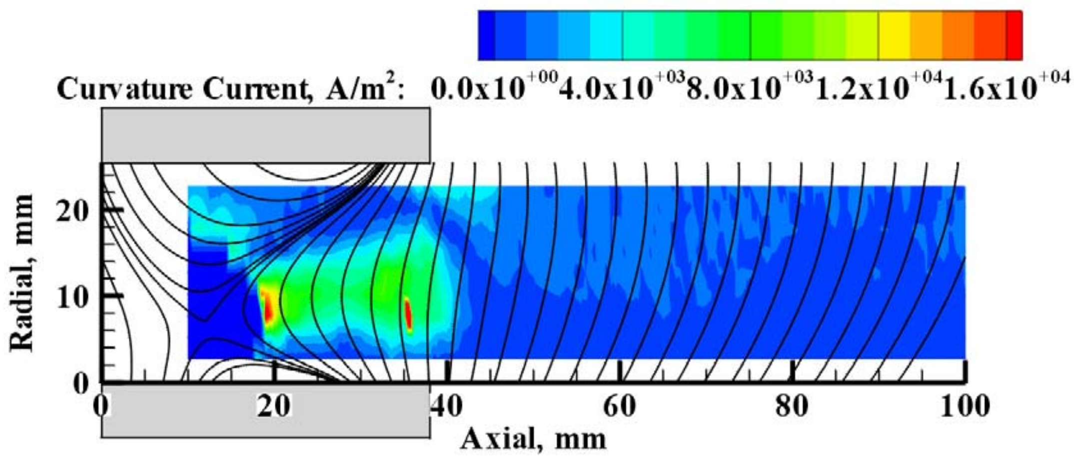

Figure 5-23. Curvature Drift Current for the 300-V Xenon Case with the Trim Coil

5.5.4.3 Grad-B Drift

Another finite-cyclotron-radius effect that results from a nonuniform magnetic field is the grad-B drift. Since the electron has a finite cyclotron radius, it will spend periods of time in stronger and weaker magnetic fields. This results in a drift perpendicular to the magnetic field lines. The gradient drift does not exist in the fluid description due to the fact that a magnetic field does not affect a Maxwellian distribution.[163] The grad-B drift can be seen in Equ. 5-56 where the perpendicular velocity is the cyclotron velocity given in Equ. 5-57. This velocity is converted into a current density and the results can be seen in Figure 5-24. In regions where the electrons are unmagnetized, the grad-B drift is set equal to zero.

$$\vec{V}_{\nabla B} = -\frac{1}{2} V_{\perp} r_c \frac{\vec{B} \times \nabla |B|}{|B|^2} = \frac{1}{2} V_{\perp} r_c \frac{B_r \frac{\partial |B|}{\partial z} - B_z \frac{\partial |B|}{\partial r}}{|B|^2} \quad (5\text{-}56)$$

$$V_{\perp} = r_c \omega_c \quad (5\text{-}57)$$

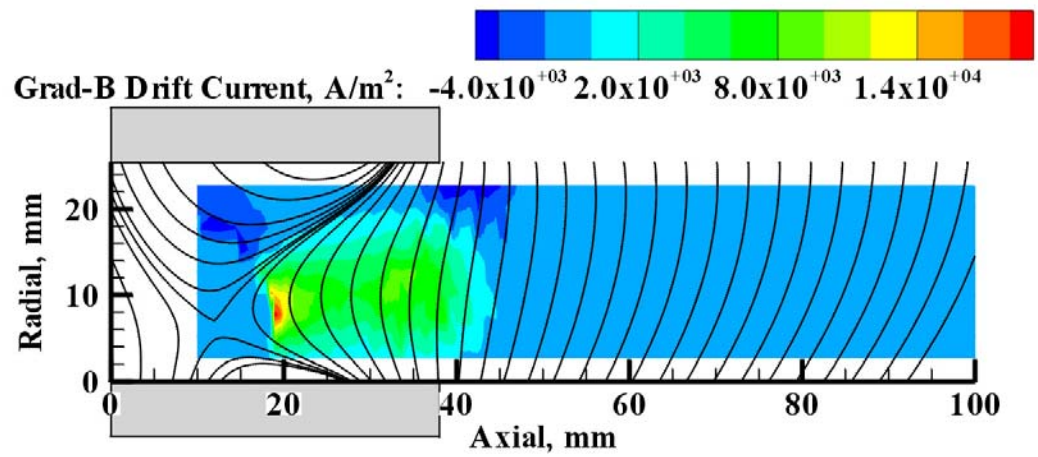

Figure 5-24. Grad-B Drift Current for the 300-V Xenon Case with the Trim Coil

The grad-B drift peak magnitude is only a few percent of the peak E×B drift. For this reason, the grad-B drift can be considered unimportant. As expected, the grad-B drift is closely related to the curvature drift.

5.6 Hall Thruster Zones

Of crucial importance in understanding the internal Hall thruster processes is the acceleration and ionization zone inside the Hall thruster. This section will characterize these internal processes by finding the boundaries of these zones. These zones are briefly discussed in Section 1.3.

5.6.1 Acceleration Zone

In this section, the acceleration zone for all of the operation points covered in Section 4.2 will be discussed (See Table 4-1). This includes a comparison between 300, 500, and 600-V xenon operation with and without the trim coil. The 600-V xenon point without the trim coil is Point C-1 in Table C-1. Additionally, krypton operation is points at 500 and 600 V are included in the discussion. Both krypton points operate with the trim coil.

The acceleration zone is the region inside the discharge channel where the plasma potential drops resulting in acceleration of the ions. For this reason, the acceleration zone is defined as the location between where 10 and 90% of the plasma potential drop has occurred. Although these criteria for determining the location of the acceleration zone are somewhat arbitrary, it was chosen to avoid error that could be introduced due to observer subjectivity.

It seems logical that a better indicator of the borders of the acceleration zone might be the magnitude of the axial electric field; unfortunately this method can fail to capture a great deal of the acceleration zone and can be difficult to implement due to noise in the electric field measurements. Still the region of peak axial electric field may be important and this region is defined as the area in which the axial electric field is greater than 15% of the maximum axial electric field. Figure 5-25 illustrates these two regions. One can see that both regions roughly coincide, although the acceleration zone is wider in general. Both the acceleration zone and the region of peak electric field are both presented in this section.

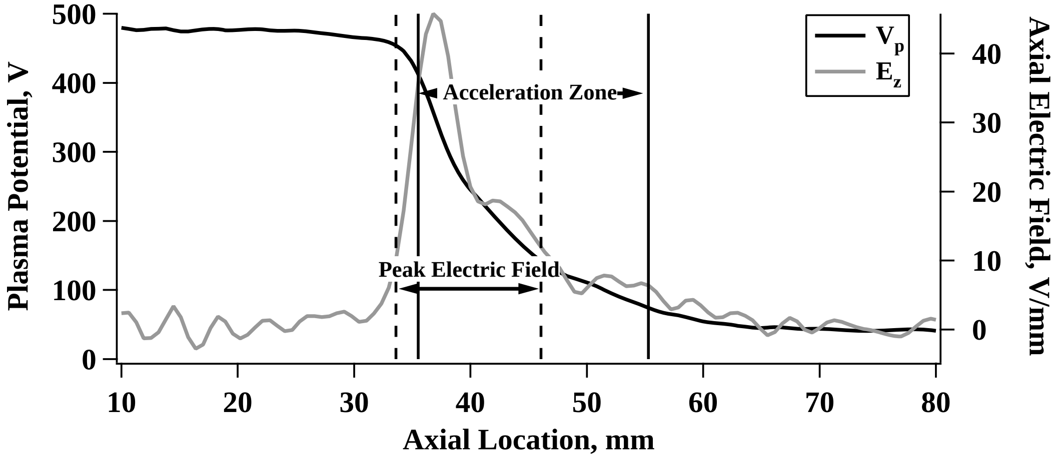

Figure 5-25. Acceleration Zone and Peak Electric Field Description

The average start, end, and length of the acceleration region and peak electric field regions appear in Table 5-2. The average is calculated by taking the mean of the five radial probe sweeps. The percentage of ion acceleration outside the discharge channel is also given in this table. From this table a few basic trends can be identified.

Table 5-2. Acceleration Zone Boundaries and Lengths

Point #	Propel.	V_d, V	Trim Coil	Acceleration Zone: Accel. Length, mm	Avg. Start, mm	Avg. End, mm	Potential Drop Outside, %	Peak Electric Field: Peak Length, mm	Avg. Start, mm	Avg. End, mm
1	Xe	300	no	16.7	37.0	53.8	80.8	13.3	35.2	48.4
2	Xe	300	yes	15.8	32.3	48.1	59.5	9.4	33.5	42.9
3	Xe	500	no	17.2	32.2	49.4	42.7	13.6	31.0	44.6
4	Xe	500	yes	17.3	33.8	51.2	51.7	12.7	32.4	45.1
5	Xe	600	no	22.6	33.4	55.9	54.2	14.3	32.2	46.5
C-1	Xe	600	yes	15.1	32.4	47.5	39.3	13.4	31.2	44.5
6	Kr	500	yes	19.9	35.5	55.4	70.5	13.2	34.4	47.6
7	Kr	600	yes	22.2	37.0	59.2	83.9	13.2	35.5	48.8

The krypton acceleration zone is located farther downstream than xenon's acceleration zone. Krypton acceleration begins between 35 and 37 mm. With exception of the 300-V non-trim coil case, the acceleration zone for xenon begins roughly between 32 and 34 mm. Also, krypton acceleration zone length is slightly longer than xenon's. Xenon acceleration zone length ranges between 15 and 22 mm and krypton's acceleration zone ranges between 20 and 22 mm. These result in a large portion of the krypton acceleration occurring outside of the discharge channel. Since the krypton acceleration zone starts farther downstream, is longer, and is almost entirely located outside of the discharge channel, it is not surprising that krypton has a larger beam divergence than xenon. The krypton ions that are accelerated away from the discharge channel centerline will have less of a chance to collide with the channel wall and therefore will accelerate freely to high angles off thruster centerline. Since krypton has a longer acceleration zone, it seems logical that krypton would have higher ion velocity dispersion (Equ. 3-32). However, this is not the case because most of krypton ionization begins upstream of the acceleration zone (Section 5.6.2).

The length of peak electric field is similar for both propellants. The peak electric field length is roughly 13-14 mm for all cases except for the 300-V, trim coil, xenon case. Again, the peak electric field is located a bit farther downstream in the krypton case.

The acceleration zone location and length are similar for almost all of the xenon cases. As discharge voltage is increased, the acceleration zone increases in length slightly and the acceleration zone start moves a bit upstream.

The acceleration zone and peak electric field for the 300, 500, and 600-V cases are shown in Figures 5-26 to 5-28. The operation points are organized by voltage in order to more easily observe trends in the magnetic field topology and propellant selection.

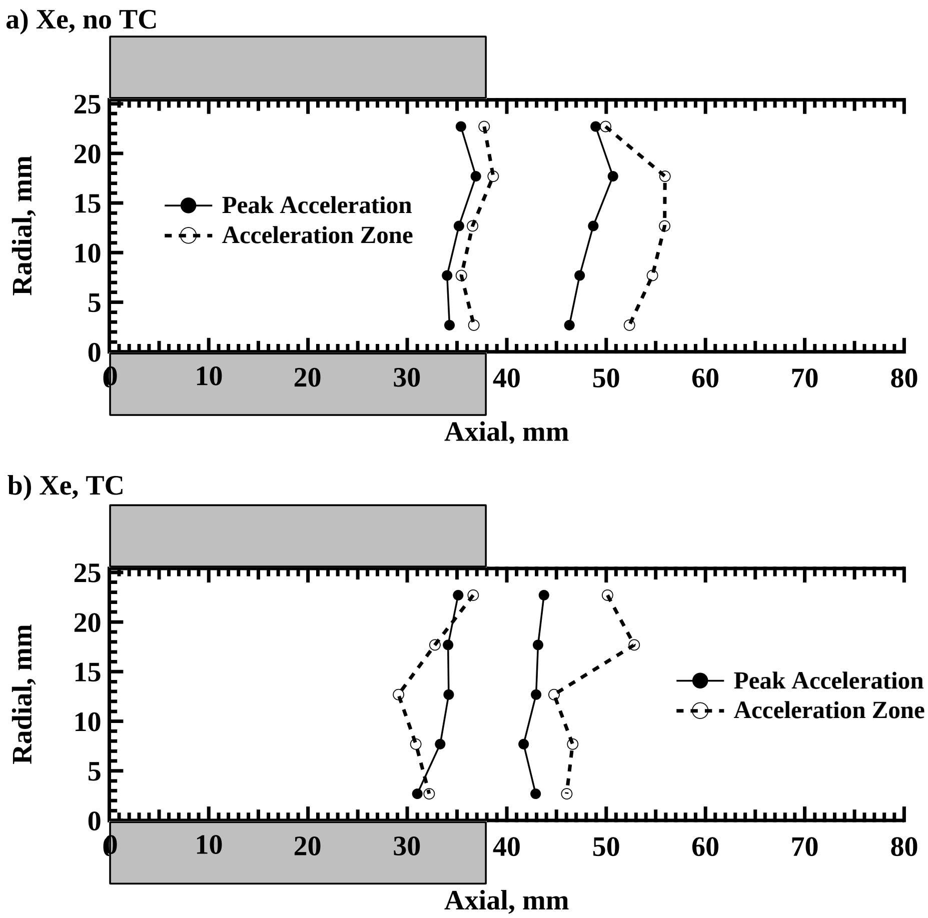

Figure 5-26. Acceleration Zones for the 300-V Xenon Case with and without the Trim Coil

For the 300-V cases, the acceleration zone has a very different shape. The acceleration zone begins further upstream in the trim coil case although the peak electric fields begin in approximately the same location (See Figure 4-7). The acceleration zone is much shorter in the trim coil case. In these figures it is possible to see the defocusing plasma potential structure in the non-trim coil case and the focusing plasma structure in the trim coil case. Also, a large percentage of the ion acceleration occurs outside of the discharge channel. Not surprisingly, the peak acceleration region corresponds well with the Hall current region. It should be noted that each 300-V case has the same inner and outer magnetic coil settings and the trim coil modifies the magnetic field to the greatest degree in the rear of the discharge channel.

The boundaries of the 500-V acceleration region are shown in Figure 5-27. This figure illustrates krypton's longer acceleration length and that krypton acceleration begins slight farther downstream. Again a large percentage of the acceleration zone appears outside of the discharge channel. The trim coil seems to have little effect on the length and location of the acceleration zone in the xenon cases. Just as in the 300-V case, the peak acceleration zones are located near the thruster exit. This is expected since this is near peak magnetic field. For each of these cases, the magnetic field topology is set by optimizing anode efficiency. This results in a different and unique magnetic field topology in each case.

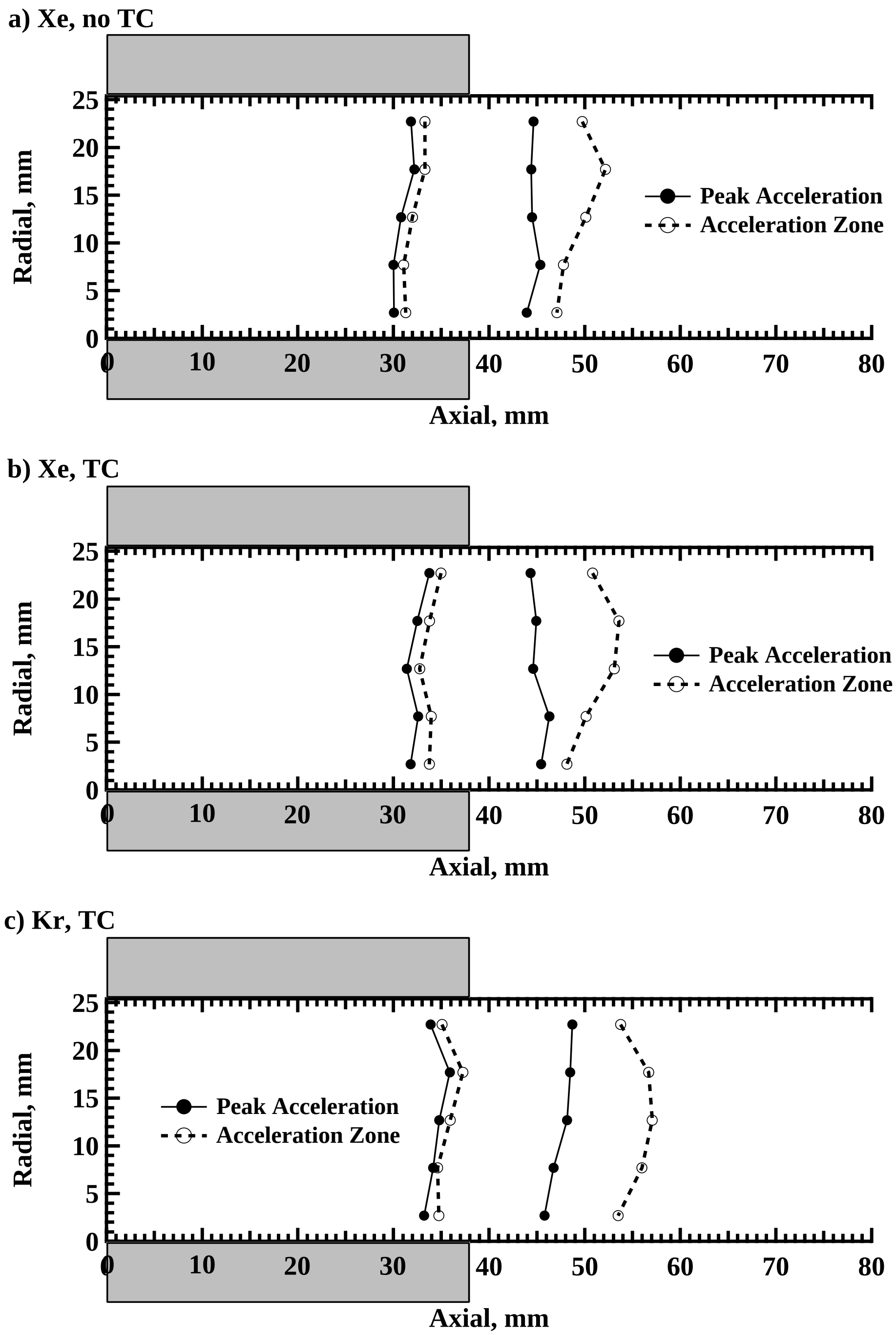

Figure 5-27. Acceleration Zones for the 500-V Xenon and Krypton Cases

The 600-V cases appear in Figure 5-28. Again the beginning of the acceleration zone is very similar for the xenon cases with and without the trim coil. The trim coil case ends much sooner and so has a much shorter acceleration zone. Just as in the 500-V case, the krypton acceleration zone begins a bit farther downstream and is longer than the xenon cases. Each of these 600-V cases have a unique and optimized magnetic field topology.

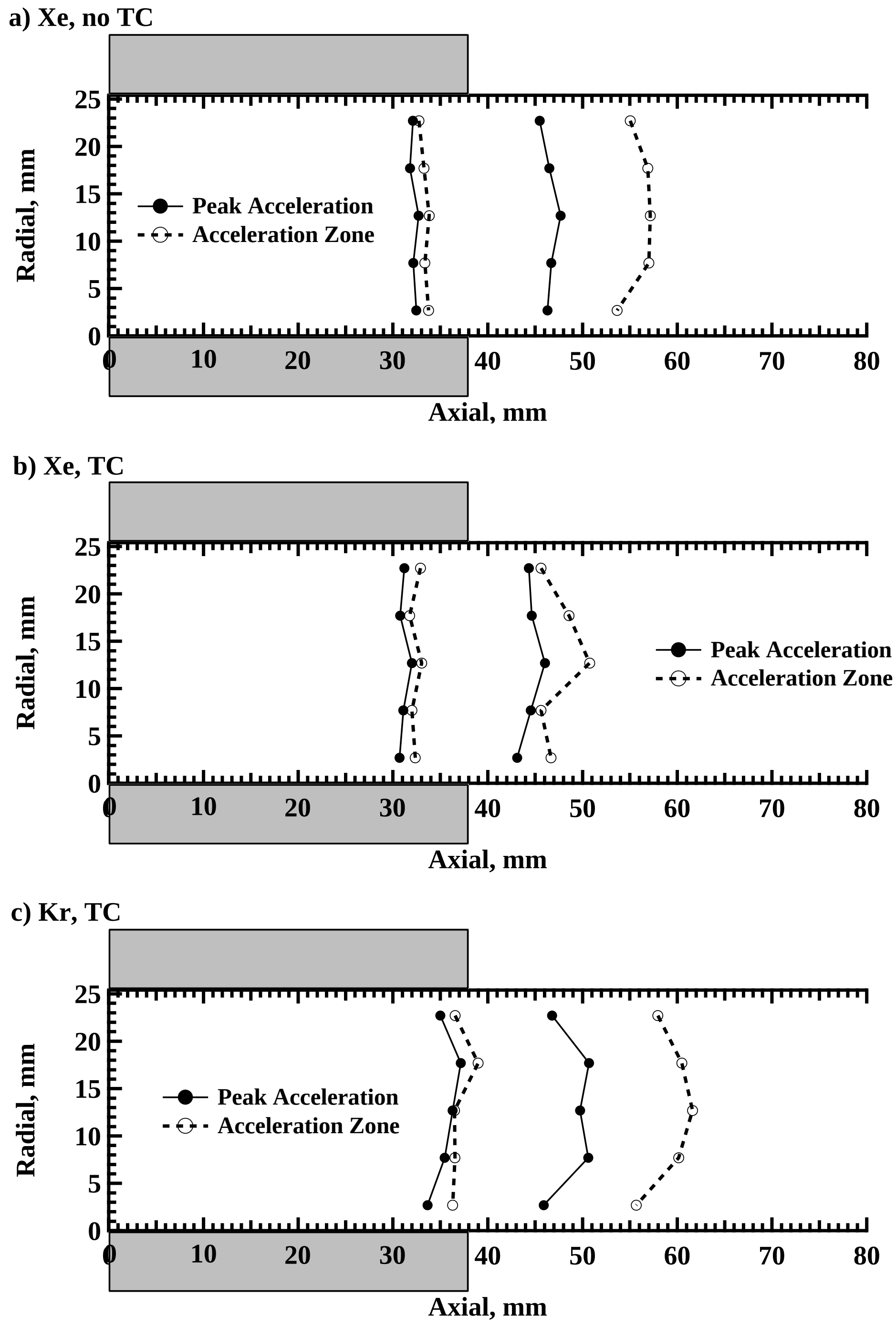

Figure 5-28. Acceleration Zones for the 600-V Xenon and Krypton Cases

The location of the peak electric field is very similar for the xenon cases and is located farther downstream in the krypton case. The length of the peak electric field region is similar for all 600-V cases. This case illustrates well the defocusing nature of the 600-V krypton case as opposed to the focusing properties of the 600-V xenon cases.

Interestingly, with exception to the 300-V non-trim coil case, the location of the peak electric field is the same for all presented xenon cases. Although these cases use different magnetic field topologies, the location of the peak magnetic field is the same for all of these cases.

5.6.2 Ionization Zone

The ionization zone is the region of significant ion production inside the Hall thruster. The ionization process is crucially important in Hall thrusters, especially in the case where krypton is used as a propellant. Unfortunately, since ionization production can not be directly measured it is also very difficult to define ionization zone boundaries. Several methods are employed in order to determine the ionization zone boundaries. Since Langmuir probe data are taken for fewer operating conditions than the emissive probe data, discussion in this section will focus on the xenon and krypton 500-V cases.

5.6.2.1 Ion Number Density Trends

The first method that can be used to give a rough idea of the location of the ionization zone is by studying the ion number density contour plots. In reality the actual ionization zone is the location of high ion production. However, there is obviously a correlation between ion number density and ion production. The ion number density for the 500-V xenon and krypton points are shown in Figure 5-29. The black bands in these figures indicate the point at which the ion number density is approximately 80% of the maximum value. A perfect example of this can be seen if Figure 5-29, part c (Point 6). In this figure, there is clearly a region of high ionization rate in the center of the magnetic mirror at approximately 20 mm. Although this method is slightly crude, it is very intuitive and easy to implement.

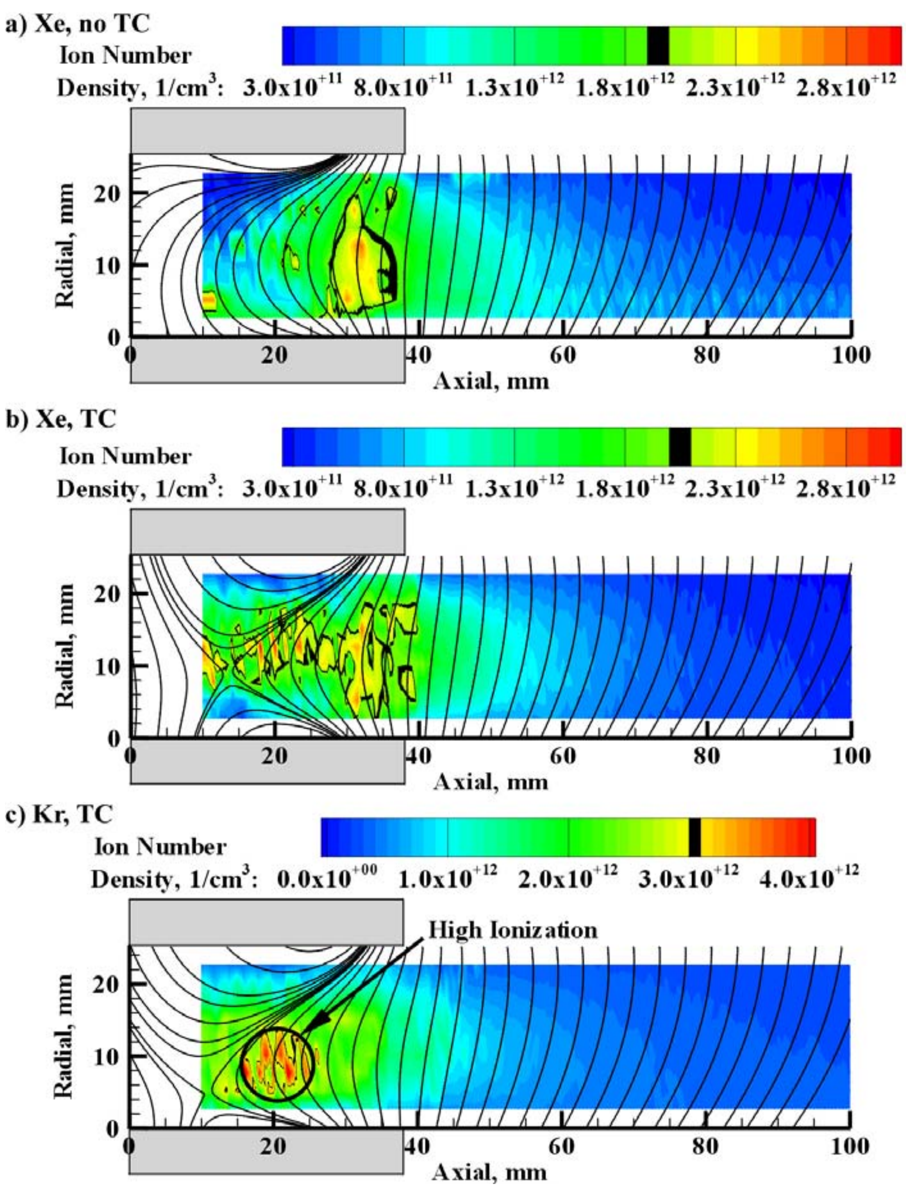

Figure 5-29. Ion Production Rate Based on Number Density

5.6.2.2 Numerical Fluid Method

The next method comes from the numerical fluid analysis of the heavy particles conducted in Section 5.4. In this method, the continuity equation (Equ. 5-26) is used to solve for the ionization rate of neutrals. Although this method seems to be very accurate it can also be very difficult to implement. An example of this method can be seen in Figure 5-30. This figure corresponds to the 500-V xenon and krypton cases. In this figure, the white region corresponds to regions of approximately zero production. The grey band outlines the region of significant ionization (approximately 10% of peak ionization rate). As discussed in Section 5.4.7.1, the recombination section downstream is a result of experimental error. However, the connection between the peak ionization and the Hall current region exists independently of the error. Although the location of the ionization zone is not affected by probe error, the magnitude of the ionization rate is too high. If there was such a high ionization rate in the Hall current region then the ion velocity would be much lower than the velocities measured in the RPA results. Still several important trends can be identified.

The Hall current plays a crucial role in the ionization process. Although this method likely over-predicts the ionization rate in the Hall current region, it is clearly an important internal process. For the krypton case, although the ionization rate peaks near the same value as the xenon cases, there is much less ion production in the Hall current region. For the trim coil cases, there is ionization occurring upstream of the regular ionization zone. This can be seen by the grey bands between 10 and 20 mm. While this method shows that upstream ionization is important, it is difficult to define exactly where the ionization is occurring. All of these cases show recombination continuing far downstream of the acceleration zone. This suggests that the CEX collision is playing an important role. This is likely the cause for the increased neutral velocity that is observed experimentally.[80,161]

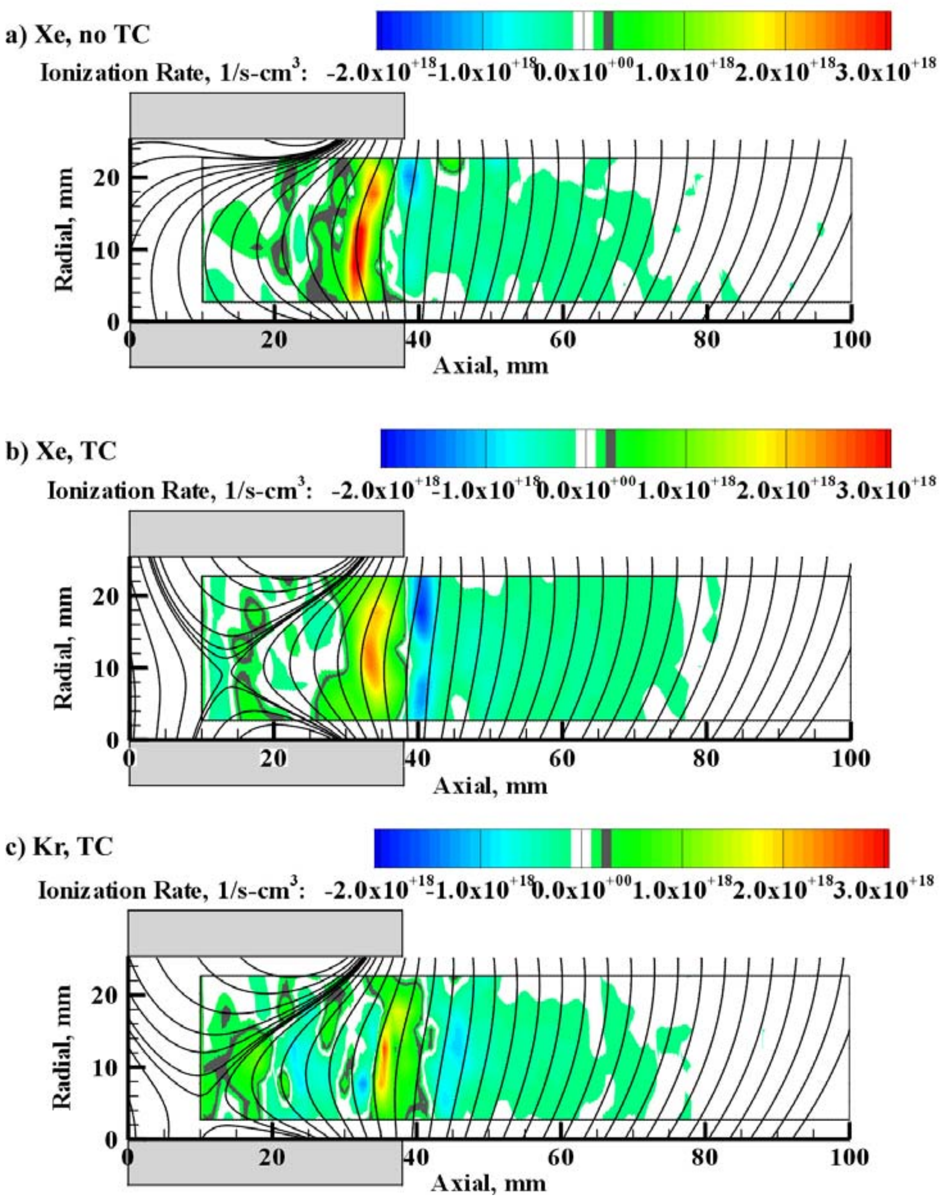

Figure 5-30. Ionization Rate Calculation Based on the Numerical Model

5.6.2.3 Electron Impact Ionization Calculation

The last method used estimates the ionization rate by calculating the electron impact ionization rate. By using this method, it is generally assumed that all of the ionization occurs from electron impact ionization. Equation 5-58 is used to calculate the ionization rate. In this equation, electron number density comes from the quasineutrality assumption, neutral number density come from the 1-D neutral density calculation, electron velocity comes from Equ. 5-49, and the total ionization collision cross section comes from tabulated values from Wetzel.[122] The ionization collision cross sections for xenon and krypton can be seen in Figure 5-31.

$$R_{Ioniz} = n_n n_e \left\langle Q_{i,tot} V_e \right\rangle \quad (5\text{-}58)$$

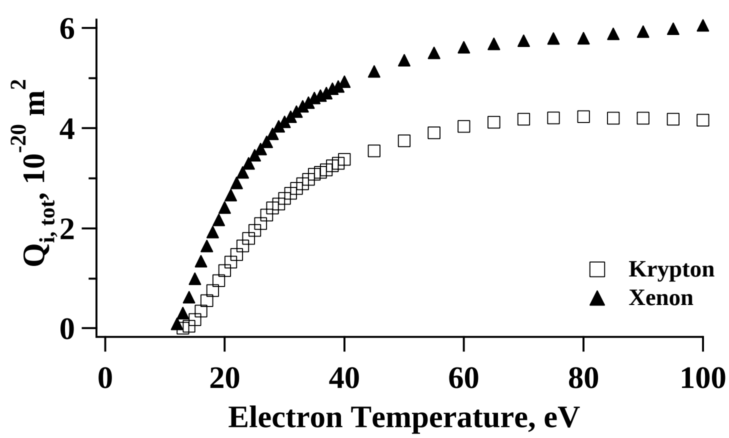

Figure 5-31. Total Electron Impact Ionization Collision Cross Sections for Xenon and Krypton

The results for the 500-V xenon and krypton cases can be seen in Figure 5-32. In this figure, the region of significant ionization (>20% of the peak ionization rate) is outlined by the black bar. Xenon has a higher ionization rate than krypton in these figures. This is not surprising given krypton's smaller ionization collision cross sections.

In this figure, it is possible to see an area of low ionization in the Hall current region. This is particularly easy to see in part b of Figure 5-32. Again, this is due to experimental error and results in an excessive depletion of neutrals in the Hall current region. Interestingly, the same phenomena that caused an unusually high ionization rate in the numerical analysis method, causes an under-prediction when this method is used.

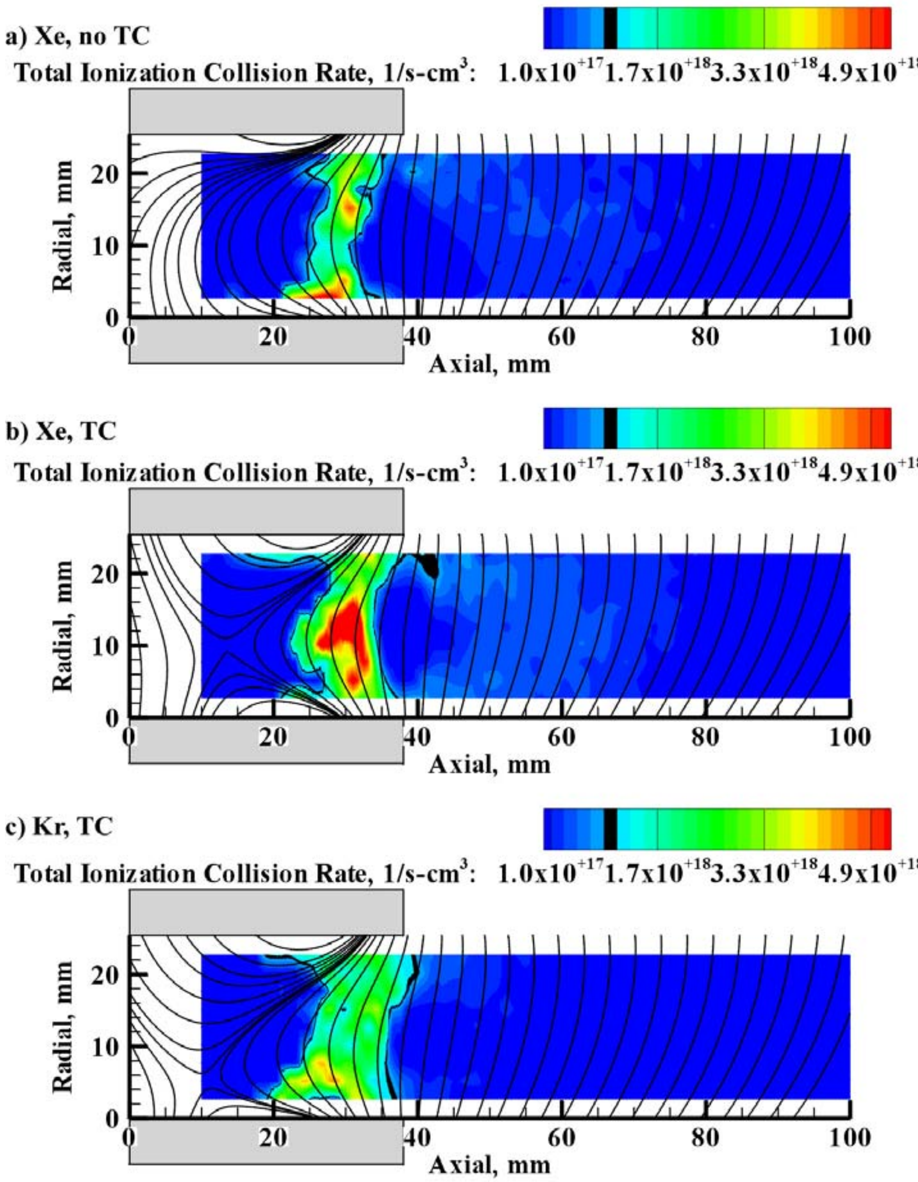

Figure 5-32. Total Electron Impact Ionization Collision Rates for the 500-V Xenon and Krypton Cases

5.6.2.4 Comparison of Methods

A comparison of these methods of finding the ionization zone is shown in Figure 5-33. This figure corresponds to the 500-V xenon case with the trim coil (Point 4). Each method appears to have strengths and weaknesses. Since none of the methods used to calculate the ionization zone are perfect, the results of these analyses will be merged to define the ionization zone. These combined results of the ionization zone analysis will appear in the summarization section to follow.

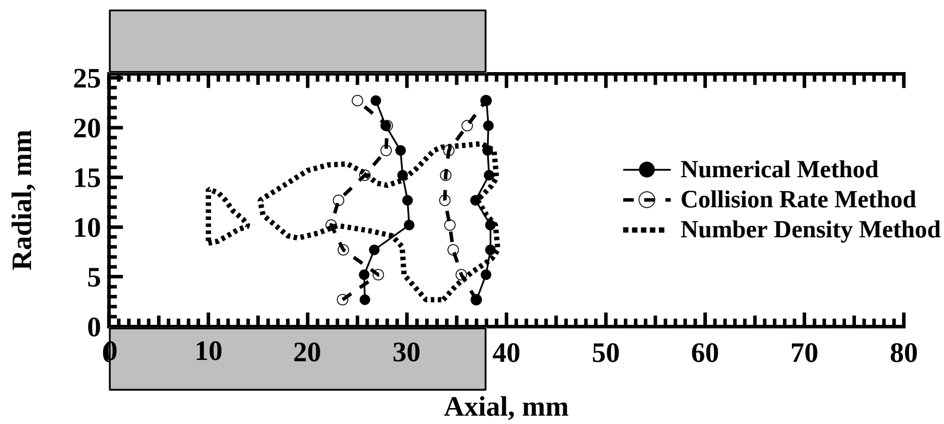

Figure 5-33. Comparison of All Ionization zone Calculation Methods for the 500-V Xenon Case with the Trim Coil

5.6.3 Summary of Hall Thruster Zones

This section will summarize the results from the acceleration zone, ionization zone, and Hall current results. The Hall current region is defined as the region where the total azimuthal current exceeds one third of the maximum azimuthal current. These three regions will be plotted together in one figure. The section will focus on the 300-V xenon cases and the 500-V xenon and krypton cases.

The 300-V xenon cases with and without the trim coil can be seen in Figure 5-34. In both cases, the Hall current coincides with the ionization zone that overlaps with the acceleration zone. This illustrates the important role of the Hall current in the ionization processes. The ionization extends well upstream of the acceleration zone in both cases. As discussed in Section 4.2.2.1 and 5.6.1, the plasma potential begins to decrease farther upstream in the trim coil case. However, the region of peak electric field matches closely in both 300-V cases. As expected, this region of peak electric field also agrees well with the Hall current region.

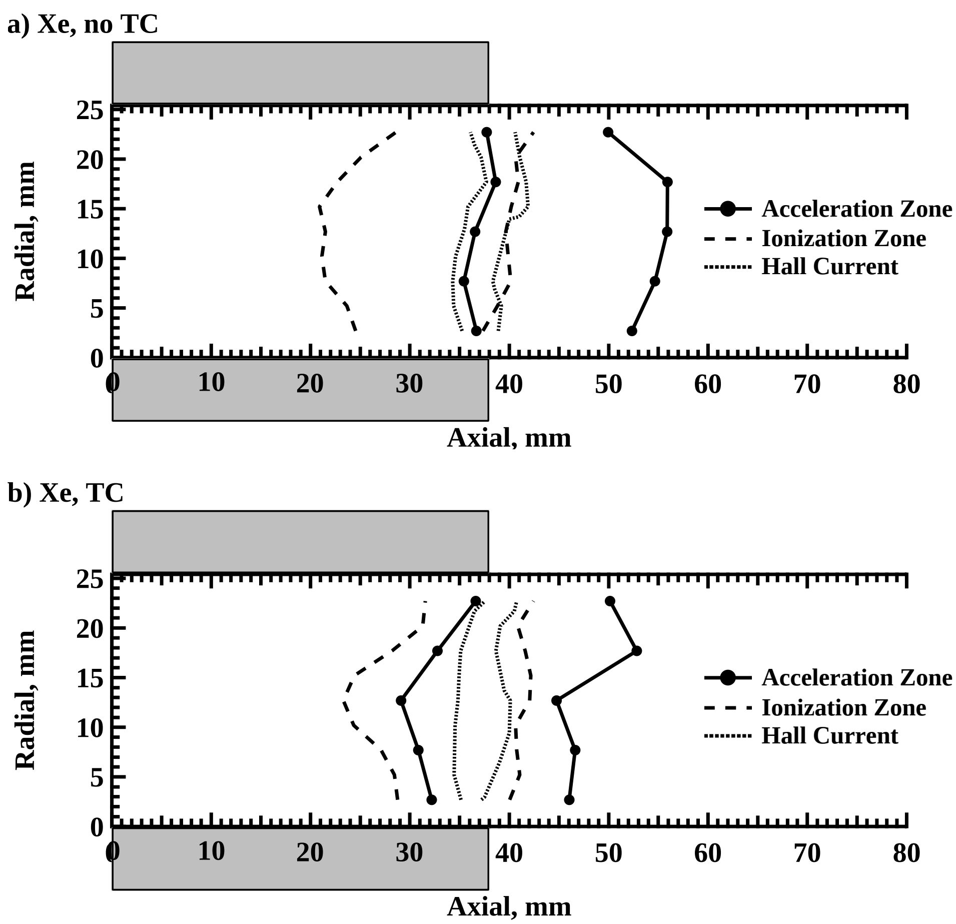

Figure 5-34. Hall Thruster Zones for the 300-V Xenon Cases

The 500-V xenon and krypton cases can be seen in Figure 5-35. In these cases, there is significant ionization upstream of the acceleration zone. The location of ionization-acceleration zone overlap closely matches the Hall current region. The non-trim coil xenon case has less ionization occurring upstream. This is likely due to a weaker magnetic mirror or the fact that the trim coil cases have unmagnetized plasma in the near anode region (Section 4.3).

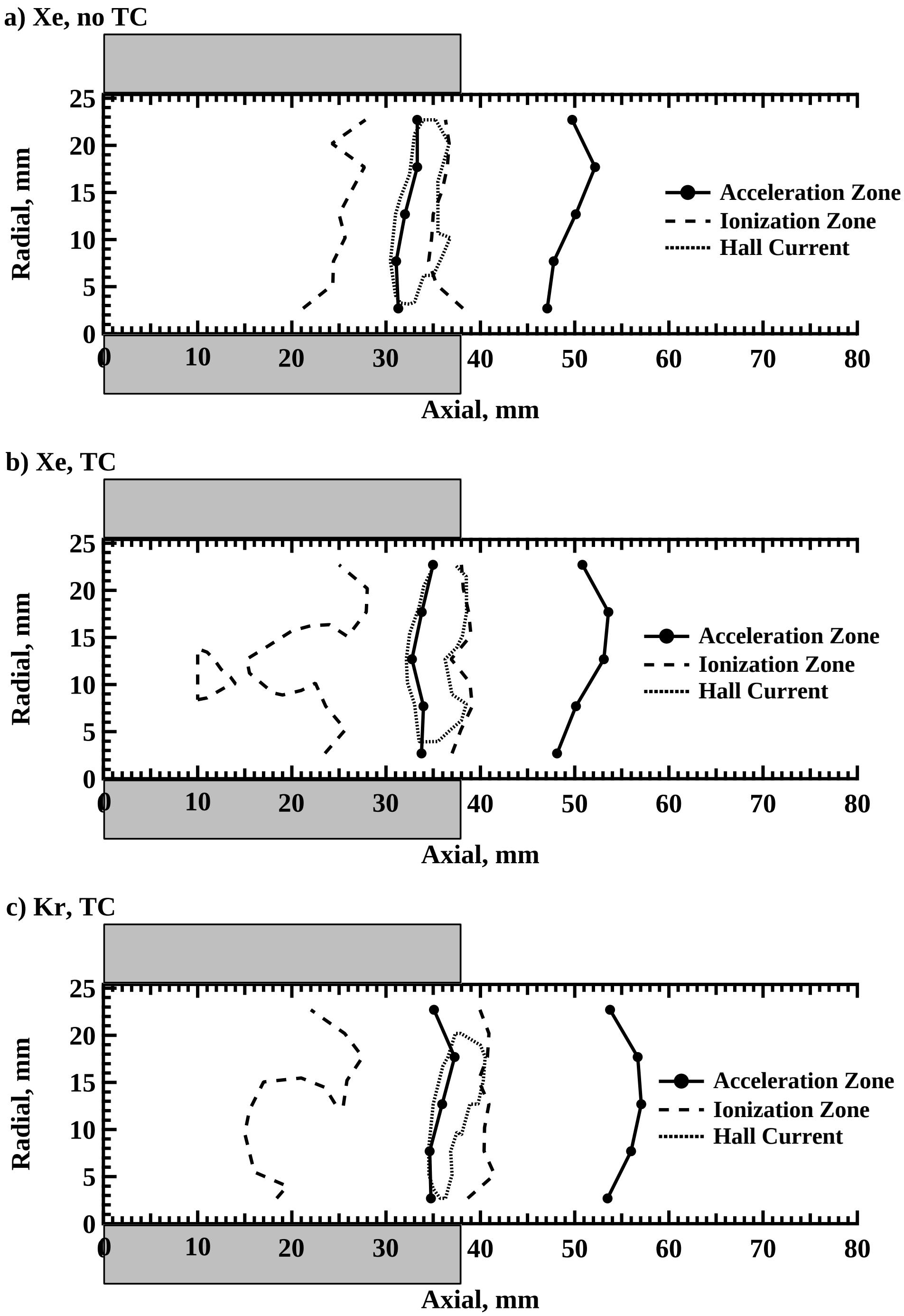

Figure 5-35. Hall Thruster Zones for the 500-V Xenon and Krypton Cases

Chapter 6.

Magnetic Field Topology Analysis

Magnetic field topology is widely accepted to be one of the most important features in the optimization of thruster performance. With this said, design of an optimal magnetic field topology is poorly understood. In particular, magnetic field optimization for krypton propellant is highly undeveloped.

The goal of this section is to develop a series of analysis tools and criteria to evaluate magnetic field topologies of Hall thrusters while still in the developmental stage. These techniques should to be easy to implement and self-contained. These analyses should be aided by the characterization of internal properties and processes presented in this thesis.

The second goal of this section is to shed light on the magnetic field features that optimize krypton and xenon performance. Of particular interest, is to understand the features necessary to further improve krypton performance. It has been demonstrated that krypton propellant requires a magnetic field topology that creates an intense ionization region upstream of the Hall current region and a strong focusing magnetic field topology in the acceleration zone.

Much of the work covered in this chapter is speculative and uncharted territory. Few researches have attempted to study the magnetic field topology in such a way and there is little background for review. This work may lay the groundwork for future Hall thruster development tools.

6.1 Modern Magnetic Field Design in Brief

In modern Hall thrusters, the centerline axial gradient of radial magnetic field is positive and peaks at a few hundred gauss near the thruster exit.[145] The positive axial gradient in radial magnetic field is required for stable thruster operation and minimal electron current. Furthermore, there should be an optimal magnetic field gradient that minimizes plume divergence and maximizes neutral ionization. Changes in the axial gradient of radial magnetic field are linked to the position of ionization and acceleration zone, which is shown to be roughly separated at the point where the radial magnetic field is equal to 80% of maximum.[19]

It is also considered to be very important to have magnetic field symmetry about the discharge channel centerline.[13,14] The combination of symmetrical field lines and a positive axial magnetic field gradient results in field lines with a concave shape. This concave shape is often referred to as a plasma lens[144,145,169] and is shown to focus ions toward the center of the discharge channel.

In modern thrusters, magnetic screens and internal trim coils have been used to control the axial gradient in radial magnetic field and create a zone of zero magnetic field near the anode.[19,179,180] The internal trim coil primarily alters the axial gradient of the radial magnetic field, which changes the radius of curvature of the field lines.

6.2 Magnetic Field Gradient

Of particular importance in the design of the magnetic circuit is the axial gradient in magnetic field. For stable and efficient Hall thruster operation it is necessary to have a positive axial gradient of magnetic field. This also helps in shaping the curvature of the magnetic field lines.

Keldysh Research Center has presented a function to quantify the magnetic field gradient perpendicular to the magnetic field lines, the F-function is shown in Equ. 6-1.[181,182] The region of peak positive magnetic field gradient is said to correspond to the region of the most intense ionization. Furthermore, the point at which the magnetic field gradient begins to decrease is also said to indicate the start of the acceleration zone. These assertions will be tested in this section. This function also aids in the visualization of the magnetic field topology and is an excellent tool to check for symmetry in the magnetic field.

$$F_{\nabla} = \left| \frac{\vec{B} \times \nabla \left| \vec{B} \right|}{\left| \vec{B} \right|} \right| \qquad \textbf{(6-1)}$$

Interestingly, this function is very closely related to the Grad-B drift (Equ. 5-56) and the curvature drift. Both of these drift components are found to be insignificantly small as compared to the overall Hall current.

Figure 6-1 compares the F-function for xenon cases with and without the trim coil. In this figure the F-function has been normalized and the axial and radial locations are not defined in accordance with ITAR (International Traffic in Arms Regulations) restrictions. The acceleration and ionization zones are overlaid on the contour plot and they appear as circles and squares, respectively. The F-function has the same peak value in the center of the discharge channel for both the trim coil and non-trim coil cases. The trim coil case has the peak F-function region occurring in a more compact region of the discharge channel.

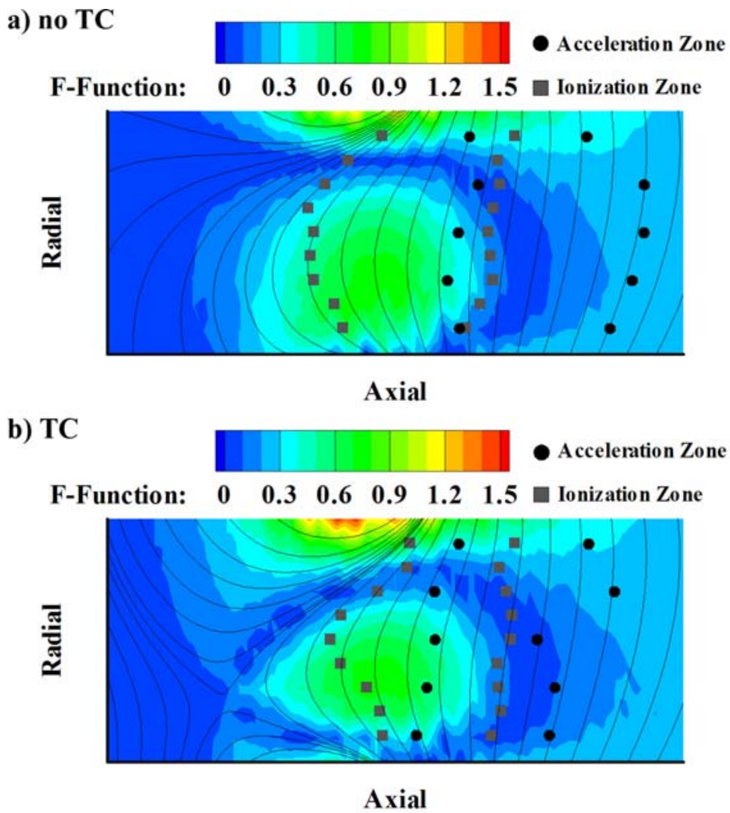

Figure 6-1. Normalized F-function Comparison With and Without the Trim Coil

It appears that there may be a correlation between the peak F-function and the location of the ionization zone although the ionization zone covers a much larger region than the peak F-function region. Also, the F-function does not capture the ionization that occurs in the Hall current region. It also seems that the acceleration zone begins approximately just after the peak in the F-function. This corresponds to where the magnetic reaches its maximum value. However, the start of the acceleration zone is at best poorly defined and this analysis gives no information as to the shape of the acceleration zone.

The F-function is somewhat useful for giving information about locations of the ionization. However, the F-function is particularly useful for qualitatively studying the symmetry in the magnetic field. Also it is excellent for quantifying the magnitude of the axial magnetic field gradient.

The F-function calculation for xenon and krypton appear in Figure 6-2. The acceleration zone is overlaid on these contour plots and appears as black circles. No trends could be found correlating ionization zone and the F-function for the krypton cases and the ionization zone is omitted from these plots. Due to fact that krypton operates with a relatively weak magnetic field, krypton has a lower peak F-function value. Also, krypton's F-function is less symmetric than xenon's. Xenon's acceleration zone begins much farther upstream toward the peak F-function region. The xenon acceleration zone begins at a point where the F-function is 85% of peak value and the krypton acceleration zone begins when the F-function is at 70% of the peak value.

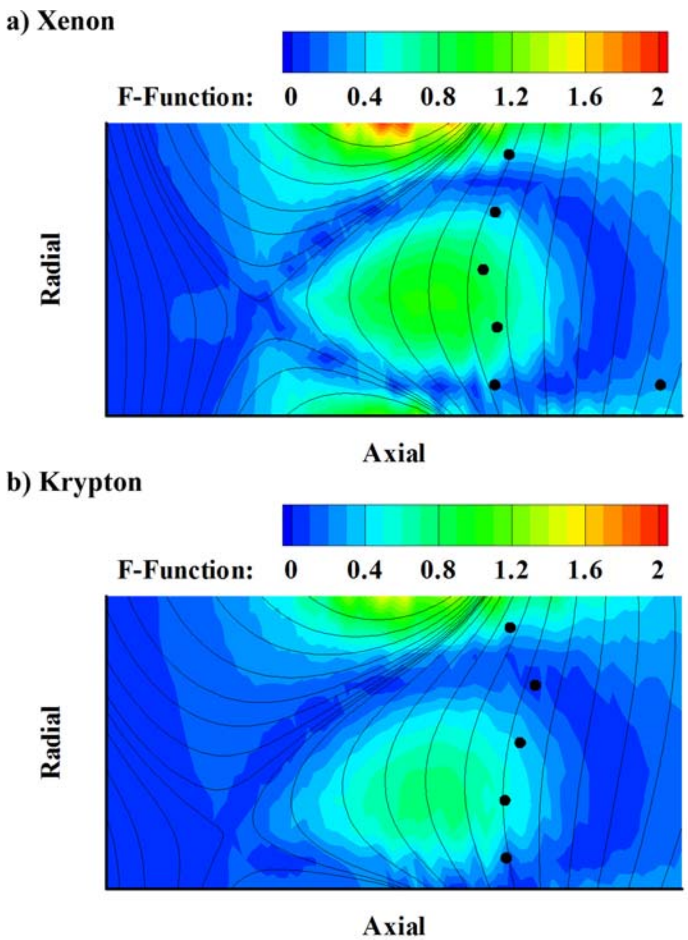

Figure 6-2. Normalized F-function for Xenon and Krypton Operation (Both with the trim coil)

6.3 Plasma Lens

An important magnetic field topological feature in any state-of-the-art Hall thruster is what is commonly referred to as a plasma lens.[13,19,34,142,144-146] To the first order, the magnetic field lines should predict the equipotential lines inside the Hall thruster. More accurately, the thermalized potential should follow the magnetic field lines. This means that the magnetic field lines will differ from the equipotential lines by an order of the electron temperature. A plasma lens topology has been shown to improve beam focusing, ion acceleration processes, and internal electron dynamics.[34,55,56] Furthermore, the plasma lens should decrease ion-wall collisions and wall erosion.

Due to the fact that krypton operates with a slightly higher electron temperature than xenon, the difference between the magnetic field lines and the equipotential lines may be greater for krypton. This shows the importance of a strong plasma lens for krypton operation.

To quantize the strength of plasma lens, the curvature will be considered. The equation for the field line curvature is shown in Equ. 6-2. Where, R_c is the radius of curvature and is given in Equ. 5-55. Although, focusing field lines are useful in the entire discharge channel, it is of particular importance in the acceleration zone.

$$\kappa \equiv \frac{1}{R_c} \tag{6-2}$$

The normalized curvature is shown in Figure 6-3 for xenon with and without the trim coil and for krypton with the trim coil. The acceleration zone boundaries are overlaid on the plot and appear as black circles. The normalized curvature value of 0.4 is outlined in a grey bar. This bar has no particular physical meaning, but is used as a point of reference to aid in the comparison between the magnetic field topologies.

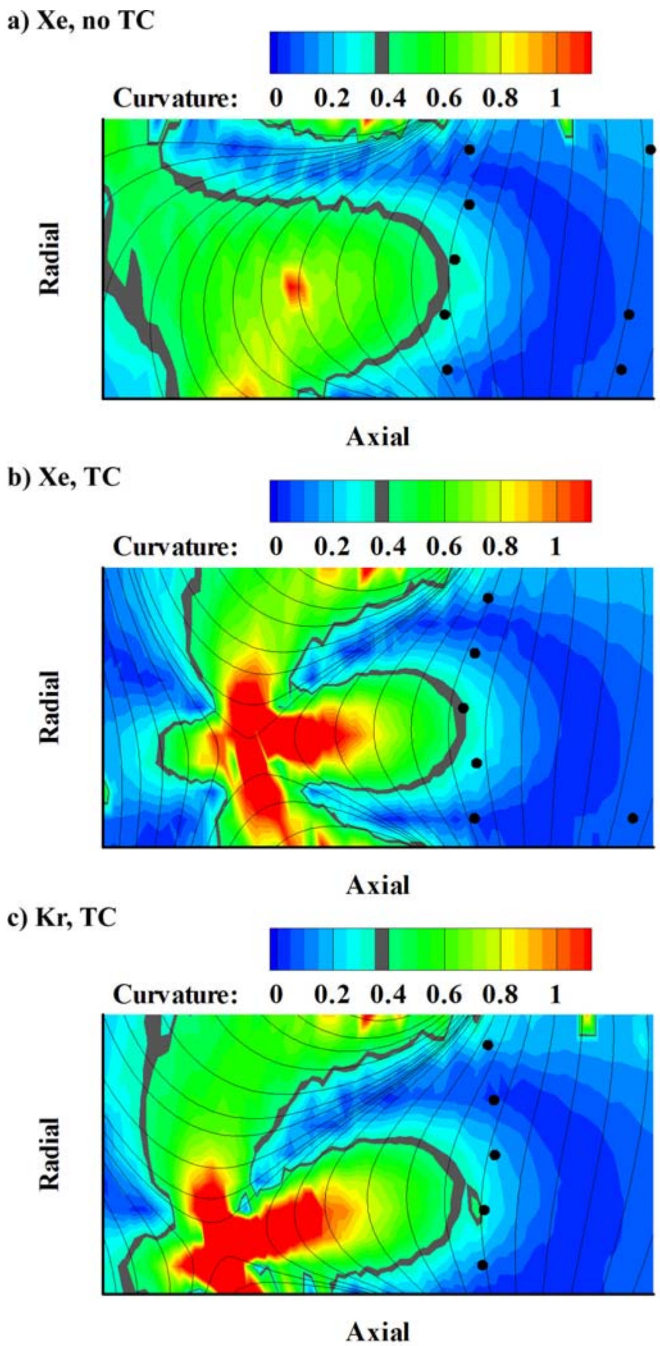

Figure 6-3. Normalized Magnetic Field Curvature

If can be seen that the trim coil creates a point where the magnetic field is equal to zero. This results in the cross shaped peak in curvature in the discharge channel. The trim coil also significantly increases the curvature in the center of the discharge channel downstream of the zero magnetic field point. This results in improved beam focusing for the trim coil case.

Very important to the performance and plume divergence of the Hall thruster is the curvature of the field lines in the peak acceleration zone. A general rule of thumb should be to maximize the curvature in the peak magnetic field region. The xenon cases have greater curvature than the krypton case at the beginning of the acceleration zone. This is related to krypton's large beam divergence.

One major difference in the krypton case as compared to the xenon trim coil case is a lack of symmetry. This calculation of curvature is an excellent test for symmetry in the magnetic field topology. It is clear that asymmetry in the equipotential lines is directly related to asymmetry in the curvature. For example, the xenon case with the trim coil has very symmetrical curvature and accordingly the beginning of the acceleration zone is focusing and symmetrical. The krypton case with the trim coil has an asymmetric curvature shape. The krypton case has worse focusing in the equipotential lines although the field lines do appear to focus slightly where the curvature is the highest.

While this discussion is interesting, this analysis has limited value since the location of the acceleration zone will not be known a priori in the development stage. Estimating the location and shape of the acceleration zone will be discussed in the coming sections.

6.4 Magnetic Mirror

A magnetic mirror results from a magnetic field magnitude near the discharge channel walls that is large in comparison to the channel centerline. The magnetic field gradient along the field lines creates a force that acts to focus the electrons toward the center of the discharge channel. This reduces electron-wall collisions and increases the electron density in the center of the discharge plasma. When an electron collides with the ceramic walls, a cool secondary electron is released and the average electron temperature decreases. The magnetic mirror acts to increase electron temperature and number density in the center of the discharge channel and consequently increases the ionization collision frequency. What is more, fewer wall collisions mean less cross-field electron mobility due to near wall conductivity.[134,170,171]

Keidar studied the effect of a magnetic mirror on potential structures inside the discharge channel.[149] In traditional thinking, the thermalized potential should match the magnetic field lines. Keidar shows that a radial magnetic field gradient may result in deviation between the electric potential and the thermalized potential, which acts to increase the potential in regions of high magnetic field. Furthermore, this study showed that a focusing potential structure could be obtained even in regions with primarily radial magnetic fields.

The magnetic mirror ratio is defined in Equ. 6-3. The mirror ratio is a relation between the local magnetic field strength and the peak magnetic field located at the wall.

$$R_m = \frac{B_{\max,wall}}{B_o} \tag{6-3}$$

Keldysh Research Center[181,182] has also developed a function to quantify the effect of the magnetic mirror. This function appears in Equ. 6-4. A magnetic mirror can be related to a corresponding loss cone[163] and Equ. 6-4 is an expression that quantifies the total angle of electron keeping. The Ω-function is a measurement of the total space angle external to the loss cone.

$$\Omega = 4\pi\sqrt{1 - \frac{1}{R_m}} \qquad \textbf{(6-4)}$$

In applying this analysis, one begins at a given location and the streamline is traced until the magnetic fields at the walls are found. Every streamline has two intersection points with the walls and the smaller of the two wall magnetic fields is used to define the mirror ratio in Equ. 6-3. The minimum wall magnetic field must be used for this analysis to make physical sense, unfortunately this causes the equation to become irrational when the mirror ratio is less than one. The electrons in these regions are poorly confined and will be lost. To avoid this problem, the minimum allowed mirror ratio is selected to be one. In order to quantify the strength of the magnetic mirror, the Ω-function is integrated over the discharge channel (0 to 38 mm) to arrive at a number to represent the mirror strength. This integral is called the mirror strength number and is given in Equ. 6-5.

$$G_M = \iint_{r,z} \Omega \, dr \, dz \qquad \textbf{(6-5)}$$

This analysis does not take into account the effect of the finite cyclotron radius. In reality, due to the electron gyration about the field line, the electron can impact the walls before the field line intersects. For this reason, the wall magnetic field may be poorly defined. In previous references,[181,182] the electron temperature is assumed to be approximately 50 eV and the wall magnetic field is corrected accordingly. This choice is a bit arbitrary and for the points studied in this section, complete internal measurements are available to aid in this analysis. However, the goal of this analysis is to develop a set of tools that are self-contained and do not rely on experimental measurements. The use of a complicated assumption is considered to be a case of diminishing returns. For this reason, the effects of the finite cyclotron radius are ignored.

The normalized Ω-function can be seen in Figure 6-4. The cases a, b and c correspond to a xenon operation without the trim coil, xenon with the trim coil, and krypton with the trim coil, respectively. The discontinuous, blocky nature of the contour plots are related to inadequate grid resolution in the magnetic field topology. The Ω-function is more intense and compressed in the trim coil cases. The krypton case has an unsymmetrical Ω-function. Again, this analysis is an excellent test for symmetry in the magnetic field topology.

When the Ω-function is integrated over the entire discharge channel, the mirror strength number (G_M) is measured. In general, the trim coil increases the mirror strength number by 30-80%. Krypton operates with 0-40% smaller mirror strength number than the xenon cases. This is due to the weaker magnetic field strength in the krypton cases.

The best example of the enhanced ionization that can result from the magnetic mirror can be seen in Figure 4-28. In this figure, krypton ion number density is greatly increased in the center of the magnetic mirror. This region of peak ion number density appears to agree nicely with the peak Ω-function region in Figure 6-4, part c.

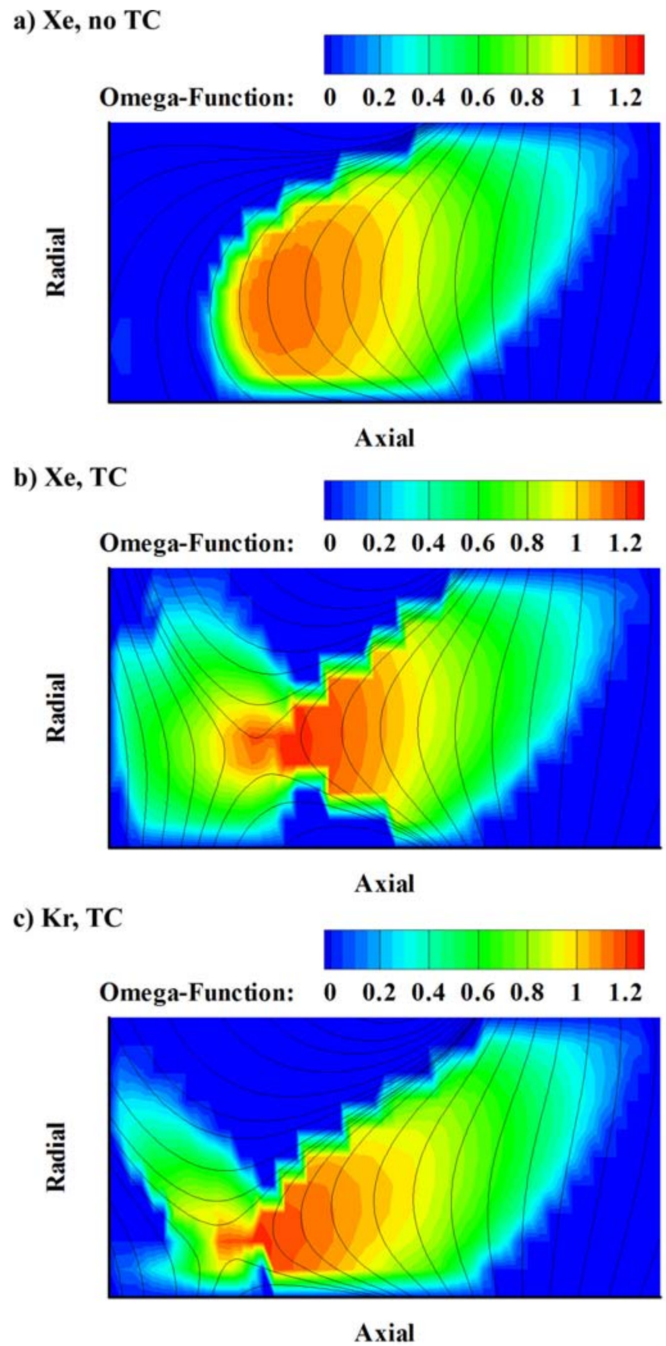

Figure 6-4. Normalized Ω-Function

An alternative way to study the effect of the magnetic mirror is to consider the effect of the magnetic mirror force (F_M). The magnetic mirror force appears in Equ. 6-6. However, the electron temperature will be unknown in most cases and Equ. 6-6 is of little use. Equation 6-7 can be uses with relative ease to quantifying the magnetic field gradient (P_M). The mirror force will be enhanced in the region of high electron temperature, however Equ. 6-7 can still give a relative measure of the magnetic mirror focusing. Equation 6-7 is then applied to same three magnetic field topologies as before and the normalized results appear in Figure 6-5.

$$\vec{F}_M = -k_B T_e \frac{\nabla_{\parallel}\vec{B}}{|B|} \tag{6-6}$$

$$P_M = -\frac{\nabla_{\parallel}|B|}{|\vec{B}|} \tag{6-7}$$

Just as in the Ω-function analysis, the mirror pressure is excellent for testing symmetry in the magnetic field. The non-trim coil has the largest mirror pressure along the walls extending through the entire discharge channel. The trim coil cases have a weaker mirror pressure along most of the wall, however this does not result in a loss in efficiency since the mirror pressure is most important in the region where the electron temperature and radial mobility is high (see Figure 5-17). The trim coil cases have very large mirror pressure near the zero magnetic field point. Electrons seem to be focused into this location. Unfortunately, the internal probe measurements do not capture the properties in this region well due to the proximity of the anode.

In general, it seems that the larger the magnetic mirror the better for thruster performance. However, it is important to remember the minimum magnetic field is limited since as magnetic field drops the electrons will become unmagnetized at some point and the mirror will not "keep" the electrons. To enhance the magnetic mirror, the peak magnetic field is the only controllable variable and is limited due to magnetic flux saturation in the magnetic circuit.

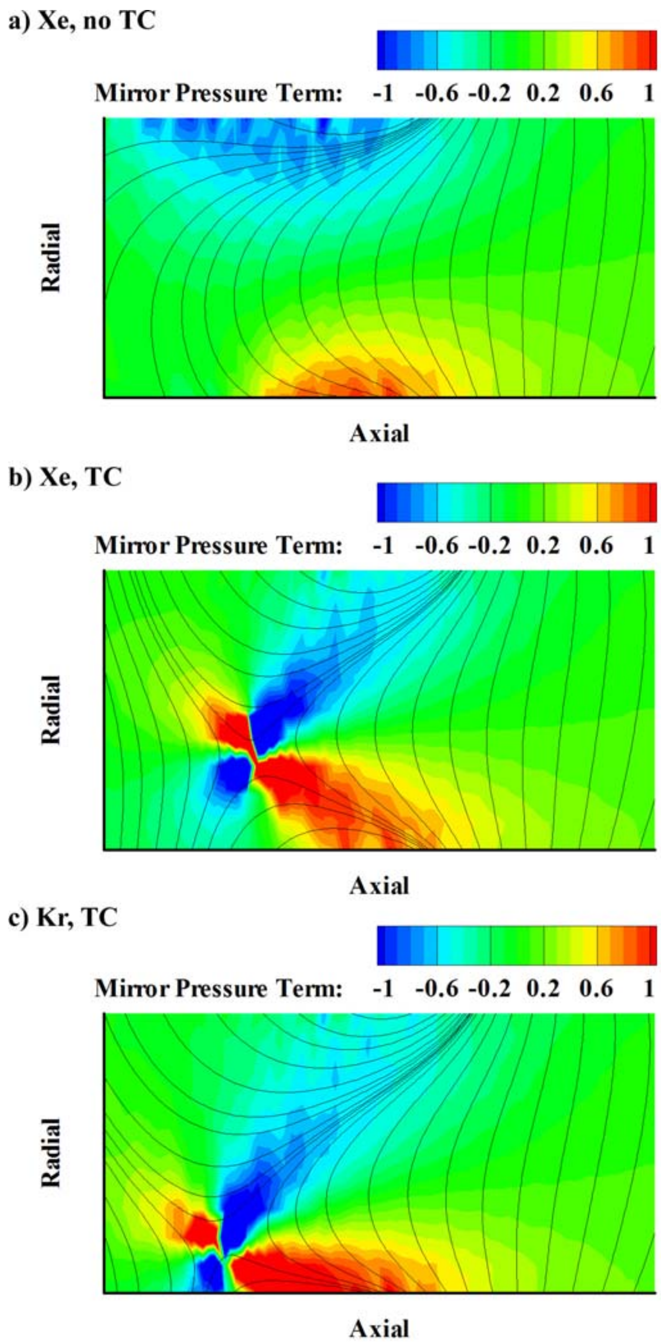

Figure 6-5. Normalized Mirror Pressure Term

The electrons are poorly magnetized in the center of the magnetic mirror where the magnetic field is very small. However, this does not mean that the magnetic mirror is not important. Electron will still be pushed toward the center of the discharge channel;

however energetic electrons will not remain contained and will more easily escape upstream to the anode.

6.5 Acceleration Zone Analysis

The purpose of this section is to develop a simple tool to estimate the location and shape of the acceleration zone. It is said the acceleration zone begins roughly at the point where the B_r=80% of the maximum centerline magnetic field.[19] The following analysis will attempt to quantify the impedance of electrons across each streamline. By finding the peak impedance, one should be able to learn important information about the acceleration zone before the Hall thruster is built. Additionally, predicting the location of the acceleration zone should give information about the location and shape of the Hall current. The Hall current occurs immediately downstream of the start of the acceleration zone, this analysis should predict roughly where the Hall current is the highest. As long as the magnetic mirror is used the Hall current will be in the center of the discharge channel where the magnetic field is the lowest ($|J_{E\times B}| \propto |E|/|B|$).

Electrons are known to move relatively freely along the magnetic field lines while their motion is greatly impeded across the field lines. Regardless if Bohm ($\propto 1/B$) or classical ($\propto 1/B^2$) type mobility is assumed, the mobility has an inverse relation with magnetic field strength. Following this train of thought, electrons are most likely to cross the field lines at the point where the magnetic field strength is the lowest. Refer to Figure 6-6 for an illustration. In this figure, μ is the electron cross-field mobility. The electrons will effectively "leak" across the magnetic field line at this minimum magnetic field location. This analysis tries to quantify the streamlines ability to contain electrons. This means that each streamline should have constant impedance along the streamline and each stream line will be roughly equipotential. The equation for field line impedance is given in Equ. 6-8 and the value a is an undefined constant. For each location in the discharge channel, the magnetic field line is traced and the minimum magnetic field magnitude is found along the streamline. This minimum streamline magnetic field is then used in Equ. 6-8. Assuming that the magnetic field topology is relatively symmetric and given the magnetic mirror effect, the centerline magnetic field should roughly estimates the minimum streamline magnetic field ($B_{SL,min}$) and the streamline electron impedance (I_m). The effect of near-wall conductivity, which can be a significant contributor to cross field electron mobility, is not captured in this analysis.

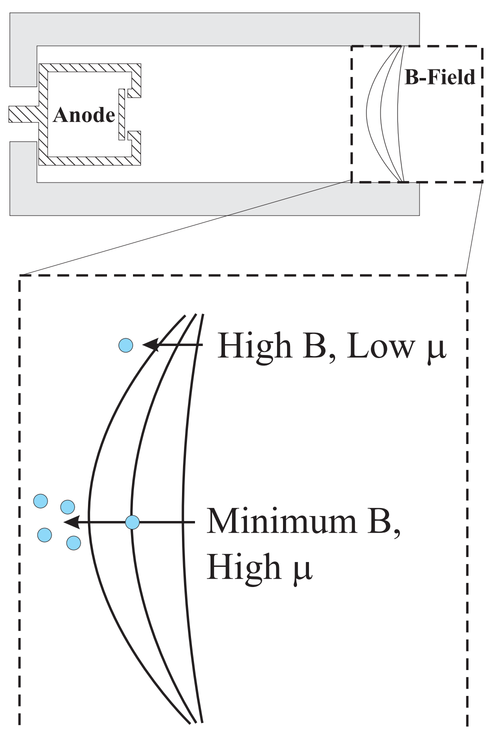

Figure 6-6. Electron Leakage Across the Field Lines

$$\mathrm{I}_m = a\, B_{SL,\min} \tag{6-8}$$

The normalized results of this analysis can be seen in Figure 6-7. In this figure, the axial and radial dimensions are left undefined in accordance with ITAR restrictions. To add and additional level of encryption, the acceleration zone results do not correspond with any data discussed in this thesis. In Figure 6-7, the 80% impedance assumption is tested and is shown by the grey band in the contour plot. The symbols that are overlaid on the contour plot represent the boarders of the acceleration zone and peak electric field region (Refer to Section 5.6.1). The boarders of the acceleration zone follow the magnetic streamlines very well and at least to the first order, this analysis should give a good estimate of the acceleration zone shape. The peak electric field region in particular has excellent agreement with the pathlines for this case. The acceleration zone has the worst agreement near the walls; perhaps due to near wall conductivity, which is not captured in this analysis. The acceleration zone also has reasonably good agreement with the 80% assumption. Although this assumption is fairly good, it appears that the acceleration zone starts a little later than expected around the streamline where the magnetic field is 85% of the peak B-field. This trend will be studied in greater detail to more accurately capture the location where the acceleration zone begins.

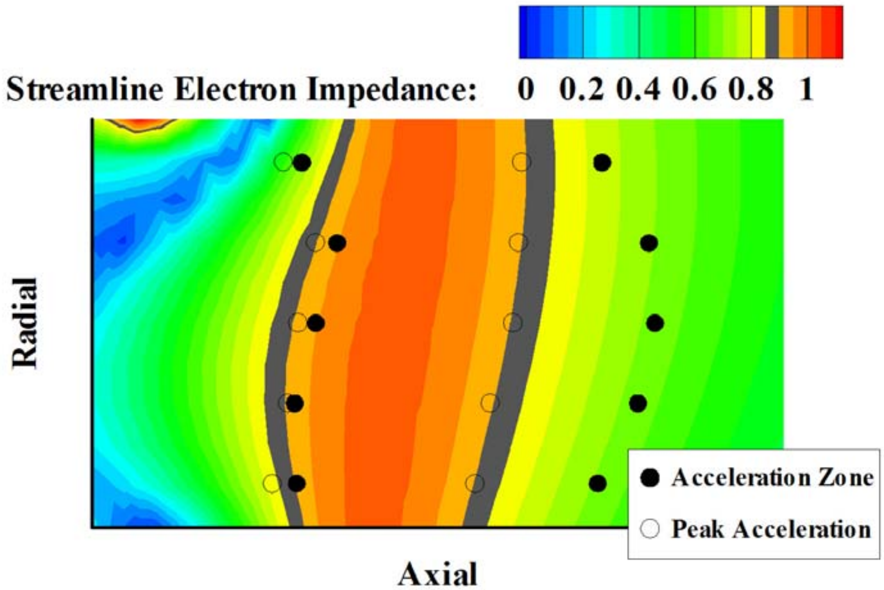

Figure 6-7. Mapping the Normalized Electron Impedance in the Acceleration Zone

Next, the centerline emissive probe results will be used to find the start and end of the peak electric field region. The peak electric field is used because changes in potential should be directly dependent on electron impedance and the peak electric field region should produce the most predictable results. In this analysis, the percentage of peak magnetic field is measured along the centerline at the start and end of the peak electric field region. This will allow the 80% assumption can be more accurately assessed. As stated earlier, the centerline magnetic field roughly estimates the minimum electron impedance along the streamlines. Several measurements from the internal emissive probe experiment are analyzed, complied, and the results can be seen in Figure 6-8.

Figure 6-8 shows that as the peak magnetic field is increased the location of the acceleration zone moves upstream. The acceleration zone begins at the point where the magnetic field is equal to 70 to 90% of the peak centerline magnetic field. The 80% assumption was extremely good although a bit of a simplification. The peak acceleration zone ends at the location where the magnetic field decreases to 75-95% of the peak centerline magnetic field. A larger peak magnetic field increases the electron impedance and allows the acceleration zone to begin farther upstream.

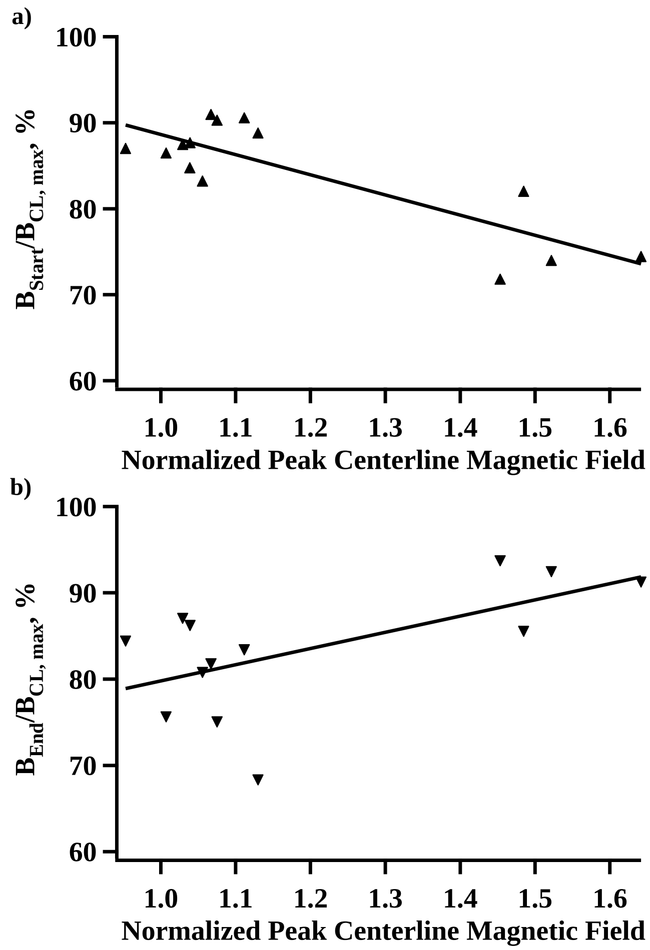

Figure 6-8. The Acceleration Zone's Start (a) and End (b) for Different Peak Magnetic Field Strengths

As the acceleration zone moves upstream, the magnetic field lines have more curvature and are more focusing. This explains why cases that operate with weaker magnetic field tend to have larger beam divergence. Examples of these cases are krypton operation, low voltage operation, or low current operation. In the internal emissive probe results, it was concluded that krypton acceleration zone starts farther downstream than the xenon cases. This finding is at the root of the krypton performance puzzle and is very important for design of high thrust/low specific impulse Hall thrusters. With this information, it will be easier to design a thruster magnetic field topology and to get a sense of the curvature and focusing characteristics in the acceleration zone prior to thruster construction.

No acceleration zone trends could be observed as a function of discharge voltage, discharge current, or propellant. Propellant is not expected to effect this behavior since the establishment of the electric field is an electron behavior. This is supported by the internal investigation in Section 4.3.4.1.

The finding suggests that beam divergence should be the efficiency component that is most directly impacted by increasing peak magnetic field strength. The most direct way to verify this finding is to study the beam divergence efficiency as a function of the peak magnetic field. The detailed efficiency analysis in Section 3.4 will be used to verify this trend and the results of this analysis can be seen in Figure 6-9.

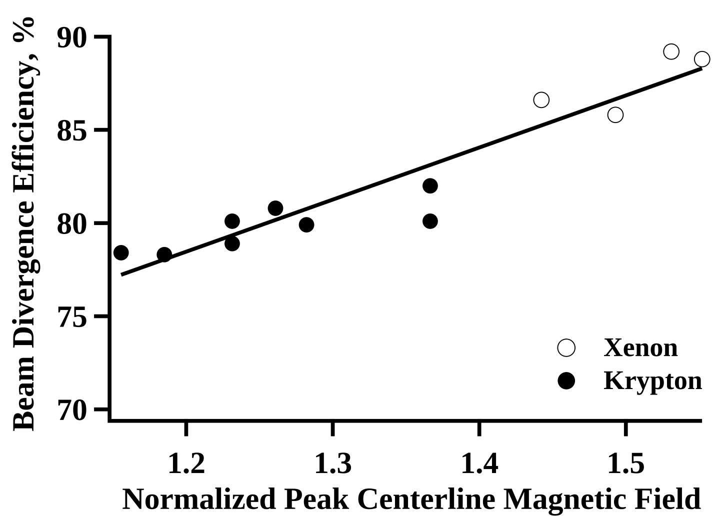

Figure 6-9. Beam divergence Efficiency as a Function of Peak Magnetic Field Strength

The beam divergence efficiency in fact increases linearly with the peak magnetic field strength. Xenon and krypton follow the same linear trend and propellant choice alone does not appear to affect the beam divergence. Also, this plot contains both trim coil and non-trim coil data. The trim coil has a smaller effect on beam divergence, but for these operating conditions, this effect is not the dominant trend.

It is not the conclusion of this analysis to say that Hall thrusters should operation with the largest possible peak magnetic field. As shown by Section 4.3.4.1, when krypton is operated with the same magnetic field topology as xenon, the acceleration zone is similar for both propellants. However, as magnetic field intensity increases beyond the optimized magnetic field setting, discharge current oscillations increases and thruster efficiency decreases. These oscillations are strongly related to the breathing mode and are illustrated in Figure 4-33. For each operation point, there is a unique optimized magnetic field and a stronger magnetic field topology is not necessarily better. Better understanding of the discharge current oscillations (particularly the breathing mode) and the dependence on magnetic field topology and propellant type is the next step in optimizing krypton performance.

Chapter 7.

Conclusions

Krypton propellant has long interested engineers as a possible propellant for use in Hall thrusters. Krypton sparked interest in the electric propulsion community due to its higher specific impulse, relative abundance, and lower price as compared to xenon. Unfortunately, due to krypton's relatively poor performance, krypton has not become the legitimate option for space missions that many have hoped. This thesis presented a thorough investigation into the physics of krypton operation in Hall thrusters. With proper thruster design and operation the xenon-krypton performance gap can be reduced to 4% and krypton can finally become a realistic propellant option.

Krypton performance was carefully analyzed and the sources of the krypton-xenon performance gap were determined. There was also a detailed internal investigation and analysis of Hall thruster operation with krypton and xenon propellant. From these investigations, several design and operation suggestions were made in order to maximize thruster efficiency in future krypton Hall thrusters. Additionally, several findings were made to improve the physical understanding of general Hall thruster physics and these findings will help to design superior xenon Hall thrusters in the future.

7.1 Flight Performance Analysis

A flight performance analysis was conducted to evaluate krypton for potential space missions. For specific missions, krypton can outperform xenon and offer significant financial savings. In general, due to its higher specific impulse, krypton can deliver larger payload fractions at the consequence of longer trip times. If trip time is flexible, krypton easily outperforms xenon for many space applications in terms of financial and mass savings.

There are significant cost benefits to using krypton for specific missions. During ground testing the greatest benefit is simply propellant cost, but for missions the cost savings are largely connected to the saving in launch costs due to krypton's smaller required propellant mass. Krypton savings are most significant for large-scale missions requiring large delta-Vs. Krypton savings are also maximized for higher thrust, lower specific impulse missions.

Storage concerns were once considered a hindrance for potential krypton missions. However, it has been concluded that for modern propellant tanks, the storage concerns associated with krypton propellant are insignificant compared to the performance advantages.

For krypton to become a strong option for mission designers, a few conditions should be met: continued development and advancement of power system technology, continued decrease in power system costs, and decrease in the krypton-xenon efficiency gap. The third of these requirements is the driving force for this research.

7.2 Krypton Performance

To fully understand the xenon-krypton performance gap, xenon and krypton performance were studied in great detail. A phenomenological performance model was also applied in order to isolate the specific reasons for the performance gap.

Regardless of the performance gap, krypton always has a superior specific impulse to xenon. Specific impulse was measured as high as 4300 s for krypton at a discharge voltage of 1200 V and corresponding to 55% anode efficiency.

A performance study showed that the NASA-173Mv1 operating with krypton propellant performs with an absolute anode efficiency gap between 2 and 15%. The xenon-krypton efficiency gap decreases with increasing voltage and anode flow rate, both of which suggest that the performance gap is related to propellant utilization. By increasing anode flow rate, krypton anode efficiency improves by as much as 10%. With optimized operating conditions, the NASA-173Mv1 with krypton propellant is capable of reaching anode efficiency levels between 55-60%. Although Faraday probe measurements confirm that the performance gap is largely related to propellant utilization, a detailed performance analysis conducted to further pinpoint the exact source of the performance gap.

Several interesting and important trends were identified in the detailed efficiency analysis. By far the most significant contributors to the xenon-krypton performance gap were determined to be propellant utilization and beam divergence efficiency. Peak propellant utilization for xenon and krypton are approximately 90 and 85%, respectively. The beam divergence efficiency is approximately 8% better for xenon, meaning that beam divergence is an important and often overlooked feature in krypton performance.

There are several other factors that differentiate xenon and krypton performance. Krypton has superior dispersion efficiency than xenon with an ion velocity dispersion that has a 25% smaller full width at half maximum. This is related to the fact that ionization occurs farther upstream in the krypton case. Due to krypton's higher ionization potentials, krypton has a 2% better charge utilization than xenon; i.e., fewer multiply-charged ions.

Both propellants have the same average ion voltage and therefore the same acceleration utilization. Also both propellants have approximately the same current utilization although under many circumstances, krypton's current utilization is superior to xenon's. This may be due to the fact that krypton's region of high radial electron mobility is largely outside of the thruster resulting in fewer electron-wall collisions.

7.3 Krypton Internal Characterization

To better understand the specific components of the xenon-krypton efficiency gap, a detailed characterization of internal Hall thruster phenomena was conducted. The internal plasma properties that were measured include electron temperature, ion number density, plasma potential, and the electric fields. Internal phenomena include the Hall current, the acceleration zone, and the ionization zone. Different features in the magnetic field topology were also studied in conjunction with the internal characterization.

The electrons are isothermal along the magnetic field pathlines. This is expected since electrons diffuse freely along the magnetic field lines and are impeded across the field lines. The maximum electron temperature for xenon at 300 V peaks between 30-40 eV. For the 500-V cases, the electron temperature peaks between 45-50 eV and 50-60 eV for xenon and krypton, respectively. Krypton has a slightly higher maximum electron temperature than xenon and this is likely due to fewer ionizing collisions in the Hall current region. The higher electron temperature may also be related to the high radial electron mobility region being located outside of the discharge channel, which results in fewer wall losses. The region of high electron temperature is located at approximately the same locations and has similar dimensions for both propellants. The high electron temperature region begins upstream of the acceleration zone and extends into the acceleration zone. The electron temperature gradient in the discharge channel is linearly dependent on plasma potential and equal to 0.07-0.08 eV/V and 0.08-0.095 eV/V for xenon and krypton, respectively.

The maximum ion number densities are approximately 3×10^{12} and 4×10^{12} cm^{-3} for xenon and krypton, respectively. The ion number density contours show that the plasma lens magnetic field topology focuses ions toward the center of the discharge channel as expected, which results in a substantial contribution to the reduction of beam divergence. For xenon cases, ions are focused directly out of the thruster while the krypton cases are directed more toward the thruster axis.

The location and magnitude of the Hall current was successfully shown for several operating conditions. The maximum Hall current density was shown to be between 1-2 MA/m^2. Due to the magnetic mirror, the Hall current is focused in the center of the discharge channel near the exit. Krypton has a similar maximum Hall current peak located in the center of the discharge channel; however the krypton case peaks over a much smaller region in discharge channel. The total integrated Hall current is approximately the same for xenon and krypton operation points. The total Hall current ranges between 33 and 36 A and is approximately 3.5 to 4 times the discharge current.

The electron drift energy was calculated and compared for xenon and krypton propellant. The krypton case has peak electron energy of approximately 70 eV whereas xenon peaks around 60 eV. The region of high electron energy is also slightly larger for the krypton case. This larger electron drift energy is related to the lower magnetic field necessary for krypton operation, and may explain partially why krypton prefers weaker magnetic fields for stable and efficient operation.

A combination of a numerical fluid dynamics code, number density trends, and an ionization collision rate calculation were used to quantify the ion production rate and to define the location of the ionization zone. For both cases, the Hall current plays an important role in the ionization process; however the Hall current ionization is much more significant in the xenon cases. For higher voltage operation, ionization begins farther upstream. This is partially due to the fact that higher voltage operation has higher electron temperatures and a wider peak electron temperature structure. Magnetic field topology also has much to do with upstream ionization. When ionization occurs upstream of the Hall current region, the peak ionization is located at the center of the magnetic mirror.

The acceleration zone was mapped for both propellants using the floating emissive probe measurements. Krypton's acceleration zone is less focusing, located farther downstream, and is wider than the xenon case. This results in a large portion of the krypton acceleration that is located outside of the discharge channel, and may explain krypton's larger beam divergence, which is an important contributing factor to the xenon-krypton efficiency gap. Although krypton is less focused than xenon, krypton ions are still focused toward the axis of the thruster due the plasma lens. Krypton's acceleration zone shape and location are due to its weaker magnetic field topology.

When krypton propellant is operated with the same magnetic field topology as the xenon case, it shares a very similar acceleration zone shape and location. This means that the acceleration zone location and shape is not a function of propellant and the establishment of the electric field is an electron behavior. Unfortunately, when the magnetic field topology for krypton is matched to the xenon case, the discharge current oscillations increase and there was greater instability in the breathing mode.

7.4 Design Suggestions for Krypton Thrusters

Based on the findings from the performance analysis and the internal discharge channel characterization, several design and operation improvements are possible to optimize krypton performance. Essentially, the goal of these suggestions is to optimize efficiency by creating an intense ionization zone upstream of a highly focusing acceleration zone.

Krypton performance is optimized for high discharge voltage and increased anode flow rate. Higher discharge voltages increase electron temperatures and ionization collision cross sections, which increase the probability of an ionizing electron-atom collision. It was shown that at discharge voltages below 300 V, it is almost impossible for krypton to rival xenon in performance. A discharge voltage of at least 500 V is suggested for optimized krypton performance.

As anode flow rate increases, the neutral density and hence ionization rate also increase. However, above a certain anode flow rate the anode efficiency plateaus and the benefit of higher flow rate is limited. Anode efficiency plateaus for an anode flow rate corresponding to an α value greater than 0.015 mg/(mm-s), where α is a function of flow rate and discharge channel dimensions $\left(\alpha = \dot{m}_a b / A_{ch}\right)$. This flow rate corresponds to a current density of about 80 mA/cm^2 and a flow density of around 1 sccm/cm^2. These numbers correspond to a discharge voltage above 500 V. At lower discharge voltages, the minimum flow rate is higher.

Performance benefits can be achieved by modifying the physical dimensions and design of the Hall thruster. A longer discharge channel will lead to longer propellant residence times, which will improve the propellant utilization. By increasing the channel length, effectively the scale of the thruster would increase including the length of the magnetic field topology, the ionization zone, and the acceleration zone. Propellant utilization can also be improved by reducing discharge channel area for a given anode flow rate to increase the neutral density.

Different propellant injection schemes could potentially aid in the ionization process of krypton. Different methods of propellant injects may produce more uniform neutral densities and improve propellant utilization. Thruster thermal management may be an effective means to reduce neutral atom temperature and increase neutral residence time.

There could potentially be several magnetic field design features that could improve krypton performance. Although these features are not unique to krypton performance alone, they are particularly important for the optimization of krypton propellant. One basic feature true to all Hall thrusters is that the magnetic field topology should be very symmetric about the discharge channel centerline.

Due to krypton's large beam divergence, the magnetic topology should have a very strong plasma lens. Increased curvature is important in the entire discharge current although most important in the region of peak acceleration. The curvature in the regions where the centerline magnetic field is equal to 70-90% of the peak centerline magnetic field most directly impacts the focusing of the magnetic field since this marks the start of the acceleration zone.

The magnetic mirror is very important in improving the ionization rate in Hall thrusters. The magnetic mirror should be maximized in the rear of the discharge channel. This requires having a very low magnetic field in the rear of the discharge channel and a very strong magnetic field near the exit of the thruster.

Peak magnetic field strength is very important in krypton Hall thrusters. Krypton propellant appears to favor weaker magnetic fields because of the enhancement in $E \times B$ drift energy associated with weaker magnetic fields. As magnetic field is increased, the ionization process can becomes less stable resulting in larger oscillations in the breathing mode. However, larger peak magnetic fields improve the ionization and acceleration process by increasing the magnetic mirror, the axial gradient in magnetic field, and decreasing beam divergence. The rear of the discharge channel near the anode should have relatively weak magnetic fields to enhance ionization and the magnetic field should increase quickly in the peak magnetic field region. For future designs of laboratory krypton thrusters, the Hall thruster should be able to operate over a large range of magnetic field strengths from moderately weak to as strong as possible. This range of magnetic field strengths should not come at the expense of symmetry or quality in the magnetic field topology.

It may be possible to increase the length of the acceleration and ionization zone through careful magnetic field topology design. A wider peak magnetic field structure should lengthen the acceleration zone and Hall current region. A longer Hall current region will increase the likelihood of krypton ionization due to the Hall current. The ionization zone is commonly considered to be located in the region of peak axial magnetic field gradient. The magnetic field topology should be designed to lengthen and increase the intensity of this region. This should increase the residence time of the neutrals in the ionization zone. The axial magnetic field gradient can be enhanced by using a small or reversed field near the anode and a large peak magnetic field.

7.5 General Hall Thruster Findings

The investigations presented in this thesis yielded several findings that are important to Hall thruster physics in general but not specific to krypton Hall thrusters. These findings are summarized below.

The plasma lens was shown to significantly aid in the focusing of ions and the equipotential lines are shown to be well correlated with the magnetic field pathlines. In most cases, the radial electric field is equal to or greater than 20% of the maximum axial electric field. This focusing is also improved with the use of the trim coil, which increases the field line curvature. The trim coil cases focus ions directly out of thruster whereas the non-trim coil cases direct ions more toward the centerline of the thruster. This effect has strong implications for future Hall thruster designs and thruster life.

The trim coil offers several other performance benefits. The overall anode efficiency is improved by 1-6% when the trim coil is energized. The trim coil was also shown to improve ionization rate in the upstream region. The increased magnetic mirror results in additional ionization that does not occur in the non-trim coil cases. However, for the xenon cases investigated, the enhanced ionization had little effect on the overall propellant utilization. The trim coil improves the electron dynamics by decreasing the electron current to the anode. The trim coil also improves the acceleration efficiency and ion dispersion efficiency.

This thesis found significant evidence to suggest that the charge exchange collision plays a significant role in the thruster plume. This is very likely the cause of the increase in neutral velocity observed in laser-induced fluoresence measurements.

The electron motion and specifically the Hall parameter inside the discharge channel was studied in great detail. The experimentally determined collision rate ranged between 10^7 and 10^8 Hz although in the peak acceleration zone the collision rate drops to approximately 10^6 Hz. The experimental Hall parameter ranges from tens to a few hundred in the Hall current region.

Upstream of the acceleration zone, the experimental collision rate agrees well with both Bohm and classical collision rates. In the near anode region the Hall parameter is on the order of tens and is approximately equal to both the Bohm and classical Hall parameters.

In the Hall current region, the experimental collision rate is very low. In the Hall current region, classical collision rate follows a similarly shaped trend as the experimental collision rate although greatly under-predicts the experimental collision rate alone. In the Hall current region and acceleration zone, the classical approach over-predicts the Hall parameter and the Bohm approach grossly under-predicts the Hall parameter. The Bohm mobility is particularly poor in the acceleration zone and is unable to predict the high Hall parameter region. Again, both the experimental and classical Hall parameters follow a similar shaped trend although the classical Hall parameter over-predicts the experimental Hall Parameter. The classical Hall parameter increases in the acceleration zone to a few thousand. The experimental Hall parameter peaks in the same location although it reaches a maximum of only a few hundred.

Downstream of the acceleration zone, the experimental mobility is greater than either the classical or the Bohm mobility alone. In the downstream region, the experimental Hall parameter is less than 10. The downstream mobility is likely a combination of classical and Bohm-like effects.

The azimuthal electron current was also studied in some detail. It was shown that the E×B current is by far the most significant portion of the azimuthal current. The maximum diamagnetic current is approximately 20% of maximum E×B current. Therefore, the diamagnetic current is a second-order effect although it is still significant. The curvature drift is on the order of only a few percent of the maximum E×B drift. Two finite Larmor radius electron particle drifts were also studied. Both the nonuniform electric field drift and the gradient drift are insignificant compared to the E×B drift. Not surprisingly, the Hall current region corresponds well with the peak electric field region.

Analyses of several magnetic field topological features were conducted using simple analysis techniques. These analyses were proposed in order to aid in the design and optimization of Hall thrusters while still in the development stage. These analyses can be used to test the symmetry of the magnetic field, optimize upstream ionization, and to roughly estimate the location and shape of the acceleration zone.

The magnetic mirror was studied and shown to enhance the ionization process in the discharge channel. Excluding the ionization due to the Hall current, the perpendicular gradient in magnetic field was also shown to roughly estimate the location of the ionization zone.

The location of the acceleration zone was studied by considering the electron impedance across the streamline. This analysis gives a rough estimate of the start of the acceleration zone. Since, the equipotential lines closely match the magnetic field lines; the shape of the acceleration zone can also be estimated. The peak acceleration zone was shown to begin at the point where the centerline magnetic field is between 70-90% of the peak centerline magnetic field strength. The peak acceleration zone ends at the point where the centerline magnetic field is between 75-95% of the peak magnetic field. The locations of the acceleration zone start and end have a linear dependence with peak magnetic field strength. The location of the of the acceleration zone moves upstream with increased peak magnetic field and beam divergence is reduced. With the location of the start of the acceleration zone known, it is possible to quantify the curvature and focusing nature of the field lines in the acceleration zone.

7.6 Suggestions for Future Work

The investigations presented in this thesis clearly define the motivation for krypton propellant in Hall thrusters, the reasons for the krypton performance gap, and several design suggestions that can be implemented to improve krypton performance and finally make krypton a strong option for space missions. These investigations also offer a detailed picture of internal Hall thruster physics and help to better explain the complex phenomena internal to the discharge channel. The following is a list of future work that is the next logical step following these present results.

1. A new krypton Hall thruster implementing the suggestions put forth in this thesis should be designed, built, and studied.
2. Krypton propellant should be tested in Hall thrusters that employ a separate propellant injector and anode. This should result in lower neutral temperatures and potentially increase propellant utilization.
3. The breathing mode should be studied in much greater detail and characterized for different propellants. Effort should be focused on how to control and decrease the discharge current oscillations. Krypton's poor discharge current stability at xenon magnetic field settings is the last remaining piece of the krypton performance puzzle that should be addressed.
4. An internal investigation using high speed data acquisition should be conducted to characterize the oscillations in the discharge channel, the breathing mode, and also to provide important information about electron mobility. This could be achieved using a variety of internal diagnostics that take instantaneous measurements. For example a floating emissive probe and faster single Langmuir probe could be employed using high speed data acquisition.[183] Probe induced perturbations would be particularly important in such an investigation.

Appendix A.

NASA-173Mv1 Performance Data

Table A-1. NASA-173Mv1 Performance Data Using Xenon Propellant, A

Point #	Pressure, Torr	V_k, V	V_D, V	I_D, A	Discharge Power, W	Anode Flow, mg/s	Cathode Flow, mg/s	Inner Coil Current, A	Outer Coil Current, A	Trim Coil Current, A	Total Power, W	Thrust mN	Anode I_{sp}, s	Anode Effic., %
A-X-1	502×10^{-6}	-11.5	300	9.23	2769	10.00	1.00	1.86	2.17	0.00	2800	179	1826	57.9
A-X-2	5.02×10^{-6}	-12.2	300	8.83	2649	10.00	1.00	1.85	2.17	-0.51	2682	180	1836	61.2
A-X-3	5.02×10^{-6}	-12.5	400	9.30	3720	10.00	1.00	2.63	2.05	0.00	3758	212	2162	60.4
A-X-4	5.02×10^{-6}	-12.7	400	9.08	3632	10.00	1.00	2.61	2.23	-0.62	3673	216	2203	64.3
A-X-5	5.04×10^{-6}	-11.3	500	9.59	4795	10.00	1.00	2.85	2.62	0.00	4863	243	2476	61.6
A-X-6	5.04×10^{-6}	-12.4	500	9.23	4615	10.00	1.00	2.85	2.81	-0.87	4697	247	2517	66.1
A-X-7	5.04×10^{-6}	-11.7	600	9.68	5808	10.00	1.00	2.68	2.67	0.00	5883	266	2711	60.9
A-X-8	5.04×10^{-6}	-12.9	600	9.44	5664	10.00	1.00	3.11	3.35	-1.07	5784	271	2762	64.8
A-X-9	5.04×10^{-6}	-11.5	700	9.82	6874	10.00	1.00	2.72	2.72	0.00	6955	286	2915	59.5
A-X-10	5.04×10^{-6}	-11.5	700	9.71	6797	10.00	1.00	2.70	2.79	-0.79	6884	287	2925	60.6
A-X-11	5.04×10^{-6}	-11.2	800	9.98	7984	10.00	1.00	3.06	2.96	0.00	8093	304	3098	57.9
A-X-12	5.04×10^{-6}	-11.8	800	10.00	8000	10.00	1.00	2.84	3.34	-1.03	8114	309	3149	59.7
A-X-13	6.07×10^{-6}	-11.9	500	12.00	6000	12.34	1.23	2.90	2.99	-1.30	6089	305	2519	62.8
A-X-14	6.07×10^{-6}	-11.5	500	12.00	6000	12.33	1.23	2.91	2.58	0.00	6066	301	2489	61.2
A-X-15	5.02×10^{-6}	-11.8	600	10.00	6000	10.24	1.02	2.79	2.90	-1.23	6052	278	2767	62.9

Table A-2. NASA-173Mv1 Performance Data Using Xenon Propellant, B

Point #	Pressure, Torr	V_k, V	V_D, V	I_D, A	Discharge Power, W	Anode Flow, mg/s	Cathode Flow, mg/s	Inner Coil Current, A	Outer Coil Current, A	Trim Coil Current, A	Total Power, W	Thrust mN	Anode I_{sp}, s	Anode Effic., %
A-X-16	5.02×10^{-6}	-11.6	600	10.00	6000	10.20	1.02	2.79	2.48	0.00	6069	276	2759	62.2
A-X-17	4.66×10^{-6}	-12.2	700	8.57	5999	8.94	0.90	2.81	2.95	-1.48	6094	258	2940	62.0
A-X-18	4.31×10^{-6}	-11.3	700	8.57	5999	8.74	0.90	2.69	2.68	0.00	6082	248	2893	58.7
A-X-19	7.46×10^{-6}	-11.5	500	16.00	8000	15.62	1.56	2.80	3.02	0.00	8095	402	2624	64.7
A-X-20	7.46×10^{-6}	-12.4	500	16.00	8000	15.66	1.57	2.80	3.42	-1.08	8118	405	2637	65.5
A-X-21	5.7×10^{-6}	-11.1	700	11.43	8001	11.38	1.14	2.90	2.87	0.00	8101	334	2991	61.2
A-X-22	5.7×10^{-6}	-11.2	700	11.43	8001	11.28	1.13	2.95	3.06	-1.53	8117	335	3028	62.2

Table A-3. NASA-173Mv1 Performance Data Using Krypton Propellant, A

Point #	Pressure, Torr	V_k, V	V_D, V	I_D, A	Discharge Power, W	Anode Flow, mg/s	Cathode Flow, mg/s	Inner Coil Current, A	Outer Coil Current, A	Trim Coil Current, A	Total Power, W	Thrust mN	Anode I_{sp}, s	Anode Effic., %
A-K-1	4.39×10^{-6}	-12.9	300	7.31	2193	6.38	0.64	1.55	1.73	0.00	2214	113	1805	45.6
A-K-2	4.34×10^{-6}	-13.2	300	7.12	2136	6.38	0.64	1.55	1.73	-0.22	2157	113	1805	46.8
A-K-3	4.34×10^{-6}	-13.3	400	7.57	3028	6.38	0.64	1.53	1.94	0.00	3054	133	2125	45.8
A-K-4	4.34×10^{-6}	-13.5	400	7.35	2940	6.38	0.64	1.53	1.94	-0.19	2953	134	2141	47.9
A-K-5	4.34×10^{-6}	-13.3	500	8.10	4050	6.38	0.64	1.55	2.12	0.00	4080	157	2508	47.7
A-K-6	4.34×10^{-6}	-14.8	500	7.30	3650	6.38	0.64	1.55	2.13	-0.41	3671	155	2476	51.6
A-K-7	4.34×10^{-6}	-13.7	600	8.18	4908	6.38	0.64	1.63	2.22	0.00	4947	183	2923	53.5
A-K-8	4.34×10^{-6}	-14.7	600	7.55	4530	6.38	0.64	1.63	2.22	-0.19	4567	183	2923	57.9
A-K-9	4.34×10^{-6}	-12.7	700	8.40	5880	6.38	0.64	2.22	2.23	0.00	5933	189	3019	47.6
A-K-10	4.34×10^{-6}	-13.7	700	7.81	5467	6.38	0.64	2.22	2.23	-0.35	5518	191	3051	52.3
A-K-11	4.34×10^{-6}	-13.2	800	8.42	6736	6.38	0.64	2.17	2.60	0.00	6802	210	3355	51.3
A-K-12	4.34×10^{-6}	-13.8	800	7.94	6352	6.38	0.64	2.18	2.60	-0.46	6416	212	3386	55.4
A-K-13	5.00×10^{-6}	-12.8	300	9.23	2769	7.34	0.73	1.47	1.48	0.00	2783	133	1847	43.5
A-K-14	4.89×10^{-6}	-13.7	300	8.83	2649	7.35	0.73	1.75	1.47	-0.41	2668	133	1845	45.4
A-K-15	4.79×10^{-6}	-13.3	400	9.30	3720	7.24	0.72	1.63	1.74	0.00	3742	165	2322	50.5

Table A-4. NASA-173Mv1 Performance Data Using Krypton Propellant, B

Point #	Pressure, Torr	V_k, V	V_D, V	I_D, A	Discharge Power, W	Anode Flow, mg/s	Cathode Flow, mg/s	Inner Coil Current, A	Outer Coil Current, A	Trim Coil Current, A	Total Power, W	Thrust mN	Anode I_{sp}, s	Anode Effic., %
A-K-16	4.86×10^{-6}	-14.5	400	9.08	3632	7.51	0.75	1.77	1.91	-0.52	3663	169	2294	52.4
A-K-17	4.86×10^{-6}	-13.3	500	9.59	4795	7.46	0.75	1.76	2.14	0.00	4827	189	2582	49.9
A-K-18	5.06×10^{-6}	-15.0	500	9.23	4615	7.81	0.78	1.76	2.23	-0.52	4652	202	2636	56.6
A-K-19	5.06×10^{-6}	-15.2	500	9.23	4615	7.81	0.78	1.76	2.23	-0.43	4657	203	2649	57.2
A-K-20	4.86×10^{-6}	-13.3	600	9.68	5808	7.46	0.75	1.95	2.14	0.00	5851	211	2885	51.4
A-K-21	5.06×10^{-6}	-14.5	600	9.44	5664	7.75	0.78	1.95	2.14	-0.46	5706	222	2920	56.1
A-K-22	4.96×10^{-6}	-14.4	700	9.82	6874	7.51	0.75	2.17	2.89	0.00	6950	232	3148	52.1
A-K-23	5.20×10^{-6}	-14.6	700	9.71	6797	7.81	0.78	2.33	2.48	-0.56	6862	244	3186	56.1
A-K-24	4.95×10^{-6}	-14.2	800	9.98	7984	7.55	0.76	2.20	2.78	0.00	8043	246	3322	50.2
A-K-25	5.21×10^{-6}	-14.5	800	10.00	8000	7.90	0.79	2.20	2.77	-0.75	8069	270	3484	57.7
A-K-26	6.23×10^{-6}	-12.2	500	12.02	6010	8.97	0.90	1.97	2.12	0.00	6054	241	2739	53.9
A-K-27	4.34×10^{-6}	-14.3	500	12.00	6000	9.62	0.96	1.83	2.58	-0.77	6053	259	2743	58.1
A-K-28	5.00×10^{-6}	-12.2	600	10.00	6000	7.58	0.76	2.20	2.41	0.00	6050	217	2919	51.8
A-K-29	5.20×10^{-6}	-13.1	600	10.00	6000	8.15	0.82	2.20	2.42	-0.76	6045	233	2915	55.5
A-K-30	4.40×10^{-6}	-13.7	700	8.57	5999	6.61	0.66	2.03	2.81	0.00	6057	199	3067	49.9

Table A-5. NASA-173Mv1 Performance Data Using Krypton Propellant, C

Point #	Pressure, Torr	V_k, V	V_D, V	I_D, A	Discharge Power, W	Anode Flow, mg/s	Cathode Flow, mg/s	Inner Coil Current, A	Outer Coil Current, A	Trim Coil Current, A	Total Power, W	Thrust mN	Anode I_{sp}, s	Anode Effic., %
A-K-31	4.64×10^{-6}	-13.9	700	8.57	5999	6.98	0.70	2.32	2.94	0.51	6080	215	3140	55.2
A-K-32	7.24×10^{-6}	-12.6	500	16.02	8010	11.42	1.14	2.48	2.47	0.00	8071	315	2812	54.2
A-K-33	7.24×10^{-6}	-13.4	500	16.02	8010	11.82	1.16	2.66	2.76	1.84	8061	337	2907	60.0
A-K-34	6.23×10^{-6}	-12.5	600	13.34	8004	9.65	0.97	2.22	2.30	0.00	8063	284	2999	52.2
A-K-35	6.23×10^{-6}	-12.9	600	13.33	7998	9.90	0.99	2.22	2.29	0.72	8059	294	3028	54.6
A-K-36	5.20×10^{-6}	-13.6	700	11.43	8001	8.47	0.85	2.52	2.86	0.00	8059	273	3287	55.0
A-K-37	5.72×10^{-6}	-14.2	700	11.42	7994	8.94	0.89	2.20	2.52	0.51	8061	284	3237	56.4
A-K-38	5.20×10^{-6}	-13.2	500	10.49	5245	7.87	0.79	1.99	1.98	0.00	5284	207	2682	51.9
A-K-39	5.20×10^{-6}	-14.8	500	9.60	4800	7.87	0.79	1.84	2.21	0.72	4843	208	2694	57.3
A-K-40	4.43×10^{-6}	-13.9	600	8.60	5160	6.51	0.65	1.78	2.17	0.00	5201	181	2836	48.8
A-K-41	4.43×10^{-6}	-15.2	600	8.01	4806	6.53	0.65	2.04	2.17	0.57	4851	182	2842	52.8
A-K-42	3.79×10^{-6}	-14.7	700	7.30	5110	5.59	0.57	2.10	2.26	0.00	5162	164	2992	47.1
A-K-43	3.84×10^{-6}	-15.4	700	7.05	4935	5.70	0.57	2.20	2.25	0.57	4985	168	3002	50.1
A-K-44	6.22×10^{-6}	-12.6	500	13.92	6960	9.97	1.00	2.27	2.18	0.00	7013	270	2761	52.5
A-K-45	6.22×10^{-6}	-13.4	500	13.17	6585	9.99	1.00	2.28	2.17	1.38	6637	269	2745	55.0

Table A-6. NASA-173Mv1 Performance Data Using Krypton Propellant, D

Point #	Pressure, Torr	V_k, V	V_D, V	I_D, A	Discharge Power, W	Anode Flow, mg/s	Cathode Flow, mg/s	Inner Coil Current, A	Outer Coil Current, A	Trim Coil Current, A	Total Power, W	Thrust mN	Anode I_{sp}, s	Anode Effic., %
A-K-46	5.20×10^{-6}	-12.6	600	11.63	6978	8.50	0.85	2.47	2.46	0.00	7037	248	2973	51.8
A-K-47	5.71×10^{-6}	-13.9	600	11.04	6624	8.61	0.86	2.39	2.54	1.23	6694	253	2994	56.1
A-K-48	4.84×10^{-6}	-14.0	700	9.75	6825	7.26	0.73	2.27	2.74	0.00	6895	225	3160	51.1
A-K-49	4.79×10^{-6}	-14.2	700	9.19	6433	7.20	0.72	2.52	2.73	1.13	6517	230	3257	57.1
A-K-50	2.91×10^{-6}	-15.1	1200	5.00	6000	3.90	0.58	2.76	3.20	0.00	6107	156	4074	52.0
A-K-51	2.91×10^{-6}	-15.8	1200	5.06	6072	3.98	0.58	2.76	3.20	1.23	6180	168	4302	58.4
A-K-52	3.11×10^{-6}	-14.6	1200	5.83	6996	4.34	0.58	2.47	2.90	0.00	7088	178	4179	52.1
A-K-53	3.32×10^{-6}	-14.2	1200	5.82	6984	4.67	0.58	2.76	2.89	1.36	7088	193	4210	57.1
A-K-54	3.48×10^{-6}	-14.1	1200	6.67	8004	5.04	0.58	2.84	2.78	0.00	8109	198	4005	48.6
A-K-55	3.73×10^{-6}	-14.4	1200	6.67	8004	5.27	0.58	2.77	2.78	1.38	8110	214	4138	54.3

Appendix B.

UM/AFRL P5 Performance Data

Table B-1. UM/AFRL P5 Performance Data Using Xenon Propellant

Point #	Pressure, Torr	V_k, V	V_D, V	I_D, A	Discharge Power, W	Anode Flow, mg/s	Cathode Flow, mg/s	Inner Coil Current, A	Outer Coil Current, A	Thrust mN	Anode I_{sp}, s	Anode Effic., %
B-X-1	4.56×10-6	-13.4	150	11.89	1782	10.00	0.98	1.09	1.50	117	1194	38.5
B-X-2	4.56×10-6	-13.2	150	11.83	1775	10.00	0.98	1.09	1.50	109	1110	33.4
B-X-3	4.30×10-6	-14.0	200	7.33	1466	6.84	0.98	1.30	1.40	90	1347	40.8
B-X-4	4.35×10-6	-13.8	200	14.65	2930	12.71	1.27	1.45	1.85	170	1361	38.7
B-X-5	4.61×10-6	-15.6	200	4.74	948	4.88	0.98	1.05	1.41	52	1084	29.1
B-X-6	4.56×10-6	-14.8	200	11.00	2201	10.00	0.98	1.48	1.41	131	1339	39.2
B-X-7	4.65×10-6	-13.7	200	11.08	2217	10.00	0.98	1.48	1.41	133	1357	39.9
B-X-8	4.56×10-6	-16.6	300	10.18	3057	10.01	0.98	1.85	2.40	173	1761	48.9
B-X-9	4.56×10-6	-15.6	400	10.16	4064	10.01	0.98	2.04	2.24	205	2086	51.6
B-X-10	4.65×10-6	-14.7	400	10.15	4060	10.00	0.98	2.09	2.30	210	2144	54.5
B-X-11	4.65×10-6	-14.2	500	10.68	5340	10.00	0.98	2.84	2.56	247	2522	57.3
B-X-12	3.57×10-6	-15.0	500	4.49	2245	4.88	0.98	1.26	2.90	109	2283	54.5
B-X-13	3.26×10-6	-15.2	500	3.60	1800	4.23	0.98	1.05	2.82	76	1824	37.6
B-X-14	5.35×10-6	-12.8	500	13.49	6745	12.71	1.27	2.37	3.01	306	2453	54.6
B-X-15	3.95×10-6	-13.2	502	7.36	3695	6.84	0.98	2.25	2.82	165	2462	54.0
B-X-16	4.65×10-6	-14.2	600	10.87	6522	10.00	0.98	2.09	3.97	263	2679	52.9
B-X-17	4.65×10-6	-12.7	700	11.12	7784	10.00	0.98	2.25	4.90	293	2986	55.1

Table B-2. UM/AFRL P5 Performance Data Using Krypton Propellant

Point #	Pressure, Torr	V_k, V	V_D, V	I_D, A	Discharge Power, W	Anode Flow, mg/s	Cathode Flow, mg/s	Inner Coil Current, A	Outer Coil Current, A	Thrust mN	Anode I_{sp}, s	Anode Effic., %
B-K-1	5.35×10^{-6}	-13.5	150	10.96	1644	6.38	0.62	0.85	1.05	59	599	16.5
B-K-2	5.30×10^{-6}	-17.6	200	9.60	1920	6.38	0.62	1.55	2.87	83	850	28.4
B-K-3	4.77×10^{-6}	-18.3	200	7.77	1554	5.30	0.62	1.55	2.85	59	721	20.9
B-K-4	4.77×10^{-6}	-18.3	200	7.77	1554	5.30	0.62	1.55	2.85	57	700	19.7
B-K-5	5.39×10^{-6}	-18.1	200	11.44	2288	7.48	0.75	1.72	2.86	97	840	27.3
B-K-6	3.86×10^{-6}	-18.7	200	4.97	994	3.74	0.62	1.20	2.09	37	645	18.5
B-K-7	5.90×10^{-6}	-17.7	200	13.84	2768	8.72	0.87	1.95	3.00	118	881	28.9
B-K-8	5.35×10^{-6}	-18.9	300	8.68	2606	6.38	0.62	1.40	2.70	109	1110	35.7
B-K-9	5.35×10^{-6}	-20.2	400	8.55	3420	6.38	0.62	1.41	2.70	132	1350	40.2
B-K-10	5.18×10^{-6}	-20.6	500	8.50	4250	6.38	0.62	1.51	3.15	156	1586	44.6
B-K-11	4.26×10^{-6}	-18.7	500	5.82	2910	4.36	0.62	1.10	3.05	101	1505	40.1
B-K-12	3.55×10^{-6}	-19.0	500	4.07	2035	3.12	0.62	0.92	1.85	59	1229	27.3
B-K-13	5.90×10^{-6}	-17.3	500	11.36	5680	8.10	0.81	1.65	3.50	206	1657	46.3
B-K-14	4.77×10^{-6}	-19.0	500	7.03	3515	5.28	0.62	1.25	3.25	122	1500	40.0
B-K-15	3.91×10^{-6}	-18.6	500	4.99	2495	3.74	0.62	1.00	3.00	78	1363	32.9
B-K-16	5.18×10^{-6}	-18.6	600	9.05	5430	6.38	0.62	1.73	3.06	180	1836	46.8

Appendix C.

Internal Emissive Probe Results

Table C-1. Additional Operation Points for Internal Emissive Probe Mapping

Point	Propel.	V_k, V	V_D, V	I_D, A	Anode Flow, mg/s	Cathode Flow, mg/s	IC Current, A	OC Current, A	TC Current, A	Thrust, mN	Anode Effic., %
C-1	Xe	-11.4	600	9.55	10.00	1.00	2.73	2.72	0.00	266	60.9
C-2	Kr	-14.8	500	7.78	6.38	0.64	1.57	2.16	0.00	157	47.7
C-3	Kr	-14.2	500	7.54	6.38	0.64	1.57	2.17	-0.41	155	51.6
C-4	Kr	-	500	9.39	7.35	0.74	1.79	2.18	0.00	189	49.9
C-5	Kr	-14.8	600	7.84	6.38	0.64	1.65	2.26	0.00	183	53.5
C-6	Kr	-14.6	600	7.49	6.38	0.64	1.65	2.26	-0.19	183	57.9
C-7	Kr	-13.3	600	9.55	7.36	0.74	1.98	2.18	0.00	211	51.4

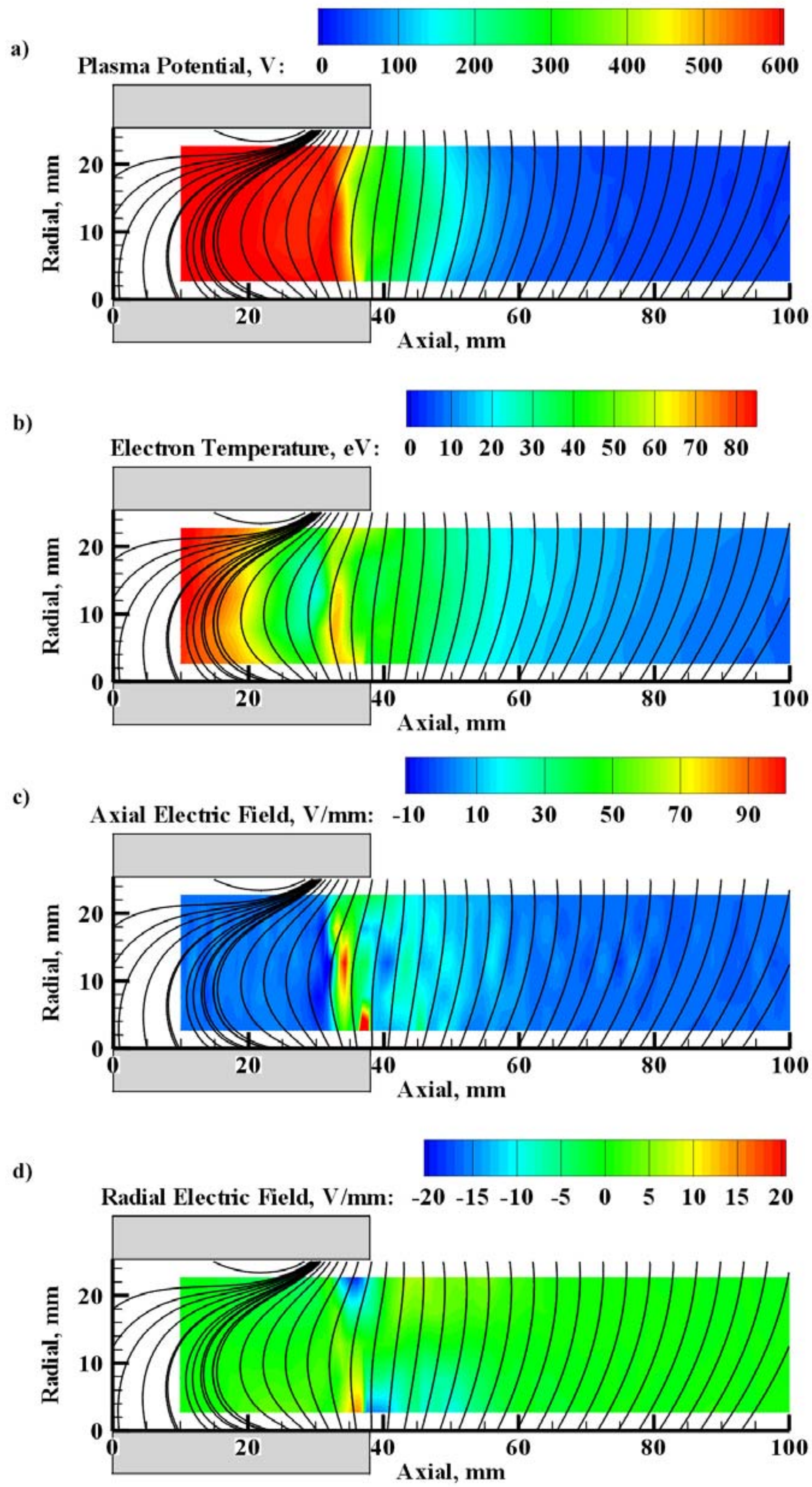

Figure C-1. Internal Emissive Probe Results for 600-V Xenon Operation without the Trim Coil (Point C-1)

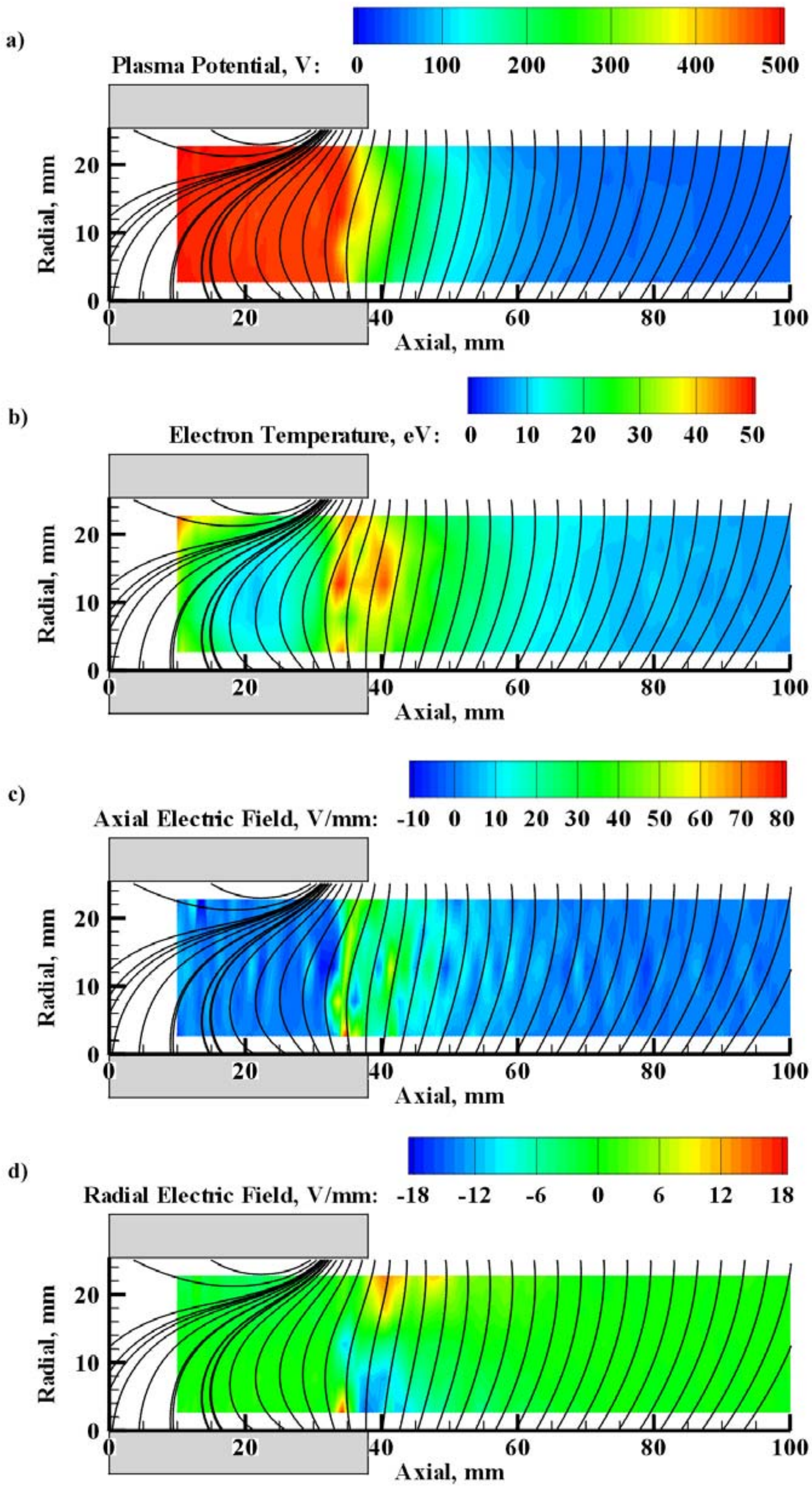

Figure C-2. Internal Emissive Probe Results for 500-V Krypton Operation without the Trim Coil and Matched Flow (Point C-2)

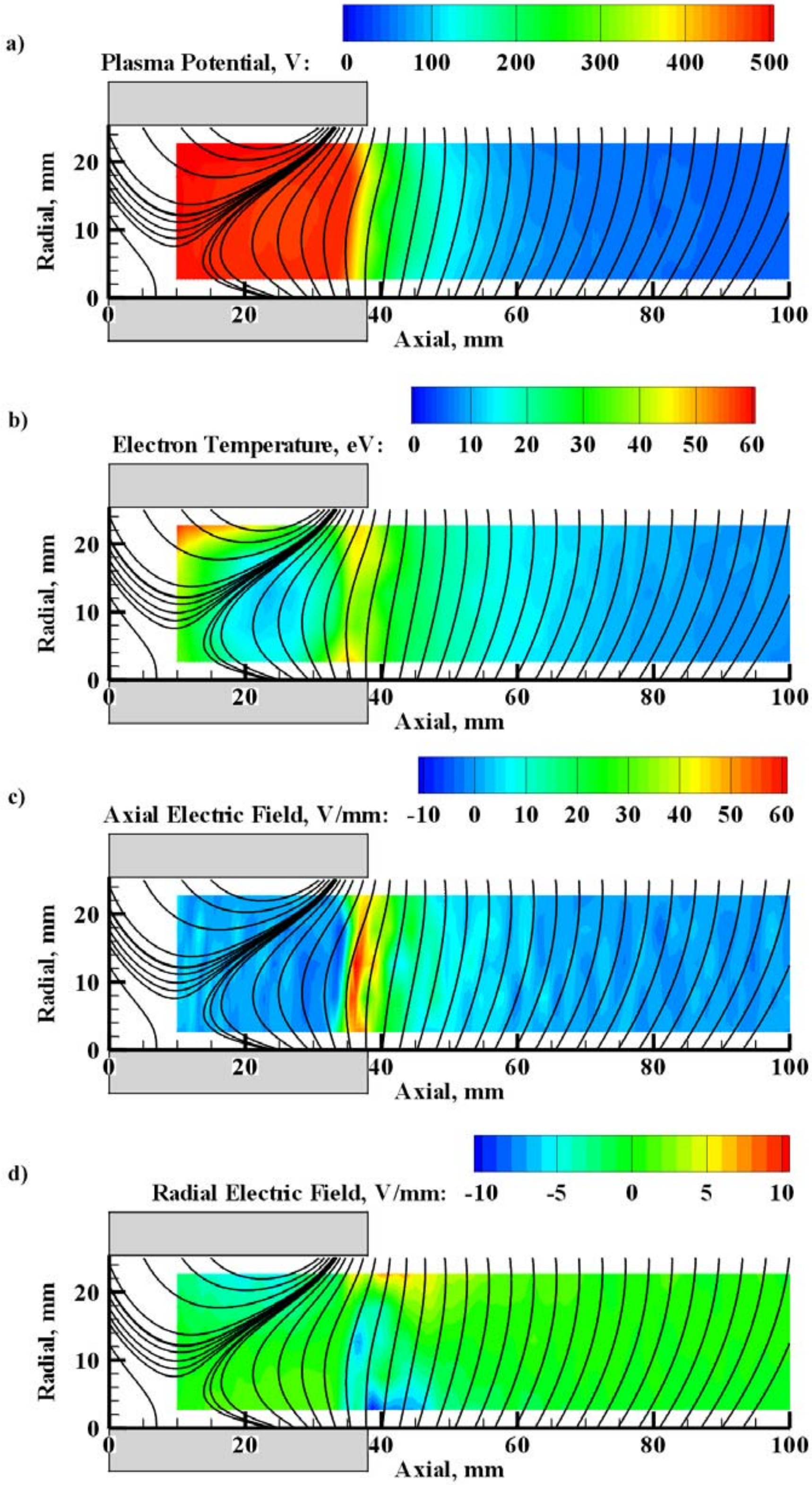

Figure C-3. Internal Emissive Probe Results for 500-V Krypton Operation with the Trim Coil and Matched Flow (Point C-3)

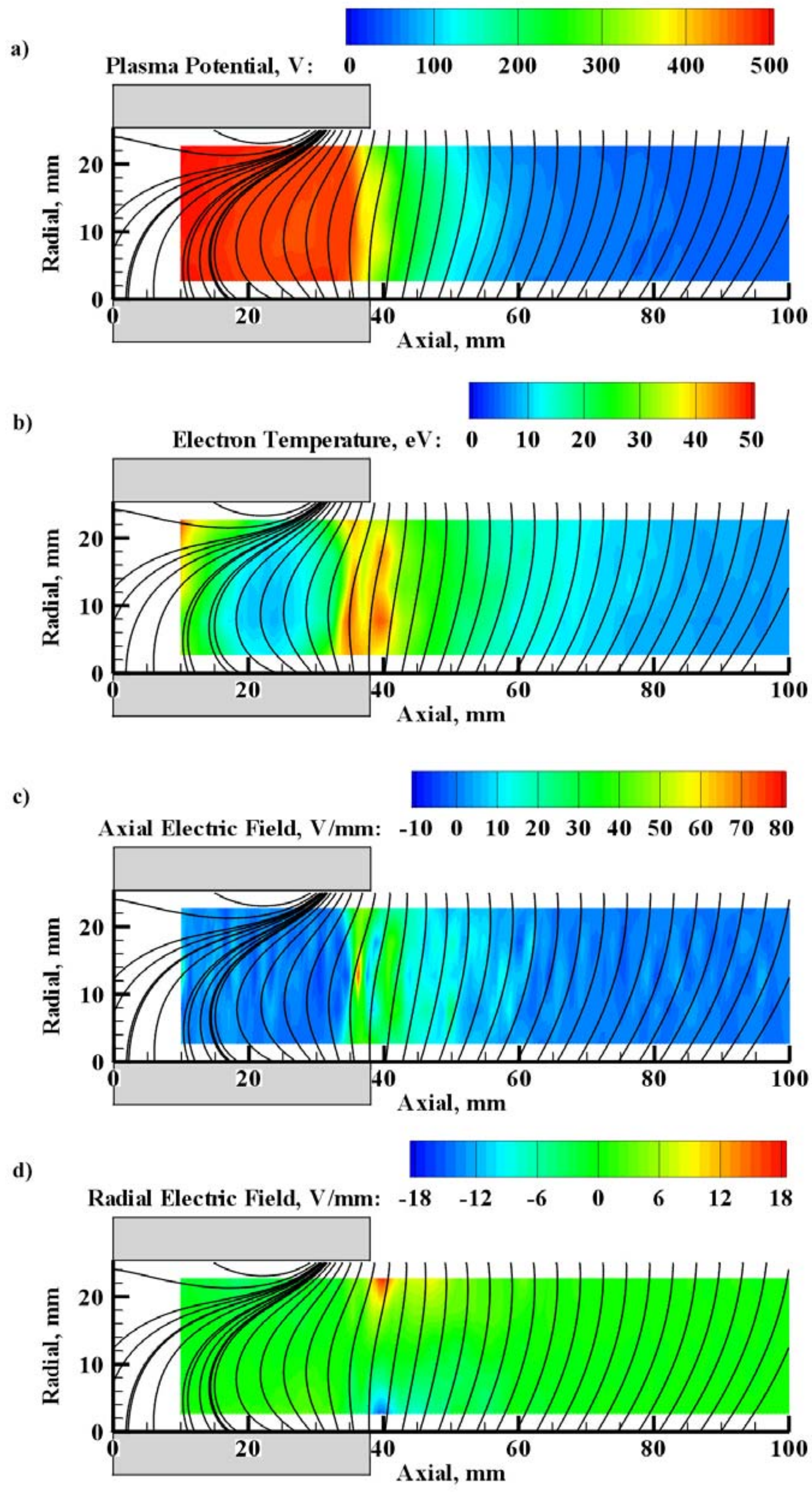

Figure C-4. Internal Emissive Probe Results for 500-V Krypton Operation without the Trim Coil and Matched Power (Point C-4)

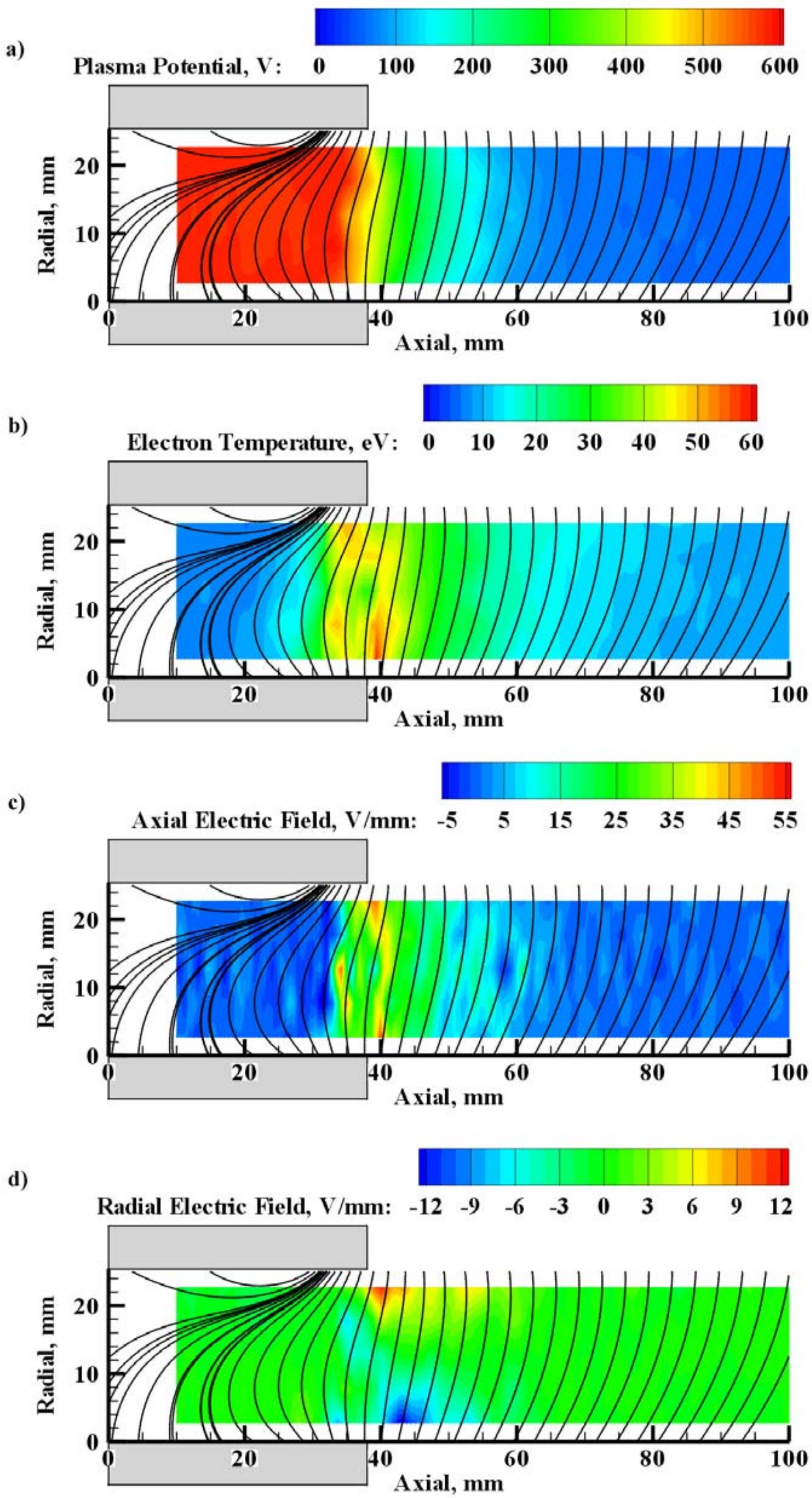

Figure C-5. Internal Emissive Probe Results for 600-V Krypton Operation without the Trim Coil and Matched Flow (Point C-5)

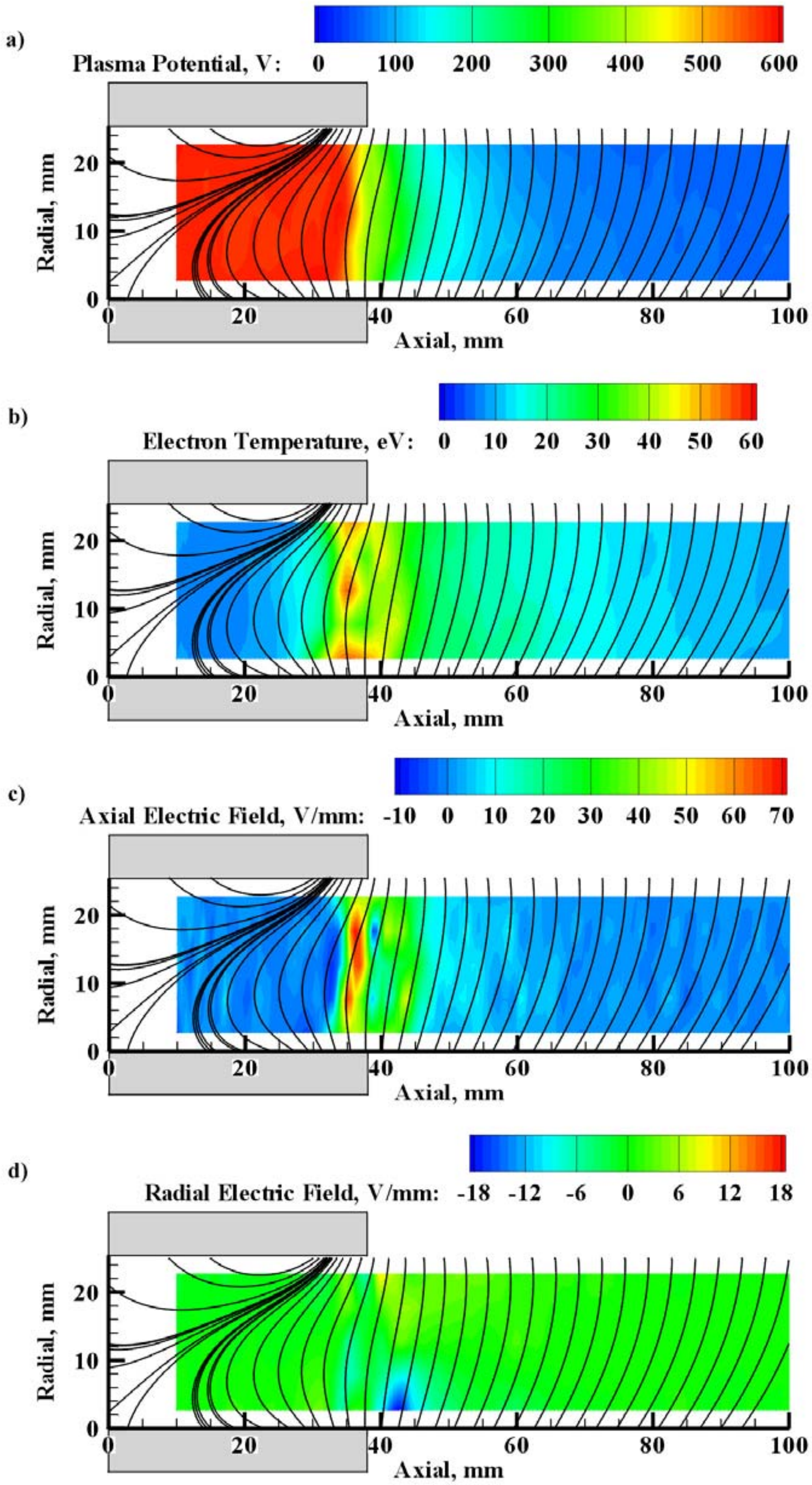

Figure C-6. Internal Emissive Probe Results for 600-V Krypton Operation with the Trim Coil and Matched Flow (Point C-6)

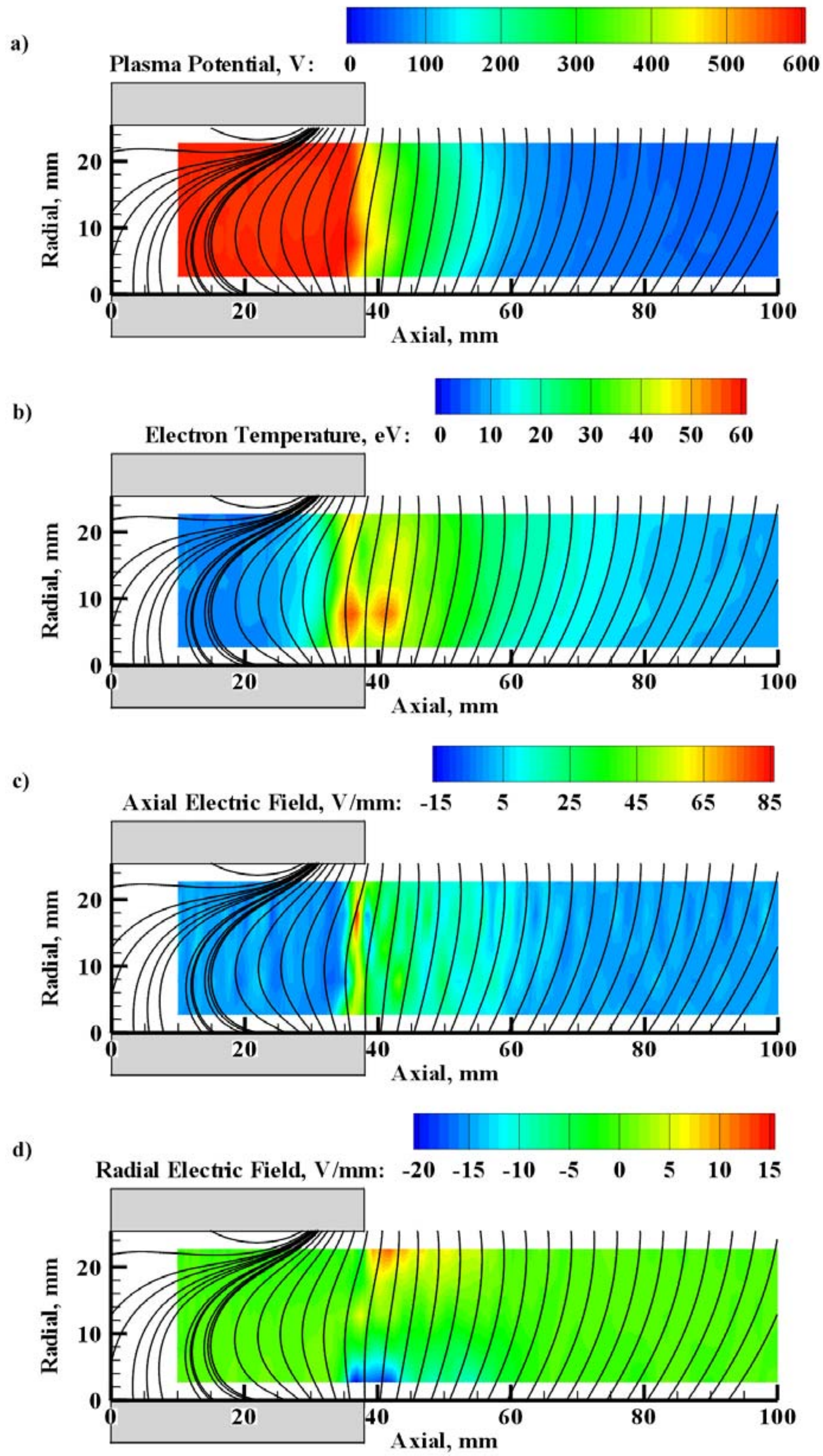

Figure C-7. Internal Emissive Probe Results for 600-V Krypton Operation without the Trim Coil and Matched Power (Point C-7)

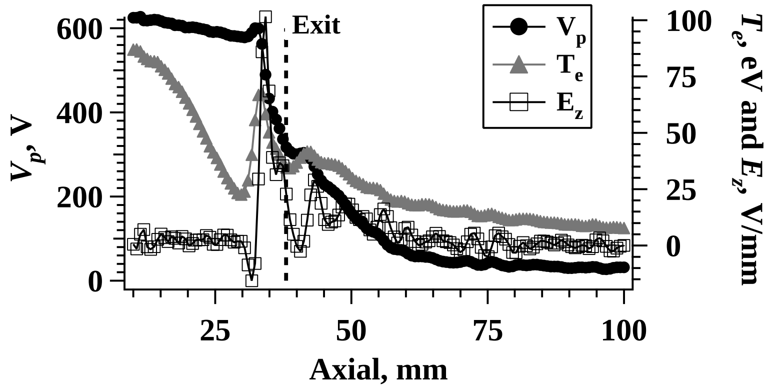

Figure C-8. Internal Langmuir Probe Centerline Properties for 500-V Krypton Operation with the Trim Coil and Matched Flow (Point C-1)

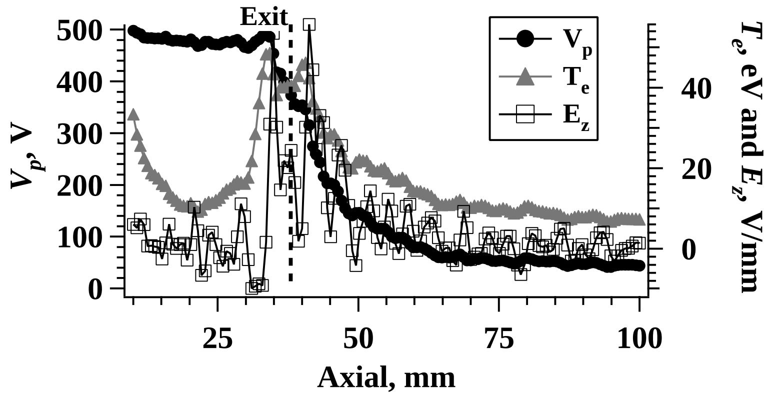

Figure C-9. Internal Langmuir Probe Centerline Properties for 500-V Krypton Operation with the Trim Coil and Matched Flow (Point C-2)

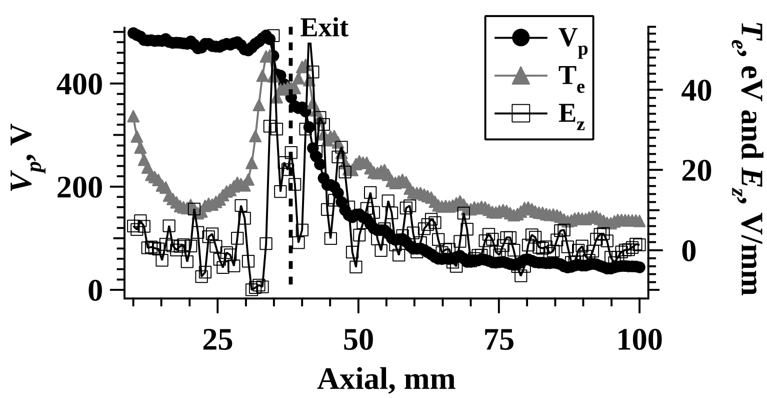

Figure C-10. Internal Langmuir Probe Centerline Properties for 500-V Krypton Operation with the Trim Coil and Matched Flow (Point C-3)

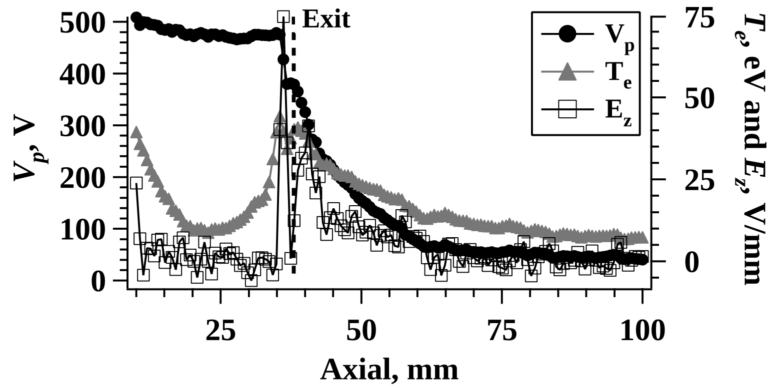

Figure C-11. Internal Langmuir Probe Centerline Properties for 500-V Krypton Operation with the Trim Coil and Matched Flow (Point C-4)

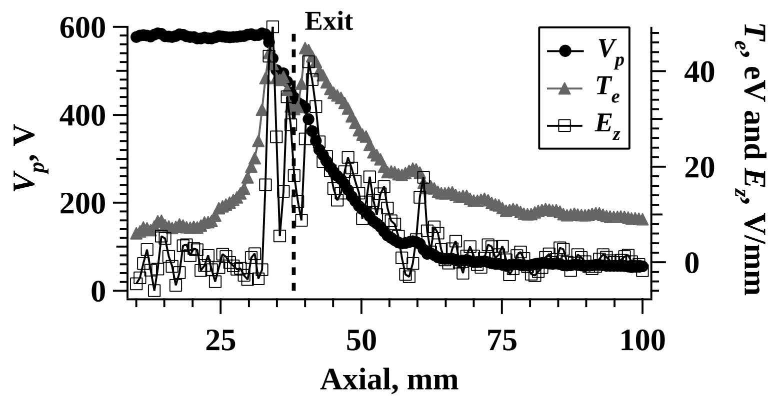

Figure C-12. Internal Langmuir Probe Centerline Properties for 500-V Krypton Operation with the Trim Coil and Matched Flow (Point C-5)

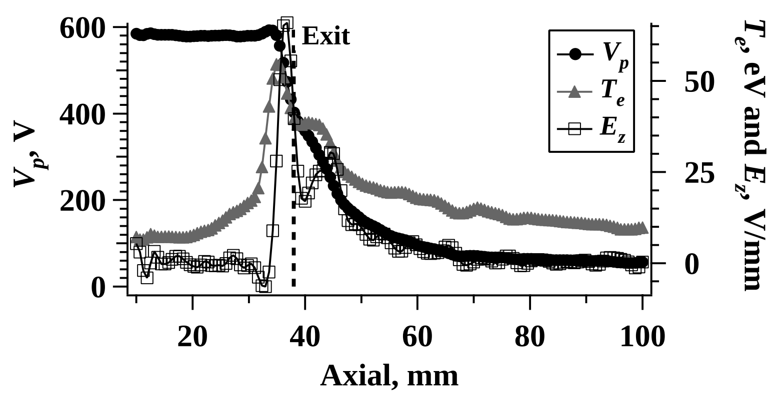

Figure C-13. Internal Langmuir Probe Centerline Properties for 500-V Krypton Operation with the Trim Coil and Matched Flow (Point C-6)

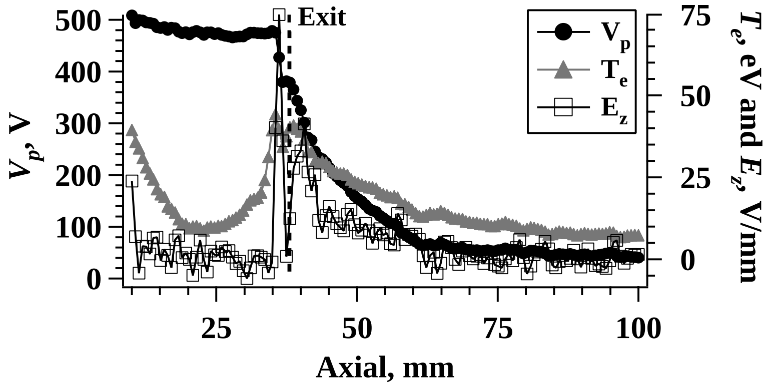

Figure C-14. Internal Langmuir Probe Centerline Properties for 500-V Krypton Operation with the Trim Coil and Matched Flow (Point C-7)

Appendix D.

Internal Langmuir Probe Results

Table D-1. Additional Operation Points for Internal Langmuir Probe Mapping

Point #	Propellant	V_k, V	V_d, V	I_d, A	Anode Flow, sccm	Cathode Flow, sccm	Inner Coil, A	Outer Coil, A	Trim Coil, A
D-1	Xenon	-13.3	300	8.94	102.4	10.24	1.89	2.21	0.00
D-2	Krypton	-15.5	500	7.36	102.4	10.24	1.57	2.17	-0.41
D-3	Krypton	-15.9	500	8.19	102.4	10.24	2.90	2.87	-0.87

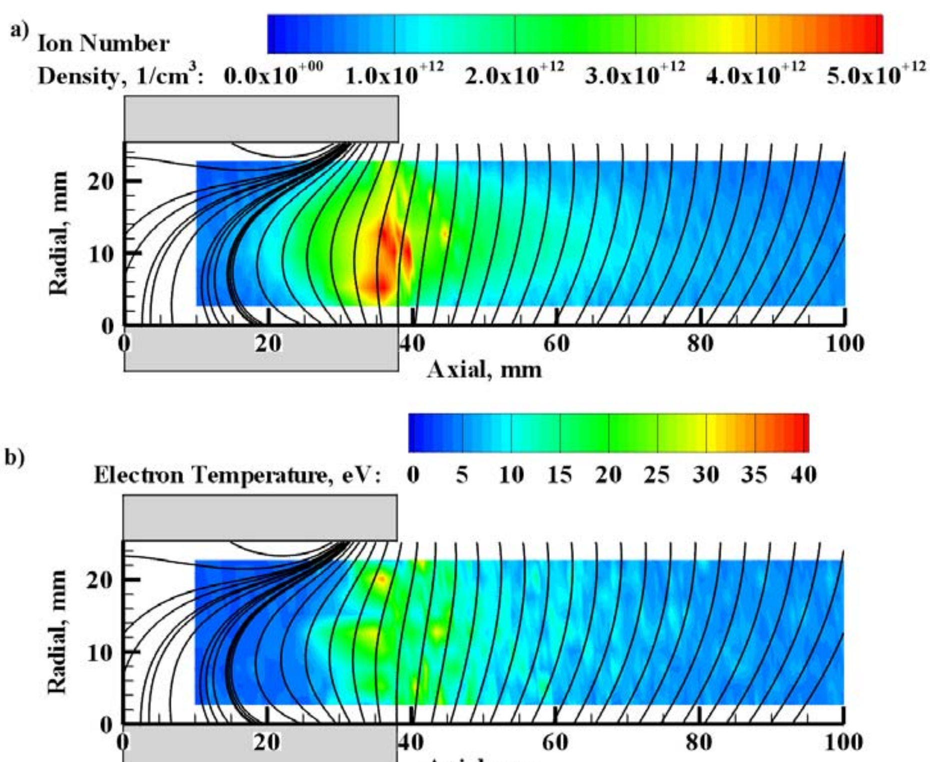

”

Figure D-1. Internal Langmuir Probe Results for 300-V Xenon Operation without the Trim Coil (Point D-1)

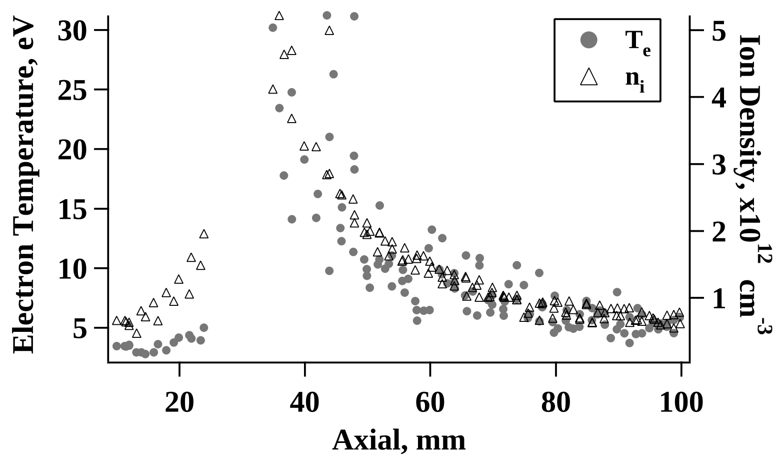

Figure D-2. Internal Langmuir Probe Centerline Properties for 300-V Xenon Operation without the Trim Coil (Point D-1)

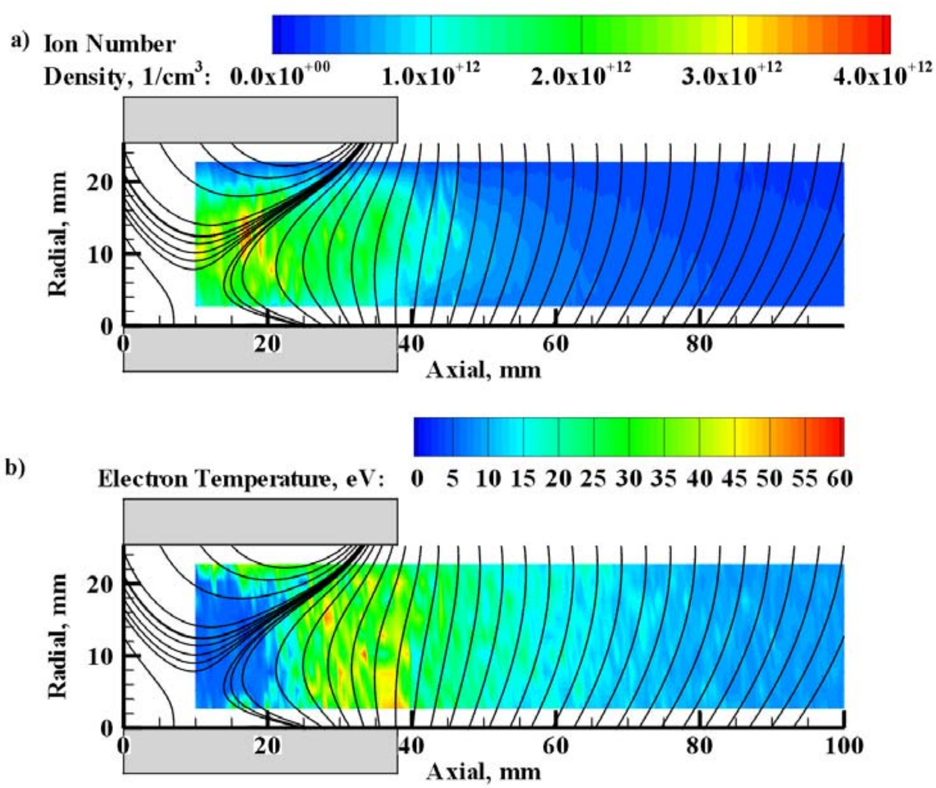

Figure D-3. Internal Langmuir Probe Results for 500-V Krypton Operation with the Trim Coil and Matched Flow (Point D-2)

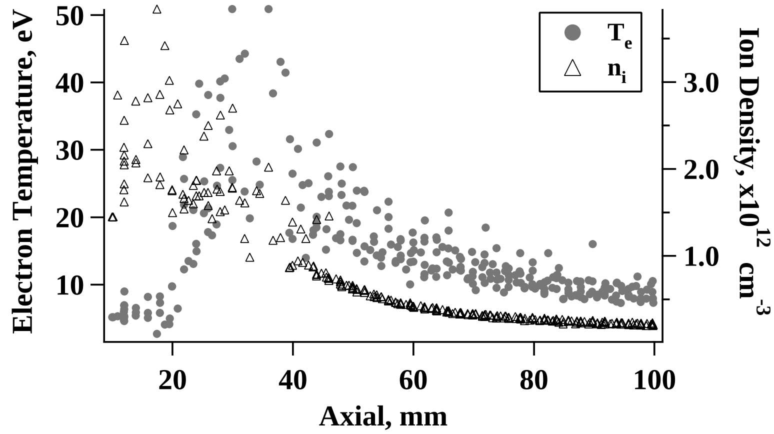

Figure D-4. Internal Langmuir Probe Centerline Properties for 500-V Krypton Operation with the Trim Coil and Matched Flow (Point D-2)

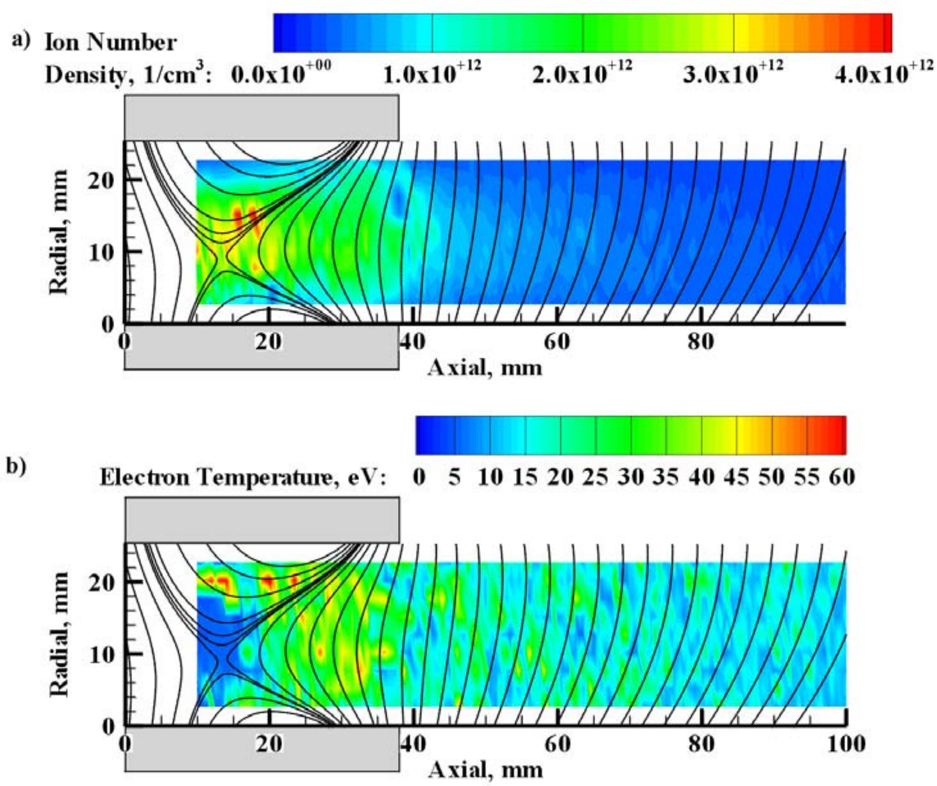

Figure D-5. Internal Langmuir Probe Results for 500-V Krypton Operation with the Matched B-Field and Matched Flow (Point D-3)

References

[1]Needham, J., *Science and Civilisation in China*, Vol. 7, 2, Cambridge University Press, 2004.

[2]Williams, B., Epstein, S., *The Rocket Pioneers: On the Road to Space*, Julian Messner, Inc., New York, 1955.

[3]Stuhlinger, E., *Ion Propulsion for Space Flight*, 1st ed. Ed., McGraw-Hill, New York, 1964.

[4]Johnson, W., "Contents and commentary on William Moore's a treatise on the motion of rockets and an essay on naval gunnery," International Journal of Impact Engineering, 16, 3, 499-521, 1995.

[5]Jahn, R. G., *Physics of Electric Propulsion*, McGraw-Hill Book Company, New York, 1968.

[6]Dunning, J. W., "NASA's Electric Propulsion Program - Technology investments for the new millennium," *37th AIAA/ASME/SAE/ASEE Joint Propulsion Conference and Exhibit*, AIAA-2001-3224, Salt Lake City, UT, July 8-11, 2001.

[7]Frisbee, R. H., Leifer, S. D., "Evaluation of propulsion options for interstellar missions," *34th Joint Propulsion Conference and Exhibit*, AIAA-1998-3403, Cleveland, OH, July 13-15, 1998.

[8]Frisbee, R., "Impact of Interstellar Vehicle Acceleration and Cruise Velocity on Total Mission Mass and Trip Time," *42nd AIAA/ASME/SAE/ASEE Joint Propulsion Conference and Exhibit*, AIAA-2006-5224, Sacramento, CA, July 9-12, 2006.

[9]Wertz, J. R., Larson, W. J., *Space Mission Analysis and Design*, 3rd Ed., Microcosm Press, Kluwer Academic Publishers, El Segundo, Dordrecht, Boston, London, 1999.

[10]Martinez-Sanchez, M., Pollard, J. E., "Spacecraft Electric Propulsion—An Overview," Journal of Propulsion and Power, 14, 5, 688-699, 1998.

[11]Pivirotto, T., King, D., Deininger, W., Brophy, J. R., "The design and operating characteristics of a 30-kW thermal arcjet engine for space propulsion," *22nd Joint Propulsion Conference*, AIAA-1986-1508, Huntsville, AL, June 16-18, 1986.

[12]Frisbee, R. H., "Advanced Space Propulsion for the 21st Century," Journal of Propulsion and Power, 19, 6, 1129-1154, 2003.

[13]Kim, V., "Main Physical Features and Processes Determining the Performance of Stationary Plasma Thrusters," Journal of Propulsion and Power, 14, 5, 736-743, 1998.

[14]Zhurin, V. V., Kaufman, H. R., Robinson, R. S., "Physics of Closed Drift Thrusters," Plasma Sources Science and Technology, 8, 1, R1-R20, 1999.

[15]Tverkokhlebov, S., Semenkin, A., Polk, J., "Bismuth propellant option for very high power TAL thruster," *40th Aerospace Sciences Meeting &Exhibit*, AIAA-2002-0348, Reno, NV, January, 2002.

[16]Belan, N. V., Kim, V. P., Oranskiy, A. I., Tikhonov, V. B., *Stationary Plasma Engines*, Khar'kov Karh'kovskiy Aviatsionnyy Institut, 1989.

[17]Grishin, S. D., Leskov, L. V., *Electric rocket engines for spacecraft*, Machinostroenie, Moscow, 1989.

[18]Tverdokhlebov, S. O., "Study of double-stage anode layer thruster using inert gases," *23rd International Electric Propulsion Conference*, IEPC-93-232, Seattle, WA, Sept. 13-16, 1993.

[19]Gavryushin, V. M., Kim, V., Kozlov, V. I., Maslennikov, N. A., "Physical and Technical Bases of the Modern SPT Development," *24th International Electric Propulsion Conference*, IEPC-1995-038, Moscow, Russia, Sept 19-23, 1995.

[20]Semenkin, A. V., Tverdokhlebov, S. O., Garcousha, V. I., Grishin, S. D., "Nonpropulsive application of the TAL technology," *25th International Electric Propulsion Conference*, IEPC-97-164, August 24-28, 1997.

[21]Semenkin, A. V., Gorshkov, G. O., "Study of Anode Layer Thruster Operation with Gas Mixtures," *24th International Electric Propulsion Conference*, 1995-078, September 1995.

[22]Arkhipov, B. A., et al., "The Results of Testing and Effectiveness of Kr-Xe Mixture Application in SPT," *27th International Electric Propulsion Conference*, 2001-064, Pasadena, CA, October 2001.

[23]Bugrova, A. I., Lipatov, A. S., Morozov, A. I., Churbanov, D. V., "On a Similarity Criterion for Plasma Accelerators of the Stationary Plasma Thruster Type," Technical Physics Letters, 28, 10, 821-823, 2002.

[24]Bugrova, A. I., Lipatov, A. S., Morozov, A. I., Solomatina, L. V., "Global Characteristics of an ATON Stationary Plasma Thruster Operating with Krypton and Xenon," Plasma Physics Reports, 28, 12, 1032-1037, 2002.

[25]Bugrova, A. I., et al., "Integral and Spectral Characteristics of ATON Stationary Plasma Thruster Operating on Krypton and Xenon," *28th International Electric Propulsion Conference*, 366, Toulouse, France, March 17-21.

[26]Kim, V., et al., "Investigation of SPT Performance and Particularities of its Operation with Krypton and Xenon Mixtures," *27th International Electric Propulsion Conference*, 2001-065, Pasadena, CA, October, 2001.

[27]Marrese, C., et al., "An Investigation of Stationary Plasma Thruster Performance with Krypton Propellant," *31st AIAA/ASME/SAE/ASEE Joint Propulsion Conference*, AIAA-95-2932, San Diego, CA, July 10-12, 1995.

[28]Marrese, C., et al., "The D-100 Performance and Plume Characterization of Krypton," *32nd AIAA/ASME/SAE/ASEE Joint Propulsion Conference*, AIAA-96-2969, Lake Buena Vista, FL, July 1-3, 1996.

[29]Patterson, M. J., G. J. Williams, J., "Krypton Ion Thruster Performance," *28th AIAA/SAE/ASME/ASEE Joint Propulsion Conference and Exhibit*, 92-3144, Nashville, TN, July 6-8, 1992.

[30]Jacobson, D. T., Manzella, D. H., "50 KW Class Krypton Hall Thruster Performance," *39th AIAA/ASME/SAE/ASEE Joint Propulsion Conference*, AIAA-2003-4550, Huntsville, AL, July 20-23, 2003.

[31]Peterson, P. Y., Jacobson, D. T., Manzella, D. H., John, J. W., "The Performance and Wear Characterization of a High-Power High-Isp NASA Hall Thruster," *41st AIAA/ASME/SAE/ASEE Joint Propulsion Conference*, AIAA-2005-4243, Tucson, Arizona, 10-13 July 2005.

[32]Gulczinski, F. S., Spores, R. A., "Analysis of Hall-effect thrusters and ion engines for orbit transfer missions," *32nd Joint Propulsion Conference*, AIAA-1996-2973, Lake Buena Vista, FL, July 1-3, 1996.

[33]Fiehler, D., Oleson, S., "A Comparison of Electric Propulsion Systems for Mars Exploration," *39th AIAA/ASME/SAE/ASEE Joint Propulsion Conference and Exhibit*, AIAA-2003-4574, Huntsville, AL, July 20-23, 2003.

[34]Hofer, R. R., "Development and Characterization of High-Efficiency, High-Specific Impulse Xenon Hall Thrusters," Doctoral Thesis, Dept. of Aerospace Engineering, University of Michigan, Ann Arbor, MI, 2004.

[35]Kieckhafer, A., King, L. B., "Energetics of Propellant Options for High-Power Hall Thrusters," Journal of Propulsion and Power, 23, 1, 2007.

[36]Morozov, A. I., Melikov, I. V., Journal of Technical Physics, 44, 544, 1974.

[37]Melikov, I. V., Morozov, A. I., Plasma Physics, 3, 388, 1977.

[38]Arkhipov, B. A., Khoromsky, I. A., Murashko, V. M., "Problems of Designing EPSs with SPTs Working on Krypton-Xenon Mixtures," *38th AIAA Joint Propulsion Conference*, 2002-3682, Indianapolis, Indiana, 2002.

[39]Kim, V., Kozlov, V., Semenov, A., Shkarban, I., "Investigation of the Boron Nitride based Ceramics Sputtering Yield Under it's Bombardment by Xe and Kr ions," *27th International Electric Propulsion Conference*, 2001-073, Pasadena, CA, October, 2001.

[40]Messerole, J. S., "Launch Costs to GEO Using Solar-Powered Orbit Transfer Vehicles," AIAA-1993-2219, June 1993.

[41]Edelbaum, T. N., "Propulsion Requirements for Controllable Satellites," ARS Journal, 1079-1089, 1961.

[42]Frisbee, R., "Evaluation of High-Power Solar Electric Propulsion Using Advanced Ion, Hall, MPD, and PIT Thrusters for Lunar and Mars Cargo Missions," *42nd AIAA/ASME/SAE/ASEE Joint Propulsion Conference and Exhibit*, AIAA-2006-4465, Sacramento, California, July 9-12, 2006.

[43]O'Neill, M. J. e. a., "Recent Technology Advances for the Stretched Lens Array (SLA), a Space Solar Array Offering State of the Art Performance at Low Cost and Ultra-Light Mass," *31st IEEE Photovoltaic Specialist Conference*, Orlando, FL, January, 2005.

[44]Hofer, R. R., et al., "Evaluation of a 4.5 kW Commercial Hall Thruster System for NASA Science Missions," *42nd AIAA/ASME/SAE/ASEE Joint Propulsion Conference*, AIAA-2006-4469, Sacramento, CA, July 9-12, 2006.

[45]Oh, D. Y., "Evaluation of Solar Electric Propulsion Technologies for Discovery Class Missions," *41st AIAA/ASME/SAE/ASEE Joint Propusion Conference*, AIAA-2005-4270, Tucson, AZ, 10-13 July, 2005.

[46]Oleson, S. R., "Mission advantages of constant power, variable Isp electrostatic thrusters," *36th Joint Propulsion Conference*, AIAA-2000-3413, Huntsville, AL, July 17-19, 2000.

[47]Deep Space Network, Future Planning Missions Office, 2006 Discovery Aperture Fee Tool, http://deepspace.jpl.nasa.gov/advmiss/, December 7, 2006.

[48]Oleson, S. R., Sankovic, J. M., "Advanced Hall electric propulsion for future inspace transportation," Cleveland, OH, 2001.

[49]Oleson, S. R., "Advanced electric propulsion for RLV launched geosynchronous spacecraft," *26th International Electric Propulsion Conference*, IEPC-99-185, Kitakyushu, Japan, Oct. 17-21, 1999.

[50]Oleson, S., "Advanced propulsion for space solar power satellites," *35th AIAA/ASME/SAE/ASEE Joint Propulsion Conference and Exhibit*, AIAA-1999-2872, Los Angeles, CA, June 20-24, 1999.

[51]Raitses, Y., Guelman, M., Ashkenazy, J., Appelbaum, G., "Orbit Transfer with a Variable Thrust Hall Thruster Under Drag," Journal of Spacecraft and Rockets, 36, 6, 875-881, 1999.

[52]Dushman, S., *Scientific Foundations of Vacuum Technique*, Vol. 4, Wiley, New York, 1958.

[53]Lide, D. R., *CRC Handbook of Chemistry and Physics*, 73rd Edition Ed., CRC Press, Boca Raton, Ann Arbor, London, Tokyo, 1992.

[54]Dymond, J. H., Smith, E. B., *The Virial Coefficients of Pure Gases and Mixtures, a Critical Compilation*, Oxford University Press, New York, 1980.

[55]Hofer, R. R., Jankovsky, R. S., Gallimore, A. D., "High-Specific Impulse Hall Thrusters, Part 1: Influence of Current Density and Magnetic Field," Journal of Propulsion and Power, 22, 4, 721-731, 2006.

[56]Hofer, R. R., Jankovsky, R. S., Gallimore, A. D., "High-Specific Impulse Hall Thrusters, Part 2: Efficiency Analysis," Journal of Propulsion and Power, 22, 4, 732-740, 2006.

[57]Walker, M. L. R., "Effects of Facility Backpressure on the Performance and Plume of a Hall Thruster," Thesis, Dept. of Aerospace Engineering, University of Michigan, Ann Arbor, MI, 2005.

[58]Haas, J. M., "Low-perturbation Interrogation of the Internal and Near-field Plasma Structure of a Hall Thruster Using a High-Speed Probe Positioning System," Doctoral Thesis, Dept. of Aerospace Engineering, University of Michigan, 2001.

[59]Haas, J. M., Gallimore, A. D., "Internal Plasma Potential Profiles in a Laboratory-Model Hall Thruster," Physics of Plasmas, 8, 2, 652-660, 2001.

[60]Manzella, D. H., Jankovsky, R., Hofer, R. R., "Laboratory Model 50 kW Hall Thruster," *38th AIAA/ASME/SAE/ASEE Joint Propulsion Conference*, AIAA-2002-3676, Indianapolis, IN, July 7-10, 2002.

[61]Crow, E. L., Davis, F. A., Maxfield, M. W., *Statistics Manual*, Dover Publications, Inc, New York, 1960, 288.

[62]Beal, B. E., "Clustering of Hall Effect Thrusters for High-Power Electric Propulsion Applications," Doctoral Thesis, Dept. of Aerospace Engineering, University of Michigan, Ann Arbor, MI, 2004.

[63]Kim, S. W., "Experimental Investigations of Plasma Parameters and Species-Dependent Ion Energy Distribution in the Plasma Exhaust Plume of a Hall Thruster," Thesis, Dept. of Aerospace Engineering, University of Michigan, Ann Arbor, 1999.

[64]Hagstrum, H. D., "Auger Ejection of Electrons from Tungsten by Noble Gas Ions," Physical Review, 96, 2, 325-335, 1954.

[65]Rovey, J. L., Walker, M. L. R., Gallimore, A. D., Peterson, P. Y., "Evaluation of a Magnetically-Filtered Faraday Probe for measuring the ion current density profile of a

Hall thruster," *The 40th Joint Propulsion Conference*, AIAA-2004-3948, Fort Lauderdale, FL, July 11-14, 2004.

[66]Rovey, J. L., "Status of Faraday Cup Magnetic Filter Design," Memorandum, Univ. of Michigan, Ann Arbor, MI, December 19, 2002.

[67]Hofer, R. R., Walker, M. L. R., Gallimore, A. D., "A Comparison of Nude and Collimated Faraday Probes for use with Hall Thrusters," *27th International Electric Propulsion Conference*, IEPC-2001-020, Pasadena, CA, October 15-19, 2001.

[68]Brown, S. C., *Basic Data of Plasma Physics*, American Institute of Physics, New York, 1994, 336.

[69]Sovey, J. S., Patterson, M. J., "Ion Beam Sputtering in Electric Propulsion Facilities," *The 27th Joint Propulsion Conference*, AIAA-1991-2117, Sacramento, CA, June 24-27, 1991.

[70]Sakabe, S., Izawa, Y., "Cross Sections for Resonant Charge Transfers Between Atoms and Their Positive Ions: Collision Velocity < 1 a.u.," Atomic Data and Nuclear Data Tables, 49, 2, 257-314, 1991.

[71]Boyd, I. D., Dressler, R. A., "Far Field Modeling of the Plasma Plume of a Hall Thruster," Journal of Applied Physics, 92, 4, 1764-1774, 2002.

[72]Manzella, D. H., "Hall Thruster Ion Beam Characterization," *31st AIAA/ASME/SAE/ASEE Joint Propulsion Conference*, AIAA-1995-2927, San Diego, CA, July 10-12, 1995.

[73]Hofer, R. R., Gallimore, A. D., "Efficiency Analysis of a High-Specific Impulse Hall Thruster," *40th AIAA/ASME/SAE/ASEE Joint Propulsion Conference*, AIAA-2004-3602, Ft. Lauderdale, Florida, July 11-14, 2004.

[74]Beal, B. E., Gallimore, A. D., "Energy Analysis of a Hall Thruster Cluster," *28th International Electric Propulsion Conference*, March 17-21.

[75]Hutchinson, I. H., *Principles of Plasma Diagnostics*, Second Ed., Cambridge University Press, 1990, 384.

[76]Smith, T. B., Ngom, B. B., Linnell, J. A., Gallimore, A. D., "Diode Laser-Induced Fluorescence of Xenon Ion Velocity Distributions," *41st AIAA/ASME/SAE/ASEE Joint Propulsion Conference*, AIAA-2005-4406, Tucson, AZ, July 10-13, 2005.

[77]Gulczinski, F. S., "Examination of the Structure and Evolution of Ion Energy Properties of a 5 kW Class Laboratory Hall Effect Thruster at Various Operational Conditions," Doctoral Thesis, Dept. of Aerospace Engineering, University of Michigan, Ann Arbor, MI, 1999.

[78]Reinsche, C. H., "Smoothing by Spline Functions," Numerische Mathematik, 10, 3, 177-183, 1967.

[79]Haas, J. M., Gallimore, A. D., McFall, K., Spanjers, G., "Development of a High-Speed, Reciprocating Electrostatic Probe System for Hall Thruster Interrogation," Review of Scientific Instruments, 71, 11, 4131-4138, 2000.

[80]Meezan, N. B., Hargus, W. A., Cappelli, M. A., "Anomalous Electron Mobility in a Coaxial Hall Discharge Plasma," Physical Review E, 63, 026410, 2001.

[81]Raitses, Y., Staack, D., Smirnov, A., Fisch, N. J., "Space Charge Saturated Sheath Regime and Electron Temperature Saturation in Hall Thrusters," Physics of Plasmas, 12, 073507, 2005.

[82]Raitses, Y., Staack, D., Keidar, M., Fisch, N. J., "Electron-Wall Interaction in Hall Thrusters," Physics of Plasmas, 12, 057104, 2005.

[83]Staack, D., Raitses, Y., Fisch, N. J., "Temperature Gradient in Hall Thrusters," Applied Physics Letters, 84, 16, 3028-3030, 2004.

[84]Linnell, J. A., Gallimore, A. D., "Internal Plasma Structure Measurements of a Hall Thruster Using Plasma Lens Focusing," *41st AIAA/ASME/SAE/ASEE Joint Propulsion Conference*, AIAA-2005-4402, Tucson, Arizona, July 10-13, 2005.

[85]Chen, F. F., "Electric Probes," Plasma Diagnostic Techniques, R. H. Huddlestone and S. L. Leonard, eds., Academic Press, New York,1965.

[86]Hobbs, G. D., Wesson, J. A., "Heat Flow Through a Langmuir Sheath in the Presence of Electron Emission," Plasma Physics, 9, 1, 85-87, 1967.

[87]Intrator, T., et al., "The Virtual Cathode as a Transient Double Sheath," Journal of Applied Physics, 64, 6, 2927-2933, 1988.

[88]Schwager, L. A., "Effects of Secondary and Thermionic Electron Emission on the Collector and Source Sheaths of a Finite Ion Temperature Plasma Using Kinetic Theory and Numerical Simulation," Physics of Fluids B: Plasma Physics, 5, 2, 631-645, 1993.

[89]Bohm, D., *The Characteristics of Electrical Discharges in Magnetic Field*, McGraw-Hill, New York, 1949.

[90]Riemann, K. U., "The Bohm Criterion and Sheath Formation," Journal of Physics D: Applied Physics, 24, 493-518, 1991.

[91]Keidar, M., Boyd, I. D., Beilis, I. I., "Plasma Flow in Plasma-Wall Transition in Hall Thruster Channel," Physics of Plasmas, 8, 12, 5315-5322, 2001.

[92]Raitses, Y., Staack, D., Dorf, L., Fisch, N. J., "Experimental Study of Acceleration Region in a 2 kW Hall Thruster," *39th Joint Propulsion Conference*, IEPC-2003-5153, Huntsville, Alabama, July 2003.

[93]Staack, D., Raitses, Y., Fisch, N. J., "Sheilded Electrostatic Probe for Nonperturbing Plasma Measurements in Hall Thrusters," Review of Scientific Instruments, 75, 2, 393-399, 2004.

[94]Dorf, L., Raitses, Y., Fisch, N. J., "Electrostatic Probe Apparatus for Measurements in the Near-Anode Region of Hall Thrusters," Review of Scientific Instruments, 75, 5, 1255-1260, 2004.

[95]Stephens, K. F., Ordonez, C. A., "Sheath and Presheath Potentials for Anode, Cathode and Floating Plasma-Facing Surfaces," Journal of Applied Physics, 85, 5, 2522-2527, 1999.

[96]Kagan, Y. M., Perel, V. I., Soviet Physics - Technical Physics, 13, 1348, 1969.

[97]Hershkowitz, N., Cho, M. H., "Measurement of Plasma Potential Using Collecting and Emitting Probes," Journal of Vacuum Science and Technology A, 6, 3, 2054-2059, 1988.

[98]Kemp, R. F., Sellen Jr., J. M., "Plasma Potential Measurements by Electron Emissive Probes," The Review of Scientific Instruments, 37, 4, 455-461, 1966.

[99]Haas, J. M., Gallimore, A. D., "An Investigation of Internal Ion Number Density and Electron Temperature Profiles in a Laboratory-Model Hall Thruster," *36th AIAA/ASME/SAE/ASEE Joint Propulsion Conference*, AIAA-2000-3422, Huntsville, AL, July 16-19.

[100]Rovey, J. L., "A Multiple-Cathode, High-Power, Rectangular Ion Thruster Discharge Chamber for Increasing Thruster Lifetime," Thesis, Dept. of Aerospace Engineering, University of Michigan, Ann Arbor, 2006.

[101]Herman, D. A., Gallimore, A. D., "Discharge Chamber Plasma Structure of a 40-cm NEXT-type Ion Engine," *41st AIAA/ASME/SAE/ASEE Joint Propulsion Conference*, AIAA-2005-4250, Tucson, AZ, July 10-13, 2005.

[102]Sengupta, A., et al., "Experimentally Determined Neutral Density and Plasma Parameters in a 30cm Ion Engine," *40th AIAA/ASME/SAE/ASEE Joint Propulsion Conference*, AIAA-2004-3613, Fort Lauderdale, FL, July 11-14, 2004.

[103]Jameson, K. K., Goebel, D. M., Watkins, R. M., "Hollow Cathode and Thruster Discharge Chamber Plasma Measurements Using High-Speed Scanning Probes," *29th International Electric Propulsion Conference*, IEPC-2005-269, Princeton, NJ, Oct. 31-Nov. 4, 2005.

[104]Goebel, D. M., Jameson, K. K., Watkins, R. M., Katz, I., "Hollow Cathode and Keeper-Region Plasma Measurements using Ultra-fast Miniature Scanning Probes," *40th*

AIAA/ASME/SAE/ASEE Joint Propulsion Conference, AIAA-2004-3430, Fort Lauderdale, FL, July 11-14, 2004.

[105]Martin, R. H., Farnell, C. C., Williams, J. D., "Direct and Remote Measurements of Plasma Properties nearby Hollow Cathodes," *29th International Electric Propulsion Conference*, IEPC-2005-294, Princeton, NJ, Oct. 31-Nov. 4, 2005.

[106]Langmuir, I., "The Interaction of Electron and Positive Ion Space Charges in Cathode Sheaths," Physical Review, 33, 6, 954-989, 1929.

[107]Mott-Smith, H. M., Langmuir, I., "The Theory of Collectors in Gaseous Discharges," Physical Review, 28, 4, 727–763, 1926.

[108]Passoth, E., et al., "An Experimental Study of Plasma Density Determination by a Cylindrical Langmuir Probe at Different Pressures and Magnetic Fields in a Cylindrical Magnetron Discharge in Heavy Rare Gases," Journal of Physics D: Applied Physics, 30, 1763-1777, 1997.

[109]Aikawa, H., "The Measurement of the Anisotropy of Electron Distribution Function of a Magnetized Plasma," Journal of the Physical Society of Japan, 40, 6, 1741-1749, 1976.

[110]Massey, D., Kieckhafer, A., Sommerville, J., King, L. B., "Development of a Vaporizing Liquid Bismuth Anode for Hall Thrusters," *40th AIAA/ASME/SAE/ASEE Joint Propulsion Conference*, AIAA-2004-3768, Fort Lauderdale, FL, July 12-14, 2004.

[111]Chung, P. M., Talbot, L., Touryan, K. J., "Electric Probes in Stationary and Flowing Plasma: Part 1. Collisionless and Transitional Probes," AIAA Journal, 12, 2, 133-144, 1974.

[112]Hutchinson, I. H., *Principles of Plasma Diagnostics*, Second Ed., Cambridge University Press, Cambridge, 2002.

[113]Schott, L., *Plasma Diagnostics*, North-Holland Publishing Company, Amsterdam, Netherlands, 1968, 668-731.

[114]Laframboise, J. G., Parker, L. W., "Probe Design for Orbit-Limited Current Collection," Physics of Fluids, 16, 5, 629-636, 1973.

[115]Laframboise, J. G., Rubinstein, J., "Theory of a Cylindrical Probe in a Collisionless Magnetoplasma," The Physics of Fluids, 19, 12, 1900-1908, 1976.

[116]Steinbrüchel, C., Journal of the Electrochemical Society, 130, 648.

[117]Hershkowitz, N., "How Langmuir Probes Work," Plasma Diagnostics, O. Auciello and D. L. Flamm, eds., Academic Press, Inc., Boston, pp. 113-184,1989.

[118]Chen, F. F., "Langmuir Probe Analysis for High Density Plasmas," Physics of Plasmas, 8, 6, 3029-3041, 2001.

[119]Herman, D. A., "The Use of Electrostatic Probes to Characterize the Discharge Plasma Structure and Identify Discharge Cathode Erosion Mechanisms in Ring-Cusp Ion Thrusters," Thesis, Dept. of Aerospace Engineering, University of Michigan, Ann Arbor, 2005.

[120]Peterson, E. W., Talbot, L., "Collisionless Electrostatic Single-Probe and Double Probe Measurements," AIAA Journal, 8, 12, 2215-2219, 1970.

[121]Narasimhan, G., Steinbruchel, C., "Analysis of Langmuir Probe Data: Analytical Parametrization, and the Importance of the End Effect," Journal of Vacuum Science and Technology A, 19, 1, 376-378, 2001.

[122]Wetzel, R. C., Baiocchi, F. A., Hayes, T. R., Freund, R. S., "Absolute Cross Sections for Electron-Impact Ionization of the Rare-Gas Atoms by the Fast-Neutral-Beam Method," Physical Review A, 35, 2, 559–577, 1987.

[123]Ahedo, E., Escobar, D., "Influence of Design and Operation Parameters on Hall Thruster Performances," Journal of Applied Physics, 96, 2, 983-992, 2004.

[124]Barral, S., et al., "Wall Material Effects in Stationary Plasma Thrusters. II. Near-Wall and In-Wall Conductivity," Physics of Plasmas, 10, 10, 4137-4152, 2003.

[125]Morozov, A. I., Melikov, I. V., "Similitude in Hall-Current Plasma Accelerators," Soviet Physics - Technical Physics, 19, 3, 340-342, 1974.

[126]Bugrova, A. I., Maslennikov, N. A., Morozov, A. I., "Similarity Laws for the Global Properties of a Hall Accelerator," Soviet Physics - Technical Physics, 36, 6, 612-615, 1991.

[127]Kim, V., et al., "Development and Characterization of Small SPT," *34th AIAA/ASME/SAE/ASEE Joint Propulsion Conference*, AIAA-1998-3335, Cleveland, OH, July 13-15, 1998.

[128]Raitses, Y., Ashkenazy, J., Guelman, M., "Propellant Utilization in Hall Thrusters," Journal of Propulsion and Power, 14, 2, 247-253, 1998.

[129]Kieckhafer, A., Massey, D., King, L. B., Sommerville, J., "Effect of Segmented Anodes on the Beam Profile of a Hall Thruster," *40th Joint Propulsion Conference*, AIAA-2004-4101, Fort Lauderdale, FL, July 11-14, 2004.

[130]Wilbur, P. J., Brophy, J. R., "The Effect of Discharge Chamber Wall Temperature on Ion Thruster Performance," AIAA Journal, 24, 2, 278-283, 1986.

[131]King, L. B., "Transport-property and Mass Spectral Measurements in the Plasma Exhaust Plume of a Hall-effect Space Propulsion System," Thesis, Dept. of Aerospace Engineering, University of Michigan, Ann Arbor, 1998.

[132]Arkhipov, B. A., et al., "The Results of 7000-hour SPT-100 Life Testing," *24th International Electric Propulsion Conference*, IEPC-95-39, Moscow, Russia, September 19-23, 1995.

[133]Mikellides, I. G., Katz, I., Kuharski, R. A., Mandell, M. J., "Elastic Scattering of Ions in Electrostatic Thruster Plumes," Journal of Propulsion and Power, 21, 1, 111-118, 2005.

[134]Morozov, A. I., Savel'ev, V. V., "Theory of the Near-Wall Conductivity," Plasma Physics Reports, 27, 7, 570, 2001.

[135]Yano, M., Walker, M. L. R., "Generalized Theory of Annularly-Bounded Helicon Waves," Physics of Plasmas, In Review, 2006.

[136]Yano, M., Walker, M. L. R., "Parametric Study of Annularly-Bounded Helicon Plasmas," Physics of Plasmas, In Review, 2006.

[137]Yano, M., Walker, M. L. R., "Plasma Ionization by Annularly-Bounded Helicon Waves," Physics of Plasmas, 13, 6, 2006.

[138]Beal, B., et al., "Development of an Annular Helicon Source for Electric Propulsion Applications," *42nd AIAA/ASME/SAE/ASEE Joint Propulsion Conference and Exhibit*, AIAA-2006-4841, Sacramento, California, July 9-12, 2006.

[139]Choueiri, E. Y., "Plasma Oscillations in Hall Thrusters," Physics of Plasmas, 8, 4, 1411-1426, 2001.

[140]Boeuf, J. P., Garrigues, L., "Low Frequency Oscillations in a Stationary Plasma Thruster," Journal of Applied Physics, 84, 7, 3541-3554, 1998.

[141]Fife, J. M., Martinez-Sanchez, M., Szabo, J., "A Numerical Study of Low-Frequency Discharge Oscillations in Hall Thrusters," *33rd AIAA/ASME/SAE/ASEE Joint Propulsion Conference*, AIAA-1997-3052, Seattle, WA, July 6-9, 1997.

[142]Hofer, R. R., Gallimore, A. D., "The Role of Magnetic Field Topography in Improving the Performance of High-Voltage Hall Thrusters," *38th AIAA/ASME/SAE/ASEE Joint Propulsion Conference*, AIAA-2002-4111, Indianapolis, IN, July 7-10, 2002.

[143]Gavryshin, V. M., Kim, V., Kozlov, V. I., Maslennikov, N. A., "Physical and Technical Bases of the Modern SPT Development," *24th International Electric Propulsion Conference*, IEPC-1995-038, Moscow, Russia, Sept 19-23, 1995.

[144]Morozov, A. I., "Focusing of Cold Quasineutral Beams in Electromagnetic Fields," Soviet Physics - Doklady, 10, 8, 775-777, 1966.

[145]Morozov, A. I., et al., "Effect of the Magnetic Field on a Closed-Electron-Drift Accelerator," Soviet Physics - Technical Physics, 17, 3, 482-487, 1972.

[146]Bugrova, A. I., Morozov, A. I., Popkov, G. B., Kharchevnikov, V. K., "Characteristics of a Plasma Lens," Soviet Physics. Technical Physics, 31, 2, 1986.

[147]Bishaev, A. M., Kim, V., "Local Plasma Properties in a Hall-current Accelerator with an Extended Acceleration Zone," Soviet Physics - Technical Physics, 23, 9, 1055-1057, 1978.

[148]Keidar, M., Gallimore, A. D., Raitses, Y., Boyd, I. D., "On the Potential Distribution in Hall Thrusters," Applied Physics Letters, 85, 13, 2481-2483, 2004.

[149]Keidar, M., Boyd, I. D., "On the Magnetic Mirror Effects in Hall Thrusters," Applied Physics Letters, 87, 121501, 2005.

[150]Hofer, R. R., Gallimore, A. D., "Recent Results from Internal and Very-Near-Field Plasma Diagnostics of a High Specific Impulse Hall Thruster," *28th International Electric Propulsion Conference*, IEPC-2003-037, Toulouse, France, March 17-21, 2003.

[151]Fruchtman, A., "The Effect of the Magnetic Field Profile on the Plume and on the Plasma Flow in the Hall Thruster," *29th International Electric Propulsion Conference*, IEPC-2005-068, Princeton, NJ, Oct-Nov 2006.

[152]Zharinov, A. V., Popov, Y. S., "Acceleration of plasma by a closed Hall current (Physical aspects of plasma accelerator using closed Hall currents, discussing equilibrium of forces and potential distribution)," Soviet Physics. Technical Physics, 12, 208, 1967.

[153]Raitses, Y., Keidar, M., Staack, D., Fisch, N. J., "Effects of segmented electrode in Hall current plasma thrusters," Journal of Applied Physics, 92, 9, 4906-4911, 2002.

[154]Yim, J. T., Keidar, M., Boyd, I. D., "An Investigation of Factors Involved in Hall Thruster Wall Erosion Modeling," *42nd AIAA/ASME/SAE/ASEE Joint Propulsion Conference*, AIAA-2006-4657, Sacramento, CA, July 2006.

[155]Anderson, J. D., *Modern Compressible Flow: With Historical Perspective*, 2 Ed., McGraw-Hill Publishing, 1990, Chap. 12.

[156]Tannehill, J. C., Anderson, D. A., Pletcher, R. H., *Computational Fluid Mechanics and Heat Transfer*, Second Ed., Taylor & Francis, Philadelphia, PA, 1997, 792.

[157]Nompelis, I., "Computational Study of Hypersonic Double-Cone Experiments for Code Validation," Doctoral Thesis, Dept. of Aerospace Engineering, University of Minnesota, Minnesota, 2004.

[158]Hofer, R. R., Gallimore, A. D., "Ion species fractions in the far-field plume of a high-specific impulse Hall thruster," *39th AIAA/ASME/SAE/ASEE Joint Propulsion Conference*, AIAA 2003-5001, Huntsville, Alabama, July 20-23, 2003.

[159]Keidar, M., Boyd, I. D., Parrilla, J., "Modeling of the Plasma Flow in High-Power TAL," *39th AIAA/ASME/SAE/ASEE Joint Propulsion Conference*, AIAA-2003-4701, Huntsville, AL, July 2003.

[160]Yim, J. T., Keidar, M., Boyd, I. D., "A Hydrodynamic-Based Erosion Model for Hall Thrusters," *29th International Electric Propulsion Conference*, IEPC-2005-013, Princeton, NJ, October 2005.

[161]Hargus, W. A., Cappelli, M. A., "Interior and Exterior Laser-Induced Fluoresence and Plasma Measurements with a Hall Thruster," Journal of Propulsion and Power, 18, 1, 159-168, 2002.

[162]King, L. B., "A (Re-) examination of Electron Motion in Hall Thruster Fields," *29th International Electric Propulsion Conference*, IEPC-2005-258, Princeton, NJ, Oct. 31 – Nov. 4, 2005.

[163]Chen, F. F., *Introduction to Plasma Physics and Controlled Fusion*, Vol. 1: Plasma Physics, Plenum Press, New York, 1984.

[164]Mutaa, H., Itagakib, N., Kawaib, Y., "Numerical investigation of the production mechanism of a low-temperature electron cyclotron resonance plasma," Vacuum, 66, 209–214, 2002.

[165]Hagelaar, G. J. M., Bareilles, J., Garrigues, L., Boeuf, J.-P., "Role of Anomalous Electron Transport in a Stationary Plasma Thruster Simulation," Journal of Applied Physics, 93, 1, 67-75, 2002.

[166]Fife, J. M., "Hybrid-PIC modeling and electrostatic probe survey of Hall thrusters," Doctoral Thesis, Dept. of Dept. of Aeronautics and Astronautics, Massachusetts Institute of Technology, Cambridge, MA, 1998.

[167]Ahedo, E., "Radial Macroscopic Model of a Plasma Flowing Along Annual Dielectric Walls," Physics of Plasmas, 9, 7, 3178-3186, 2002.

[168]Ahedo, E., Gallardo, J. M., Martinez-Sanchez, M., "Effects of the Radial Plasma-Wall Interaction on the Hall Thruster Discharge," Physics of Plasmas, 10, 8, 3397-3409, 2003.

[169]Morozov, A. I., et al., "Plasma Acceleration with Closed Electron Drift and Extended Acceleration Zone," Soviet Physics - Technical Physics, 17, 1, 38-45, 1972.

[170]Morozov, A. I., "Conditions for efficient current transport by near-wall conduction," Sov.Phys. Tech.Phys., 32, 8, 901-904, 1987.

[171]Bugrova, A. I., Morozov, A. I., Kharchevnikov, V. K., "Experimental investigation of near wall conductivity," Sov.Journal of Plasma Physics, 18, 963, 1992.

[172]Keidar, M., Boyd, I. D., "Progress in Hydrodynamic Modeling of Hall Thrusters," *29th International Electric Propulsion Conference*, IEPC-2005-044, Princeton, NJ, October 31 - November 4, 2005.

[173]Keidar, M., Beilis, I. I., "Electron Transport Phenomena in Plasma Devices With ExB Drift," IEEE Transactions on Plasma Science, 34, 3, 804-814, 2006.

[174]Ivanov, A. A., Jr., A. A. I., Bacal, M., "Effect of plasma–wall recombination on the conductivity in Hall thrusters," Plasma Physics and Controlled Fusion, 44, 8, 1463-1470, 2002.

[175]Sin Fai Lam, L. T., "Relativistic effects in electron scattering by atoms III. Elastic scattering by krypton, xenon and radon," Journal of Physics B: Atomic, Molecular and Optical Physics, 15, 119-142, 1982.

[176]Pack, J. L., R. E. Voshall, Phelps, A. V., Kline, L. E., "Longitudinal electron diffusion coefficients in gases: Noble gases," Journal of Applied Physics, 71, 11, 5363-5371, 1992.

[177]Fon, W. C., Berrington, K. A., Hibbert, A., "The elastic scattering of electrons from inert gases: IV. Krypton," Journal of Physics B: Atomic, Molecular and Optical Physics, 17, 3279-3294, 1984.

[178]Hayashi, M., "Determination of electron-xenon total excitation cross sections, from threshold to100 eV, from experimental values of Townsend's alpha," Journal of Physics B: Atomic, Molecular and Optical Physics, 16, 581-589, 1983.

[179]Morosov, A. I., "Stationary plasma thruster (SPT) development steps and future perspectives," *23rd International Electric Propulsion Conference*, IEPC-93-101, Seattle, WA, Sept. 13-16, 1993.

[180]Bugeat, J. P., Koppel, C., "Development of a second generation of SPT," *24th International Electric Propulsion Conference*, IEPC-95-35, Moscow, Russia, Sept. 19-23, 1995.

[181]Blinov, N. V., Gorshkov, O. A., Shagayda, A. A., "Experimental Investigation of Magnetic Field Topology Influences on Structure of Accelerating Layer and Performance of Hall Thrusters," *29th International Electric Propulsion Conference*, IEPC-2005-033, Princeton, NJ, Oct-Nov 2005.

[182]Gorshkov, O., Shagayda, A., Irishkov, S., "The Influence of the Magnetic Field Topology on Hall Thruster Performance," *42nd AIAA/ASME/SAE/ASEE Joint Propulsion Conference and Exhibit*, AIAA-2006-4472, Sacramento, California, July 9-12, 2006.

[183]Albarède, L., Mazouffrea, S., Bouchoule, A., Dudeck, M., "Low-frequency electron dynamics in the near field of a Hall effect thruster," Physics of Plasmas, 13, 063505, 2006.